Modeling the Influence of Cosmic Rays and Photons on the Gas Dynamics in Extreme Astrophysical Systems

Xiaoshan Huang

Chengdu, Sichuan, China

B.S. Applied Physics Sichuan University, 2015
M.S. Astronomy, University of Virginia, 2019

A Dissertation Presented to the
Graduate Faculty of the

University of Virginia

in Candidacy for the Degree of

Doctor of Philosophy

Department of Astronomy

University of Virginia
July 2023

Committee Members:
Shane W. Davis
Aaron S. Evans
Zhi-yun Li
David A. Nichols

iii

ABSTRACT

Radiation plays a unique role in a variety of astrophysical systems because it is both the major observation messenger and a key driver of dynamics. This dissertation discusses physics of astrophysical systems where radiation dominates either the dynamics or thermodynamics, including radiatively efficient accretion onto black holes and star formation feedback driven by radiation and cosmic rays. The new generation of wide-field variability surveys and multi-band extra-galactic surveys provide new constraints that challenge our theoretical pictures of these sources. Our current understanding is limited by the challenge of modeling radiation forces in complex, evolving geometries. This dissertation is putting effort to use state-of-the-art numerical tools, such as Athena++, to improve and expand our models of these systems.

The first three chapters are focusing on star formation feedback. Observations suggest that galactic outflow is ubiquitous, with complex multiphase structures that can be traced by molecular, weakly ionized and neutral gas. With significant mass and momentum loading, galactic outflows may be able to suppress or even quench star formation, acting as an important star formation feedback mechanism. It is still unclear, however, precisely what drives these outflows, although popular ideas include entrainment by hot winds from supernova activity, or *non-thermal* driving such as radiation or cosmic rays from star forming region.

Chapter 2 investigated radiation pressure's ability to launch molecular outflow. I study the dynamics of multiphase gas with high temperature contrast with full time-dependent calculation of a two-frequency-band (ultraviolet (UV) and infrared (IR)) radiation field. I find that in contrast to earlier works that focused solely on IR radiation, adding UV component is generally detrimental to cold gas survival during the acceleration, suggesting that radiation pressure acceleration is most promising where IR dominates the spectral energy distribution.

Chapter 3 focuses on cosmic rays (CRs) as another promising candidate for star formation feedback, which are charged particles originate from supernovae activity. I investigate CRs ability to expel ionized outflow from an originally warm, hydrostatic atmosphere. Similar to radiation, I explore the 'CR Eddington flux' for galaxies with given surface density and surface star formation rate. The 'CR Eddington flux' roughly quantifies CRs ability to disperse gas against gravity and launch outflow. I find that CRs are more likely to be important for galaxies falls on the higher surface density end of Kennicutt-Schmidt relation. Analyzing simulations, I found that the momentum transfer from CR to gas is usually efficient, but the energy transfer depends on various factors such as CR flux and the relative importance of diffusion and streaming.

Continuing investigating CR's role in feedback, I compare multiphase outflows driven by CRs and thermal wind in Chapter 4. Consistent with earlier studies without CRs, I find that when entrained in a hot wind, cold gas can grow instead of evaporate if radiative cooling in turbulent mixing layer is efficient. In contrast, for CR driving, cold gas mass generally decreases even with efficient cooling, albeit at a much slower rate. I show that such different cold gas evolution is related to the intrinsically different nature of CR and thermal pressure gradients near the multiphase interfaces, especially when streaming dominates CR transport. Such different pressure structure can lead to distinct multiphase structure when driven by CR or entrainment in hot wind. For example, they produce outflow with different characteristic column and velocity distributions that can potentially be testing by observations.

In Chapter 5, I discuss radiation's role in another regime: tidal disruption events, which are transient events powered by accretion near black holes. The disruption of a star by the tidal force from a supermassive blackhole can power a bright transient flare in multiple wavebands that lasts a few weeks to months. However, the origin of detected electromagnetic emission from tidal disruption events is an unresolved puzzle, especially the optical-ultraviolet emission. In this work, I study a potentially important pre-peak emission mechanism: stream-stream collision by series of three-dimensional radiation hydrodynamical simulations. I show that for a range of fallback rates, the stream-stream collision can efficiently convert debris' kinetic energy to radiation, powering prompt emission of $\sim 10^{42-44}$erg s^{-1}. n addition, I found that the strong radiation pressure can drive aspherical optical-thick outflow, creating photosphere roughly consistent with pre-peak optical observations. Extending this

work, I also introduce the follow-up research project in Chapter 6 to simulate the TDE fallback system in more global calculation domain, aiming to provide insights to the source of early TDE emissions in different wavebands.

"Radiation field and my dear cat Stormy, you both keep me up at night, and I will never fully understand you."

vi

ACKNOWLEDGEMENTS

I am incredibly lucky to have so much love and support from all the people around me, having you around is what hold my life together while I'm far from my families. It would be impossible to name each one of you, but here are some special thanks:

My Committee members: David, thank you generously being my committee member, it is such a great help in my overwhelmed time! Aaron, you helped me so much coordinating the defense, and always bring me cool insights for researches throughout all the 9999 meetings. Li, I enjoyed every research question from you, being your students and TA are my consistent happy experiences from beginning and to the end of grad school. Also thanks for being such a great DGS and handling my panic moments.

To my mom and dad, you are always so supportive and proud of me. I cannot possibly express how grateful I am to grow up having you by my side. I appreciated that you, at your very best, show me to always be open to the world around me, to be humble at highs and be kind at lows, to appreciate the joy of thinking, to enjoy nature, to love without fear, and most importantly, to be a kind person and eat vegetables (*yes mom, I don't have allergies, it's all in my head*). Thank you for always being there to back me up.

To my bigger families, grandma and grandpa, I had so many great Spring Festivals at your place. I know you probably will not be proud of me for all these research works (*yes grandma, radiation is bad for my health, I should never get close to it.*), you loved me just because who I am. To my cousins, Gengrong and Yidan, I never had a chance to have siblings, I (selfishly) tell others you are my siblings. Thank both of you for being there for me over some of my hardest time when I lost my dad. I wish you the best. To my cousin families, Liuliu, Peilong, Yuanguang, Zhaonan, your life stories inspire me and keep Chengdu close to me in my heart. Also congratulations

to your babies and becoming parents! We need to get hotpot together.

My deepest gratitude to my advisor, Shane. You are one of the biggest reasons I enjoyed graduate school and research. I am so thankful for all your advice, support, encouragement and patience. Your dedication to mentoring your students, caring for my career paths and personal well-being is a life-long gift for me. I am glad that couple weeks ago, we finally have the conversation of why we decided on our mentor-mentee relationship six years ago (under the supervision of Bri, Connor, Daniel, Huazhi and eleven beers you paid for us). It turns out the only reason is our bars were simultaneously low. Life is full of contingency but it rewarded me a great advisor, many exciting research topics, decent working ethic and philosophy I can carry on for a long, long time. I am so honored and grateful to be your first student, and to have the privilege of gaining so much from you.

I cannot be more thankful to my amazing collaborators: Yan-fei, you saved me so many times from running out of ideas and being stuck in research. Your encouragement of trying different possible solutions and learning new things constantly motivates me. It is such a pleasure to work and talk with you, I can't wait to see what's coming up next.

Enrico, thank you for hosting me warmly every time I'm in Santa Cruz. Discussing science with you is one of my favorite things in the seaside town, along with local coffee roasters and taquerias. You are so supportive in my chaotic times, and generously got me to meet many friendly fellow students and postdocs.

Connor, Bri and Sergei, I'm appreciated to have you around at UVa. Our (not-always-research-focused) group gathering is my safe place to ask silly questions and complain research difficulties, and how kind of you that always offering me discussion and ideas. Shane owe us a decent group lunch and a lot of sandwiches, I owe you a lot of baking goods.

Yiqing, I hesitated mention you as collaborator or friend. We became friends way before realizing our researches actually overlap, and our friendship grows working together. Our (not-strictly-) weekly star formation discussion maintained my mental wellness during COVID times, and everything I know about radio observation is from you. Walking Ellie together and spending time with Caroline made some of my favorite evenings in Charlottesville.

Sophie and Sierra, it cheers me up every time meeting up with you. I am proud to see the amazing progresses you made, and I am even more proud of how both of

viii

you choose to stay with all the transitions in your life.

And very importantly, to my partner and also my best friend, Huazhi. I am pretty sure I would not be able to finish all these works without you. Your unconditional support and love hold me together many times throughout grad school. People may see you as a smart and hard-working person, I cherish your gentle soul and big heart. Your words of "When I am $\sim 15cm$ from you, my gravity pull to you is the same as Jupiter's to you." demonstrate how "attractive" you are, and it makes me smile when I think of it (Sorry I never actually done the calculation, but now it's documented, hope you did the math right). My only complain is Stormy thinks you are the alpha cat in the house, I am jealous of that. Having you by my side is the firm source of my courage to face life. We boat against the current and drift with turbulence together, you are the Loaf of my life.

Danyang, I cannot count how many times we call each other in our happiest and lowest times. You know me too well, I am proud of our record of late night talks for ten years. Our life spiral up and down on different tracks, but your friendship is my constant safe house. I can't wait to be a godmother!

Thank you, Gabby and Whitney, you really build up astro department to be a warm place and make life much easier. Thanks for bringing cute puppies around and create a wholesome space!

To my dear, incredible fellow friends,

Bri, you feel like academic sister (or a true sisterhood) to me. We experienced many "first-times" together, and I'm glad we finally did the Cassertation talk as the best finale of grad school. For many times, your sweet friendship makes me feel like a person. We need to get more Almond bars, and you need to stop getting more cats (ok probably one more is fine). I am truly happy for every brave movement you have in your life, as you said, I'm excited to see where life takes us.

Lucia, your characters always bright up my days. It was such a precious time we spent together at the compact New York apartment in middle of the pandemic. We adventured the city and tried out good food. Spending time with you is so fun that I sometimes forget that we met on a working occasion as roommate, which could totally led to a different end. I am thankful that we take every chance to meet up and nurture our friendship.

Meng, or MSun, as you wish, you are still so far the only person I know from my undergrad school. You gave me encouragement and strength, as well as endless

meals. Thank you for keeping my heart soft, your passion to research and science is always inspiring.

Molly, I cannot imagine if you were not there for my grad school years. Thank you for being so inclusive to me, embracing my quirks and awkwardness. (Major) Tom is always cuddling and fluffy, I am glad Harvey is taking me in too.

My cohort, Bruce, Ian, Molly, I enjoyed having you there for the first year, and the southwest trip is so much fun. Mengyao and Yu, so glad to having you joining UVa, I miss the nights we spent in the basement office and the little adventure we made to Lovingston. Chris, Robby, David, Andy Lam, Having you in the office and fill the candy bar helped me survive the first few years. Matt, Thankful, Trey, thank you for always hosting social gathering and getting people together. All of you really build the community that embraces me at UVa astro, helped me feel settled in CVille.

My two Dark Sky, Bright Kids summer camps with Molly, Matt, Robby and Nick are my special summer memories. Thank you for taking good care of me. Your passion about spreading astronomy to broader community is so meaningful to me (" Put your butt on the chair and you'll get ice-cream", plus after-work beers, these are for sure all I learnt about child education). I also so much appreciate everyone's effort to keep DSBK running and flourishing.

To Andres, Alejandro, Lianis, who generously feed me snacks and offer me the magical couch for naps. Jordan, Nick, Hanna R., Abby, Deryl, Rachel, my office buddies, you are one of the main reason I drag myself out of bed and want to work in astro-building. Korash, Deven, Xinlun, Yisheng, Samer, Daniel, I wonder what is the mean free path we came across each other in astro-building, but it always lift my mind to chat with you.

Wanqi, I will not survive my first year without you. Thank you for sharing your life with me, feeding me well and cheer me up. I love every trip we made together. Yujia, my heart is sad about your leaving but my liver is probably happy. I'm surprised we can do morning hiking and late-night drinking together. Yuanyuan and Zhengkun, tennis with or without table are all so much fun. Xiaoting, Di, Yuan, Dijia, Tian, Wenhao, I feel so lucky to meet you at the last year of grad school. Board game nights and hearing Sociology and Architect give me fun breaks from Astronomy, cheers to Room 283 at Law library.

For my mom,

for all your love, your resilience and your kind heart.

Thank you for being the home I can always come back to.

For my dad,

I still think of the biking trip we did around the city along Fu-Nan River when I was a kid. Through my life, we had the greatest journey together.

Now you are my dark matter, I cannot see you anymore, but your love is the gravity I feel as always.

Table of Contents

LIST OF FIGURES

CHAPTER 1

AN INTRODUCTION TO NON-THERMAL ASTROPHYSICAL ENERGY SOURCES AND THEIR APPLICATION

1.1 INTRODUCTION TO MODELING PHOTONS AND COSMIC RAYS AS ASTROPHYSICAL FLUIDS

1.1.1 Constants in A Changing Universe: Momentum and Energy Budget

In the modern astrophysical point of view, our universe is a highly dynamic system. As we observe it with greater span in both space and time, we see the astrophysical events occurring on vastly different timescales, from transient events flickering between hours, to galaxy evolution that can take millions to billions of years.

One of the important aspects to understanding these astrophysical events is understanding the energy and momentum exchange among the components making up the system. The variety of extremely high energy sources of pressure in astrophysical systems can drive unique dynamics and largely determines the appearance of the observed universe. For example, in a star forming region, intense supernova explosions can release significant amounts of energy and change the surrounding pressure. Some of the energy heats up the materials that were originally bound to the star; some energy goes to push the surrounding interstellar gas, imparting momentum and

accelerates them, causing them to expand; some energy becomes the light that we observe. In many scenarios, we can directly observe electromagnetic signals carried by photons or high energy particles, or infer the energy and momentum distribution indicated by bulk motion of the gas. We gain first principle pictures of dynamical processes by analyzing the energy and momentum: where they possibly originate, how they transform and how they lead to what we observed.

1.1.2 A Brief Introduction to Cosmic Rays and Photons

In this dissertation, we focus on two of the important non-local energy sources in the interstellar medium and accreting systems: radiation energy and cosmic rays. Thermal energy is probably the most familiar form of energy to us. Any substance with non-zero temperature is emitting electromagnetic radiation, which is known as thermal radiation. Its spectral energy density can be well described by the black body distribution, therefore, the emission spectrum is solely determined by the local temperature. When radiation is well coupled to matter, we describe it as being in local thermodynamics equilibrium. Radiation, however, can travel larger distances between interactions with matter and in this case the radiation field can deviate strongly from local thermodynamic equilibrium. CRs, also being relativistic fluids, share similar properties. Although they interact (pitch angle scatter) with disturbances in the magnetic fields, they rarely collide directly with matter in typical interstellar medium conditions. Therefore, both CRs and photons can play an important and unique role in transfer momentum and energy across distances and scales in astrophysical environments.

Radiation plays a unique role in a variety of astrophysical systems because it is both the major observation messenger and a driver of dynamics. In the classical micro-physical view, a photon with frequency ν has energy $h\nu$ and momentum h/λ, where ν and λ are photon frequency and wavelength, and h is Planck constant. When photon flux interacts with interstellar gas, the momentum flux from photons can sometimes be the prevailing pressure, the energy flux received by observers indicates rich information about the emission source and mechanism.

CRs are charged relativistic particles that are thought to originate primarily from supernovae activity in star forming regions, When they are *streaming* along or *diffusing* through magnetic fields in the interstellar medium (ISM) or circumgalactic medium (CGM), they can interact with gas via magnetic fields, imparting energy

and momentum first to the field and then, ultimately, to gas. CRs can generate synchrotron radiation when they are gyrating along magnetic fields, radio astronomers refer to these synchrotron components seen in their data as the "non-thermal" emission, referring to these spectral energy in addition to the thermal continuum.

From a kinetic theory view, both CRs and photons can be considered as collections of relativistic particles. Therefore, the number of particles within a volume element centered on x and a momentum element centered on p in phase space can be described by their *distribution function* $f(\mathbf{x}, \mathbf{p}, t)$. The distribution function is determined by the physical processes in which photons or cosmic rays interact with matter or themselves. For CRs, primarily protons, usually the dominant force is the gyration force from background magnetic field. One can show that the Larmor radius is significantly smaller than astrophysical scales, so the distribution function is nearly independent of gyration phase. The interaction between CRs and disturbances (waves or turbulence) in magnetic field on length scale comparable to the Larmor radius that tend to isotropize their angular distribution in the rest frame of the disturbances.

Photons primarily interact with matter through emission, absorption, and scattering, which together determine their angular distribution. When absorption and scattering mean-free-paths are large compared to scales of the system, the angular distribution can deviate significantly from isotropy. In the following section, we discuss the numerical method and challenges of modeling radiation and CRs in astrophysical context.

1.2 NUMERICAL METHOD OF MODELING RADIATION AND COSMIC RAYS

The primary numerical tool we use in the dissertation is the finite volume Eulerian code Athena++ (Stone et al., 2020). Directly solving the Boltzmann equation for photons or Valasov equation for CRs will be numerically expensive. In Athena++, we treat CRs as a fluid by integrating their distribution function over angles, taking the first two moments two generate fluid-like equations representing conservation of energy and momentum. For the energy distribution, ground detection suggest that the CRs energy spectrum quickly falls off for energy higher than $\gtrsim 10^{10} eV$. Therefore, we assume the CR energy is dominated by $\sim$Gev CRs and solve a "grey" energy equation. The CR flux evolves according to the time-dependent momentum equation, assuming

isotropic pressure tensor.

The treatment for photons, however, is designed to evolve the possible complexity in the angular distribution. Instead of adopting a moment-equation scheme, we directly solve the radiation transfer equation (Jiang, 2021), which is equivalent to the photon Boltzmann equation. But, as in the case of CRs, we adopt a "gray" approach where we integrate over the photon energy (frequency) distribution. The current radiation transfer module in Athena++ applies Lorentz transformation to intensity, calculate radiation transfer equation source terms in comoving frame, then transform them back to lab frame. Gas and radiation are coupled by gas source terms, which are then obtained by taking moments of lab frame transfer equation source terms. Such a scheme dispenses with the expansion of gas source terms at $\mathcal{O}(v/c)$ that was often adopted in previous works.

RMHD in Athena ++

The explicit radiation transfer module in Athena++ solves the following frequency-integrated equations (Jiang, 2021).

$$\frac{\partial \rho}{\partial t} + \nabla \cdot (\rho \mathbf{v}) = 0, \tag{1.1}$$

$$\frac{\partial (\rho \mathbf{v})}{\partial t} + \nabla \cdot (\rho \mathbf{v}\mathbf{v} - \mathsf{P}) = -\mathbf{G} + \rho \mathbf{a}_{\mathrm{grav}} \tag{1.2}$$

$$\frac{\partial E}{\partial t} + \nabla \cdot [(E + P)\mathbf{v}] = -cG^0 + \rho \mathbf{a}_{\mathrm{grav}} \cdot \mathbf{v}, \tag{1.3}$$

$$\frac{\partial I}{\partial t} + c\mathbf{n} \cdot \nabla I = cS_I \tag{1.4}$$

$$S_I \equiv \Gamma^{-3}[\rho(\kappa_s + \kappa_a)(J_0 - I_0)$$
$$+ \rho(\kappa_a + \kappa_{\delta P})\left(\frac{a_R T^4}{4\pi} - J_0\right)] \tag{1.5}$$

$$cG^0 \equiv 4\pi c \int S_I d\Omega \tag{1.6}$$

$$\mathbf{G} \equiv 4\pi \int \mathbf{n} S_I d\Omega \tag{1.7}$$

Equation 1.1 - Equation 1.3 are hydrodynamic equations for gas, where ρ, $\mathbf{v}$, $E = E_g + (1/2)\rho v^2$ are fluid density, velocity and total energy density. We assume gas is ideal, so gas internal energy E_g and pressure P are related by $E_g = P/(\gamma - 1)$. P is the pressure tensor. In the right-hand side of Equation 1.2 and Equation 1.3, radiation couples with gas through the components of the radiation four force $-\mathbf{G}$ and $-cG^0$, which are the momentum and energy imparting from radiation to gas.

Equation 1.4 - Equation 1.7 represent the frequency integrated radiation transfer equation and the source terms couple to the gas momentum and energy. In the Athena++ implementation, the specific intensities I are first transformed to the fluid comoving frame, where the opacities and emissivities are the simplest. The radiation source terms S_I, $\mathbf{G}$ and cG^0 are evaluated and updated implicitly along with the comoving frame gas internal energy equation. The intensities are then transformed back to the lab frame, and the resulting source terms are evaluated by integrating the intensities over angle as described in Jiang (2021). Here, c is the light speed. I_0 and J_0 are the comoving frame intensity and mean intensity. $\Gamma = \Gamma(\mathbf{n}, \mathbf{v}) = \gamma(1 - \mathbf{n} \cdot \mathbf{v}/c)$ is the scaled Lorentz factor, with $\gamma = 1/\sqrt{1 - (v/c)^2}$ is the Lorentz factor. Equation 1.6 and 1.7 represent radiation's effect on gas energy and momentum. In the source term, a_R is the radiation constant, κ_s and κ_a are scattering opacity and Rosseland mean absorption opacity, $\kappa_{\delta P}$ is the difference between the Planck mean and Rosseland mean opacity.

$\mathbf{n}$ is the unit vector corresponding to rays in discretized angular grids, with the same angular discretization in Davis et al. (2012). In the simulations, we used $n_\mu = 3$ angles per octant, resulting $n_{\text{oct}} n_\mu (n_\mu + 1)/2 = 48$ angles in $n_{\text{oct}} = 8$ octants.

Please note that the radiation transfer module adopted in Section 2.2 is slightly different from above set of equations, with a two-band frequency-dependent treatment instead of grey radiation transfer. The frame transformation during calculating gas source terms are also slightly differently. We specify the details in Section 2.2.

CR MHD in Athena++

The CR-magneto hydrodynamic module in Athena++ solves the following equations based on the two-moment scheme (Jiang & Oh, 2018)

$$\frac{\partial \rho}{\partial t} + \nabla \cdot (\rho \mathbf{v}) = 0, \tag{1.8}$$

$$\frac{\partial (\rho \mathbf{v})}{\partial t} + \nabla \cdot (\rho \mathbf{v}\mathbf{v} - \mathbf{B}\mathbf{B} + \mathsf{P}^*) = \\ \sigma_{\mathrm{CR}} \cdot [\mathbf{F}_{\mathrm{CR}} - \mathbf{v} \cdot (E_{\mathrm{CR}}\mathsf{I} + \mathsf{P}_{\mathrm{CR}})] \quad , \tag{1.9}$$

$$\frac{\partial E}{\partial t} + \nabla \cdot [(E + P^*)\mathbf{v} - \mathbf{B}(\mathbf{B} \cdot \mathbf{v})] + \nabla \cdot \mathbf{Q} = \\ (\mathbf{v} + \mathbf{v}_{\mathrm{s}}) \cdot \sigma_{\mathrm{CR}} \cdot [\mathbf{F}_{\mathrm{CR}} - \mathbf{v} \cdot (E_{\mathrm{CR}}\mathsf{I} + \mathsf{P}_{\mathrm{CR}})] + Q_{\mathrm{cool}}, \tag{1.10}$$

$$\frac{\partial \mathbf{B}}{\partial t} - \nabla \times (\mathbf{v} \times \mathbf{B}) = 0, \tag{1.11}$$

$$\frac{\partial E_{\mathrm{CR}}}{\partial t} + \nabla \cdot \mathbf{F}_{\mathrm{CR}} = \\ -(\mathbf{v} + \mathbf{v}_{\mathrm{s}}) \cdot \sigma_{\mathrm{CR}} \cdot [\mathbf{F}_{\mathrm{CR}} - \mathbf{v} \cdot (E_{\mathrm{CR}}\mathsf{I} + \mathsf{P}_{\mathrm{CR}})] \tag{1.12}$$

$$\frac{1}{V_{\mathrm{m}}^2}\frac{\partial \mathbf{F}_{\mathrm{CR}}}{\partial t} + \nabla \cdot \mathsf{P}_{\mathrm{CR}} = \\ -\sigma_{\mathrm{CR}} \cdot [\mathbf{F}_{\mathrm{CR}} - \mathbf{v} \cdot (E_{\mathrm{CR}}\mathsf{I} + \mathsf{P}_{\mathrm{CR}})] \quad . \tag{1.13}$$

Here ρ, $\mathbf{v}$, E are fluid density, velocity and total energy, $\mathbf{B}$ is magnetic field strength. P^* is the sum of gas pressure and magnetic pressure, P^* is the corresponding pressure tensor. $\nabla \cdot \mathbf{Q}$ represents the energy change due to thermal conduction, where $\mathbf{Q} = -\kappa \nabla T$ is the heat flux and κ is the thermal conductivity. Q_{cool} is the external energy source terms.

Equation (1.12) and Equation (1.13) are the CR momentum and energy equation, i.e. the first and second moment integration over the energy and angle of the CR advection-diffusion equation (Skilling, 1971). The CR streaming velocity is $\mathbf{v}_{\mathrm{s}} = -\mathbf{sgn}(\mathbf{B} \cdot \nabla P_{\mathrm{CR}})\mathbf{v}_A$. It has the magnitude of Alfvén velocity and points opposite to the CR pressure gradient.

This CR transport description is based on the "self-confinement" assumption. In this framework, CRs excite Alfvén waves as they stream through the plasma. When the streaming velocity exceeds the local Alfvén velocity, the Alfvén wave is amplified and eventually saturates. As the Alfvén wave grows and perturbs the magnetic field, magnetic field irregularities will scatter the CRs and change their pitch angles, thus

reducing the CR streaming velocity to near the Alfvén speed. Hence, the CRs must stream at the Alfvén speed and down the CR pressure gradient. The resulting wave damping enables the momentum and energy exchange between CRs and gas.

E_{CR} and $\mathbf{F}_{\mathrm{CR}}$ are the cosmic ray energy density and flux. The two-moment scheme evolves the time-dependent Equation (1.13) to update $\mathbf{F}_{\mathrm{CR}}$, which differs from one-moment schemes that only evolve E_{CR} and prescribe a form for $\mathbf{F}_{\mathrm{CR}}$ based on E_{CR}. Such treatment is less diffusive for calculating the streaming velocity near the CR pressure gradient maximum, where the discontinuous streaming velocity is better captured. V_{m} is the maximum CR propagation velocity, which is assumed to be constant. It replaces the speed of light c in Equation (1.13) to relax the timestep. As long as V_{m} is significantly larger than the maximum flow or Alfvén velocity, the impact to gas dynamics is limited.

σ_{CR} is the CR-gas interaction coefficient:

$$\sigma_{\mathrm{CR}}^{-1} = \sigma_{\mathrm{CR}}^{\prime\,-1} + \frac{\mathbf{B}}{|\mathbf{B} \cdot (\nabla \cdot \mathsf{P}_{\mathrm{CR}})|} \mathbf{v}_{\mathrm{A}} \cdot (E_{\mathrm{CR}}\mathsf{I} + \mathsf{P}_{\mathrm{CR}}), \qquad (1.14)$$

where $\sigma_{\mathrm{CR}}^{\prime\,-1} = \kappa_{\mathrm{diff}}$ is the conventional CR diffusion coefficient. The second term is an effective streaming coefficient $\sigma_{\mathrm{str}}^{-1}$. The format indicates that streaming requires non-zero CR pressure gradient for the coupling between CR and gas.

1.3 APPLICATION: THE BIRTH AND DEATH OF STARS

1.3.1 The Feeding of Black Holes: Tidally Disrupted Stars and Subsequent Accretion

Supermassive blackholes sit in the center of most galaxies. They drive gas dynamics at large scale, impacting the star formation gas cycling and shaping galaxy evolution. Evidence from the highest redshift quasars suggests that these supermassive blackholes can grow to billions of solar masses in less than a billion years. At such high rates of growth, the accretion process is likely in the super-Eddington regime, where radiation force can be comparable to or larger than gravity. Such super-Eddington regime of blackhole accretion is not extensively observed and challenging to model theoretically. Gas that is being accreted at super-Eddington rates may radiate across the electromagnetic spectrum, offering constraints on blackhole growth and extreme relativistic physics. Tidal disruption events (TDEs) are ideal lab-

oratories to study super-Eddington accretion. Stars that wander too close to these (supermassive) blackhole in galaxies can be disrupted by the strong tidal force. The stellar debris is likely to form a thin, elongated stream that falls back onto the disrupting black hole. TDEs happen when the pericenter of star's orbit is within the tidal radius $R_{\mathrm{T}} = R_*(M_{\mathrm{H}}/M_*)^{1/3}$, where M_* and R_* are the mass and radius of the star, M_{H} is the mass of the blackhole. After disruption, roughly half of the material escapes the blackhole's gravity on hyperbolic trajectory, while the other bound half returns to the pericenter in highly eccentric orbit.

Such tidal destruction of stars and accretion of stellar debris can produce prominent emission, resulting in luminous transient events peaked in optical-ultraviolet (UV) or X-ray that declines over months to years. The decaying timescale often approximately follows the $t^{-5/3}$, which is set by the rate of debris returning to blackhole (Rees, 1988). The peak luminosity can be significantly super-Eddington for a $10^{5-6}M_\odot$ blackhole, the thermal emission from gas is at temperatures of about 10^{5-6} K. The *ROSAT* survey firstly detected TDE as strong X-ray flares from quiescent galaxies (Grupe et al., 1999; Greiner et al., 2000). Several similar X-ray events have been captured by *XXM-Newton* and *Chandra* subsequently (Lin et al., 2011; Saxton et al., 2012; Lin et al., 2018a; Wevers et al., 2019). These high spatial and spectral resolution data from *Chandra* and XXM-Newton Slew Survey reveals great diversity in TDEs, such as accretion around intermediate mass black holes (Lin et al., 2018b), TDEs in galaxy clusters (Maksym et al., 2013). The advent of extended, high-cadence monitoring on the X-ray light curves or spectra with *Swift* (Komossa, 2015; Gehrels & Cannizzo, 2015), has further aided the detection of TDEs. It also provides rapid follow-up observations for events identified by other transient surveys. These multiband observations provide well-covered light curves and sets constrains to the physics in these extreme environments.

Complementing these X-ray observations, the optical-UV is another important channel to detect TDEs. For example, the Galaxy Evolution Explore satellite (*GALEX*) discovered the first few optical-UV TDE candidates (Martin et al., 2005; Gezari et al., 2013). And a large fraction of TDEs are identified in optical transient sky surveys such as Sloan Digital Sky Survey (SDSS), Pan-STARRS, ASAS-SN and Zwicky Transient Facility (ZTF). Figure 1.1 shows inferred black body light curve for 17 ZTF and Swift/UVOT samples from Van Velzen et al. (2021). The optical events has typical rise with orders of 10 days, followed by months-long decay. The estimated black body
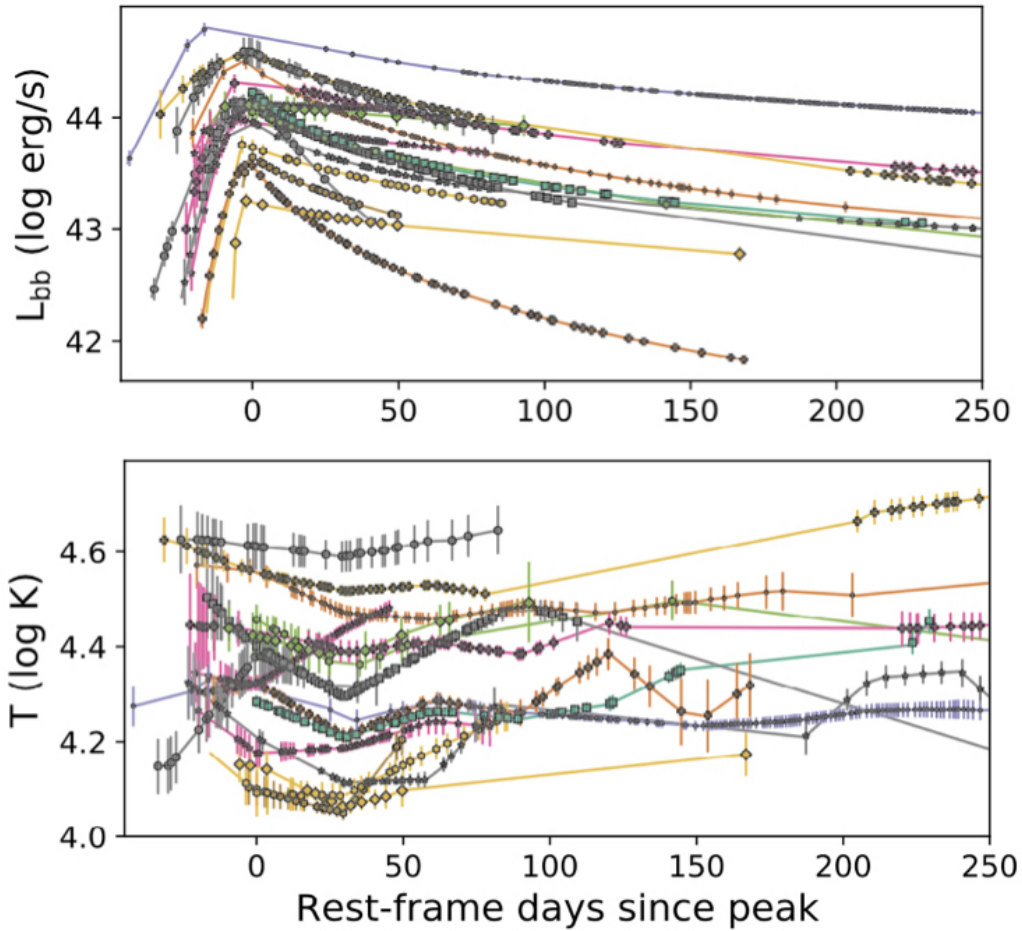
Figure 1.1: The inferred black body luminosity (upper panel) and rest-frame blackbody temperature (lower panel) for the 17 TDEs in sample with ZTF and Swift/UVOT observations, adapted from Van Velzen et al. (2021).

temperature are usually relatively constant in the decaying phase.

Interestingly, the optical-UV candidates and the X-ray identified candidates may represent different populations of sources. First, optical-UV bright TDEs rarely have X-ray emission. Second, the blackbody temperature of X-ray TDEs is about $\sim 10^{5-6}$K, which is consistent with the picture of emission from an accretion disk formed from the captured debris. However, the continuum temperature derived in optical-UV TDEs is usually an order of magnitude lower than the X-ray TDEs. In addition, the optical/UV candidates usually show more smooth light curves while the X-ray candidates tend to show more variability. As more TDEs are expected to be

discovered by *XXM*-Newton, Rubin Legacy Survey of Space and Time (LSST) and ULTRASAT, understanding the distinct views of TDE in optical-UV and X-rays is an important task and motivates further theoretical and numerical work.

1.3.2 The Feedback from Star Formation in Galaxies

The general picture that stars are formed from collapsing gas is widely agreed upon. However, it has long been a problem that the observed star formation rate (SFR) is usually below what is predicted by the simple assumption of gravitational collapse of gas clouds on dynamical timescales. Galaxy evolution simulations indicate that the energy and momentum feedback from star formation is a key component to explain the inefficient conversion from gas to stars in galaxies. Three popular mechanisms driving feedback in star forming galaxies include supernova, radiation, and cosmic rays. Such feedback can happen via numerous channels but the driving of (observed) outflows of multiphase gas via entrainment in a hot supernova-driven wind, radiation pressure on dust, or cosmic rays is likely important. Figure 1.2 shows the prominent, multiphase outflow observed from the starburst galaxy M82. The multiphase outflow has complex structure, revealing temperatures ranges from cold, molecular gas to hot to shock-heated x-ray gas.

There are a number of interesting studies that focus on each of these driving mechanisms, on both small scales that resolve individual clouds and local instabilities, as well as large scales where the gravitationally stratified gas disk or halo is modeled. A key question is the relative importance of different mechanisms. The answer almost certainly depends on the environment. For example, in the galaxies with efficient supernova activity, the pressure of supernova wind is able to expel warm or cold gas and suppress star formation. While in luminous infrared galaxies and ultra luminous infrared galaxies that usually are obscured by dust, simulations show that radiation pressure might efficiently transfer momentum to dust-coupled gas and drive cool outflow

Cosmic rays (CR), being roughly in energy equipartition in our local universe, have long been thought of as an attractive energy source. Recently numerical simulations further show that CRs are potentially able to drive warm outflow to a large distance (Wiener et al., 2019, 2017), help explain the observed SFR and modifies global galaxy properties such galactic disk morphology, and impact the gas content and ionization structure of circum-galactic medium (Butsky & Quinn, 2018; Buck

Figure 1.2: The starburst galaxy M82 seen in multi-wavelength. Optical light from stars (yellow-green/Hubble Space Telescope) shows the galaxy disk. The Spitzer Space Telescope infrared image (red) shows prominent outflow, where cool gas and dust are being enjected. Chandra's X-ray image (blue) reveals shock-heated hot gas that extend from the disk to outer radius of the galaxy. Credit: X-ray: NASA/CXC/JHU/D.Strickland; Optical: NASA/ESA/STScI/AURA/The Hubble Heritage Team; IR: NASA/JPL-Caltech/Univ. of AZ/C. Engelbracht

et al., 2019; Hopkins et al., 2020).

Given the complex nature of multi-phase gas in galactic winds and the environment-dependent validity of these feedback mechanisms, it is conceivable that instead of domination by a single feedback mechanism, these different sources of energy and momentum input might contribute to feedback simultaneously. Incorporating multiple outflow driven mechanisms in small scale simulations provides a consistent picture of the interaction between multi-phase gas and the various stellar momentum and energy sources, aiding the interpretation of observations and informing subgrid models of feedback in cosmological simulations.

Among the popular feedback mechanisms, CR and radiation pressure are perhaps the least well explored modes in numerical simulations, owing to the computational complexities and expense of their transport equations. For example, supernova winds are naturally described by the hydrodynamics or magnetohydrodynamic equations. In contrast, studying either radiation or CRs requires solving additional equations. For radiation, the angular-dependent nature of the radiation transfer equation creates a dilemma of either solving equations with approximations or solving equations with significant numerical cost. While for the CRs, numerical difficulties arise from the commonly used streaming prescriptions, as we discuss in the following section. We are also constrained by our limited observational knowledge about the physical properties of the radiation field and CRs in star forming galaxies.

Radiation Driven Molecular Outflow in LIRGs/ULIRGs

The star formation regions in galaxies differ from more quiescent galactic environments for the complex dynamics, versatile energy conversion and unique stellar population. The active star formation creates unusually high concentrations of glowing massive young stars, emitting at ultraviolet bands and ionizing surrounding gas up to $\sim 10^4$K. The radiation pressure from these young stars is thought to be one of the potential pressure sources that prevent gas clouds from collapsing into stars.

In addition to photon-ionization, the UV photons can be absorbed or scattered by dust grains and re-emitted as IR photons. Dust grains gain momentum from photons via these interactions, and collide with gas, the drag force allows momentum exchange between dust and gas. If the dusty gas gains sufficient momentum to escape the gravitational bound near the star forming region, it will likely become galactic outflow that further constrains the star formation processes. Murray et al. (2005)
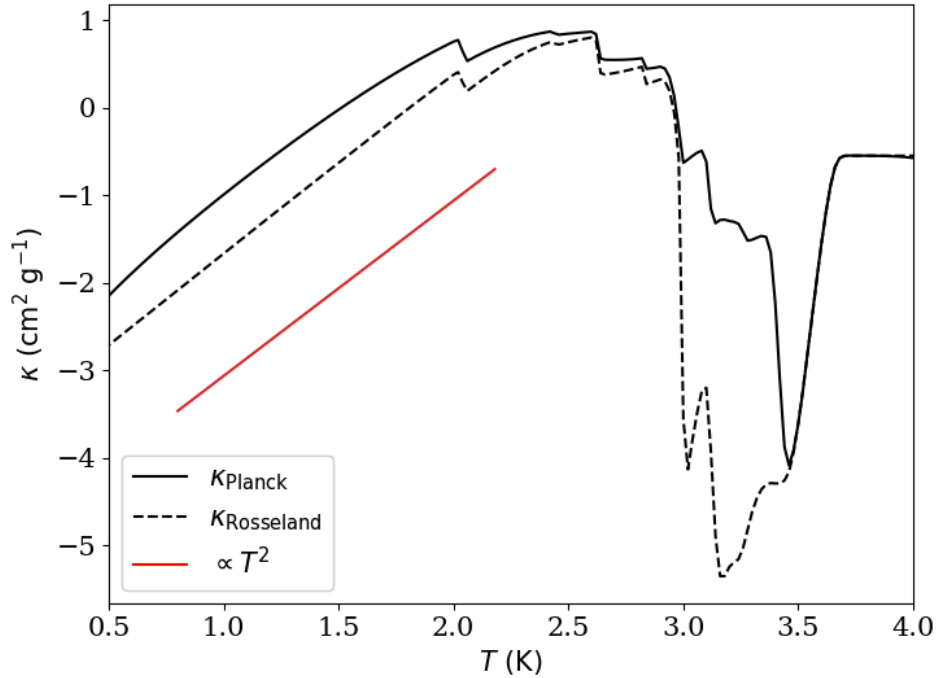
Figure 1.3: The Planck mean opacity (black solid line) and Rosseland mean opacity (black dashed line) with gas density $\rho = 10^{-19} g\ cm^{-3}$ with silicate dust model, generated from the public available code provided by (Semenov et al., 2003).

estimated that the dust and gas can be dynamically coupled by this way for hundreds of kpc, which is significantly larger than the scale of outflow launching. However, the dust particles may sublimate instead of grow if the temperature is too high. (Zhang, 2018) shows that the low density in dust driven wind, however, can lead to thermal decoupling between dust and gas, allowing a lower dust temperature than the surrounding gas environment, so dust can potentially survive in the wind with a temperature much higher than the dust sublimation temperature.

The dust opacity to UV radiation is usually high for molecular temperature. For example, Figure 1.3 shows an example of opacity function adapted from Semenov et al. (2003). Therefore, for typical surface density of starburst regions, the dusty gas is opaque to UV radiation. However, the radiation flux from some of the most extreme star-forming galaxies (luminous or ultraluminous IR galaxies, hereafter LIRGs and ULIRGs) are dominated by IR radiation reprocessed from UV.

Earlier numerical simulations found that the interaction between IR radiation and relatively optically-thin gas can be more complex than the analytical models. Due to a Rayleigh–Taylor-like instability developed at the interface between cold and hot gas, radiation can preferentially diffuse out from lower density channels without extensive interaction with gas (Jacquet & Krumholz, 2011; Krumholz & Thompson, 2012). Later numerical works with improved radiation transfer algorithms suggest that even if gas is optically thin to radiation and such instability creates multiphase gas structure, noticeable fractions of IR radiation momentum can be imparted to cold gas and launch galactic outflow (Jiang et al., 2013; Davis et al., 2014; Zhang et al., 2018).

These findings suggest that UV and IR radiation interacts with cold, dusty gas in significantly different ways, and dust is continuously reprocessing UV radiation to IR radiation. Hence, understanding the interplay between IR, UV radiation and multiphase gas is essential to resolving multiphase outflow structure. The problem is intrinsically challenging for numerical simulations because it requires accurate treatment of the dust-radiation interaction and tracking turbulent gas over a large distance.

Model Radiation-multiphase Outflow Interaction: Numerical Challenges

A classic set-up to study feedback-multiphase gas interaction is the so-called "wind-tunnel" simulations. Such set-up focuses on the dynamics of an individual cloud in multi-phase outflow at high resolution (Proga et al., 2014; Scannapieco & Brüggen, 2015; McCourt et al., 2015; Wiener et al., 2017; Scannapieco et al., 2020). This idealized set-up allows us to isolate the physical processes of the gas-radiation interaction and study them in detail. Cloud scale simulations can be helpful to quantify the momentum exchange between multiphase gas and the radiation field, both to evaluate the overall feasibility of the mechanism and better calibrate models of radiation feedback in large scale galaxy simulations.

Even with this simple set-up, the simulations are intrinsically challenging for several reasons. First, the radiation field that pushes on the cloud in our simulation is multi-band in order to better account for the spectral energy distribution (SED) of radiation from star forming galaxies. Unlike the assumption of grey opacity used in many previous studies, this allowed us to consider limits where the gas is either opaque or optically-thin to ultraviolet (UV) radiation, while optical-thin to infrared

(IR) radiation. When irradiated by UV radiation, the dust in the cloud will reprocess UV to IR radiation. Since we solve the radiation transfer equation directly for a large number of angles, even 2D simulations can be computationally intensive. Second, we need to study the dynamical process of cold gas moving at significant speed relative to a background medium that is 10^{5-6} times hotter. Given such strong temperature contrast and high relative speed, we need to resolve small scale turbulence and instabilities well and follow the cloud as it accelerates over large distances.

In order to better track gas evolution in the dynamical process, I also implemented a passive scalar module to the main code for this project. The scalar serves a dual purpose as it is used to implement a cloud following scheme where the simulation domain is boosted each time step to keep the majority of cold gas centered in the domain. It also allows us to track dust evolution which is essential because both UV and IR radiation pressure are dominated by dust.

Cosmic Rays as Source of Feedback

Cosmic rays (CRs) are another interesting possibility other than ram pressure or radiation pressure on dust for driving outflows. CRs originate from supernovae activity in star forming regions, *streaming* along or *diffusing* through magnetic fields in the interstellar medium or CGM. Given that CR's provide comparable energy density with thermal energy density and in magnetic field in local ISM, they may be an important source of heating and momentum in our galaxy. This may also be true in star forming galaxies. In fact, gamma-ray observations suggest that in some star burst galaxies, for example M82 and NGC253, CR energy density can be orders of magnitude higher than what it is in the Milkyway galaxy(VERITAS Collaboration et al., 2009; Paglione & Abrahams, 2012). Thus CR is recently thought to have an important impact on galaxy gas dynamics. While CR feedback has been a focus of recent research, however, inadequacies in our understanding of the properties of CR transport and how they couple to gas via irregularities in magnetic fields lead to significant uncertainties.

The recent re-emergence of interest in CR's role in star formation feedback has mainly focused on driving outflows or shutting down gas fall back(Socrates et al., 2008; Ruszkowski et al., 2017; Wiener et al., 2019a). A promising application is the driving of warm galactic outflows with temperature $\sim 10^4$K. Unlike a thermally driven wind, the CR driven wind does not experience rapid radiative cooling, so that less energy

may be radiated away. This can lead to a more robust acceleration mechanism, even if CRs represent a smaller fraction of the energy budget. There are also semi-analytical models showing that CR driven wind allows forming effective velocity profile that increases outward, in better agreement with observations.

Model Cosmic Rays Transportation: Numerical Challenges

Although CRs seems to be a promising feedback driving mechanism and source of free energy, the treatment of CR transfer in numerical simulations has been a challenge. This is partly due to uncertainties in the details of the CR transport model, but also due to numerical difficulties associated with the equations to be solved. A popular framework of CR transfer is "self-confinement". In this picture, when CRs stream through plasma, they excite Alfven waves. When the streaming velocity exceeds the Alfven velocity, Alfven waves are amplified. As the Alfven wave grows and saturates, the resulting perturbed magnetic field will scatter the CRs and change their pitch angle, thus reducing the CR streaming velocity to near the Alfven speed. So the CRs stream primarily along the magnetic field lines and down the CR pressure gradient. The wave damps in the gas via plasma damping, enabling momentum and energy exchange between CRs and gas.

The canonical treatment of CR transport in gas usually includes two pieces: streaming and diffusion. Interesting theoretical and simulation work has been performed in either limit. In this project, we plan to use magnetohydrodynamic (MHD) simulations to study CR driven galactic outflow with the two-moment scheme implemented in the Athena++ code (Jiang & Oh, 2018). The two-moment method has significant advantages over previous methods when streaming dominates and allows a more consistent calculation when both streaming and diffusion are present. Instead of using steady-state CR flux, the two-moment scheme solves an evolution equation for the CR flux (the CR momentum equation), which is the second moment of the advection diffusion equation for CR transport proposed by Skilling (1971) based on the "self-confinement" model. Solving separate CR energy and momentum equations also makes the code less diffusive because it better handles streaming velocity where the CR pressure gradient is flat.

CHAPTER 2

DUSTY CLOUD ACCELERATION WITH MULTIBAND RADIATION

2.1 INTRODUCTION

Galactic outflow are observed ubiquitously in star-forming galaxies (Veilleux et al., 2005). In many cases, the observed outflow rates and velocities imply the outflows must have an important impact in the evolution of galaxies. These outflows almost certainly play a role in regulating star-formation (e.g. Benson et al., 2003; Bower et al., 2012; Puchwein & Springel, 2013; Bolatto et al., 2013), but also affect the chemical evolution of galaxies as well as the circumgalactic and intergalactic medium (Aguirre et al., 2001; Erb, 2008; Finlator & Davé, 2008; Oppenheimer et al., 2010).

Multiphase winds have been observed in many star-forming galaxies, including molecular gas (e.g. Veilleux et al., 2009; Cicone et al., 2014; Walter et al., 2017; Oosterloo et al., 2017; Geach et al., 2018; Spilker et al., 2018; Leroy et al., 2015; Krieger et al., 2019), neutral atomic gas (e.g. Heckman et al., 2000; Rupke et al., 2002; Martin, 2005; Morganti et al., 2016; Schulz et al., 2018), and ionized gas (e.g Martin, 1998; Shopbell & Bland-Hawthorn, 1998; Muñoz-Vergara et al., 2019; Tadhunter et al., 2019). Although not observed directly, constraints on hot gas outflows are provided by X-ray observations of star forming galaxies (Strickland & Heckman, 2007; Zhang et al., 2014).

It has generally been believed that these outflows are driven primarily by supernova feedback. In high star formation rate galaxies, the overlapping supernova remnants merge to form giant bubbles of hot gas that break out of the cooler interstellar medium (ISM) gas. The cooler gas is then entrained in these hot outflows (Chevalier & Clegg, 1985a; Strickland & Heckman, 2009). However, it is not entirely clear that the much cooler gas will survive long enough to reach the inferred velocities due to shredding and mixing with the hotter background flow (Klein et al., 1994; Begelman & Fabian, 1990; Scannapieco & Brüggen, 2015; Zhang et al., 2018). One possibility is that magnetic fields suppress the disruption due, to purely hydrodynamics instabilities (McCourt et al., 2015; Banda-Barragán et al., 2016) but it is unclear if the magnetic field strengths and geometries are present in such outflows. Another possibility is that the gas is destroyed but condenses out of the hot flow due to radiative cooling at larger distances from the galaxy. (Thompson et al., 2016).

It is possible that a number of different acceleration mechanisms play a role in launching outflows, with different mechanisms possibly dominating in different environments or a different stages in the acceleration (Hopkins et al., 2012; Zhang, 2018). In addition to entrainment, plausible mechanisms include radiation pressure of starlight on dust (e.g. Murray et al., 2005, 2011), cosmic ray pressure (e.g. Ipavich, 1975; Socrates et al., 2008; Ruszkowski et al., 2017; Wiener et al., 2019b), and active galactic nuclei (Fabian, 2012; Heckman & Best, 2014).

In this work we focus on the role played by radiation pressure of starlight on dust. This mechanism has already been extensively studied with detailed radiation hydrodynamic numerical simulations at different scales and with varying assumptions and set-ups. An important question has been the role of Rayleigh-Taylor instabilities in limiting the effectiveness of acceleration (Krumholz & Thompson, 2012, 2013; Skinner & Ostriker, 2015). Despite the presences of such instabilities, it seems that some fraction of the radiation can be accelerated to large velocities (Davis et al., 2014; Tsang & Milosavljević, 2015; Zhang & Davis, 2017) and may allow cold gas to survive longer than entrainment allows (Zhang et al., 2018). With the exception of Skinner & Ostriker (2015), which studied the effect of radiation pressure in the local star cluster environment, most of these studies focus on infrared (IR) radiation pressure. This is sensible for considering the role of radiation pressure on galactic scales since the vast majority of the light in the most extreme star-forming galaxies (luminous or ultraluminous infrared galaxies, hereafter LIRGs and ULIRGs) is reprocessed into the IR.

However, most of the radiation originates from starlight radiated in the ultraviolet (UV) band. It is possible that UV plays a greater role in the launching of gas close to the star clusters or in galaxies which lower dust obscuration. Therefore, we are motivated to consider the relative role played by UV and IR opacities in accelerating clouds.

The plan of this paper is as follows. In section 2.2 we describe our numerical simulation methods and problem set-up. In section 2.3 we report on the results of variety of simulations with differing assumptions about parameters of interest such as IR to UV flux ratios, optical depths as well as sensitivity to assumptions in the numerical method and simulation set-up. We discuss the primary implications of our results in section 2.4 and summarize our conclusions in section 2.5.

2.2 METHOD

2.2.1 Radiation Hydrodynamics Equations

We solve the equations of hydrodynamic and radiation transfer using the Athena++ (Stone et al., 2020). As discussed in Chapter 1.2, the equations includes conservation of mass, momentum and energy. The source terms $\mathbf{G}$ and G_0 represent the components of the radiation four force, which are calculated by taking moments of the radiation transfer (RT) equation. The total energy density is

$$E = \frac{P}{\gamma - 1} + \frac{1}{2}\rho v^2, \tag{2.1}$$

where γ is the adiabatic index and the terms represent the gas internal energy and kinetic energy, respectively. The radiation four-force is computed from the specific intensity I_ν, which is evolved according to the time-dependent RT equation :

$$\frac{\partial I_\nu}{\partial t} + c\mathbf{n} \cdot \nabla I_\nu = S_\nu(\mathbf{n}). \tag{2.2}$$

Here $S_\nu(\mathbf{n})$ is the radiation source term, $\mathbf{n}$ represents a unit vector parameterizing the direction, and c is the speed of light. The RT equation is solved using an explicit-implicit scheme in Eulerian frame, similar to the method described in (Jiang et al., 2014). The main difference is that Jiang et al. (2014) evaluate radiation source

---

The RT equations and algorithm are slightly different from the RT method discussed in Chapter 1.2

terms in the Eulerian frame by expanding to second order in v/c. In the Athena++ implementations, the specific intensities are first transformed to the fluid comoving frame, where the opacities and emissivities are simplest. The relevant source terms are evaluated and updated implicitly along with the comoving frame gas internal energy equation. The resulting source terms are integrated over frequency and angle and then transformed back to the Eulerian frame.

In this work, we integrate Equation (2.2) over frequency assuming the radiation field can be approximated with two radiation band representing infrared (IR) and optical/ultraviolet (UV) contributions to the radiation field. The resulting RT equations solved are:

$$
\begin{aligned}
\frac{1}{c}\frac{\partial I_{\mathrm{uv}}}{\partial t} + \mathbf{n}\cdot\nabla I_{\mathrm{uv}} &= -\Gamma(\mathbf{n})\kappa_{\mathrm{uv}}\rho I_{\mathrm{uv}}, \\
\frac{1}{c}\frac{\partial I_{\mathrm{ir}}}{\partial t} + \mathbf{n}\cdot\nabla I_{\mathrm{ir}} &= \Gamma(\mathbf{n})\kappa_{\mathrm{ir}}\rho\left(\frac{a_r T^4}{4\pi} - I_{\mathrm{ir}}\right),
\end{aligned}
\tag{2.3}
$$

where a_r is the radiation constant. The subscripts uv and ir label the ultraviolet and infrared opacities and radiation fields, respectively. Note that we have assumed there is no source of UV emission within the domain and that the UV radiation is only provide from an external source via the boundary conditions. The $\Gamma(\mathbf{n})$ accounts for transformations between the comoving and Eulerian frames and corresponds to

$$
\Gamma(\mathbf{n}) = \gamma_{\mathrm{L}}\left(1 - \frac{\mathbf{v}\cdot\mathbf{n}}{c}\right),
\tag{2.4}
$$

where γ_{L} is the Lorentz factor. The specific intensities I_{ir} and I_{uv} are evaluated in the Eulerian frame and the opacities κ_{ir} and κ_{uv} are evaluated in the comoving frame. However, we emphasize that the differences between the comoving and Eulerian frames are quite small in these simulations. In the limit of zero velocity, the corresponding momentum and energy source terms are

$$
\mathbf{G} \to -\left(\frac{\kappa_{\mathrm{uv}}\rho}{c}\mathbf{F}_{\mathrm{uv}} + \frac{\kappa_{\mathrm{ir}}\rho}{c}\mathbf{F}_{\mathrm{ir}}\right),
\tag{2.5}
$$

$$
G_0 \to \kappa_{\mathrm{ir}}\rho(E_{\mathrm{ir}} - a_r T^4) + \kappa_{\mathrm{uv}}\rho E_{\mathrm{uv}}.
\tag{2.6}
$$

Here $\mathbf{F}_{\mathrm{ir}}$ and $\mathbf{F}_{\mathrm{uv}}$ are the IR and UV radiation flux, respectively, and E_{ir} and E_{uv} are IR and UV radiation energy density, respectively. These equations are approximate

because we have ignored the frame dependence in using the Eulerian frame radiation
fluxes and energy densities, but the correct covariant formulation is implemented in
the code.

The UV dust opacity κ_{uv} depends on dust grain sizes and species as well a fre-
quency, but we use a constant representative value. The IR opacity κ_{ir} is assumed
to be a temperature dependent Rosseland mean opacity using the approximation of
Krumholz & Thompson (2012). To focus on the cold cloud dynamics, we ignore the
scattering opacity, setting scattering opacity to zero. The dust opacity is

$$
\begin{aligned}
\kappa_{\mathrm{ir}} &= 10^{-3/2} \left(\frac{T}{10\mathrm{K}} \right)^2 s \ \mathrm{cm}^2/\mathrm{g}, \\
\kappa_{\mathrm{uv}} &= 100 s \ \mathrm{cm}^2/\mathrm{g}.
\end{aligned}
\tag{2.7}
$$

This assumes a Milky-Way-like dust-to-gas ratio and κ_{ir} is a reasonable approximation
for $T \lesssim 100\mathrm{K}$ and flattens at higher temperature(Semenov et al., 2003). Hence, we
assume a constant value of $10^{1/2}$ cm^2/g for $T > 100$ K. The quantity s represents a
scaled ratio of dust-to-gas fraction.

In order to track dust evolution, we initialize cold cloud gas with $s = 1$ and cells
in the hot background gas with $s = 0$. We then evolve s as a passive scalar via a
continuity equation

$$
\frac{\partial s}{\partial t} + \mathbf{v} \cdot \nabla s = 0,
\tag{2.8}
$$

which assumes that there is no source of dust other than the initial dust in the
cloud. However, we adopt a simple prescription to account for the decoupling and
destruction of the dust when it mixes with the hotter, less dense background gas,
setting the passive scalar to zero for cells above a fiducial temperature of 500K. This
is approximately the temperature where some of the grain constituents begin to be
destroyed (Pollack et al., 1994), resulting in drops in the opacity (Semenov et al.,
2003). Mixed gas at this temperatures also typically has densities low enough that it
is no longer clear that dust remains dynamically well-coupled with the gas, due to the
increase in the mean-free-path of dust-gas collisions (Krumholz & Thompson, 2013).
A more sophisticated model of grain-gas interaction and grain destruction will be of
interest in future studies but our simple scheme serves its primary purpose, which is
to decouple hotter and more diffuse gas from the radiation field. We choose 500K as
a conservative value but we have checked that increasing our decoupling/destruction

temperature to 1000K has no significant impact on our inferred survival times.

Since the transport portion of the transfer equation is solved explicitly, the Courant-Friedrichs-Lewy (CFL) condition in the code is set by the speed of light, which is much larger than the flow velocity or sound speed. Hence, it is advantageous to adopt the reduced speed of light approximation, where c in Equation (2.3) is replaced by $\tilde{c} = Rc$. Assuming $R \leq 1$ allows one to take time steps that are a factor of R^{-1} larger. As long as R is not chosen to be too low, the time-dependent term remains small and the radiation flux close to quasi-steady on the flow timescale.

The conditions for validity of reduced speed of light approximation are described by Skinner & Ostriker (2013) in section 3.2. The main constraint is the need to preserve the correct ordering of characteristic timescales. The light-crossing (i.e. radiation diffusion) time should always be smaller than the dynamical time. The radiation travels at reduced light speed $\min(\tilde{c}, \tilde{c}/\tau_{\max})$, where $\tau_{\max}$ is the maximum optical depth in the system. For a system with characteristic length l_0, $l_0/\min(\tilde{c}, \tilde{c}/\tau_{\max}) \ll l_0/v_{\max}$, where the dynamical timescale $l_0/v_{\max}$, v_{max} is the velocity determines the dynamical timescale. For the modest flow velocities and low optical depths considered here, these constraints are easily obeyed for $R = 0.01$.

2.2.2 Simulation Setup

We initialize all simulations with a cold dense cloud in pressure equilibrium with a hotter, less dense background gas. The cloud geometry is circular (2D) or spherical (3D) and it is initialized at rest in the center of the domain. A summary of simulation parameters is provided in Table 2.1. We initialize the cloud to our fiducial temperature $T_0 = 50$K. We define a corresponding characteristic flux $F_0 = ca_r T_0^4$. We first model the UV radiation from a galaxy or star-forming region within the galaxy as a constant uniform flux $F_{\mathrm{uv}} = 1.4F_0 \approx 4.9 \times 10^{12} \mathrm{L_\odot/kpc^2}$, and inject the radiation flux from the bottom boundary. The radiation flux in our simulation is scaled to the luminosity of ultraluminous infrared galaxies (ULIRGs). This choice of F_{uv} is about an order of magnitude smaller than typical IR radiation flux from ULIRGs (Zhang et al., 2018), which is higher than typically observed. We choose a high value for our fiducial flux to provide favorable conditions for acceleration, but consider lower values in other calculations. In Section 4.5 we discuss the impact of varying the radiation flux on cloud dynamics.

Given T_0, the characteristic speed v_0 is chosen to be the sound speed $c_{\mathrm{s}}^2 =$

$kT_0/(\mu m_H)$, and we assume the mean molecular weight $\mu = 1.0$ for simplicity. Zhang et al. (2018) showed that varying μ has limited impact on cloud dynamics. For our fiducial run, we choose a characteristic initial density $\rho_0 = 1.0 \times 10^{-19} \mathrm{g/cm^3}$. We applied a random perturbation on cloud density to make it moderately inhomogeneous. We set the characteristic length scale l_0 to the initial cloud diameter $D_\mathrm{c} = 0.4$ pc, which corresponds to a column density of $N_\mathrm{H} = 7 \times 10^{22}$ cm^{-2}. The corresponding initial optical depths to IR and UV radiation are $\tau_\mathrm{ir} = 0.1$ and $\tau_\mathrm{uv} = 12.7$, so the cloud is optically thick to the UV radiation and optically thin to IR emission. The cloud is embedded in the interstellar medium with temperature $T_\mathrm{bkgd} = 10^5 T_\mathrm{c} = 5 \times 10^5 \mathrm{K}$ and the background density is lower by 10^{-4} to maintain pressure equilibrium.

With T_0 and ρ_0 defined, we introduce two dimensionless parameters

$$\mathbb{P} = \frac{a_r T_0^4}{\rho_0 v_0^2}, \quad , \mathbb{C} = \frac{c}{v_0} \tag{2.9}$$

$\mathbb{P}$ represents the ratio of radiation pressure and gas pressure, $\mathbb{C}$ represents the ratio of light speed and sound speed. With $\mathbb{P}$ and $\mathbb{C}$, the hydrodynamic equations and RT equation can be written in dimensionless form (Jiang et al., 2014). The code solves the dimensionless versions of hydrodynamical equations, Equation 2.2 and Equation 2.8.

In the simulations, all the hydrodynamic boundaries are set to outflow boundary conditions. Except for the lower x boundary, all radiation boundary conditions are set to outflow boundaries. At the lower x boundary, we impose a uniform incoming radiation flux.

The vertical (x) and horizontal (y or z) sizes of the simulation domain are $10l_0$ and $4l_0$ respectively. We also put pressure floor $P_\mathrm{floor} = 10^{-5}\rho_0 v_0^2$ and density floor $\rho_\mathrm{floor} = 10^{-5}\rho_0$. We use $R = 10^{-2}$ and $C_{CFL} = 0.4$ for all 2D runs except TLUV_R, in which we use $R = 10^{-3}$. In TLUV_3D, we adopted $R = 10^{-2}$ and $C_{CFL} = 0.3$.

We find it useful to define the cloud mass as total mass of cold gas, which is tracked by dust and labeled by the passive scalar s. Then cloud mass is

$$M_\mathrm{c} \equiv \sum_i s_i \rho_i V_i \tag{2.10}$$

where i runs over every grid cell in the simulation domain and V_i is the volume of cell i.

Initially (at $t = 0$), the passive scalar is set to be $s = 1$ within the cloud, and

$s = 0$ in the background material. Hence, M_c is a representation of the mass of dusty gas within the calculation domain. At later times, the cloud mass is the initial mass $M_{c,0}$ minus the accumulative overheated gas mass:

$$M_c(t) = M_{c,0} - \int \dot{M}_{loss}(t)dt \qquad (2.11)$$

where $\dot{M}_{loss}(t)$ represents the sum of all gas that has exited the domain or been lost to mixing with the hotter background gas. Note that the latter mechanism (mixing with hot gas) is the dominant loss channel in all simulations.

In order to focus on cloud evolution, we adopted a cloud-following frame approach, so the center of mass of the cloud remains fixed in the calculation domain.

In the cloud following scheme, the x component of the mean velocity of dusty gas is computed at the end of every time step as

$$\Delta v_{mean} = \frac{\int v_x \rho s dV}{\int \rho s dV}. \qquad (2.12)$$

Then Δv_{mean} is subtracted from v_x for every cell in the simulation domain. These boosts are then summed to keep track of the velocity v_{mean} of the total cloud velocity after each time step. The hydrodynamics of the cloud is unaffected by these boosts due to the Gallilean invariance of the underlying hydrodynamic equations. In contrast, the radiation equations are not Galilean invariant but Lorentz invariant. Hence, the radiation intensities differ at second order in v/c from the true Eulerian frame. For the calculations presented here, thes discrepancies remain quite small and have almost negligible impact on our results.

2.2.3 A Simple Model

A characteristic hydrodynamical timescale is set by the sound crossing time:

$$t_0 = \frac{l_0}{v_0} \approx 6.25 \times 10^5 \left(\frac{50K}{T_0}\right) \left(\frac{l_0}{0.4pc}\right) \text{ yr.} \qquad (2.13)$$

There are several radiation timescales of interest. The first is the bulk acceleration timescale. We estimate this by ignoring the detailed geometry and assuming the cloud is an opaque rectangle with opacity κ_{uv}, density ρ_0 ,length $L_X \sim l_0$, and uniform UV flux F_{uv} along x direction. The radiation attenuates in the opaque cloud as

$F_{UV}e^{-\kappa_{uv}\rho_0 x}$. The equation of motion is then

$$\int \rho_0 \frac{dv}{dt} \, dx \, dA = \int \frac{\kappa_{uv}\rho_0}{c} F_{uv} e^{-\kappa_{uv}\rho_0 x} \, dx \, dA \qquad (2.14)$$

Integrating Equations (2.14) and assuming that the cloud is rigidly accelerated gives the average acceleration

$$a = \frac{d\langle v \rangle}{dt} = \frac{\kappa_{uv}F_{uv}}{c} \frac{1 - e^{-\tau_u}}{\tau_{uv}}, \qquad (2.15)$$

with $\tau_{uv} = \kappa_{uv}\rho_0 l_0$. When $\tau_{uv} > 1$, Equation (2.15) yields a characteristic acceleration rate $a \approx \kappa_{uv}F_{uv}/(c\tau_{uv}) \equiv a_{uv}$.

The UV radiation field heats the cold cloud while pushing on it. This heating is predominantly balanced by cooling via the IR radiation so we estimate the approximate cloud equilibrium temperature T_{eq} by setting the UV absorption rate to balance the IR emission rate

$$a_r \kappa_{ir}(T_{eq})T_{eq}^4 = \left(\frac{\kappa_{uv}F_{uv}}{c} + \frac{\kappa_{ir}F_{ir}}{c} \right). \qquad (2.16)$$

The resulting value is $T_{eq} = 129$K for the fiducial run.

The radiation field doesn't just accelerate and heat the cloud, but also acts to compress it. This is particularly true when the dusty cloud is opaque to the UV radiation and there is significant radiation pressure gradient across the cloud. If we neglect the internal pressure support of the cloud, the time to crush it is simply determined by the relative acceleration of the cloud surface relative to the cloud center. With this assumption, we define a radiation crushing timescale as

$$t_{rad} = \sqrt{\frac{l_0}{\Delta a_{uv}}} \qquad (2.17)$$

where $\Delta a_{uv} = \kappa_{uv}F_{uv}(1 - e^{-\tau_{uv}/2})/c$ represents the radiation acceleration difference between the outer radius of the the cloud and its center due to the self-shielding of the UV flux.

Table 2.1: Summary of Simulation Parameter

Name	τ_{IR}	τ_{UV}	$F_{UV}{}^a$	$F_{IR}{}^a$	$T_{\text{eq}}{}^b$	l_0 (pc)	$N_x \times N_z$
TLUV	0.1	12.658	2.0×10^3	0.0	2.58	0.4	1000×400
TSUV_L	0.01	1.266	2.0×10^3	0.0	2.58	0.04	1000×400
TSUV_D	0.01	1.266	2.0×10^3	0.0	2.58	0.4	1000×400
TSUV_DL	0.001	0.127	2.0×10^3	0.0	2.58	0.04	1000×400
TLIR_E	0.1	12.658	0.0	2.0×10^3	1.08	0.4	1000×400
TLIR_H	0.1	12.658	0.0	2.0×10^4	1.94	0.4	1000×400
TLMF_10	0.1	12.658	2.0×10^3	2.0×10^4	2.76	0.4	1000×400
TLMF_5	0.1	12.658	1.0×10^3	2.0×10^4	2.45	0.4	1000×400
TLMF_1	0.1	12.658	2.0×10^2	2.0×10^4	2.07	0.4	1000×400
TLUV_3D	0.1	12.658	2.0×10^3	0.0	2.58	0.4	$500^2 \times 200$
TLUV_HR	0.1	12.658	2.0×10^3	0.0	2.58	0.4	2000×800
TLUV_LR	0.1	12.658	2.0×10^3	0.0	2.58	0.4	500×200
TLUV_R	0.1	12.658	2.0×10^3	0.0	2.58	0.4	1000×400

[a] Flux in units erg/s/cm^2
[b] T_{eq} in units of $T_0 = 50$K

2.3 Results

We preformed a series of 2D and 3D simulations to study various factors that impact on the cloud dynamics. We list the relevant parameters used in all simulations in Table 2.1. First we report the fiducial run TLUV in Section 2.3.1, which is an opaque cloud accelerated by pure UV radiation flux. Parameters in this run were chosen with the expectation that they would provide favorable conditions for cloud survival. Next, we describe the impact of varying the optical depth in Section 2.3.2. Since the cloud responds differently to IR and UV radiation fluxes, we also report on the impact of varying the ratio of IR to UV flux in Section 2.3.3. We discuss the dependence of ours results on dimensionality, resolution, and our choice for the reduced speed of light in Section 2.3.4.

2.3.1 UV Optically Thick Cloud

The TLUV run examines an optically thick cloud irradiated by a large UV radiation flux. This setup assumes a rather large UV flux that would only be possible close to a very compact, high star formation rate region within a luminous galaxy.
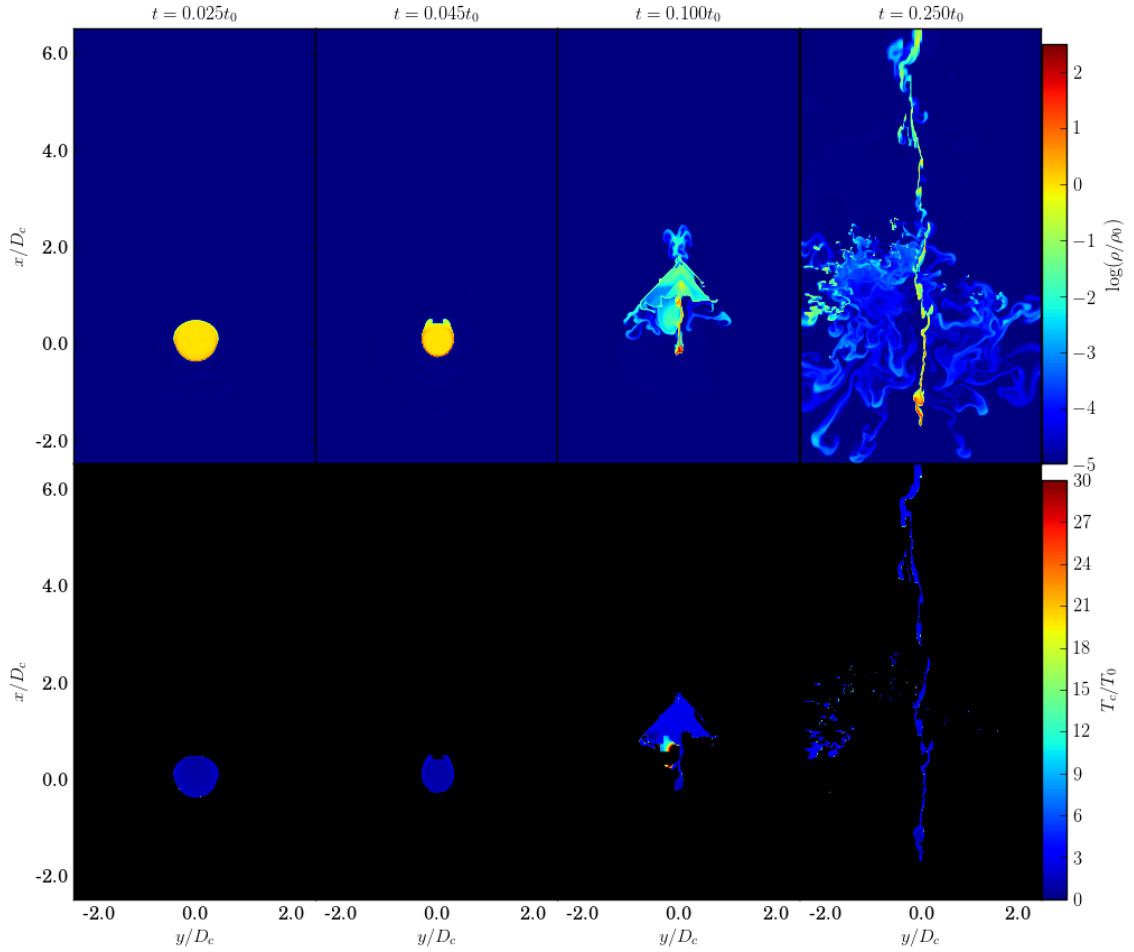
Figure 2.1: Simulation snapshots from TLUV. Top panels: density snapshots of both cold and hot gas. Lower panels: temperature of cold gas with pure background medium masked by black. The maximum temperature in color bar corresponds to the temperature at which we set the passive scalar to zero, representing the overheating of cold gas. $t_0 = 6.26 \times 10^5$yr, $l_0 = 0.4$pc, $\rho_0 = 10^{-19}$g/cm^3 and $T_0 = 50$K.

The column and gas density are also quite large, so much so that it would be unstable to gravitational collapse if self-gravity were modeled here. A large column is chosen because we would like to explore the optical depth effects on the cloud. This combination might be expected to be favorable to cloud acceleration (large UV flux) and survival (significant self-shielding).

In this run, $\tau_{\mathrm{ir}} = 0.1$, $\tau_{\mathrm{uv}} = 12.7$. The incoming radiation flux from the lower x boundary is pure UV flux. Figure 2.1 shows density and temperature snapshots from this simulation. The first row shows density of both hot and cold gas, the second row shows only temperature of dusty gas ($s \neq 0$). At early times $(t, 0.1t_0)$, the opaque cloud is compressed by the radiation pressure gradient within the cloud, which causes the side of the cloud facing the radiation field to be accelerated more strongly than the side opposite this face. Since the cloud is optically thick to UV radiation, radiation only directly acts on the gas near the cloud surface. A dense distorted front is formed, and Rayleigh-Taylor-like instabilities grow at the interface between the hot and cold gas. The interior of the cloud is shielded from radiation and stays cold. As the radiation continues compressing the cloud, the gas pressure increases, with the cloud reaching its volume minimum near $t \sim 0.1t_0$.

After this point the gas pressure gradient counterbalances radiation pressure, and the the cloud re-expands and loses its initial spherical symmetry. In the re-expansion phase, the dense core of the cloud remains cold ($T \sim T_{\mathrm{eq}}$) and is stretched slightly, primarily along the direction of motion. The lower density envelope of gas becomes turbulent and filamentary. Although the center of mass of the dusty gas remains fixed on the grid, the boosts associated with the cloud following scheme result in a significant velocity in the background medium towards the bottom x boundary, roughly at the value of v_{mean} in Figure 2.3. The combination of the large relative velocity of the background flow and the radiation pressure from the UV drive Kelvin-Helmholz like instabilities that facilitate the mixing with the hotter background gas. On any single time step, a small fraction of the gas is heated above the assumed destruction temperature. The detailed morphology of low density gas at late times is sensitive to the assumed initial condition, which we tested by considering different random perturbations, but the qualitative picture of compression, re-expansion, and mixing outlined here was qualitatively similar in all runs.

In Figure 2.2, the black solid line shows the evolution of the cloud mean velocity v_{mean} (top panel), velocity dispersion σ_v (middle panel) and cold gas mass M_{c} (bottom

panel). The black dashed lines in the first row is the velocity evolution corresponds to a constant acceleration at a (Equation 2.15). Despite the simplicity of the model, a provides a good estimation of cloud bulk acceleration within one radiation crushing time.

At around $t \approx 0.1 t_0$, the cloud acceleration drops relative to the a prediction. The cloud enters the re-expansnternalon phase and the velocity dispersion σ_v increases. The lower density outer layers of the cloud begin to mix with the background, exceeding 500K and are no longer considered part of the cloud mass even as outflow through the simulation boundary remains low. Hence, the cloud mass begins to drop significantly. We stop the simulation at $t = 0.2 t_0$, when outflow through the boundaries starts to become significant, but a large fraction of the initial cold cloud mass has already mixed with the background.

The black solid line in Figure 2.3 is the evolution of average density $\bar{\rho}$ and temperature $\bar{T}$ of cold gas in TLUV. The mean density rises as the radiation keeps compressing the cloud. After $t \sim 0.125 t_0$, $\bar{\rho}$ drops below the initial density later in the re-expansion phase. The average temperature of the cold gas is slightly below the estimated equilibrium temperature T_{eq} in the compression phase, and gradually rises toward $\approx T_{\mathrm{eq}}$ in the re-expansion phase. The average temperature is always well below the dust destruction temperature, indicating that only a small fraction of the dusty gas is mixing with the background on any time step. In other words, there is a continuous flux of cooler, higher density gas leaving the cloud, mixing with the background, and being destroyed. We emphasize that this process happens via mixing on the radiation hydrodynamic timescales. Efficient IR cooling prevents the radiation from simply over heating the cloud on the radiation crossing time.

2.3.2 UV Optically Thin Clouds

As noted above, the TLUV run corresponds to a rather large cloud mass and column. Here we consider UV optically thin runs, with lower cloud columns that might be more typical of outflowing gas in star forming environments. We studied two runs with optical depth of about unity, both with $\tau_{\mathrm{uv}} = 1.266$, a factor of 10 lower than TLUV. The UV optical depth $\tau_{\mathrm{uv}} = \kappa_{\mathrm{uv}} \rho_0 l_0$, can be made smaller by either reducing the radius or lowering the density. The cloud with lower density is in TSUV_D, the cloud with smaller radius is in TSUV_L. For a third run, TSUV_DL, we reduce both the density and length, giving $\tau_{\mathrm{uv}} = 0.127$. In all cases, the optical

depth to IR radiation τ_{IR} is reduced by the same factors.

Figure 2.2 compares the cloud bulk motion of optically thin clouds to the optically thick cloud in TLUV. In both TSUV_L (blue) and TSUV_D (green), estimated acceleration in Equation (2.15) (shown as a dashed curve) is about 10 times larger than TLUV. Both optically thin runs roughly follow this curve, falling slightly below during the re-expansion stages. The compression and re-expansion is qualitatively similar to what is seen in the TLUV run, leading to similar evolution of velocity dispersion and cloud mass, but occurring on an even shorter timescale. This is particularly notable for the cloud mass, which is substantially depleted by $t = 0.1t_0$, corresponding to physical timescales of 6.25×10^4yr. The TSUV_DL run is accelerated by greater amount consistent with the expectations from Equation (2.15) and the velocity dispersion tends to be lower. The mass loss initially follows the TSUV_L run and is destroyed on a comparable timescale.

Figure 2.4 compares the density snapshots of the optically thin clouds. The morphology and evolution of TSUV_L and TSUV_D are qualitatively similar. Due to the smaller optical depth, the radiation is more uniformly distributed than in the TLUV run. The clouds do not show a dense front at cloud-radiation interface like in TLUV, where the radiation is absorbed. Hence, the clouds are more uniformly compressed by radiation pressure at early times. As the clouds re-expand, the core of the dense gas is somewhat stretched along the direction of motion. As in TLUV, lower density gas pushed by both radiation pressure and the interaction with the background gas leading to a turbulent, filamentary structure. The low density regions ejected by the cloud mix with hot background, gradually heating the gas to the destruction temperature. The TSUV_DL run follows a similar evolution at early times, but there is much less overall compression because the radiation field is much more uniform. In fact, the average density in the cloud drops as the outer layers expand. Nevertheless, the subsequent evolution is qualitatively similar to the re-expansion phases of the other runs. Shear at the interface with the background ISM disrupts the cloud and drives mixing with the hotter background and heats the cold gas to $T > 500$ K.

Despite this overall similar acceleration and mass evolution, TSUV_D and TSUV_L show some modest dynamical differences due to the different densities and radii. Figure 2.3 shows the difference in their average density $\bar{\rho}$ and temperature $\bar{T}$. Note that TSUV_D has both lower cloud and background density, so the density and temperature contrast between the cloud and background is the same as TLUV. As noted
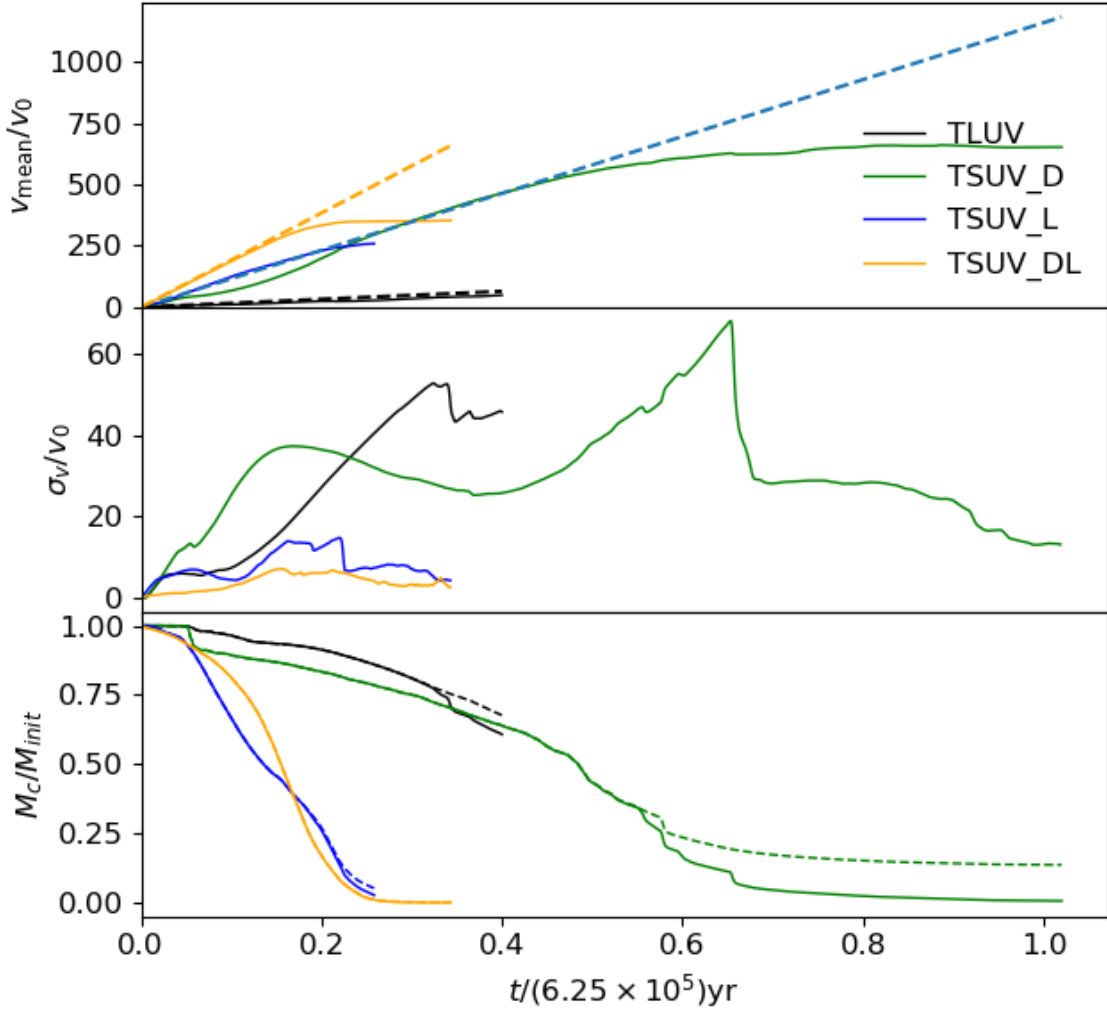
Figure 2.2: Mean velocity Δv_{mean} (top panel), velocity dispersion σ_v (middle panel) and cloud mass M_{c} (bottom panel) evolution of TLUV (black), TSUV_D (green), TSUV_L (blue) and TSUV_DL(orange). In the top panel, the dashed line with the same color is the time integration of a (Equation 2.15) of each run, excepting TLUV_D and TLUV_L has the same a. In the bottom panel, solid lines are M_{c}, dashed line with the same color is $M_{\mathrm{c}}(t)$ of each run. We ended the simulations when M_{c} and $M_{\mathrm{c}}(t)$ starts to diverge, meaning that cold gas exiting the simulation box starts to effect total mass loss. $v_0 = 0.64 \mathrm{km/s}$.
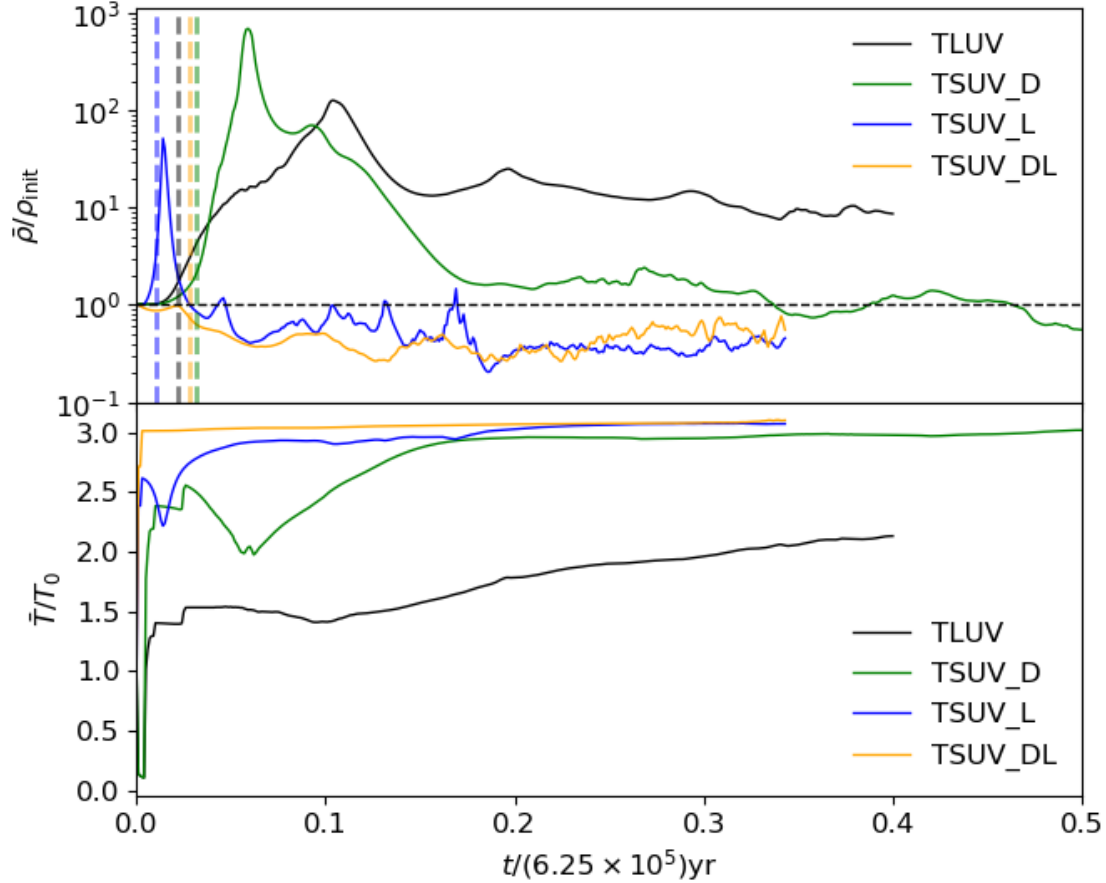
Figure 2.3: Average density (top panel) and temperature (bottom panel) of cold gas for TLUV (black), TSUV_D (green), TSUV_L (blue) and TSUV_DL (orange). $\rho_{\text{init}} = \rho_0 = 10^{-19}\text{g/cm}^3$. TSUV_D has lower $\rho_0 = 10^{-20}\text{g/cm}^3$. $T_0 = 50\text{K}$. The vertical dashed lines in the first row is the radiation crushing time t_{rad} for corresponding simulations.

above the TSUV_DL run does not show the compression and re-expansion behavior that is seen in the more optically thick runs. The mean density drops continuously. After an initial increase in temperature to slightly above the nominal T_{eq}, the temperature remains flat for the rest of the run, suggesting the optically thin cloud is in radiative equilibirium with the incoming radiation field. The evolution is roughly similar to the optically thin simulations in Proga et al. (2014), but with larger relative velocity between the cloud and background.

The differences in evolution between optically thick and optical depth unity runs can be attributed primarily to the gas pressure distribution within the clouds. Initially, both clouds are in pressure equilibrium with the background medium. After radiation has swept through the cloud, different parts of cloud experience different radiation forces. The radiation pressure gradients are modest in the optically thin runs but self-shielding leads to strong gradients in the UV optically thick run. These radiation pressure gradients compress the cloud until a comparable gas pressure gradient develops to oppose it. Figure 2.5 shows the pressure snapshots of TSUV_L, TSUV_D, TSUV_DL and TLUV at the same compression stage. TSUV_L and TSUV_D are at optical depths of unity, so the gas pressure gradient is relatively small. In contrast, the gas pressure is strongly enhanced near the surface in the optically thick TLUV runs (right). The outward pressure gradient forces supports the clouds and slow down the compression. TSUV_DL is even more optically thin and show almost no pressure gradient at early times.

Initially, these gas pressure effects are modest and our estimate of the cloud crushing time t_{rad} in Equation (2.17) yields a good order of magnitude estimate the time for both the optically thick and optical depth unity clouds to reach their maximum average density. However, if we look more quantitatively we can see the impact of the gas pressure gradient force, which is not accounted for Equation (2.17). Our estimates of t_{rad} are shown as vertical dashed lines in Figure 2.3. They provide better estimates of the time when the cloud reaches peak density in the two optical depth unity runs, but the maximum compression of the optically thick cloud is slightly delayed due to the resistance from the gas pressure gradient. Note that compression is somewhat faster in the TSUV_L run because $t_{rad} \propto \sqrt{l_0}$ and l_0 is smaller in this run. Modest compression does occur in the TSUV_DL run, but it doesn't show up in this average density plot because the outer envelope of the cloud expands by a greater amount than the core of the cloud contracts.
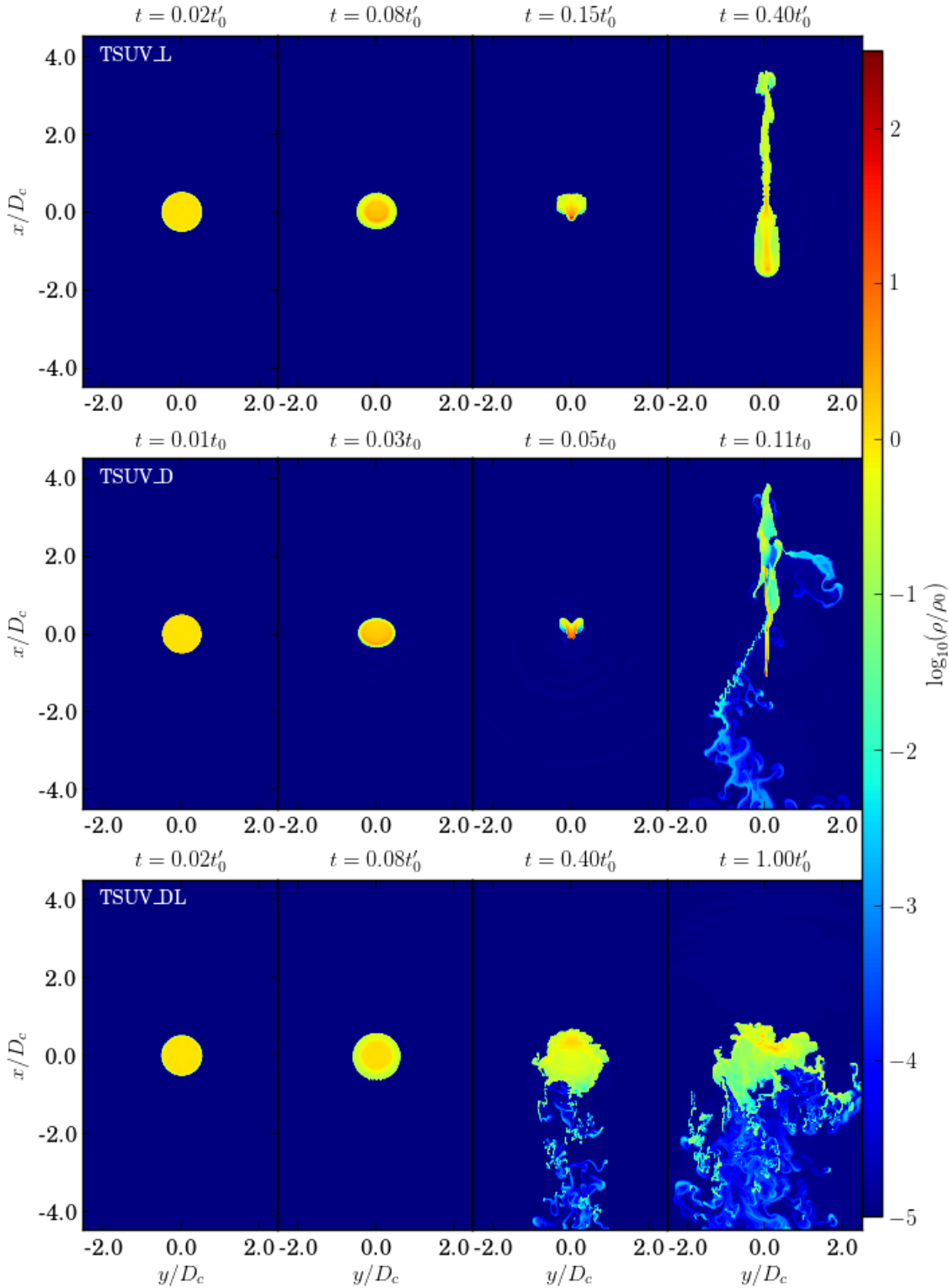
Figure 2.4: Density snapshots of TSUV_L (top panels) ,TSUV_D (middle panels) and TSUV_DL (bottom panels), the cloud is more optically thin compared to TLUV in these runs. The first row: TSUV_L, where the cloud has smaller radius $r = 0.1l_0$. The second row panel: TSUV_D is the cloud with lower density $\rho = 0.1\rho_0$. The third row: TSUV_DL, the cloud has both lower density and smaller radius. Notice that the t_0 and l_0 of TSUV_D and TSUV_DL are different than TSUV_D.

Since the temperature is similar in both optical depth unity runs, the lower initial density in the TSUV_D run means that it has a lower pressure than the TSUV_L run. As a result, the cloud needs to be compressed significantly more than in the other runs before the gas pressure gradient can become large enough to support the cloud against radiative compression. Hence it has largest peak average density $\bar{\rho}_{peak}$ (green solid line) in Figure 2.3.

2.3.3 Acceleration with Both IR and UV Irradiation

In contrast to UV radiation flux, cloud acceleration with IR radiation is generally gentler due to the smaller optical depth and the fact that IR radiation acts both to compress the cloud (incident radiation) but also provides a support against compression (re-radiated IR). Previous work has suggested that clouds accelerated solely by IR radiation might survive longer than cloud entrained in a hot outflow (Zhang et al., 2018). Hence, we have performed a number of runs with an incident IR flux to compare with the pure UV results discussed above. We first consider two purely IR runs: TLIR_E with an incident IR flux equal to the UV runs above and TLIR_H, which has a flux a factor of 10 larger. For both cases, we set the initial IR optical depth $\tau_{\mathrm{ir}} = 0.1$.

Figure 2.6 shows the cloud mean velocity v_{mean} (the first row), velocity dispersion σ_v (the second row) and cold gas mass M_{c} (the third row) for TLIR_E (green) and TLIR_H (red), with TLUV (black) included for comparison. TLIR_E is accelerated much more slowly than TLUV due to the smaller opacity, which gives rise to an acceleration $a_{\mathrm{ir}} \approx \kappa_{\mathrm{ir}} F_{\mathrm{ir}}/c < a_{\mathrm{uv}}$ when $F_{\mathrm{ir}} = F_{\mathrm{uv}}$. Since the IR driven cloud is not compressed significantly, the cloud is more weakly disrupted and retains its initial structure longer, leading to lower velocity dispersion. The mean acceleration is nearly constant, giving rise to a nearly linear velocity profile. A similar evolution is seen for TILIR_H, but the factor of 10 increase in F_{ir} compensates for the lower opacity and ultimately leads to a more rapid acceleration than seen for TLUV.

Figure 2.8 shows the cold gas average density (upper panel) and temperature (lower panel) for TLIR_H (black) and TLIR_E (orange). In contrast to the UV runs, both the mean density and temperature remain relatively constant for these runs. In fact, the average density shows a slight drop as the radiation pressure associated with the re-emitted IR leads to the cloud becoming weakly over-pressured relative to the background and expanding slightly. There is a brief initial transient when the
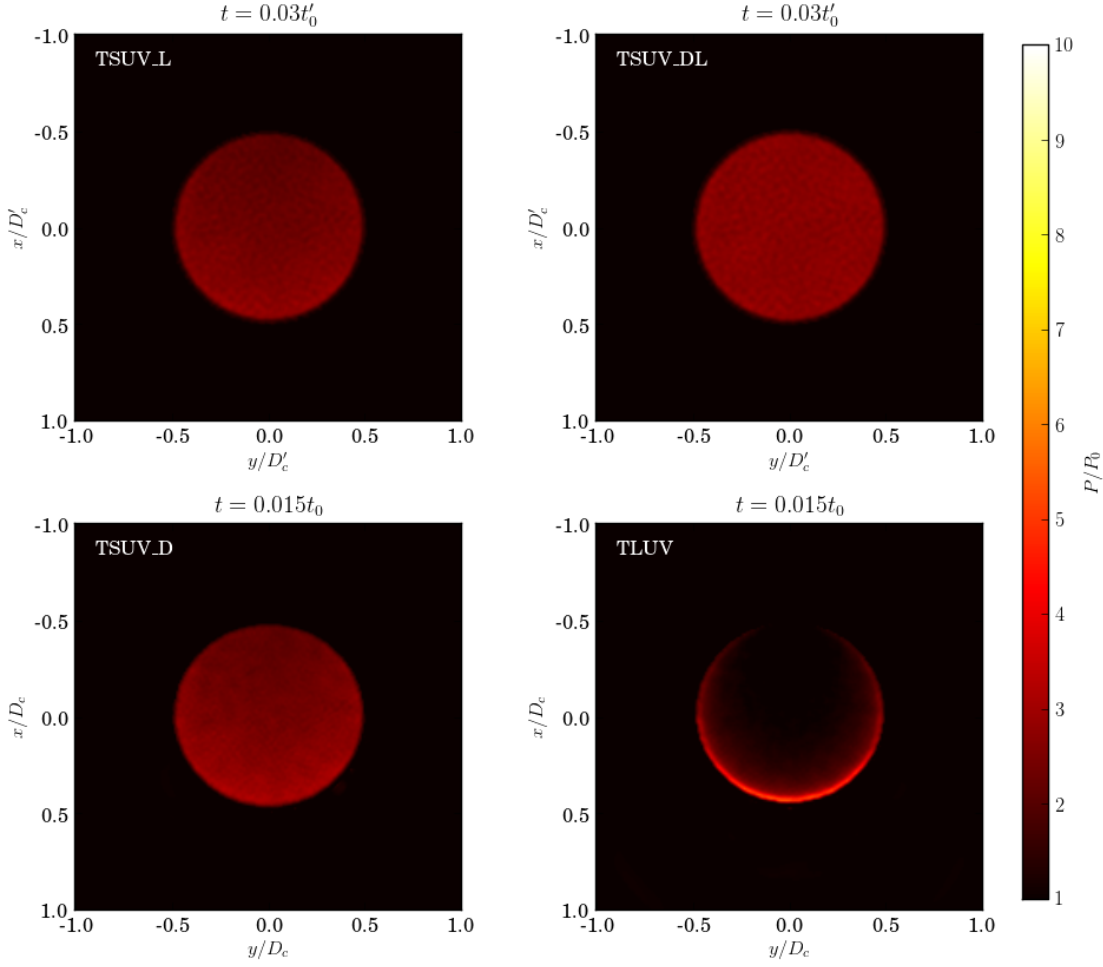
Figure 2.5: Gas pressure distribution of TSUV_L (upper left), TSUV_DL (upper right), TSUV_D (lower left) and TLUV (lower right) at same compression stage. $t_0' = 0.1t_0$, $l_0' = 0.1l_0$. Characteristic pressure $P_0 = \rho_0 v_0^2$, $P_0 = 4.12 \times 10^{-10}$dyne/cm^2 for TSUV_L and TLUV, $P_0 = 4.12 \times 10^{-11}$dyne/cm^2 for TSUV_D and TSUV_DL.
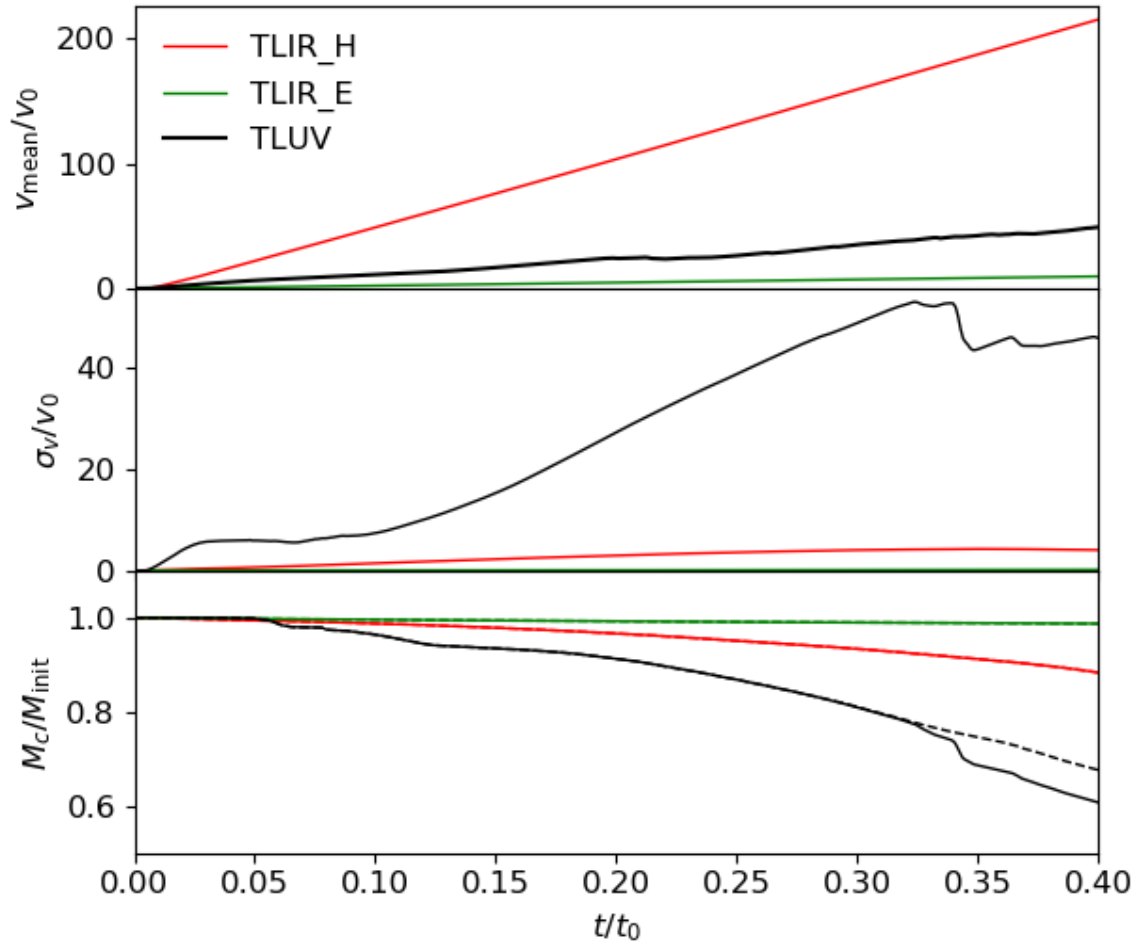
Figure 2.6: Mean velocity Δv_{mean} (top panel), velocity dispersion σ_v (middle panel) and cloud mass M_{c} (bottom panel) evolution of of TLIR_H (red), TLIR_E (green) and TLUV (black). $v_0 = 0.64\mathrm{km/s}$, and $t_0 = 6.25 \times 10^5\mathrm{yr}$

radiation sweeps across the cloud and heats it to the equilibrium temperature, where it remains for the rest of the evolution. Overall, our results are in good agreement with the large scale optically thin cloud simulations performed by Zhang et al. (2018).

Given the disparate evolution histories and survival times in the IR-only and UV-only runs presented thus far, it is natural to ask how a combination of UV and IR driving affects the cloud evolution. For highly star-forming galaxies, such as ULIRGs, the UV usually represents a small fraction $\lesssim 1\%$ of the total observed emission. Most of this radiation is thought to be originally emitted in the optical and UV by stars, and then reprocessed in the IR due to the large dust optical depths along most lines of site. However, it is plausible the UV will have been less attenuated in the location where the outflows are launched, motivating an exploration of different ratios of UV to IR flux.

We consider three simulations all with the same incident IR flux, which is equivalent to TLIR_H. These simulations also have an incident UV flux corresponding to 1% (TLMF_1) , 5% (TLMF_5), and 10% (TLMF_10) of the IR flux. The parameters are listed in Table 2.1. The cloud is optically thick to UV radiation ($\tau = 12.7$) and optical thin to IR radiation ($\tau_{IR} = 0.1$).

As with UV only runs, the UV provides a differential radiation force that acts to first compress the cloud until gas pressure rises and drives re-expansion. This density evolution is seen most clearly for TLMF_5 and TLMF_10 in Figure 2.8, but is only modest for TLMF_1, which is similar to the IR only runs. This also results in enhanced mixing between the dusty cloud gas and the hot background, which drives a slight increase in temperature above the equilibrium temperature at late times in the highest UV fraction runs.

Figure 2.7 shows the mean velocity (the first row), velocity dispersion (the second row), and mass evolution (the third row) for these with the pure IR run (TLIR_H) for comparison. As we add more UV flux, there is a slight enhancement in the acceleration at early times but the effect is mostly modest for the lower two runs, with the strongest enhancement coming at later time in the run with 10% UV flux after cloud has already been substantially disrupted. This evolution is also responsible for the increasing velocity dispersion associated with the cloud disruption as the UV fraction increases. As in the UV only runs, the mixing leads to substantial losses of dusty gas in the TLMF_5 and TLMF_10 runs, but the TLMF_1 run is similar to the IR-only runs. The evolution of the TLMF_10 run is qualitatively similar to the
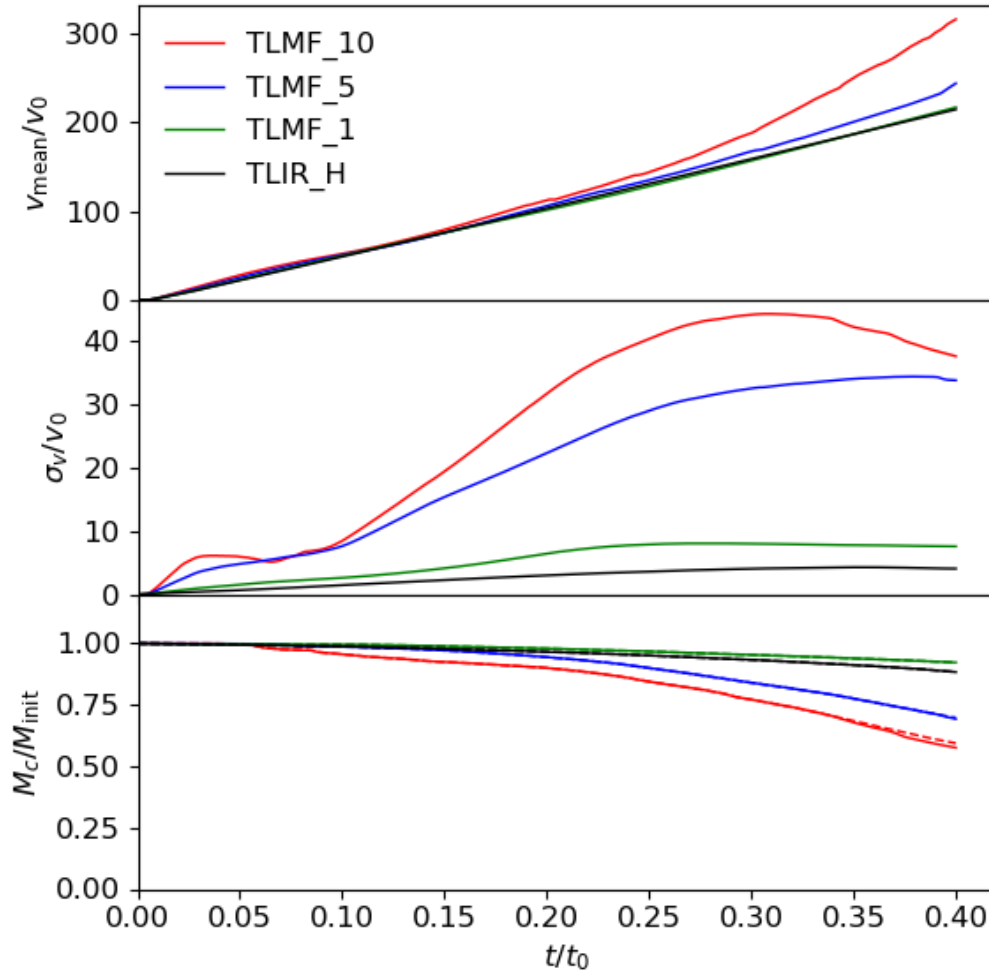
Figure 2.7: Mean velocity Δv_{mean} (top panel), velocity dispersion σ_v (middle panel) and cloud mass M_{c} (bottom panel) evolution of TLMF_10 (red), TLMF_5 (blue), TLMF_1 (green), TLIR_H (black) . $v_0 = 0.64$ km/s, and $t_0 = 6.25 \times 10^5$ yr
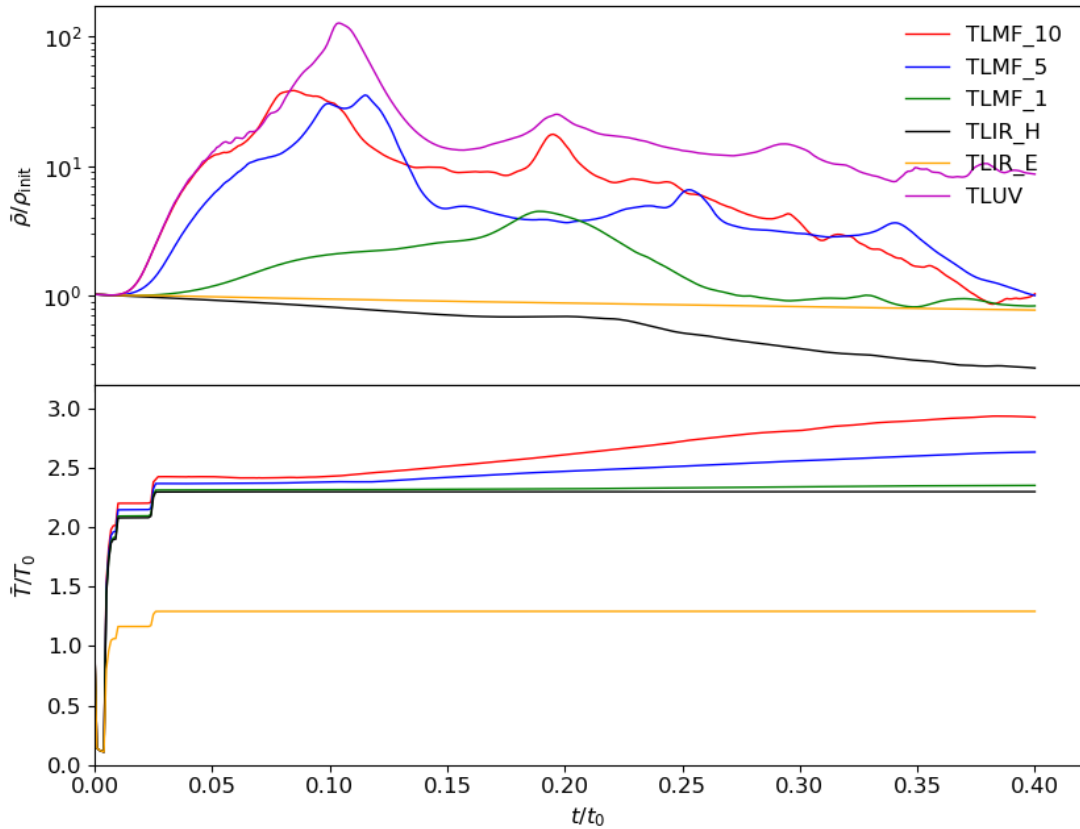
Figure 2.8: Average density (top panel) and temperature (bottom panel) of cold gas for multi-frequency runs TLMF_10 (red), TLMF_5 (blue), TLMF_1 (green) and infrared radiation runs TLIR_H (black), TLIR_E (orange). $\rho_{\text{init}} = \rho_0 = 10^{-19}\text{g/cm}^3$, $T_0 = 50\text{K}$.

TLUV run, which has the same incident UV flux, and more than half the dusty gas is removed by $t = 0.125 t_0$.

The overall impression is that the acceleration and survival of dusty gas is sensitive to the relative contributions of UV and IR radiation that drives. Since the temperature of the majority of the gas remains close to the equilibrium temperature, it is not a matter of the UV directly heating the gas, but instead driving dynamical evolution of the cloud that enhances mixing with the hotter background gas

2.3.4 Dimensionality, Resolution, and Reduced Speed of Light

The hydrodynamics interactions that drive mixing and cloud destruction are potentially sensitive to resolution. We considered the effects of resolution by rerunning

our fiducial run at two additional resolutions. The TLUV_HR and TLUV_LR runs are performed at resolution that is a factor of two higher and lower, respectively, in both dimensions relative to the TLUV run (see Table 2.1). Figure 2.9 shows the bulk motion and mass evolution of the cloud for different resolutions. Evolution of the mean density and temperature are shown in Figure 2.11.

The motion and mass evolution of the runs are all qualitatively similar to each other, although there are modest deviations in later evolution, when the non-linear effect start to dominates. These later time deviations are at about the same level as we see when changing the random initial perturbations on the cloud density. Slightly more sensitivity is seen in the evolution of the mean density, where the maximum compression seems to be somewhat larger in the highest resolution run. However, almost all runs asymptote to similar values of density at late times and follow show little variation in temperature evolution. Hence, our results do not seem to be substantially impacted by resolution for the conditions considered here.

All the simulations presented above were 2D, but the hydrodynamic effects that lead to mixing with the background might depend on dimensionality so we also performed a 3D simulation. Since 3D runs are considerably more expensive we only carry out one run (TLUV_3D) to see how well our 2D results generalize to 3D. Due to the increased computational cost, the resolution of TLUV_3D is chosen to be equivalent to the TLUV_LR run. Comparing these runs in Figure 2.9, we find that the acceleration and survival times are rather similar for both runs.

Figure 2.10 compares a 2D slice from TLUV_3D with a density snapshot at the same time in the TLUV_LR run. The compression of the 3D cloud is qualitatively consistent with the compression of the 2D cloud, with slightly higher compression occurring near the surface where the UV flux is absorbed. Comparison of mean density in Figure 2.11 indicates that the 3D run experiences somewhat higher maximum compression, which is consistent with the cloud being compressed nearly homologously in three rather than two dimensions. However, as with resolution, the simulations asymptote to similar densities at later times and we conclude that dimensionality has relatively little effect on the cloud acceleration or survival time for this setup.

Finally, we also test the effect of the speed of light reduction factor R on cloud dynamics. In TLUV_R, we chose a reduction factor of $R = 10^{-3}$. In other words, the speed of light is 10 times smaller than the TLUV run, allowing for time steps that are 10 times larger. As a result it takes 10 times longer for the radiation from the
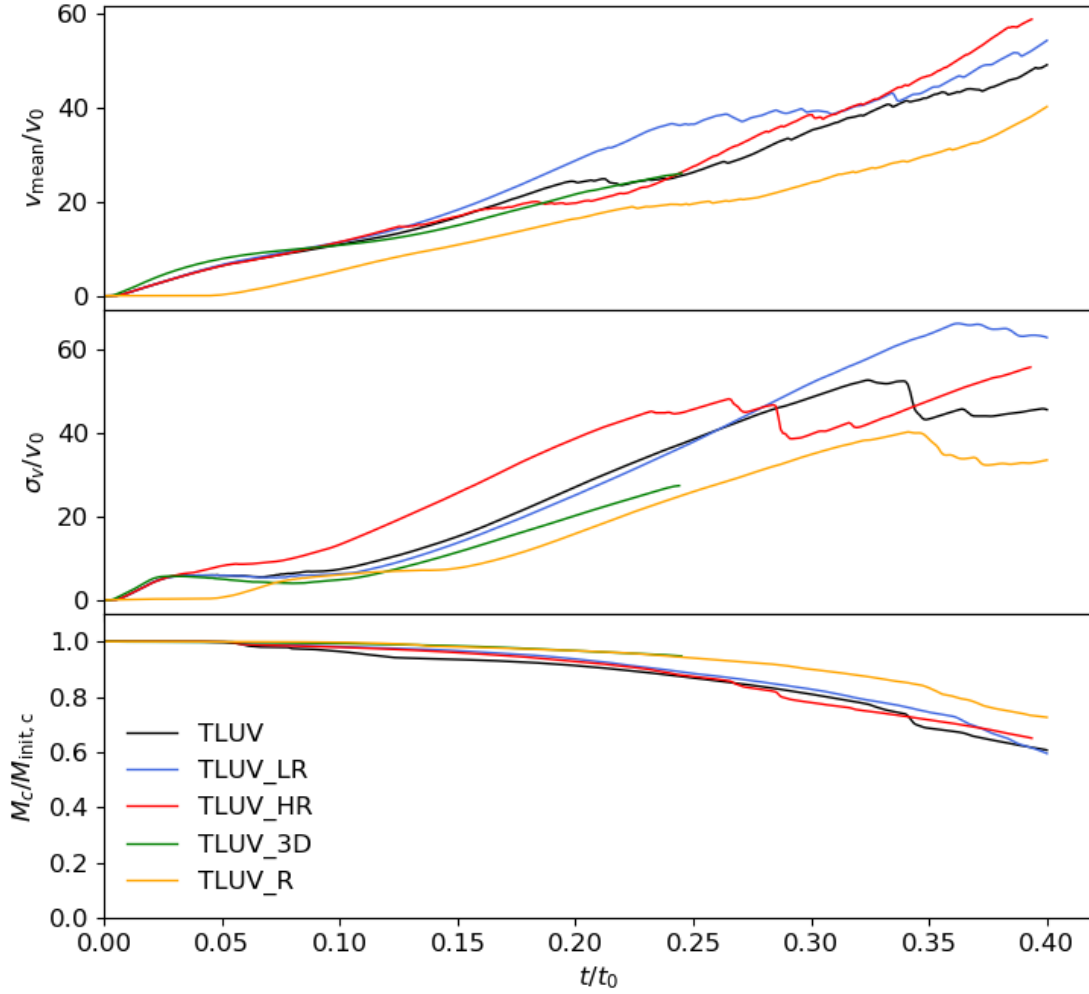
Figure 2.9: Mean velocity Δv_{mean} (top panel), velocity dispersion σ_v (middle panel) and cloud mass M_{c} (bottom panel) evolution of TLUV_3D (green), TLUV (black) ,TLUV_LR (blue), TLUV_HR (red), TLUV_R (orange). In TLUV_R, the radiation flux travels 10 times slower than other runs because of lower reduction factor. $v_0 \approx 0.64\,\mathrm{km/s}$, $t_0 \approx 6.25 \times 10^5\,\mathrm{yr}$.
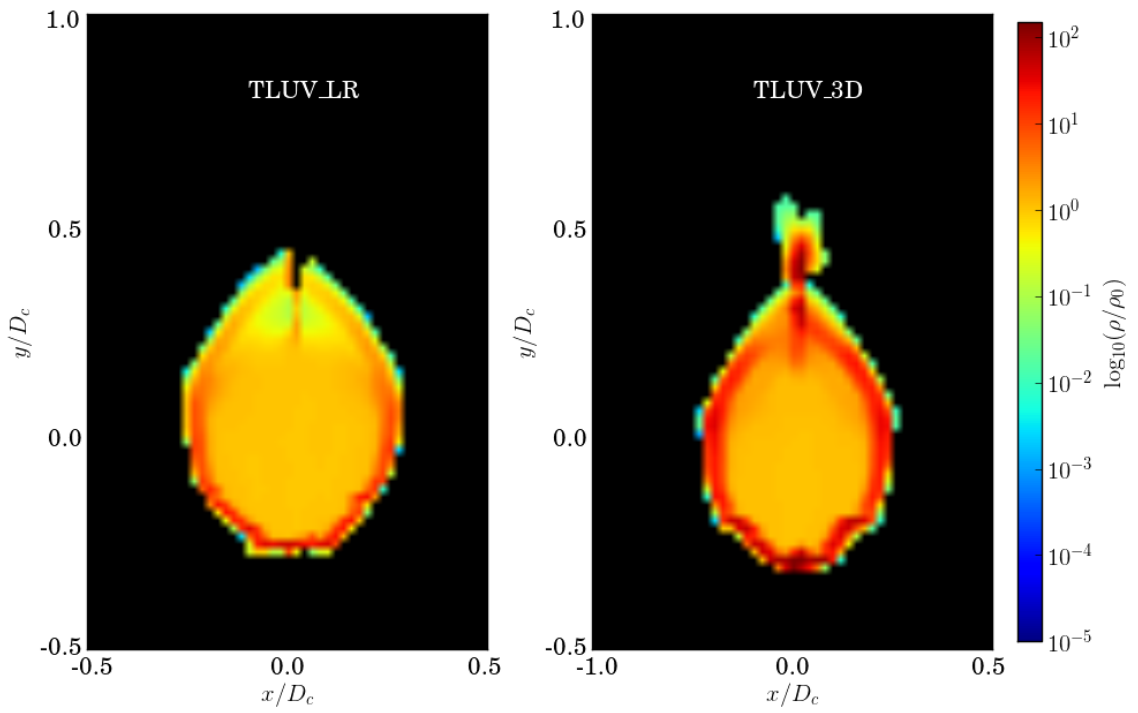
Figure 2.10: Dust density snapshots of TLUV_LR (Left) and TLUV_3D (Right) at $t = 0.06t_0$, the hot background medium is masked by black. $t_0 = 6.25 \times 10^5 \mathrm{yr}$, $\rho_0 = 10^{-19} \mathrm{g/cm^3}$.
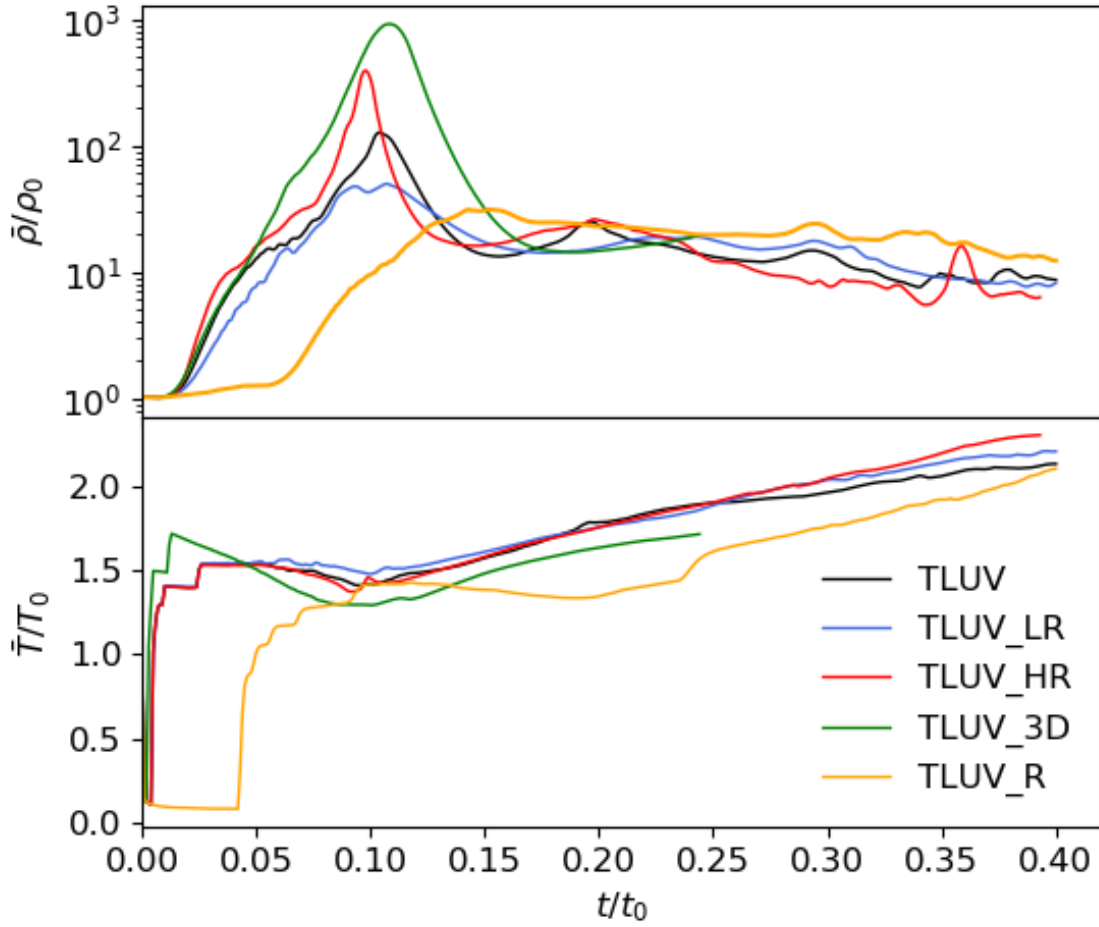
Figure 2.11: Average density (upper panel) and temperature (lower panel) of cold gas in TLUV_3D (green), TLUV (black) ,TLUV_LR (blue), TLUV_HR (red), TLUV_R (orange). $\rho_{\text{init}} = \rho_0 = 10^{-19}\text{g/cm}^3$, $T_0 = 50$K. In TLUV_R, the radiation flux travels 10 times slower than other runs because of smaller reduction factor, we moved the curves of TLUV_R $0.01t_0$ earlier in order to compare the cloud dynamics with other runs.

lower x boundary to reach the cloud. Once this offset is accounted for, the cloud bulk motion, velocity dispersion, mass (Figure 2.9), and mean density and temperature evolution (Figure 2.11) are all similar to TLUV. There seems to be a slightly delay in the compression of the cloud happens slightly later in this run, but the maximum compression is similar and the simulations asymptote to similar mean cloud densities. Hence, we do not believe our simulations are sensitive to our choice for R.

2.4 DISCUSSION

2.4.1 Destruction Mechanism for Cold Gas

Our primary interest in this problem is assessing whether radiative acceleration could play an important role in accelerating the outflows observed in molecular and atomic transitions. Therefore, an important constraint is that the gas cannot be too hot for the observed transitions to be present. Since the optimal temperature ranges for different species can vary significantly, there is no single temperature cutoff that describes all transitions. We have utilized the presence of dusty gas $s > 0$ as the criterion for survival. Since we have a adopted 500K as our dust destruction/decoupling temperature this can be thought of as a proxy for molecular gas. We do not believe our results are significantly sensitive to this choice of temperature because the bulk of the cloud stays close to the radiative equilibrium temperature $T \lesssim 100$K, and only a modest fraction is a temperatures significantly higher than this. The dusty gas (defined by $s > 0$) at temperature significantly higher than the equilibrium temperature is being rapidly heated by mixing with the background gas to temperatures near the assumed background temperature ($T \gtrsim 10^5$K). For this reason test runs with a larger destruction/decoupling temperature (1000K instead of 500K) are not significantly different because the gas reaching 500K continues heating and quickly exceeds 1000K shortly after reaching 500K. Hence, our results should not be sensitive to the assumed destruction temperature as long as this temperature is well below the background temperature and well above the equilibrium temperature.

As discussed in Section 2.3, the process of cloud disruption and heating is primarily a radiation hydrodynamical rather than simply radiation transfer process. In other words, the cloud is not simply heated to high temperature by the ultraviolet flux. The efficient infrared dust cooling allows the majority of gas to remain close to the radiative equilibrium temperature. Instead, the radiation pressure forces drive compression and

re-expansion of the gas. The mass loss is most significant when the cloud starts to re-expand after the radiation compression. During the re-expansion, a significant fraction of lower density dusty gas is heated by mixing with the hotter background ISM. In the optically thin limit, the compression and re-expansion phase is much more subdued, but the dynamics still leads to mixing of the outer layers and destruction of the cloud on comparable timescales.

Figure 2.12 shows the density distribution of hot and cold gas in the cloud ($s \neq 0$) for the TLUV run at three different times. The blue solid lines are the density distribution of cold gas (left y-axis labels). The red solid lines are the density distribution of hot gas (right y-axis labels), which we defined as gases with temperature higher than 95% of dust destruction temperature. The first row is before compression, the absence of red solid line means at $t = 0.042t_0$, there is no hot dusty gas. The second row is almost at volume minimum, where the mean cloud density is near its extremum. The hot dusty gas (red) has a density about 2 order of magnitude smaller than majority of cold dusty gas (blue). The bottom panel shows the density distribution right after the compression, with hot gas still corresponding to lower densities than most of the cold gas. In effect, there is a continuous flux of cold dense gas towards lower densities due to expansion and mixing that is heated and incorporated into the background ISM.

The implied rapid mixing with the background ISM is consistent with expectations from purely hydrodynamic models, driven by Kelvin-Helmholtz instabilities (Begelman & Fabian, 1990). We assume a mixing time scale $t_{\mathrm{mix}} \sim t_{\mathrm{KH}} \sim (\rho_c/\rho_h)^{1/2} t_{\mathrm{edd}}$, with ρ_c the density of cold material, and ρ_h the density of hot material, and t_{edd} is the timescale for eddies to cross mixing layer. We estimate $t_{\mathrm{edd}} \sim 0.1 l_0/\sigma_v$ and $\rho_c/\rho_h \sim 10^{-2}$, yielding $t_{\mathrm{mix}} \approx 0.02t_0 < t_{\mathrm{rad}} < t_0$. Therefore it is not surprising that gas driven to lower densities by hydrodynamic processes in the cloud surface rapidly mixes with the background.

2.4.2 Cloud Survival Time

A number of numerical studies of purely hydrodynamic entrainment Scannapieco & Brüggen (2015); Brüggen & Scannapieco (2016); Zhang et al. (2018) concluded that entrainment in a hot wind is unlikely to accelerate the cloud to the observed speed before the cloud is shredded. However, Zhang et al. (2018) found that clouds accelerated by an IR radiation field can survive longer if a sufficiently larger infrared
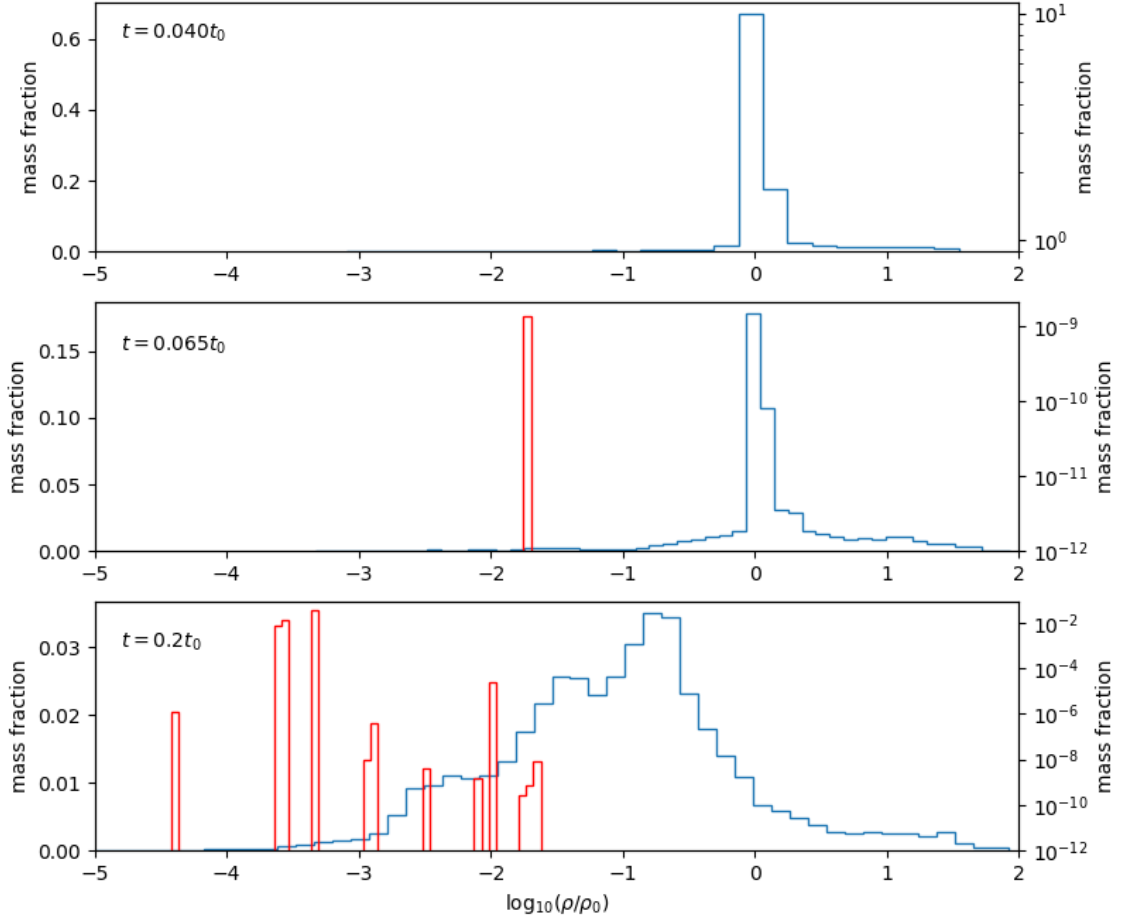
Figure 2.12: Cold gas density distribution of TLUV at $t = 0.04t_0, 0.075t_0, 0.11t_0$ (the first, second, third row respectively). The distribution of all dusty material in the calculation domain is the blue solid line (with labels at left). The distribution of hot material, which we defined as material that with temperature higher than 95% of the assumed dust destruction temperature, is the red solid lines (with labels at right).

flux is available to accelerate them. Our focus here was to consider the degree to which the addition or substitution of UV radiation impacts this conclusion.

Following Zhang et al. (2018), we define the cloud surviving time as the time when the cloud lost half of its initial mass. Our definition of cloud mass follows from Equation (2.10), which includes mass loss both from mixing and advection out of the domain. In Figure 2.13, the solid lines correspond to M_c, the dashed line with same color excludes mass loss associated with advection through the domain boundary. In other words it assumes (conservatively) that cold gas advected through the boundary remains cold and only gas overheated within the domain is accounted for. Since we stop the simulations when the mass loss out of the domain begins to become significant, almost all of the mass loss shown in the figures is due to mixing and overheating within the simulation domain.

A potentially important characteristic timescale for estimating the cloud survival time is the radiation crushing time t_{rad} from Equation (2.17). For runs with $\tau_{\text{uv}} \geq 1$ the mass loss occurs primarily after maximum compression, when the cloud starts to re-expand and the timescale for re-expansion is comparable to or slightly longer than t_{rad}. Hence, for this regime it provides an approximate estimate of the survival time but the dependence on τ_{uv} is not borne out. It implies that the most optically thick clouds will crushed the fastest but this is not what we found. The difference arises because t_{rad} neglects the impact of the pressure support from gas and reradiated IR radiation.

Since the UV radiation acts to compress the cloud without providing pressure support, one might expect the optically thick cloud accelerated by UV radiation alone to have shorter surviving time than one supported by IR alone and this is consistent with our results. Figure 2.13 compares the cloud mass evolution of the UV driven runs that are optically thick (TLUV) to optically thin (TSUV_D ,TSUV_L and TSUV_DL) with the IR driven run (TLIR_H). The cloud mass drops significantly faster when accelerated by UV radiation. Even though the higher opacity to UV radiation allows for more rapid acceleration (for the same flux), the total survival time is significantly shorter, limiting the velocity to less than is typically inferred from observations.

With the exception of the pure IR runs (which are run for the same time as the fiducial run), we end all the simulations when outflow out of the simulation domain starts to become the dominant mass loss mechanism. At this point, TLUV only has
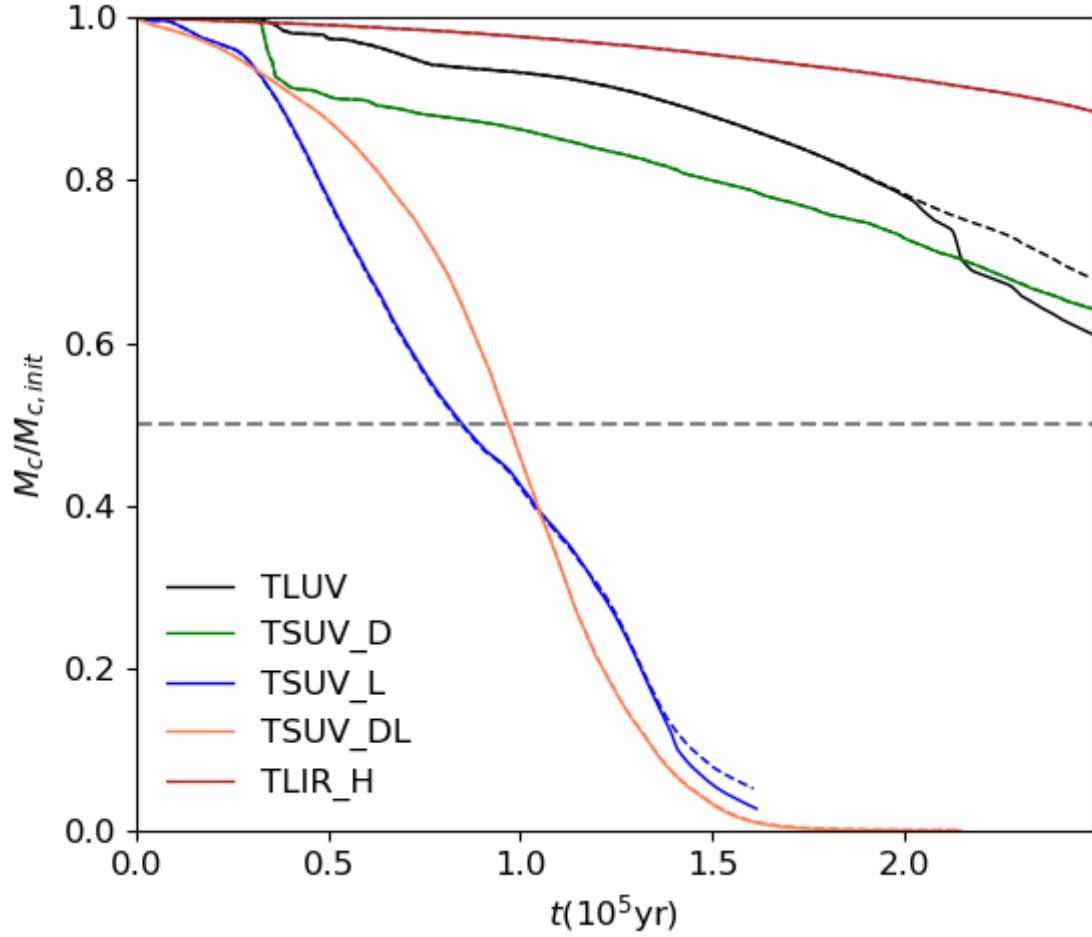
Figure 2.13: Cloud mass evolution for different runs. The horizontal grey dashed line labels when cloud mass is half of initial mass, corresponding to the cloud surviving time. Black lines are for TLUV. The blue lines are TSUV_L, green lines are TSUV_D, and orange lines are TSUV_DL. Red lines shows mass evolution of the optical thick cloud in TLIR_H, which is accelerated by pure IR radiation. For each color, the solid line is M_c (Equation 2.10), the dashed line is corresponding $M_c(t)$ (Equation 2.11).

Table 2.2: Flying distance and final velocity

Name	z (pc)	v_{fin} (km/s)	t_{tot} (yr)
TLUV	1.07	19.99	1.25×10^5
TSUV_D	8.12	137.12	1.25×10^5
TSUV_L	2.5	78.25	6.55×10^4
TSUV_DL	8.03	163.74	9.29×10^4
TLIR_E	0.19	3.14	1.25×10^5
TLIR_H	4.21	68.69	1.25×10^5
TLMF_10	4.91	82.67	1.25×10^5
TLMF_5	8.76	103.92	1.77×10^5
TLMF_1	4.21	67.01	1.25×10^5

a speed $v_{\mathrm{mean}} \approx 19.2$km/s, while $M_{\mathrm{c}}/M_{\mathrm{c,init}} \approx 60\%$, much smaller than the observed velocities, which are 100s of km/s . Integrating the mean velocity over time we can estimate the "flying" distance $z \sim \int v_{\mathrm{mean}} dt \approx 2.67 l_0 \approx 1.07$pc, which is small compared to the typical size of star forming region. Therefore, we do not expect optically thick UV-driven clouds to survive long enough to explain observed outflows. TSUV_D and TSUV_L have larger acceleration and therefore reach somewhat larger velocities of ~ 75km/s, but flying distance remains small due to the short survival times.

In contrast, clouds driven by the IR radiation flux accelerate the cloud as a whole for several dynamical timescales (Zhang et al., 2018). Incident radiation energy is converted efficiently into cloud kinetic energy. Although there is still some turbulent motion in the cloud outer layers and associated mixing with the background, it is much less than in the UV and the cloud survival time is much longer.

2.4.3 Effects of Multiband Irradiation

Since a cloud absorbs both UV and IR radiation, but only re-emits IR radiation (Equation 2.6), the UV and IR radiation interact very differently with the clouds. UV radiation tends to accelerate the opaque cloud faster but also compresses the cloud and eventually drives greater mixing with the hot background ISM. In contrast, the IR radiation flux accelerates the cloud more uniformly without significant compression, leading mixing to occur on much longer timescales. A cloud's interaction with a

mixture of IR and UV flux is somewhat more complicated. Figure 2.14 shows the cloud mass evolution from the multiband irradiating flux runs. TLMF_10 has the same UV flux as TLUV (black), and same IR flux as TLIR_H (red). However, because the extra compression from IR radiation pressure is not entirely balanced by the clouds internal IR cooling radiation, the mass drop of TLMF_10 is even faster than TLUV. By the time we stopped the simulation, TLUM_10 is accelerated to ~ 80km/s, but about 80% of cold gas in the cloud has been heated over 500K.

Lowering the UV flux fraction in the TLMF_5 and TLMF_1 runs produces mass evolution increasingly similar to the pure IR irradiation case. Note the difference in mass and average density (Figure 2.8) evolution between 5% and 1% of UV radiation flux is somewhat sharp. Comparing the different UV fraction runs in Figure 2.7, shows that increasing UV radiation from 1% to 5% does not significantly increase bulk acceleration because of the small absolute value of UV flux. But the effect on the compression of the cloud is much more significant. Hence, even a modest UV fraction can disrupt the cloud without significantly improving the acceleration. However, the similarity between the TLUV and TLMF_10 runs also suggests it is the value of the UV flux rather than simply the fraction that matters here. Our results suggest that if the UV flux and/or optical depth are large enough to produce significant differential acceleration, compression of the cloud will drive re-expansion and disrupt the cloud in a manner that will significantly enhance mixing with the background flow. This would suggest that the most optically thick star-forming environments, such as ULIRGs where the vast majority of stellar light is reprocessed into the infrared, may be the most efficient locations for driving molecular outflows if radiation pressure dominates.

2.4.4 Model Uncertainties and Approximations

The primary goal of this work is to examine the relative role of UV and IR radiation pressure in accelerating outflows of cold molecular gas that are observed in star-forming galaxies. Since we focus on this mechanism, we implicitly ignore other possibilities such as entrainment in hot outflows or acceleration due to cosmic ray pressure (e.g. Scannapieco & Brüggen, 2015; McCourt et al., 2015; Zhang et al., 2018; Wiener et al., 2019b). In principle, these other acceleration mechanism may all act in concert to drive outflows or radiation may be an entirely subdominant process. Our primary motivation for neglecting other acceleration mechanisms is that it al-
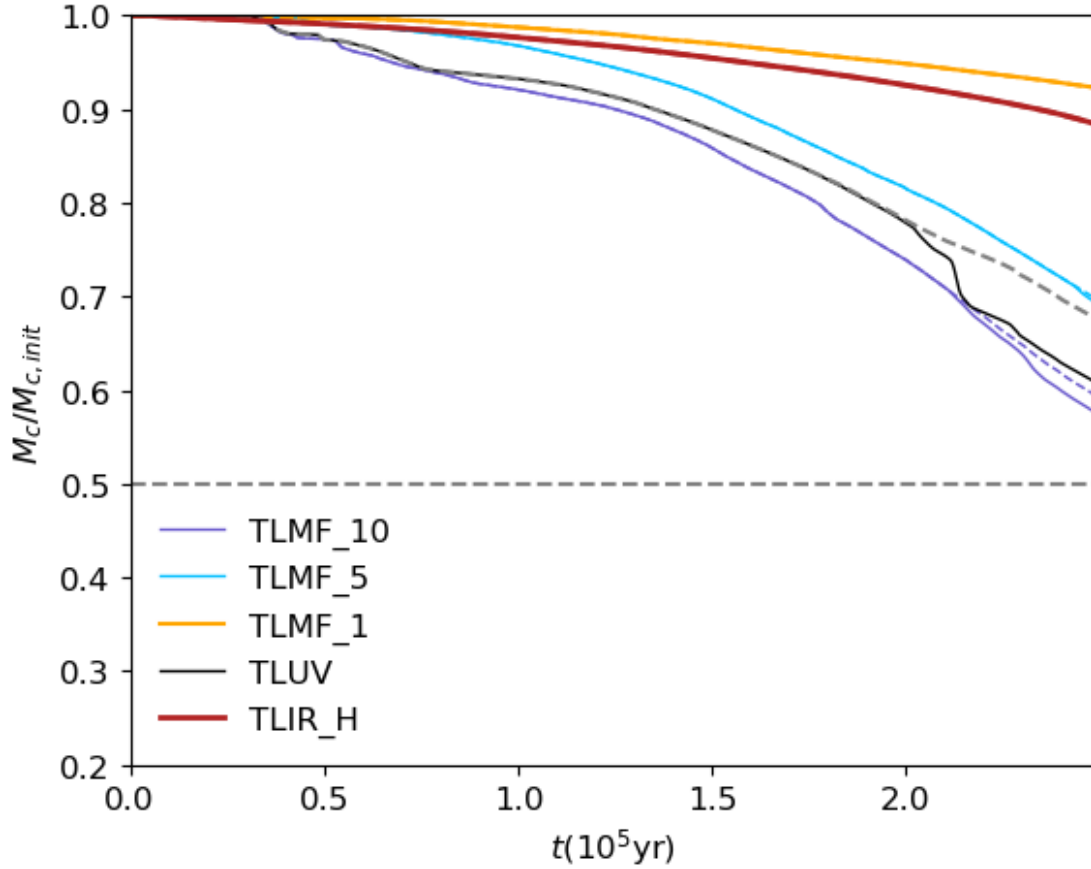
Figure 2.14: Cloud mass evolution for multi-frequency runs. The horizontal grey dashed line labels half of cloud initial mass, so the time reach it corresponds to the cloud surviving time. The red lines are TLIR_H, the black lines are TLUV. The purple lines are the multi-frequency flux TLMF_10, its UV flux is the same as TLUV and IR flux is the same as TLIR_H. Then we fix the IR flux value, lower the UV flux fraction to 5% of IR flux in TLIR_5 (light blue), 1% of IR flux in TLIR_1 (orange). The solid lines are Equation (2.10) and the dashed lines are Equation (2.11).

lows us to focus on and better understand the radiation hydrodynamics, but given the uncertainties, we view radiation dominated acceleration as a physically plausible limit.

Due to the expense of solving the radiation transfer equations, even the mostly 2D simulations presented here are relatively computationally expensive. This requires us to make trade-offs in our modeling. Our simulations focus on the radiation hydrodynamics of the acceleration process, but improve on earlier work by studying the interaction of dusty gas with a multiband irradiating flux under differing assumptions about the optical depths and UV and IR fluxes. However, we simplify or neglect some of the more complex physics that may be relevant to realistic outflows. Future work could benefit from including the overall galaxy gravitational potential and any self-gravity of the gas, studying the effects of magnetic fields (McCourt et al., 2015), modeling dilution of the radiation field far from the original source, including additional complexity in the background interstellar medium, a detailed treatment of photoionization (e.g Namekata et al., 2014), modeling of conduction (Brüggen & Scannapieco, 2016), or the process of cloud formation (e.g. Proga & Waters, 2015; Waters & Proga, 2016). We also utilized a simplified prescription for the dust opacity (Semenov et al., 2003) and adopted simple temperature criterion to determine when the dust is destroyed or decoupled (Krumholz & Thompson, 2013) from the gas. Future work may benefit from more elaborate treatments of the dust, including its coupling to gas, destruction mechanisms, and opacity.

2.5 SUMMARY

.

We consider the effect of UV radiation pressure acceleration of cold, dusty gas. In contrast to earlier work that focused on IR radiation alone, we find that replacing the IR with UV radiation or including a large fraction of UV radiation is generally detrimental to the cloud survival. This is due to the UV radiation pressure distorting and compressing the cloud, driving mixing with the hotter background ISM, with mixing ultimately leading to overheating and dust destruction. In contrast, simulations dominated by IR radiation are more robust, with longer survival times in agreement with earlier work (Zhang et al., 2018). We attribute this difference to the IR radiation's role in both accelerating the cloud but also in providing an internal radiation pressure due to dust reemission that maintains a more uniform cloud structure and

limits mixing.

We also consider the impact of optical depth on the cloud dynamics. All simulations considered here are optically thin to the IR, but range from optically thin ($\tau_{\mathrm{uv}} = 0.13$) to optically thick ($\tau_{\mathrm{uv}} = 13$) in the UV. Generally speaking, decreases in the UV optical depth of the cloud lead to faster disruption times. For moderate to large optical depths, this happens after an initial phase of compression and re-expansion but for the optically thin runs, the process is nearly continuous with no overall compression of the cloud.

With the high radiation fluxes considered here, the UV driven cloud can be accelerated to reasonably high velocities ($\gtrsim 100$ km/s) in the relatively short time ($\lesssim 10^5$ yr) they survive, but they do not travel very far from there in initial location with a "flying distance" of only a few parsecs. In contrast, the IR clouds reach the same distances and nearly as large of velocities, but with most of the initial gas still intact after 10^5 yr. Hence, we conclude that a radiation field dominated by emission at IR wavelengths is the most optimal for radiation pressure acceleration. This suggests that radiation pressure acceleration will be most relevant in highly obscured star-forming galaxies where the UV fractions are low. In contrast, disruption and mixing will likely tend to destroy clouds in more UV dominated starburst galaxies. These considerations combined with the need for large radiation fluxes (Zhang et al., 2018) suggest ULIRGs and high redshift star-forming galaxies as the environments where radiation pressure is most likely to play a role in driving outflows of cold molecular gas.

CHAPTER 3

THE LAUNCHING OF COSMIC RAY DRIVEN OUTFLOWS

3.1 ABSTRACT

Cosmic rays (CRs) are thought to be an important feedback mechanism in star-forming galaxies. They can provide an important source of pressure support and possibly drive outflows. We perform multidimensional CR-magnetohydrodynamic simulations including transport by streaming and diffusion to investigate wind launching from an initially hydrostatic atmosphere by CRs. We estimate a characteristic Eddington limit on the CR flux for which the CR force exceeds gravity and compare it to simulated systems. Scaling our results to conditions in star-forming galaxies, we find that CRs are likely to contribute to driving outflows for a broad range of star formation environments. We quantify the momentum and energy transfer between CRs and gas, along with the associated mass outflow rates under different assumptions about the relative importance of streaming and diffusion for transport. In simulations with streaming, we observe the growth and saturation of the CR acoustic instability, but the CRs and gas remain well coupled, with CR momentum transferred efficiently to the gas even when this instability is present. Higher CR fluxes transfer more energy to the gas and drive stronger outflows. When streaming is present, most of the transferred energy takes the form of Alfvén wave heating of the gas, raising its pressure

and internal energy, with a lower fractional contribution to the kinetic energy of the outflow. We also consider runs with radiative cooling, which modifies gas temperature and pressure profiles but does not seem to have a large impact on the mass outflow for super-Eddington CR fluxes.

3.2 INTRODUCTION

The general picture that stars are formed from collapsing gas is widely agreed upon. However, it has long been a puzzle that the observed star formation rate (SFR) is usually below what is predicted by the simple assumption of gravitational collapse of gas clouds on dynamical timescales (Kennicutt Jr, 1998; Krumholz & Tan, 2007; Kennicutt Jr & Evans, 2012). Cosmological simulations resolving galaxy formation indicate that the energy and momentum feedback from star formation is a key component for explaining the inefficient conversion from gas to stars (Somerville & Davé, 2015). Such feedback can happen via numerous channels. Galactic outflow, which is observed in wide range of galaxies (Veilleux et al., 2005; Spilker et al., 2020; Veilleux et al., 2020), is thought to be an important feedback mechanism for removing gas from galaxies, shaping the circum-galactic/inter-galactic medium, and modifying galaxy evolution.

The origin of galactic outflow is not completely understood. There are several promising mechanisms for launching outflows, but their relative importance in different types of galaxies is still a matter of debate (Zhang, 2018). Although there is evidence AGN may be relevant in some cases, the outflows correlate with star formation activity (Martin, 2005; Veilleux et al., 2005), implying that mechanisms tied to star-formation operate. Hot supernova-driven thermal winds are almost certainly present in some galaxies (Chevalier & Clegg, 1985b). Entrainment of colder gas in these hot winds (Strickland & Heckman, 2009; Scannapieco & Brüggen, 2015; Fielding et al., 2018; Gronke & Oh, 2020), and radiation pressure on dust (Krumholz & Thompson, 2012; Zhang et al., 2018; Huang et al., 2020; Kim et al., 2021) are promising mechanisms for explaining the molecular and weakly ionised gas that is observed. We refer to the latter mechanism as non-thermal feedback since relativistic particles (photons) are doing the driving rather than hot gas.

Another non-thermal feedback candidate is cosmic ray (CR) pressure. Being roughly in energy equipartition in our local universe (Boulares & Cox, 1990; Ferriere, 2001), CRs are thought to be an attractive source to drive outflows in Milky Way-like

systems (Ipavich, 1975; Breitschwerdt et al., 1991, 1993; Everett et al., 2008), as well as in star-bursting systems (Socrates et al., 2008). Meanwhile, numerical works also suggest that CR can drive outflow with significant mass-loading and effectively regulate the star formation rate (Jubelgas et al., 2008; Uhlig et al., 2012; Booth et al., 2013; Hanasz et al., 2013; Salem & Bryan, 2014).

Recent semi-analytical and numerical simulations further elaborate CR's feedback role in terms of driving outflow, modifying galaxy evolution and shaping circum-galactic environment at different scales. For example, cosmological and galaxy formation simulations suggest that when compared to simulations only including thermal feedback, adding CRs changes the star formation history, especially in massive galaxies (Ruszkowski et al., 2017; Butsky & Quinn, 2018; Hopkins et al., 2020). CRs usually enhance outflow, constrain wind morphology and thicken the galaxy disk (Bustard et al., 2020; Buck et al., 2020). Interestingly, both analytical work and numerical studies suggest that the CR driven wind is likely distinct from a typical momentum or energy driven wind, leaving a unique wind profile (Salem & Bryan, 2014; Mao & Ostriker, 2018; Girichidis et al., 2018). In the circum-galactic medium (CGM) or intra-galactic medium (IGM), CRs are an important pressure source that supports gas in addition to thermal pressure and potentially allows a cooler halo (Butsky & Quinn, 2018; Buck et al., 2020). The collisionless and collisional loss of CR energy is also an important energy component in the CGM (Bustard et al., 2020; Crocker et al., 2021).

The cosmological and galaxy evolution simulations including CRs provide straightforward comparisons with observation, showing that CRs are an important feedback mechanism. In addition, high resolution local simulations with resolved multi-phase gas structure are another channel to diagnose CR physics and its interaction with radiative cooling, conduction, and magnetic field evolution. For example, CRs are able to drive an initially cold cloud that embedded in hot background to roughly the observed outflow velocities without complete disruption by local dynamical instability (Wiener et al., 2019c; Brüggen & Scannapieco, 2020). In the CGM, CRs modify the onset of thermal instability and subsequent multi-phase gas formation Butsky et al. (2020); Kempski & Quataert (2020).

To connect the cloud-wind interaction scale and the galaxy formation scale, in this work, we investigate the CR's role in launching an outflow from dense atmosphere against gravity near the disk with high resolution simulations. Similar studies

of radiative feedback found that the wind-launching process could be impacted by the presence of dynamical instabilities (Krumholz & Thompson, 2012; Davis et al., 2014). Resolving local dynamics and potential instability (Begelman & Zweibel, 1994; Heintz & Zweibel, 2018) is an essential step for bridging the gap between well-resolved simulations of individual cloud evolution and incorporating CR to galaxy evolution framework employing sub-grid models.

Despite the importance of CR feedback, our knowledge about the CR transfer mechanism is limited by the lack of direct extra-galactic observation. The canonical treatment of CR transfer usually includes two processes: streaming and diffusion (Skilling, 1971). The latter process models CR transfer as classical diffusive process with effective diffusivity. Transport by streaming means that CRs stream along the magnetic field and excite waves, with subsequent wave damping enabling energy and momentum exchange with gas. The streaming velocity is usually determined by the balance between wave growth and wave damping, as well as local ionisation condition, ranging from Alfvénic to super-Alfvénic streaming (Skilling, 1971; Holguin et al., 2019; Bai et al., 2019; Bustard & Zweibel, 2020; Zweibel, 2020; Bambic et al., 2021). Extensive studies show that the transfer mechanism has significant impact on the disk and halo morphology, the outflow properties and the energetics of CGM and IGM (Wiener et al., 2013; Ruszkowski et al., 2017; Wiener et al., 2017; Buck et al., 2020; Ramzan et al., 2020).

This work aims to study the efficiency of CR driving from a disk atmosphere as a function of a prescribed CR flux, under different assumptions about the transport mechanism.We adopt the two-moment scheme proposed by Jiang & Oh (2018), which solves CR transfer equations including both streaming and diffusion self-consistently. We perform a series of adiabatic simulations, primarily with Alfvénic streaming and isotropic diffusion to explore how relative importance of streaming and diffusion changes CR feedback. We also briefly consider the role of radiative cooling on the launching CR winds. A detailed study of radiative cooling in CR driven multi-phase outflow and its impact on cold gas survivability will be presented in a companion paper.

The plan of this paper is as follows: in Section 3.3 we describe the equations solved, simulation set-up and our prescription for a CR Eddington limit. The simulation results are reported in Section 3.4. We discuss the primary implication from our results and relevance to star-forming galaxies in Section 3.5, and summarise the main

conclusions in Section 3.6.

3.3 Numerical Method

3.3.1 Cosmic Ray Transport Equations

The equations we solve are ideal magneto hydrodynamics (MHD) equations and cosmic rays (CR) transportation equations, which is based on the two-moment scheme proposed by Jiang & Oh (2018). We discussed the details numericla method in Chapter 1.2, here we list the two CR transport equations for the convenience of discussions in this work.

$$\frac{\partial \mathbf{B}}{\partial t} - \nabla \times (\mathbf{v} \times \mathbf{B}) = 0, \tag{3.1a}$$

$$\frac{\partial E_\mathrm{c}}{\partial t} + \nabla \cdot \mathbf{F}_\mathrm{CR} =$$
$$-(\mathbf{v} + \mathbf{v}_\mathrm{s}) \cdot \sigma_c \cdot [\mathbf{F}_\mathrm{CR} - \mathbf{v} \cdot (E_\mathrm{c}\mathsf{I} + \mathsf{P}_\mathrm{c})] \tag{3.1b}$$

$$\frac{1}{V_\mathrm{m}^2} \frac{\partial \mathbf{F}_\mathrm{CR}}{\partial t} + \nabla \cdot \mathsf{P}_\mathrm{c} =$$
$$-\sigma_c \cdot [\mathbf{F}_\mathrm{CR} - \mathbf{v} \cdot (E_\mathrm{c}\mathsf{I} + \mathsf{P}_\mathrm{c})]. \tag{3.1c}$$

3.3.2 Eddington flux for Cosmic Rays

A primary goal of this study is to examine the impact of the CR transport mechanism (specifically streaming versus diffusion) on the efficiency of wind launching and acceleration. But, the launching is also sensitive to the flux of CRs through the atmosphere, so we begin by estimating what magnitude of CR flux we expect to be necessary to drive winds in the limit that either streaming or diffusion dominates. Motivated by Socrates et al. (2008), we formulate this in terms of a CR Eddington flux, where the acceleration due to CR forces just balance the local gravitational acceleration g, which we take to be constant. For a given flux $F_\mathrm{c,x}$ at the base of the atmosphere, we define the CR Eddington flux F_Edd as the flux that satisfies $-\partial P_\mathrm{CR}/\partial x = -\rho g$, where P_CR is the CR pressure. We assume that the CRs are nearly isotropic so that $E_\mathrm{CR} = 3P_\mathrm{CR}$.

First we derive an expression for F_edd in the CR streaming limit. When streaming dominates the CR transport, $v_\mathrm{s} = v_\mathrm{A}$ if E_CR is monotonic. Because V_m is usually

significantly larger than any velocity in the simulation, we further assume that the time-dependent term in Equation (3.1c) is negligible, so that $F_{c,x} \approx 4(v_s + v_x)P_{CR}$, where v_x is the gas velocity along x direction. In other words, the CR flux is the sum of advective flux and streaming flux. In the launching region of the flow, v_x is small and $v_A \gg v_x$, so we further assume that $F_{c,x} \approx 4v_A P_{CR}$. The CR energy Equation (3.1b) in 1D geometry becomes:

$$\frac{\partial E_{CR}}{\partial t} + 3v_A \frac{\partial P_{CR}}{\partial x} + 4P_{CR} \frac{\partial v_A}{\partial x} = 0, \tag{3.2}$$

In steady state, the time-dependent term vanishes, resulting $\partial(P_{CR}v_A^{4/3})/\partial x = 0$.

With these assumptions, we can approximate

$$-\frac{\partial P_{CR}}{\partial x} \simeq \frac{4P_{CR}}{3v_A}\frac{\partial v_A}{\partial x} = -\frac{2P_{CR}}{3\rho}\frac{\partial \rho}{\partial x}, \tag{3.3}$$

where the second equality follows from assuming $\mathbf{B}$ is constant. Defining $H_\rho \equiv (-\partial \ln\rho/\partial \mathrm{x})^{-1}$, and setting $\partial P_{CR}/\partial x = \rho g$, we can solve for

$$F_{Edd,str} = 6v_A g\rho H_\rho, \tag{3.4}$$

which we define as the Eddington flux for CRs in the streaming limit. Note that unlike the expression for radiation with electron scattering opacity, this expression is not constant, depending on the background density and density gradient. This means that for a given flux, the acceleration of the flow against gravity will generally be most effective at lower densities. In contrast, to radiation dominated atmospheres, we might expect that streaming CRs will more generically drive outflows, but possibly only in superficially low density regions of the atmosphere. This may lead to effective acceleration, but only for a relatively small amount of gas.

The diffusion limit is simpler, with $F_{c,x} \approx -\kappa_{diff}(\partial P_{CR}/\partial x)$, where κ_{diff} is a characteristic CR diffusivity. So the Eddington flux in the diffusion limit is

$$F_{Edd,diff} \equiv -\kappa_{diff}\frac{\partial P_{CR}}{\partial x} = \kappa_{diff}\rho g. \tag{3.5}$$

For κ_{diff} approximately constant, this is somewhat more like the radiative Eddington limit, but with an opacity that is inversely proportional to density, so the result again

suggest that lower density gas will be more readily accelerated.

3.3.3 Simulation Setup

Units and Scaling

When cooling is neglected, Equations (3.1a)-(3.1c) can be non-dimensionalised and rescaled via three free parameters, which we will take to be the characteristic length scale l_0, temperature T_0, and density ρ_0. The characteristic velocity v_0 is set to an isothermal sound speed using $v_0 \equiv c_{s,0} = \sqrt{k_b T_0/(0.6 m_p)}$, where k_B is Botzmann's constant, m_p is the proton mass. This leads to dimensionless time $t_0 = l_0/v_0$, energy density $E_0 = \rho_0 v_0^2$, flux $F_0 = \rho_0 v_0^3$, and acceleration $a_0 = v_0^2/l_0$. The choice of T_0, ρ_0, and l_0 can be rescaled to match varying galactic environments, as discussed in section 3.5.2. The exception will be where cooling is discussed in section 3.4.3, as cooling depends explicitly on the choice of temperature and density.

In the rest of paper, we report the dimensionless numbers unless otherwise noted. The fiducial vertical (x) and horizontal (y or z) sizes are $L_x = 400$ and $L_y = 50$, with 8000×1000 total cells for the fiducial resolution. The aspect ratio of calculation domain varies between the simulations to adjust for specific problems as well as to minimize the computation cost. We discuss the effect of domain aspect ratio in Section 3.4.4. In all simulations, we set the pressure floor $P_{\text{floor}} = 10^{-7}$ and density floor $\rho_{\text{floor}} = 10^{-8}$. We set the fiducial $V_{\text{m}} = 1000$ and discuss the effect of V_{m} in Section 3.4.4.

Initialization and boundary conditions

We envision our simulation as an atmosphere situated above a star forming environment (e.g. a galactic disk). The gravity g is created by the gas and stars below the atmosphere and a CR flux is provided by the stellar winds and supernovae occurring in the (unsimulated) environment below. Although idealised, this setup allows us to isolate and explore the impact of varying the CR flux in the launching region of the outflow, which is uncertain due to open questions about CR production, transport and destruction within the star forming environment. The downside of this setup is that it does not admit steady state wind solutions of the form present in spherical symmetry or other geometry that allows the wind to expand into a larger cross-sectional area as it moves out (Ipavich, 1975; Mao & Ostriker, 2018; Quataert et al., 2021).

We initialise the gas density to an isothermal profile in hydrostatic equilibrium

with static background gravity. The gas density is uniform in the y direction. In the x direction, the distribution is the maximum of $\rho_0 \exp(-x/h)$ and $\rho_{\text{bkgd}} = 7.988 \times 10^{-5}$. We choose a scale height $h = 2.018$. The initial isothermal temperature $T_{\text{init}} = 1.667$. Hydrostatic equilibrium for $\rho > \rho_{\text{bkgd}}$ requires $g = -0.826$. The magnetic field is initialised to be uniform with $B_x = B_0 = 2$ and all other components set to zero.

In the streaming limit, we set an isotropic diffusivity with $\kappa_{\text{diff}} = 10^{-8}$. In the streaming-diffusion and non-streaming runs, we adopt isotropic diffusion with the values reported in Table 3.1. The only exception is HSE_1F_hd_aniso, where the diffusivity parallel to the field $\kappa_{\text{diff},\parallel} = 100$ and the diffusivity perpendicular to the magnetic field $\kappa_{\text{diff},\perp} = 10^{-8}$.

The boundaries are periodic in the horizontal (y and z) directions. For the x direction, the top MHD boundary is outflow, while the bottom MHD boundary is reflecting for hydro variables and outflow for magnetic field variables. In order to prescribe a uniform CR flux, we fix the CR flux $F_{\text{c},x}$ in the bottom ghost zones and copy the CR energy density, y (and z for three dimensional runs) component of the CR flux to the ghost zones from the last active zone. For the top CR boundary condition, we copy the CR flux and energy from the last active zone. For the diffusion-only simulations, we implemented an alternate right MHD boundary that prevents any gas inflow, avoiding unphysical oscillations in the non-streaming simulations. We confirmed that the streaming runs were insensitive to this choice for the top MHD boundary condition.

Although we target a constant CR flux, we cannot precisely control the CR flux entering the domain when streaming dominates due to impacts from the CR "bottleneck" effect. After an initial transient phase, the boundary settles to a nearly constant CR flux that is usually slightly below the target $F_{\text{c},x}$, with temporal variations of several percent or less of the average value. Higher target fluxes provide results closer to the target value. For the fiducial expected $F_{\text{c},x} = 15.0$, the time average between $5.0 < t < 25.0$ of CR flux across the boundary in the simulation is $\overline{F}_{\text{CR,in}} = 12.2$. We define the average difference

$$\overline{\Delta F}_{\text{c,in}} = \frac{\int_t \left| < \mathcal{F}_{E_c} > - \bar{F}_{\text{c,in}} \right| dt}{\int_t dt},$$

where $< X >= \int_{\text{in}} X dA / \int_{\text{in}} dA$ is volume average of X at the bottom boundary, $\mathcal{F}_{E_c}$

is the flux of CR energy returned by Riemann solver at the bottom boundary. For a target flux $F_{c,x} = 15.0$, the fluctuation $\overline{\Delta F}_{c,in}/\overline{F}_{c,in} = 7.5\%$. For target CR fluxes $F_{c,x} = 60.0$ and $F_{c,x} = 135.0$, the average CR flux at the boundary is $\overline{F}_{c,in} = 59.074$, $\overline{F}_{c,in} = 134.451$, and fluctuation are only 1.1% and 0.5% accordingly.

3.4 RESULTS

3.4.1 The Effect of CR Flux on Streaming: from sub-Eddington to super-Eddington

The five streaming dominated simulations are HSE_hF_str HSE_1F_str, HSE_4F_str, HSE_9F_str and HSE_20F_str, the diffusivity is set to be $\kappa_{\text{diff}} = 10^{-8}$, so that $\sigma_c^{-1} \approx \frac{\mathbf{B}}{|\mathbf{B}\cdot(\nabla\cdot\mathsf{P}_c)|}\mathbf{v}_A \cdot (E_c\mathsf{I} + \mathsf{P}_c)$. We estimate the Eddington flux according to Equation 3.4. Assuming v_s is calculated using the initial density $\rho_{\text{init}} = \rho_0$ at the base of the atmosphere and the initial uniform magnetic field B_0, the estimated Eddington flux $F_{\text{edd,str}} = 20.0$.

We select HSE_1F_str with CR flux $F_c = 15.0$ as our fiducial run. This is somewhat sub-Eddington at the base of the domain, but becomes super-Eddington as the density drops.

Figure 3.1 shows density snapshots from HSE_1F_str for the bottom half of the domain. At early time $t = 1.5$, while the CR is streaming in the dense atmosphere, the gas density profile remains close to the initial distribution. This is shorter than the timescale for CRs to stream out of the gas, which we approximate as the Alfvén-wave crossing time:

$$t_{\text{str}} = \int_0^{2l_0} \frac{dx}{v_s(x)} = \frac{2h_0}{B_0/\sqrt{\rho_0}}\left(1 - e^{-\frac{l_0}{h_0}}\right),$$

which gives $t_{\text{str}} \sim 2.0$ for fiducial values. At later times, we see that a substantial fraction of the gas is lofted up as the atmosphere expands outward under a combination of CR and gas pressure. Since mass is conserved, the density drops near the base. Snapshots at $t = 18.0$ and $t = 24.0$ are similar, suggesting the gas is reaching a quasi equilibrium density profile, even though a modest outflow is present at these later times. There is also evidence of abrupt jumps in the density that show up more clearly in Figure 3.2. We attribute these inhomogeneities to the development of an acoustic instability, as discussed in section 3.5.3. Figure 3.1 shows that this instability

Table 3.1: Summary of Simulation Parameters

Name	κ	F_c	B_0	$L_x \times L_y$ [b]	$N_x \times N_z$ [b]	V_m
HSE_1F_str	10^{-8}	15.0	2.0	400×50	8000×1000	1000
HSE_hF_str	10^{-8}	7.5	2.0	400×50	8000×1000	1000
HSE_4F_str	10^{-8}	60.0	2.0	800×50	16000×1000	1000
HSE_9F_str	10^{-8}	135.0	2.0	800×50	16000×1000	1000
HSE_20F_str	10^{-8}	300.0	2.0	800×50	16000×1000	1000
HSE_1F_ld	1.0	15.0	2.0	200×5	4000×100	1000
HSE_1F_cd	10.0	15.0	2.0	200×25	4000×500	1000
HSE_1F_hd	100.0	15.0	2.0	200×5	4000×100	1000
HSE_1F_hd_aniso	100.0	15.0	2.0	200×5	4000×100	1000
HSE_1F_hd_ns[a]	100.0	15.0	2.0	200×25	4000×500	1000
HSE_1F_ld_ns[a]	1.0	15.0	2.0	200×25	4000×500	1000
HSE_1F_str_sc[c]	10^{-8}	15.0	2.0	400×50	8000×1000	1000
HSE_1F_str_wc[c]	10^{-8}	15.0	2.0	400×50	8000×1000	1000
HSE_9F_str_sc[c]	10^{-8}	135.0	2.0	400×50	8000×1000	1000
HSE_1F_str_b1	10^{-8}	15.0	1.0	200×5	4000×100	1000
HSE_1F_str_b4	10^{-8}	15.0	4.0	200×5	4000×100	1000
HSE_1F_str_VM	100.0	15.0	2.0	400×50	8000×1000	2000
HSE_1F_str_LR	10^{-8}	15.0	2.0	400×50	4000×500	1000
HSE_1F_str_HR	10^{-8}	15.0	2.0	400×50	16000×2000	1000
HSE_1F_str_3D	10^{-8}	15.0	2.0	$400 \times 25 \times 25$	$4000 \times 250 \times 250$	1000

[a] Streaming is turned off, equivalently setting $\mathbf{v}_\mathrm{s} = 0$ in Equation 1.10, Equation 3.1b, $\mathbf{v}_\mathrm{A} = 0$ in Equation 1.14.

[b] The reported dimension corresponds to the largest simulation domain for each set of parameters. Notice that some of the simulation has lower aspect ratio L_y/L_x, we discuss the effect of aspect ratio in Section 3.4.4

[c] The three adiabatic simulations with different cooling strength are scaled to different physical units.
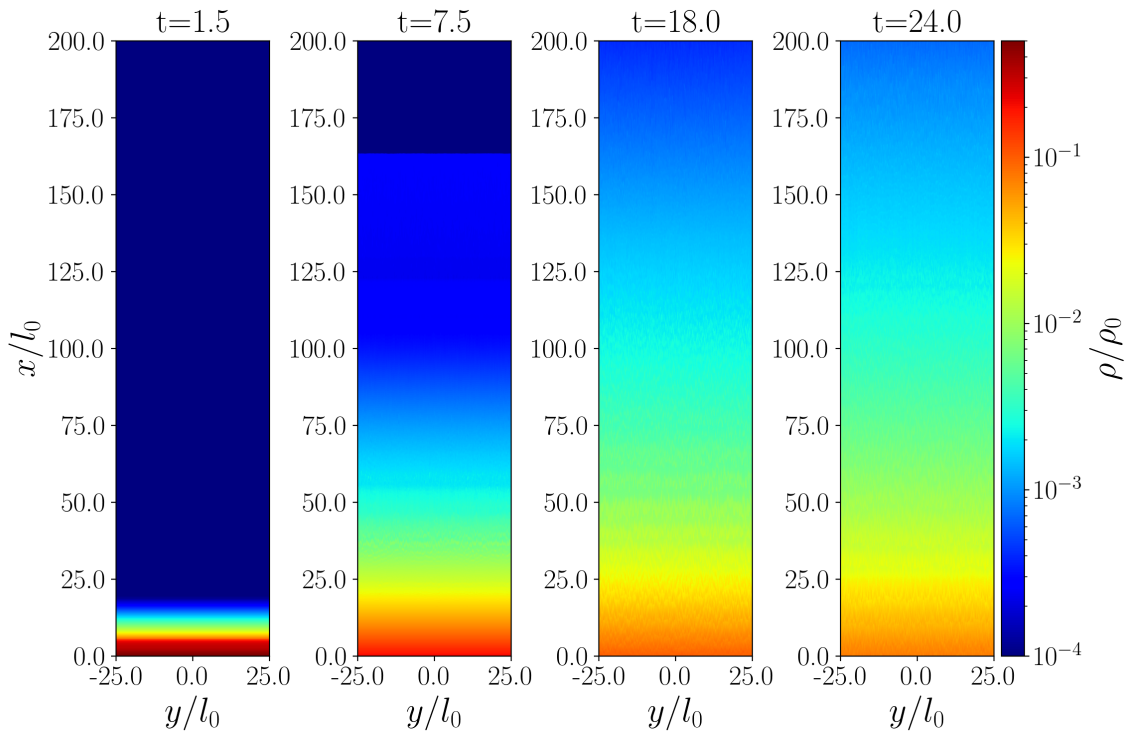
Figure 3.1: The density snapshots of HSE_1F_str. From left to right, t=1.5, 7.5, 18.0 and 24.0. The picture shows only half of the simulation domain in the x direction.

does not lead to large amplitude variations on the horizontal dimensions, at least for the magnetic field strength and geometry used here.

Figure 3.2 show horizontally averaged quantities and illustrates the "bottleneck" effect. When the CR force acts on gas and streaming dominates the CR flux, the streaming velocity $v_s \propto 1/\sqrt{\rho}$, increasing as the gas density drops. When CRs stream into the atmosphere, CRs tend to pile up in the dense region where they stream slower, resulting in a CR pressure gradient from dense gas to diffuse gas, producing the "bottleneck". Given the monotonic density profile, $P_{\rm CR}$ reaches its maximum at the base of the atmosphere and decreases outward.

Around $t = 1.8$, the gas density is similar to the initial profile and nearly unperturbed. The gas pressure closely follows the CR pressure, and the combined pressure gradients exceed the gravitational force, launching the atmosphere upward. By $t = 5.0$, the CRs begin to stream out of the dense gas and drive the expansion, enhancing both the CR and gas pressure in the initially low density background region ($x \gtrsim 20$). The large enhancement in gas pressure is driven by CR heating. Gas velocities are quite high for $x < 100l_0$, due to the combined acceleration by CR and gas pressure gradients.

As more gas is pushed towards the upper boundary, the density gradient becomes shallower and the Alfvén velocity gradient consequently decreases (the B field remains more constant). Therefore, the CR streaming "bottleneck" is less effective, the CR pressure gradient decreases, providing less heating and acceleration. The velocity decreases as more mass is swept up in the outflow and continues to do work against the constant gravitational acceleration. The combined gas and CR pressure gradients still exceed gravity, with velocity increasing upward due to the resulting acceleration. At $t = 18.0$, the diffuse gas starts to flow out of the domain, carrying away a modest faction of the initial mass. After this point and before we end the simulation at $t = 25.0$, all the quantities shown in this plot are changing slowly, with pressure and density gradients gradually becoming more shallow with time.

Even after horizontal averaging, the effects of the instabilities noted above can be discerned as the growth of a series of shocks in the gas density, pressure, and velocity profiles for $45 \lesssim x \lesssim 75$ at $t = 18.0$. We identify them as the result of CR acoustic instability and discuss them in more detail in Section 3.5.3. The instability, however, saturates at a level where it does not significantly change the volume averaged CR force. Despite the instability, the magnetic field is relatively unperturbed, making
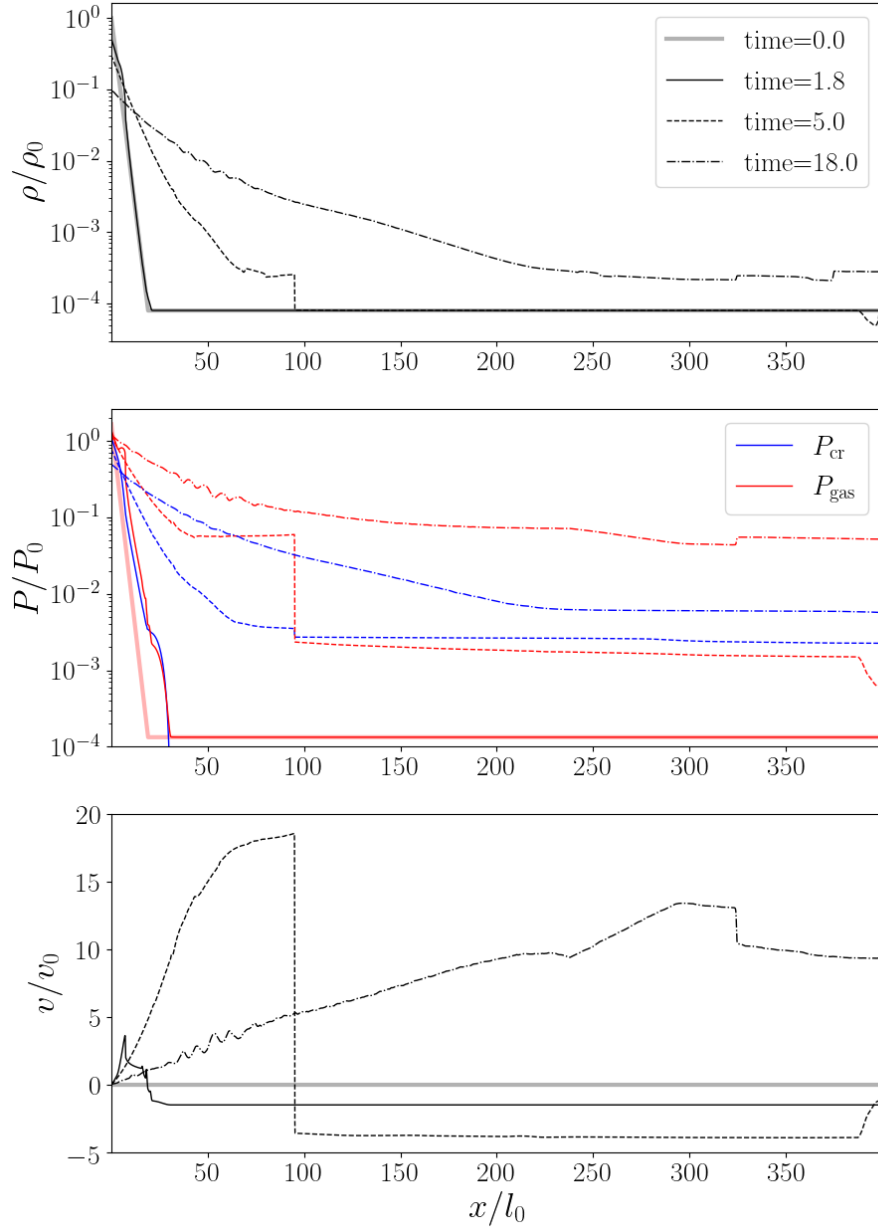
Figure 3.2: The y direction averaged density (the first row), CR pressure (the blue lines in the second row), gas pressure (the red lines in the second row) and gas velocity (the third row) of HSE_1F_str. The line style corresponds to different time, the thick solid lines in each panel are the initial profile. Other sampled times are t=1.8 (the thin solid lines), t=5.0 (the dashed lines) and t=18.0 (the dashed dotted lines).
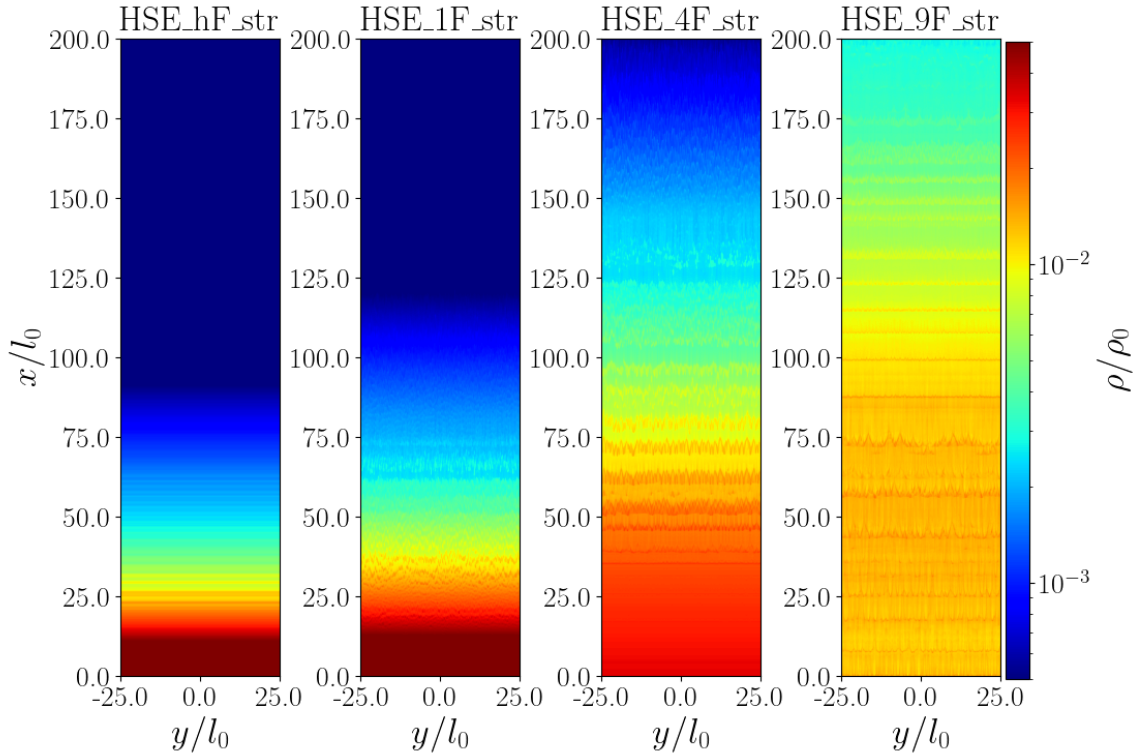
Figure 3.3: The density snapshots at $t = 10.0$ for four streaming dominated simulations with different CR flux. From left to right, the injected CR flux $F_c = 7.5$(HSE_hF_str), 15.0(HSE_1F_str), 60.0(HSE_4F_str), 135.0(HSE_9F_str). We only show part of the domain in the x direction (see L_x in Table 3.1).

CRs effectively stream along the uniform magnetic field. Hence, there is no analogue of the Rayleigh-Taylor instability that regulates the acceleration of gas in radiatively driven atmospheres (Krumholz & Thompson, 2012).

The overall dynamical picture is that CRs accelerate gas against gravity even with this moderate CR flux, but a significant fraction of the energy goes into heating. According to Equation 1.10, CRs heat the gas at the rate of $\mathbf{v}_A \cdot \nabla P_{CR}$. Since $v_A \propto 1/\sqrt{\rho}$, the lower density regions tend to experience greater heating. Gas is in the low density background can be heated by over two orders of magnitude with the lowest density gas experiencing the largest heating. These results suggest radiative cooling could play a significant role and we consider its impact below.

Figures 3.3 and 3.4 show the impact of varying the target CR flux injected at the base of the atmosphere. We consider simulations with CR fluxes 0.5 (HSE_hF_str),

4 (HSE_4F_str), 9 (HSE_9F_str) and 20 (HSE_20F_str) times the flux in the fiducial run. Although the overall dynamics are similar, HSE_4F_str and HSE_9F_str produce more significant gas outflow in shorter time. In contrast, in the sub-Eddington case HSE_hf_str with half of the fiducial CR flux, the atmosphere expands outward over a longer timescale, but by the time we finish other simulations at $t = 25$, there is no significant gas outflow. Figure 3.3 compares the gas density snapshot at $t = 10.0$ of these simulations. As we increase the CR flux from sub-Eddington to super-Eddington, the atmosphere is more dispersed and the outflow carries larger mass and momentum. We see that as the CR flux increases, the shocks driven by acoustic instability become more prominent, but the amplitude never becomes large enough to have a significant feedback on the gas acceleration.

Figure 3.4 shows the volume average of the mass outflow rate per area $\dot{M}_{\text{out}}$ (the upper panel) and averaged outflow velocity v_{out} (the lower panel) at $x = 400l_0$ as a function of time. $\dot{M}_{\text{out}}$ and v_{out} are calculated as:

$$\dot{M}_{\text{out}} = \frac{\int_t \int_{\text{out}} \mathcal{F}_\rho dy dt}{\int_t \int_{\text{out}} dy dt}, \quad v_{\text{out}} = \frac{\int_t \int_{\text{out}} \rho v v dx dy dt}{\int_t \int_{\text{out}} \mathcal{F}_\rho dy dt}, \tag{3.6}$$

where $\mathcal{F}_\rho$ is the density flux returned by Riemann solver on the outer boundary, $\rho v v|_{\text{out}}$ is the $\rho v v$ calculated at the outer boundary, $\int_{\text{out}}$ denotes integration on the outer boundary. At early times, there is modest inflow and velocities are negative due to the fact that the isothermal and constant density background has no pressure gradient to support the gas against gravity. For the sub-Eddington run, the combination of CR and gas pressure is never sufficient to overcome gravity and this inflow persists to the end of the simulation. For the marginal and super-Eddington cases, the CR and gas pressure forces eventually exceed gravity and drive outflows. The general trend is that both the velocities and mass outflow rates increase as the injected CR flux increases.

The outflow rates in simulations reflect the different force balance in sub-Eddington systems and super-Eddington systems. Figure 3.5 shows the x direction forces as a function of time for the fiducial near-Eddington case (HSE_1F_str) and a super-Eddington case (HSE_9F_str). Here we only explicitly plot the gas pressure gradient force (the red dashed line) and CR pressure gradient force (the purple dashed line), the sum with other forces including gravity, magnetic field force and advected
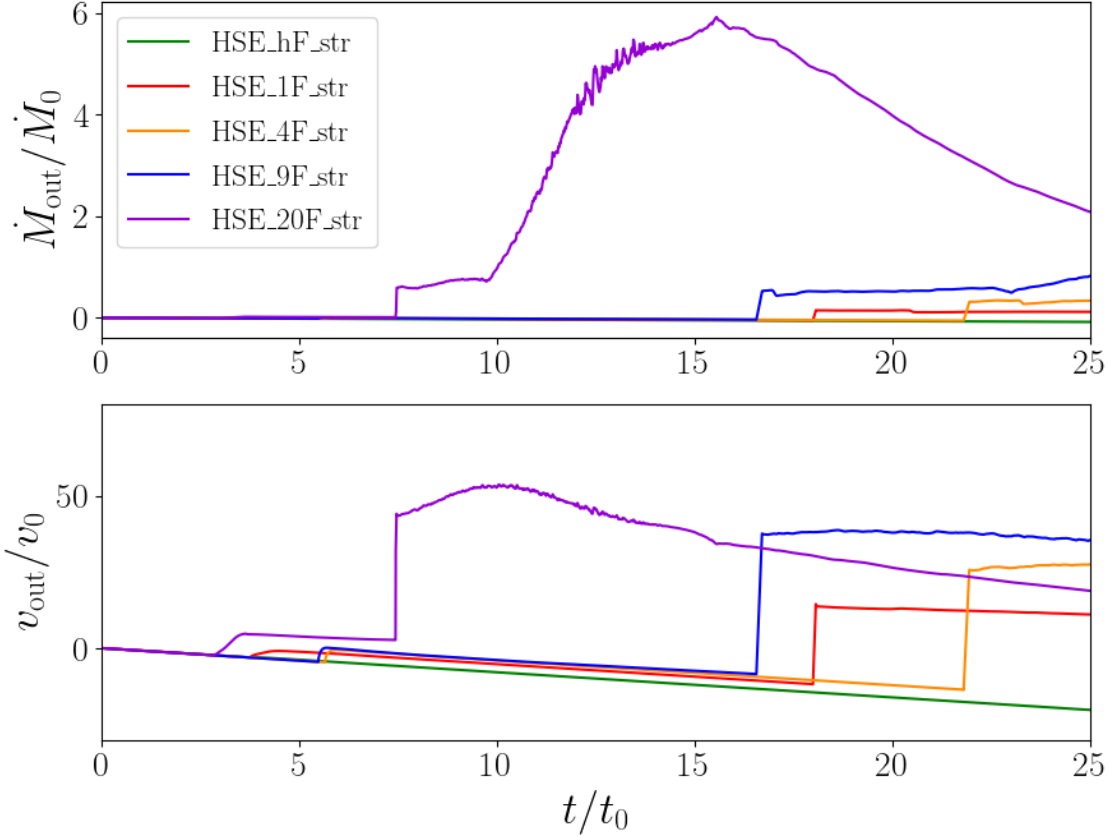
Figure 3.4: The gas outflow from simulations in the streaming limit with different injecting CR flux: HSE_hF_str (green), HSE_1F_str (red), HSE_4F_str (red), HSE_9F_str (blue) and HSE_20F_str (purple), measured at $x = 400l_0$. In this plot, we report the results from simulations with the same box size $L_x = 400$ instead of the reported L_x in Table 3.1. Upper panel: the mass outflow rate per unit area. Lower panel: the average outflow velocity. Both defined as Equation 3.6
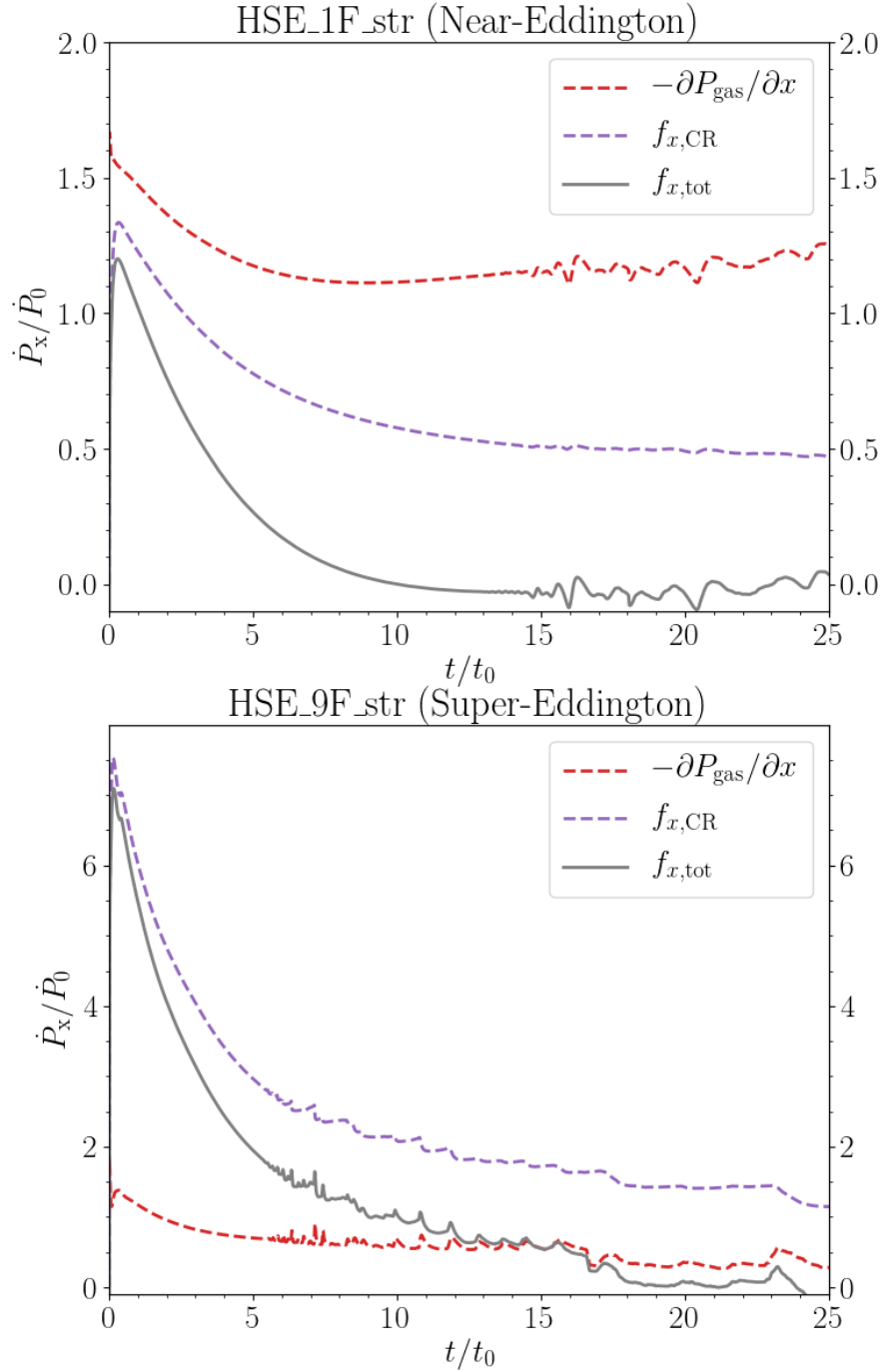
Figure 3.5: Force terms in the x direction as a function of time for the nearly-Eddington (the top panel) HSE_1F_str and the Super-Eddington case HSE_9F_str (the bottom panel). The force terms are summed over across the domain. In both panels, the red dashed line is gas pressure gradient force, the purple dashed line is CR pressure gradient force, and the gray solid line is total x direction force. The rate is sampled every $\Delta t = 0.001$.

momentum is the grey solid line. A direct difference between near-Eddington and super-Eddington is the inversion of CR and gas pressure gradient force. We also examine other simulations with different CR flux, the super-Eddington runs always have a higher CR force than gas pressure gradient force, and vice versa for the sub-Eddington and near-Eddington cases.

Despite the different interplay between gas pressure and CR forces, the CR force (dashed purple lines) follows similar time evolution: it peaks at the beginning, then relaxes to a lower value in a few t_{str}, and slowly decreases. This is because the "bottleneck" effect relies on gas density gradient. However, as gas is accelerated and dispersed, the density gradient becomes shallower and even vanishes, so the CR pressure gradient forces drops commensurately at later time. The gas pressure gradient is modified by CR-gas interactions, and contributes to support against gravity. Although the total force tends to be relatively constant and close to zero at later times, there is no steady state wind developed in our simulations since the initial gas is redistributed and slowly depleted. Nevertheless, our results confirm that the CR Eddington flux is a good criterion for distinguishing the presence of significant levels of CR driven outflow.

3.4.2 The Effect of CR Transport Mechanism: Streaming versus Diffusion

In this section, we consider the relative importance of CR diffusion and streaming. Although all the streaming runs reported above have a small nominal diffusive component ($\kappa_{diff} = 10^{-8}$), the CR flux is completely dominated by streaming. We first consider three hybrid cases where both streaming and diffusion are present: low diffusivity (HSE_1F_ld $\kappa_{diff} = 1.0$), comparable diffusivity (HSE_1F_cd, $\kappa_{diff} = 10.0$), and high diffusivity (HSE_1F_hd, $\kappa_{diff} = 100.0$) but parameters are otherwise set to match the fiducial run (HSE_1F_str). We also consider two diffusion (non-streaming) simulations with high diffusivity (HSE_1F_hd_ns, $\kappa_{diff} = 100.0$) and low diffusivity (HSE_1F_ld_ns, $\kappa_{diff} = 1.0$). These non-streaming simulations have $\mathbf{v}_s = 0$ and $\mathbf{v}_A = 0$ in Equation 3.1a-3.1c and Equation 1.14, so CRs cannot heat the gas via wave damping.

We first look at the diffusion-only simulations. The CR flux $\mathbf{F}_{CR} \sim -\kappa_{diff}\nabla P_{CR}$, so $\nabla P_{CR} \sim -\mathbf{F}_{CR}/\kappa_{diff}$. If we ignore the time-dependent term in Equation (3.1c), the CR contribution to gas momentum is ∇P_{CR}. So for a given CR flux, larger κ_{diff} gives
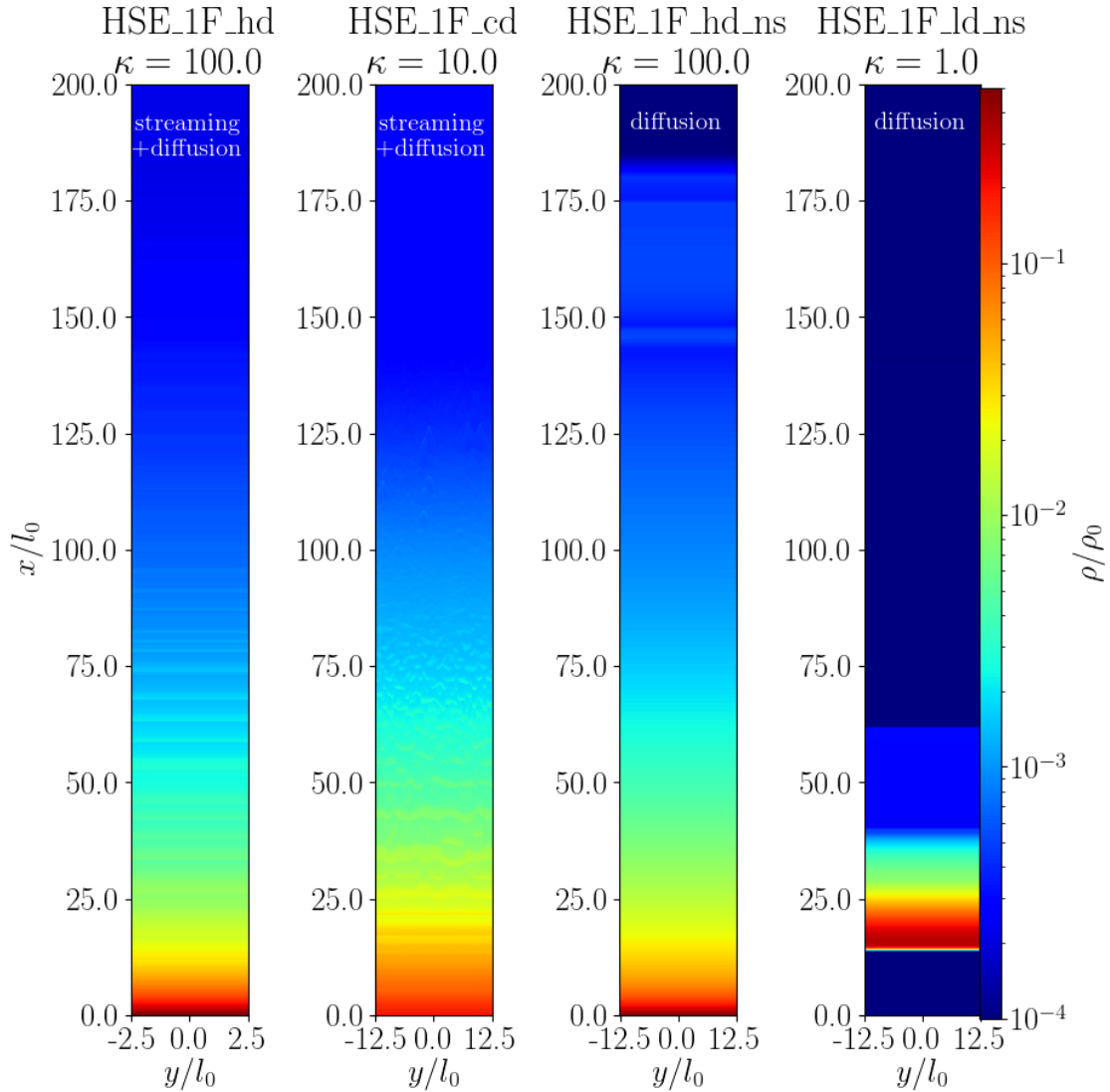
Figure 3.6: The density snapshots at $t = 10.0$ for different CR transport models. From left to right, the first two columns are streaming and diffusion, the diffusivity is $\kappa_{\mathrm{diff}} = 10.0$(HSE_1F_cd) and $\kappa_{\mathrm{diff}} = 100.0$ (HSE_1F_hd). The thrid and fourth columns are pure diffusion without streaming. The diffusivity are accordingly $\kappa_{\mathrm{diff}} = 100.0$ (HSE_1F_hd_ns) and $\kappa_{\mathrm{diff}} = 1.0$ (HSE_1F_ld_ns). The aspect ratio of plots are adjusted for the purpose of visual comparison with each other, the Y labels indicate the actual size of calculation domain.

the smaller acceleration since CRs diffuse through the gas more quickly without much interaction. The gas density for HSE_1F_hd_ns and HSE_1F_ld_ns at $t = 10.0$ is shown in the third and fourth column in Figure (3.6) respectively. In HSE_1F_ld_ns CRs cannot diffuse through the gas rapidly, so a strong CR pressure gradient develops at the base of the atmosphere, with the CR force exceeding gravity and lofting the entire atmosphere. Presumably, there would be feedback on the injected CR flux in a more realistic set-up but the key result here is that CRs are capable of collectively launching and accelerating the gas against gravity, with no instabilities (e.g. Parker or Rayleigh-Taylor like) present to disrupt the shell.

In contrast, HSE_1F_hd_ns experiences a more gentle acceleration. CRs diffuse through the gas expanding the atmosphere in a manner more similar to the streaming runs but with very little outflow. This difference between $\kappa_{\mathrm{diff}} = 100.0$ and $\kappa_{\mathrm{diff}} = 1.0$ dynamics also can be interpreted in terms of the CR Eddington flux. For the injected CR flux $F_{\mathrm{c}} \approx 15.0$, the low diffusivity ($\kappa_{\mathrm{diff}} = 1.0$) run is super-Eddington at the base ($F_{\mathrm{edd}} \approx 0.83$), but the high diffusivity ($\kappa_{\mathrm{diff}} = 100.0$) run is substantially sub-Eddington ($F_{\mathrm{edd}} \approx 82.62$) so the atmosphere relaxes to steady state with a larger scale height rather than driving outflow.

We turn on both streaming and diffusion in HSE_1F_ld, HSE_1F_cd and HSE_1F_hd. The gas momentum source term is proportional to the interaction coefficient σ_{c}. The first term in the interaction coefficient is the classical diffusivity, the second term is $\sigma_{\mathrm{str}}^{-1}$ is an effective "diffusivity" for streaming. We estimate it based on the initial value at the base of atmosphere: $\sigma_{\mathrm{str,init}}^{-1} \approx 4v_{\mathrm{A}}/(\partial \ln P_{\mathrm{c}}/\partial x) \approx -6v_{\mathrm{A}}H_{\rho} \approx 24.2$ (see similar derivation in Equation 3.4). In HSE_1F_ld we set $\kappa_{\mathrm{diff}} = \sigma_{\mathrm{c}}'^{-1} = 1.0$, so that the interaction coefficient is dominated by the effective streaming coefficient, while in HSE_1F_hd $\kappa_{\mathrm{diff}} = 100.0$, so the diffusivity dominates. The isotropic diffusivity in HSE_1F_cd is $\kappa_{\mathrm{diff}} = 10.0$, which is about the same order of magnitude as $\sigma_{\mathrm{str,init}}^{-1}$.

The first two columns in Figure 3.6 compare the density snapshots for the streaming-diffusion simulations: HSE_1F_cd and HSE_1F_hd at $t = 10.0$. The gas distribution in HSE_1F_ld (not shown) is almost identical to the streaming simulation HSE_1F_str with the same CR flux shown in Figure 3.1. In HSE_1F_ld, the small diffusivity does not lead to a large CR pressure gradient as the pure diffusion case because σ_{c}^{-1} is now dominated by the streaming component. By preventing the development of large gradients, CR streaming limits the CR force when CR diffusivity is low. At the other end where the diffusivity is large, the gas density profile in

HSE_1F_hd is similar to the non-streaming case HSE_1F_hd_ns with the same diffusivity, except for the presence of shocks formed from the acoustic instability. In HSE_1F_cd, where streaming and diffusion are comparable, the result falls between these limits, but most similar to the HSE_1F_ld run.

When κ_{diff} is small, the interaction coefficient is dominated by the streaming component, and the dynamics is similar to streaming limit. Increasing κ_{diff} will ensure that $\sigma_c^{-1} \sim \kappa_{\mathrm{diff}}$ but also lower the interaction coefficient, which usually leads to a reduction of the CR pressure gradient, reducing the CR force on the gas. The upper panel of Figure 3.7 illustrates the decrease in the CR pressure gradient as κ_{diff} increases in the streaming-diffusion runs at early time ($t = 1.5$), approximately when the CR force peaks.

The bottom panel shows the total CR flux (the solid lines) and the streaming flux (the dashed line) at the same time. Since gas has not yet received a significant acceleration, the advection flux ($4v_{\mathrm{x}}P_{\mathrm{c}}$) is small. Thus, the difference between total CR flux and streaming flux is dominated by the diffusive flux. When diffusivity is low, the CR flux is dominated by the streaming flux ($4v_{\mathrm{A}}P_{\mathrm{CR}}$), but the diffusive flux is significant wherever the pressure gradient is present and diffusivity is large. To illustrate the difference, we also show the CR flux for the diffusion-only run with $\kappa_{\mathrm{diff}} = 100.0$ as the grey solid line, which does not have the streaming component. Although changing κ_{diff} modifies the balance of streaming and diffusive flux, the total flux is fixed by our boundary condition, so σ_{c} roughly controls the amount of momentum that CR transfers to gas. The upshot is that for a given CR flux, the overall momentum transfer from CRs to gas is generally reduced when streaming operates.

3.4.3 The Impact of Cooling

In this section, we study the effect of radiative cooling by comparing three streaming-dominated simulations with different cooling times. A more detailed treatment of cooling and the effects of thermal instability on CR driven outflows will be presented in a companion paper (Huang, Jiang & Davis, in preparation). We adopt an optically thin radiative model with cooling rate $n_H^2\Lambda(T)$ and a constant supplemental heating rate $n_H\Gamma$. The cooling function $\Lambda(T)$ is taken from Wiener et al. (2019c), which is an approximation to fit the CLOUDY data from Wiersma et al. (2009) assuming solar
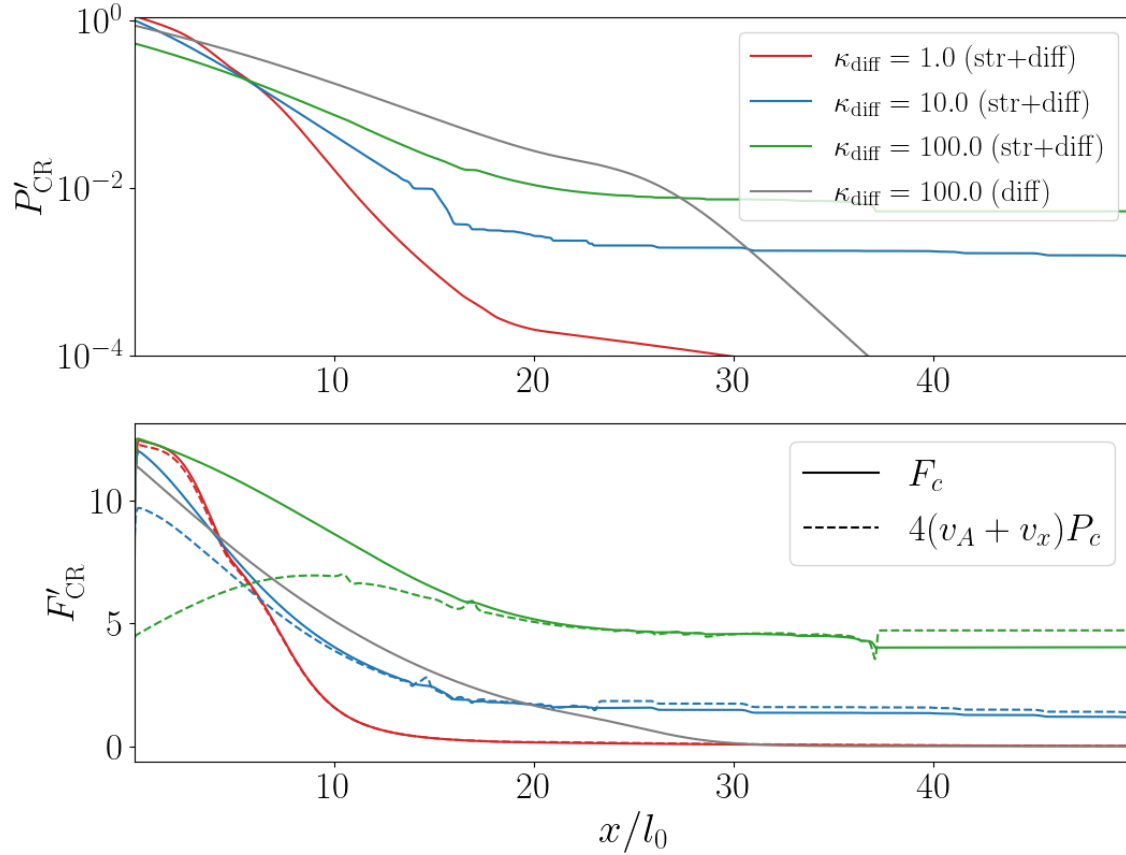
Figure 3.7: y direction averaged CR pressure (the first row), total CR flux (solid lines in the second row), the streaming flux component (dashed lines in the second row) for $0 < x < 50$ at $t = 1.5$ for the diffusion runs: HSE_1F_hd (grey solid line) and the three streaming-diffusion simulations: HSE_1F_str_ld (red lines), HSE_1F_str_cd (blue lines), HSE_1F_str_hd (green lines). Note that there is no grey dashed curve because streaming is not relevant here.

metallicity:

$$\Lambda(T) = 1.1 \times 10^{-21} \times 10^{\Theta(\log(T/10^5 \mathrm{K}))} \mathrm{erg} \ \mathrm{cm}^3 \ \mathrm{s}^{-1}, \tag{3.7}$$

where

$$\Theta(x) = 0.4x - 3 + \frac{5.2}{e^{x+0.08} + e^{-1.5(x+0.08)}} \tag{3.8}$$

We cut off the radiative cooling for gas with temperature below 10^4K.

Because cooling is proportional to n_H^2, the cooling time significantly increases as the gas density decreases with height. The initial cooling timescale at two scale heights is larger than the cooling timescale at the base by more than two orders of magnitude. We report our simulations in terms of t_{cool}/t_0, the ratio of the cooling time to sound crossing time at the base of the simulation, but this will overestimate the importance of cooling higher in the simulation where densities are lower. If $t_{\mathrm{cool}} < t_0$ we expect cooling to impact the gas pressure gradient, but if $t_{\mathrm{cool}} > t_0$, cooling may not be important for the gas dynamics.

In contrast to our non-radiative simulations, introduction of cooling fixes the density and temperature of the simulation, removing the scaling freedom that was previously present. HSE_1F_str_wc has $t_{\mathrm{cool}}/t_0 = 0.7$ (initially) at the base. The density scaling unit is $\rho_0 = 2.35 \times 10^{-27}$g cm^{-3}, the length unit is $l_0 = 1.54 \times 10^{20}$cm, and the temperature unit $T_0 = 9.9 \times 10^4$K. For HSE_1F_str_sc and HSE_9F_str_sc the density scaling unit is $\rho_0 = 2.35 \times 10^{-25}$g cm^{-3}, the length unit is $l_0 = 1.54 \times 10^{20}$cm, and the temperature unit $T_0 = 9.9 \times 10^3$K, yielding $t_{\mathrm{cool}}/t_0 = 0.06$ at the base. However, we continue to report results in dimensionless numbers to facilitate comparison to non-radiative simulations.

Figure 3.8 shows snapshots of horizontally (y) averaged gas density (top panel), CR pressure (middle panel) and gas pressure (bottom panel) at $t' = 20$. The blue solid line shows the profile of the non-radiative run HSE_1F_str, and the other two solid lines are the radiative simulations. The red dashed lines shows the non-radiative super-Eddington flux simulation HSE_9F_str, and the purple dashed line is the corresponding radiative simulation: HSE_9F_str_sc.

For simulations with near-Eddington CR flux the orange lines show the profiles from the radiative run HSE_1F_str_wc. The gas pressure at the base is lower due to the cooling, but because the cooling is relatively moderate, it has limited effect on the overall dynamics. The gas density and CR pressure are similar to non-radiative simulations.
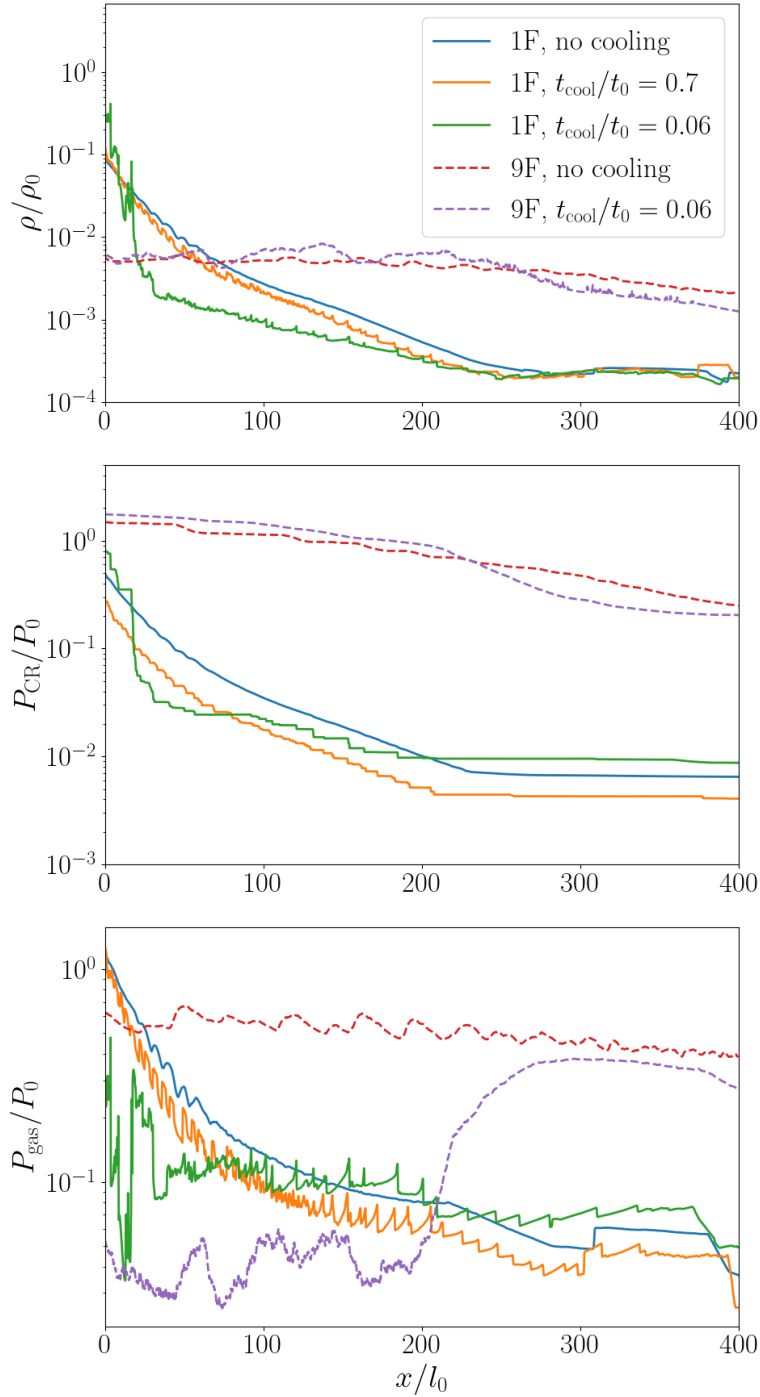
Figure 3.8: The y direction averaged gas density (the first row), gas pressure (the second row), CR pressure (the third row) for the marginal-Eddington flux: HSE_1F_str (blue solid lines, no cooling), HSE_1F_str_wc (orange solid lines, weak cooling) and HSE_1F_str_sc (green solid lines, strong cooling), and the super-Eddington flux HSE_9F_str (red dashed lines, no cooling) and HSE_9F_str_sc (purple dashed lines, strong cooling) The snapshots are sampled at $t = 20$.
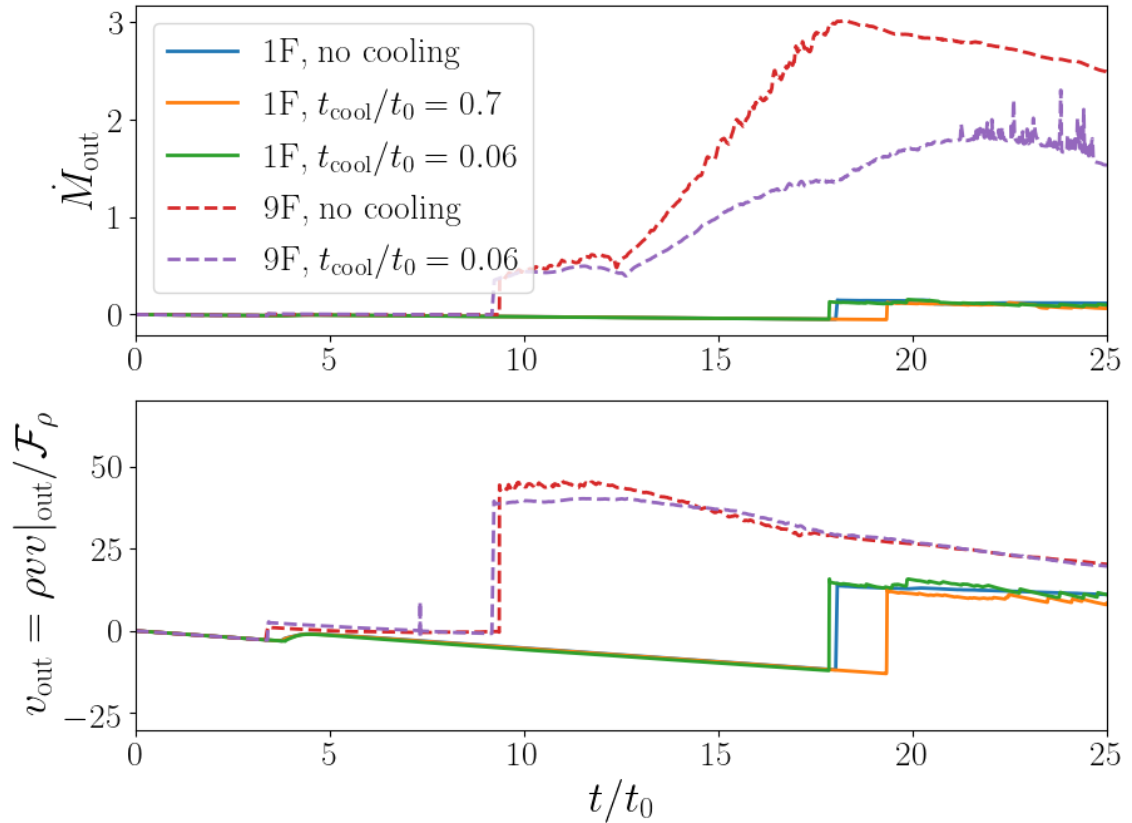
Figure 3.9: The mass outflow rate per unit area (the upper panel) and average velocity (the lower panel) for the marginal-Eddington flux: HSE_1F_str (blue solid lines, no cooling), HSE_1F_str_wc (orange solid lines, weak cooling) and HSE_1F_str_sc (green solid lines, strong cooling), and super-Eddington flux HSE_9F_str (red dashed lines, no cooling) and HSE_9F_str_sc (purple dashed lines, strong cooling). Comparing the simulations without cooling, with short cooling timescale and long cooling timescale, the three marginal-Eddington runs shows similar outflow properties, the two super-Eddington runs have different mass outflow rate, but similar velocity.

The green lines are the profiles from HSE_1F_str_sc, where the short cooling time significantly alters the gas profile at the base compared to HSE_1F_str. Since the internal energy is radiated away, the gas lacks pressure support and falls toward the base, forming a much sharper density gradient and is less dispersed compared to the non-radiative and moderate cooling runs. The sharper density gradient increases the bottleneck effect for CR streaming, leading to a stronger CR force on the gas.

The horizontally averaged gas density profile is more strongly clumped in both radiative runs. The shocks created by acoustic instability are enhanced by cooling. Since the shocks are relatively isothermal, the enhanced density in the shock increases the cooling rate, lowering gas pressure relative to the shocks in non-radiative runs. The relatively lower pressure support allows the gas to condense more effectively.

Despite the differences in the gas density profiles, the outflow properties from the three near-Eddington runs shows in Figure 3.9 are similar. The outflow we observed in the simulations with near-Eddington CR flux are composed primarily of low density gas, where the cooling time is significantly longer than dynamical timescales. An interesting contrast is provided the super-Eddington simulation HSE_9F_str_sc, which also has a short cooling time and corresponds to the purple dashed line in Figure 3.8 and Figure 3.9.

In the lower panel of Figure 3.8, the gas pressure is significantly reduced by cooling and the gas pressure gradient is inverted compared to the initial profile. The gas density profile is similar to its non-radiative counterpart simulation HSE_9F_str (red dashed line), however, because the CR force dominates over the gas pressure force. The momentum transfer between CRs and gas that primarily determines the gas density and velocity distribution in super-Eddington systems is only indirectly impacted by radiative cooling. Figure 3.9 shows that the mass outflow rates are reduced by cooling but the effect is less than 50% and velocities are relatively unimpacted. The upshot is that cooling is likely to be important in setting density profiles in the wind launching regions, but is probably less important in the super-Eddington cases, where CR forces are more important than cooling. Cooling may still be very important in the subsequent outflow dynamics (Wiener et al., 2017; Bustard et al., 2020; Hopkins et al., 2020, Huang, Jiang & Davis, in prep.) or in the overall structure of the CGM (Ji et al., 2020).

3.4.4 The Effect of Simulation Parameters

In this section, we briefly discuss a number of factors in our setup and their impact on the numerical results, including the simulation dimensions and aspect ratio in Section 3.4.4, along with resolution, dimensionality, and choice of $V_{\max}$ in Section 3.4.4.

Aspect Ratio and Domain Size

Some of the simulations listed in Table 3.1 are performed with different aspect ratios. While the fiducial box size is $L_x \times L_y = 400 \times 50$, we have some simulations with longer L_x or shorter L_y. First we discuss the effect of varying L_x, then the effect of varying L_y.

We increase L_x in streaming dominated runs with larger CR flux, because the larger acceleration requires large box size to capture the gas - CR interactions. For the higher CR flux runs, the efficiency of momentum and energy transfer between CR and gas depends on L_x. We define the x direction momentum transfer efficiency $\dot{p}_{\to g}/\dot{p}_{x,\mathrm{CR}}$ and energy transfer efficiency $\dot{E}_{\to g}/\dot{E}_{\mathrm{CR}}$ as:

$$\dot{p}_{x,\to g}/\dot{p}_{x,\mathrm{CR}} = \frac{\int \sigma_c \hat{\mathbf{n}}_x \cdot [\mathbf{F}_{\mathrm{CR}} - \mathbf{v}\cdot(E_c\mathsf{I} + \mathsf{P}_c)]dV}{\int_{\mathrm{in}} \mathcal{F}_{F_c} dA} \qquad (3.9)$$

$$\dot{E}_{\to g}/\dot{E}_{\mathrm{CR}} = \frac{\int (\mathbf{v}+\mathbf{v}_s)\cdot(\nabla\cdot\mathsf{P}_c)dV}{\int_{\mathrm{in}} \mathcal{F}_{E_{\mathrm{CR}}} dA} \qquad (3.10)$$

where $\mathcal{F}_{F_c}$ and $\mathcal{F}_{E_{\mathrm{CR}}}$ are the flux of CR momentum in x direction and CR energy returned by Riemann solver. So the x direction momentum (or energy) transfer efficiency describes what fraction of total injected x direction CR momentum (or CR energy) is given to the gas in the domain.

Figure 3.10 shows the momentum transfer efficiency a function of time for different choices of box length L_x. In general, L_x has a relatively insignificant effect on the simulations with sub-Eddington fluxes (red and green curves). However, the box size largely impacts the result of super-Eddington cases where the gas outflow is significant. For example in HSE_9F_str (blue curves), both momentum and energy transfer efficiency between CR and gas increases significantly as we go from shorter ($L_x = 200$) to longer ($L_x = 800$) boxes due to the capturing of more out-moving gas. Equivalently, the vertically longer domain allows more time for the CR forces to act on the gas, transferring a larger momentum fraction.
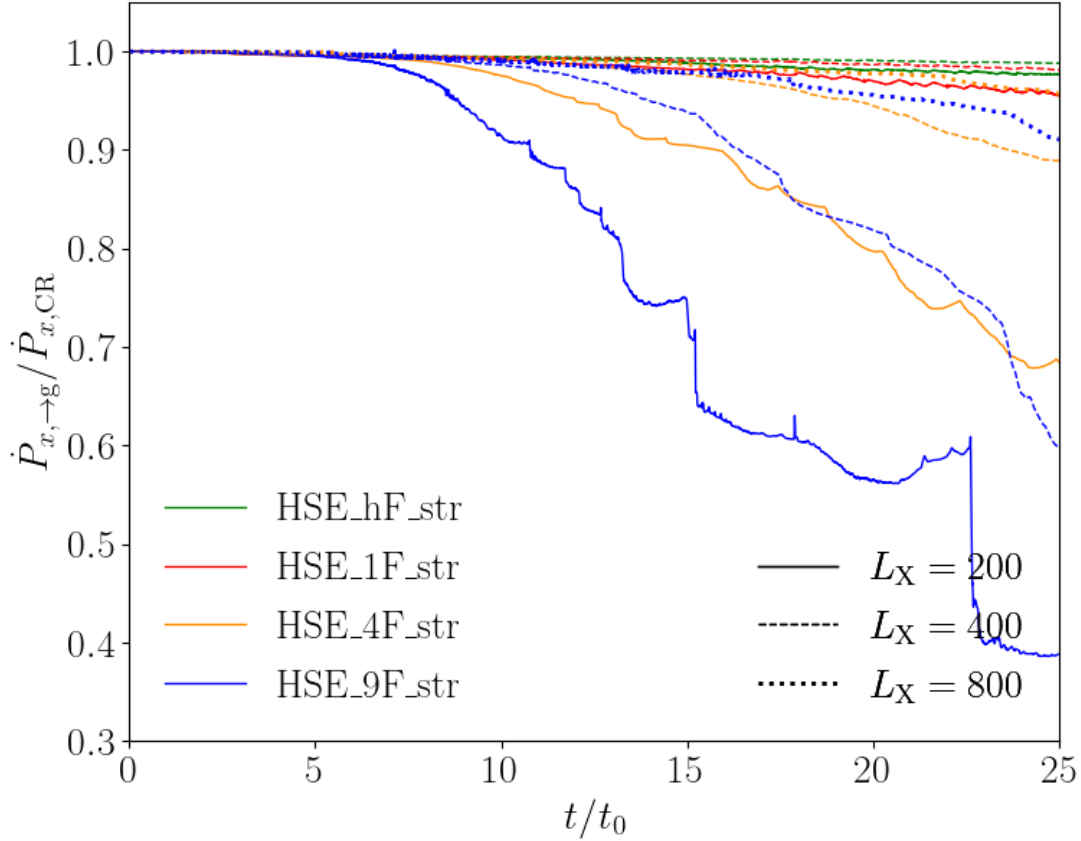
Figure 3.10: The effect of box size on momentum transfer efficiency. The lines are time evolution of the ratio between total momentum transferred to gas from CR and total injected CR momentum for HSE_hF_str (green lines), HSE_1F_str (red lines), HSE_4F_str (orange lines) and HSE_9F_str (blue lines). The line style shows the domain width L_x, where solid lines are for $L_x = 200$, dashed lines are for $L_x = 400$ (fiducial), and dotted lines are for $L_x = 800$.
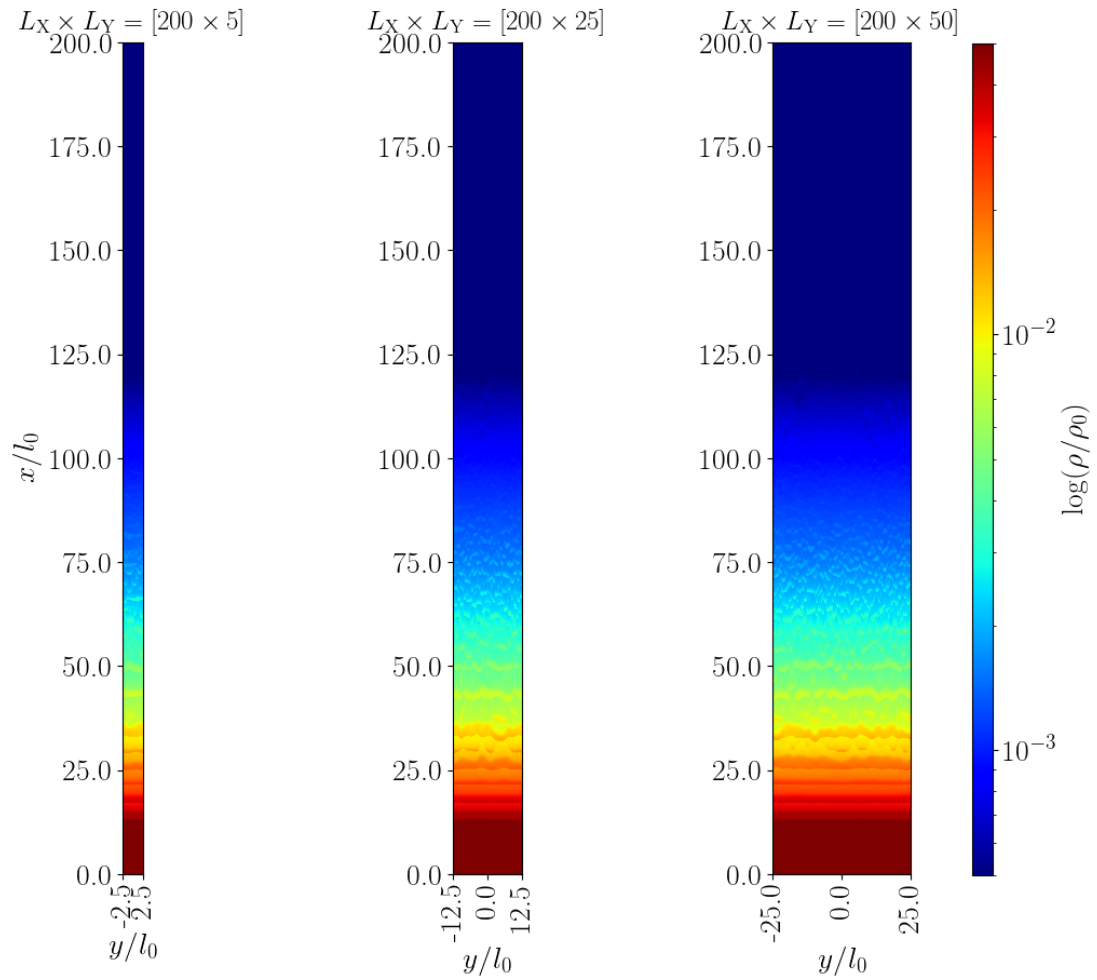
Figure 3.11: The gas density snapshots from HSE_1F_cd at $t = 10.0$. From left to right: $L_y = 5, 25, 50$. The aspect ratio of the third row is adjusted for the purpose of visual comparison, the y/l_0 labels denote the actual width.

For our nearly plane-parallel geometry and nearly vertical magnetic field, the width of the simulation domain L_y seems to have negligible results on the overall dynamics. Figure 3.11 shows the gas density snapshots at $t = 10.0$ for HSE_1F_cd, in which both streaming and diffusion are operating with $\kappa_{\mathrm{diff}} = 10.0$. There is a modest impact on the growth of the acoustic instability, but the differences have insignificant impact on the dynamics in the vertical direction.

Resolution, Dimensionality and V_{max}

Figure 3.12 shows a comparison of results at $t = 10$ from high resolution (HSE_1F_str_HR), moderate resolution (HSE_1F_str), and low resolution (HSE_1F_str_LR) runs. We fix the vertical and horizontal dimensions, increasing the number of zones in both directions by a factor of two for each increased resolution run. Aside from a modest effect on the development of the acoustic instability, the runs are insensitive to the resolution adopted here. The momentum and energy transfer efficiencies between gas and CR are also insensitive to resolution. Note that the amplitude of the shocks depends on resolution, with lower amplitude in the HSE_1F_str_LR run, and nearly disappearing in even lower resolution test runs (not shown). But, the amplitude seems to be converging between HSE_1F_str_HR and HSE_1F_str.

To study the impact of our two-dimensional assumption, we also perform a three-dimensional simulation, which is shown as the purple curve in Figure 3.12. As with resolution, there is no evidence of significant dependence on dimensionality, at least for the streaming simulations and magnetic field geometry employed here.

Finally, we consider the dependence on V_m, which acts like a reduced speed of light for the time-dependent term in Equation 3.1c. This approximation allows us to take larger timesteps, which scale inversely with V_m. Previous tests have indicated that this is a reasonable approximation as long as V_m is larger than other physical velocities in the simulation. In simulations presented here, the maximum physical speed tends to be the Alfvén speed in the diffuse background medium, which is about $v_{\mathrm{A,max}} \approx 224$, while we use $V_m = 1000$ in all the simulations except HSE_1F_str_VM, where $V_m = 2000$. In our dynamical problems, the time-dependent term $(1/V_m^2)\partial \mathbf{F}_{\mathrm{CR}}/\partial t$ in Equation 3.1c is much smaller than the other terms, so we expect our choice of V_m should not impact our results. Jiang & Oh (2018) point out that the main physical effect of using V_m is overestimation of the momentum carried by CRs by c^2/V_m^2, but this has little impact on the CR force, which determines momentum transfer to the
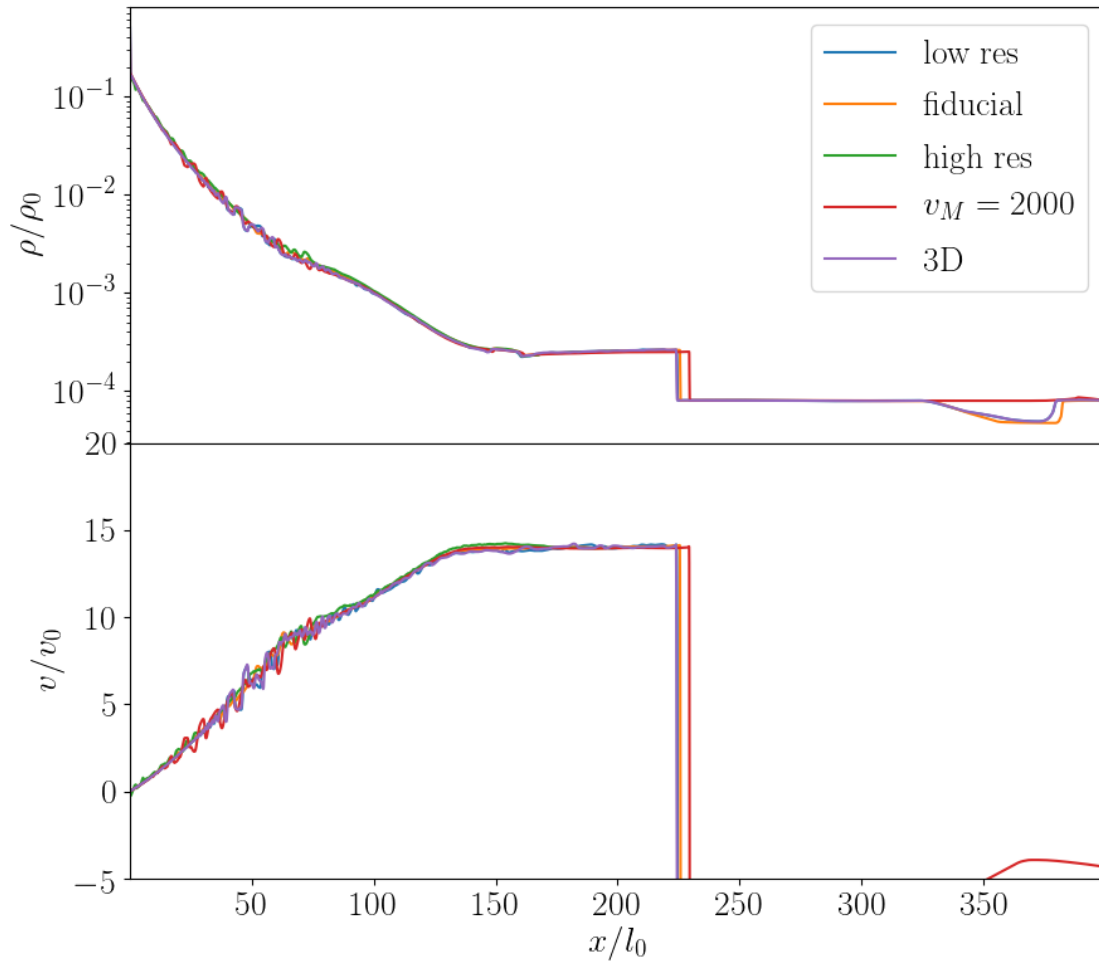
Figure 3.12: The y direction averaged gas density (upper panel) and x direction velocity (lower panel) of HSE_1F_str_LR (blue), HSE_1F_str (orange), HSE_1F_str_HR (green), HSE_1F_str_VM (red). HSE_1F_str_3D (purple) is the 3D simulation that is performed with the same resolution as HSE_1F_str_LR, in which we show the profile averaged through y and z directions.

gas.

The red curve in Figure 3.12 shows the density snapshot of HSE_1F_str_VM, also at $t = 10.0$. The gas distribution and velocity are similar to others, with only modest differences in the development of the acoustic instability. The momentum and energy transfer efficiency agree with the $V_\mathrm{m} = 1000$ simulations.

3.5 DISCUSSION

3.5.1 Momentum and Energy Transfer

Our simulation results described in section 3.4 explore a number of factors that impact the momentum and energy exchange between CRs and gas. To further quantify this exchange, we define the momentum efficiency $\dot{p}_\mathrm{x,togas}/\dot{p}_\mathrm{x,CR}$ and energy efficiency $\dot{E}_\mathrm{togas}/\dot{E}_\mathrm{CR}$ in Equation 3.9 and Equation 3.10 respectively by taking the ratio of total momentum (energy) transferred from CRs to gas and the total injected CR momentum (energy). Table 3.2 tabulates the time averaged efficiencies at a point when these simulations roughly reach quasi-steady state.

The first column of Table 3.2 lists the momentum exchange efficiencies. In most of the simulations, $\gtrsim 95\%$ of momentum carried by the injected CR flux is transferred to gas within the simulation box, whether the flux is transported primarily by streaming or diffusion. The exception is HSE_20F_str, in which the momentum efficiency is $\sim 77\%$. The relatively low efficiency is due to rapid acceleration and subsequent outflow produced in this simulation. Figure 3.10 shows that small boxes cannot adequately capture the acceleration region, so the expectation is that the CR flux escaping through the upper boundary would continue to accelerate the gas if the simulation domain were extended.

Other effects that would limit coupling, such as preferential escape along low impedance channels appears to be absent. This contrasts with radiatively accelerated outflows, where the impact of the radiative Rayleigh-Taylor instability likely limits the coupling between radiation and dusty gas by creating low density channels through with radiation can preferentially escape (Krumholz & Thompson, 2012; Davis et al., 2014). It is not entirely clear whether similar effects would be expected to be present in CR driven outflows, but the non-linear development of instabilities such as the CR acoustic instability (Begelman & Zweibel, 1994) or Parker instability (Parker, 1966; Ryu et al., 2003; Heintz & Zweibel, 2018) could plausibly act in a fashion similar

Table 3.2: Energy and Momentum Budget

Name	$\dot{p}_{x,\to g}/\dot{p}_{x,CR}$	$\dot{E}_{\to g}/\dot{E}_{CR}$	$\dot{E}_{\to g,KE}/\dot{E}_{\to g}$	$\dot{E}_{\to g,H}/\dot{E}_{\to g}$
HSE_hF_str	98.9%	65.0%	4.1%	95.9%
HSE_1F_str	98.4%	59.2%	7.1%	92.9%
HSE_4F_str	96.9%	52.0%	16.7%	82.3%
HSE_9F_str	93.8%	44.2%	24.1%	74.9%
HSE_20F_str	77.3%	29.1%	35.1%	64.9%
HSE_1F_ld	96.2%	52.9%	6.9%	93.1%
HSE_1F_cd	96.7%	53.7%	6.4%	93.6%
HSE_1F_hd	96.7%	52.7%	8.3%	91.7%
HSE_1F_hd_aniso	96.8%	52.6%	8.3%	91.7%
HSE_1F_hd_ns	99.9%	27.9%	100.00%	_[b]
HSE_1F_ld_ns	99.9%	18.6%	100.00%	_[b]
HSE_1F_str_b1	99.0%	56.8%	16.0%	84.0%
HSE_1F_str_b4	96.5%	53.0%	4.0%	96.0%

[a] The energy and momentum exchange efficiency is averaged over $t = 20.0t_0 - 25.0t_0$. The time interval is as when the simulation reaches quasi-steady exchange rate. The simulations in this table correspond to the L_y reported in Table 3.1 to avoid significant CR momentum and energy outflow.

[b] Because streaming absent, there is no direct CR heating.

to Rayleigh-Taylor instability in radiatively driven flows. Indeed, we attribute the shocks seen in our simulations to the CR acoustic instability, as discussed further in section 3.5.3 below. In these simulations, however, the growth of the instability does not seem to be modifying the momentum coupling, although it concentrates heating near the pressure jumps. Nor do we see any evidence of the Parker instability, although this is likely impacted by our adoption of a nearly vertical field in the acceleration region. Other simulation results suggest this instability may play an important role in overall structure of the gas disk (Heintz et al., 2020).

The transfer of energy between the CRs and gas is more complex. The third column in Table 3.2 lists the time-averaged total energy transfer efficiency, and the fourth and fifth column list the fractions of kinetic energy and CR heating respectively. As with momentum transfer, we find that the CR energy transfer is sensitive to our domain size, with outflow from the top boundary carrying away a significant CR energy flux that is expected to generate further heating in larger boxes. Hence, it is difficult to judge the overall level of coupling, which will inevitably depend on the global structure of the flow and galaxy potential. Nevertheless, we can draw conclusions about the relative importance of CR heating to CR acceleration.

Comparison of the third and fourth columns shows that for streaming runs, the majority of the energy transfer is due to CR heating. This is true even in hybrid simulations where diffusion is significant. In contrast, there is no explicit CR heating in the diffusion runs, due to the assumptions of our CR transport model and all energy transfer increases the kinetic energy of the gas.

We show the time evolution of energy transfer components in Figure 3.13 for varying CR transport mechanisms. After an initial transient stage on the order of the Alfvén wave crossing time, the efficiency is relatively constant. The two non-streaming simulations (brown and yellow dashed curves) have only a kinetic energy term, and share similar transfer efficiency corresponding to about $20\% - 30\%$ of total injected CR energy. The CR heating is weakly sensitive to the diffusivity, showing a trend towards increased heating efficiency when CR diffusivity is lowered.

In Figure 3.15 we show how the energy transfer depends on the magnetic field strength by comparing runs with initial magnetic fields a factor of two larger (HSE_1F_str_b4) or smaller (HSE_1F_str_b1) than our fiducial run. For the range explored here, modifying the magnetic field modifies the CR heating's fractional contribution, but the results are relatively mild. The stronger (weaker) **B** in HSE_1F_str_b4 (HSE_1F_str_b1)
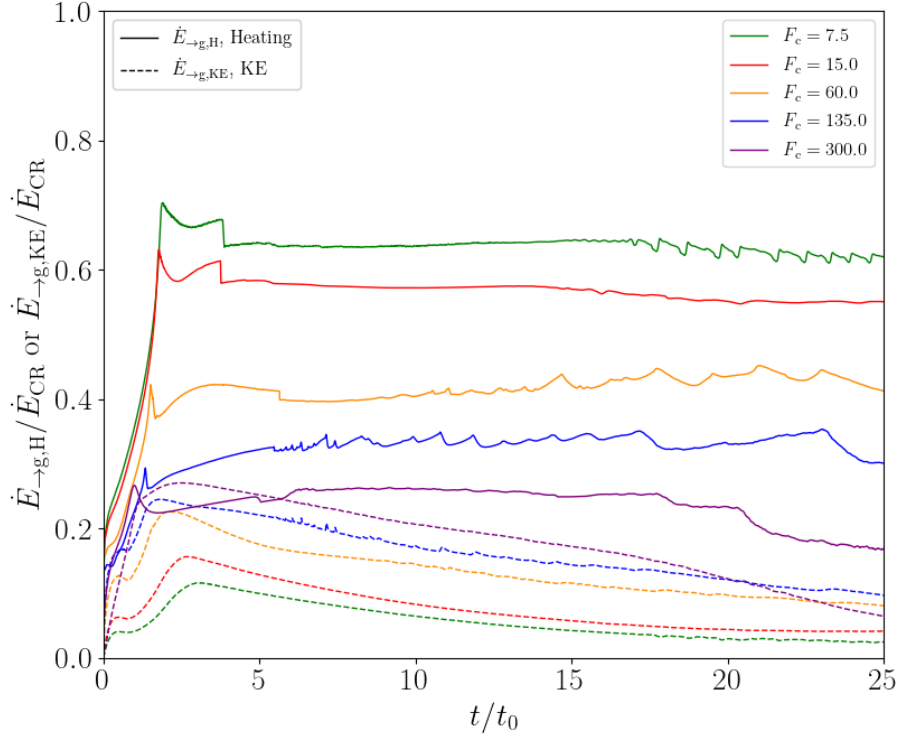
Figure 3.13: The energy transfer efficiency as a function of time for simulations with diffusion. The total energy transferred to the gas from CR includes heating (the solid line) and kinetic energy (the dashed line). HSE_1F_str (red) is the streaming simulation with $\kappa_{\mathrm{diff}} = 10^{-8}$. HSE_1F_ld (black), HSE_1F_cd (light blue) and HSE_1F_hd (green) are streaming-diffusion simulations with $\kappa_{\mathrm{diff}} = 1.0,\ 10.0,\ 100.0$ respectively. HSE_1F_ld_str (brown) and HSE_1F_str (orange) are pure diffusion simulations with $\kappa_{\mathrm{diff}} = 1.0,\ 100.0$ respectively.
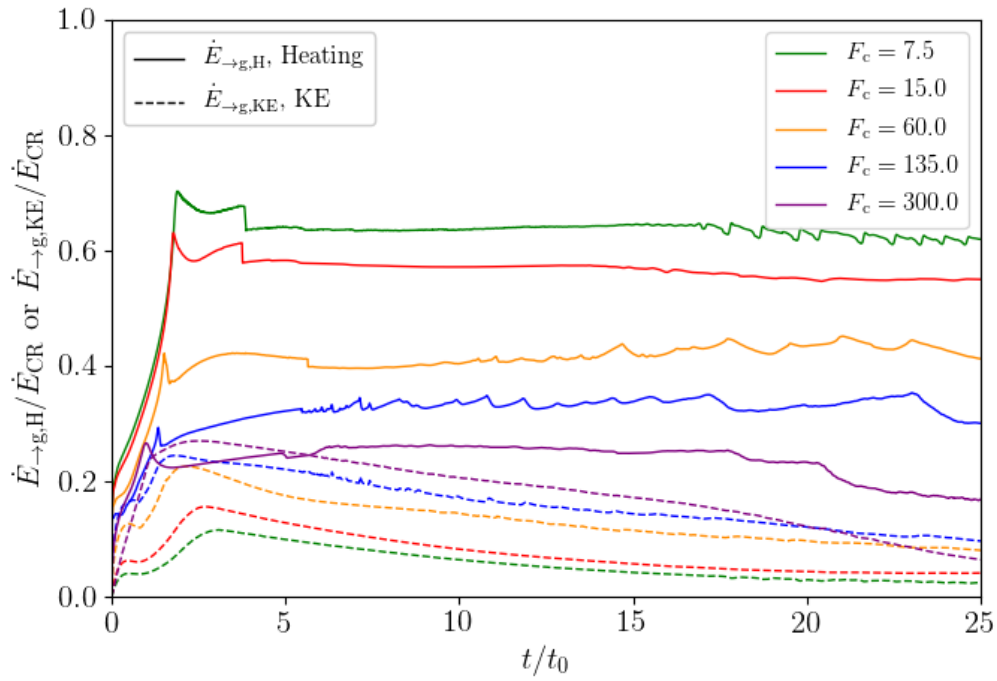
Figure 3.14: The energy transfer efficiency as a function of time for simulations with diffusion. The total energy transferred to the gas from CR includes heating (the solid line) and kinetic energy (the dashed line). These are all streaming simulations with different CR flux: HSE_hF_str (green), HSE_1F_str (red), HSE_4F_str (orange) and HSE_9F_str (blue) and HSE_20F_str (purple).
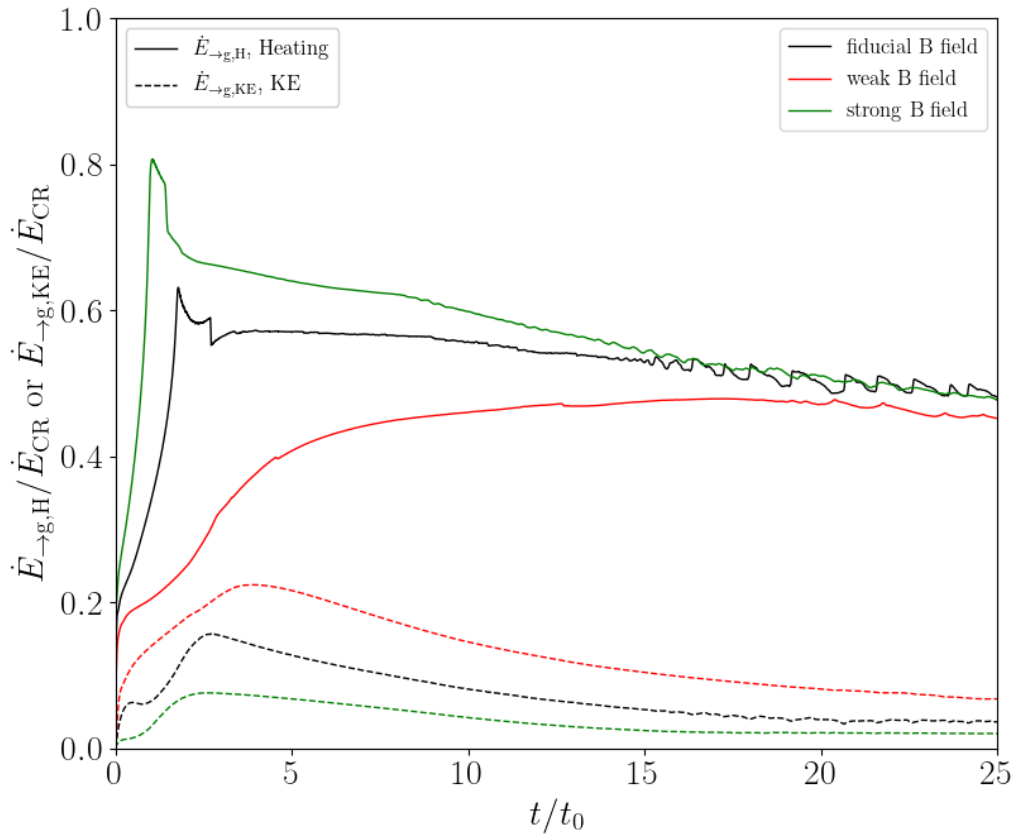
Figure 3.15: Similar to Figure 3.14, HSE_1F_str_b1 (the red lines) has initial magnetic field $B' = 1.0$ and HSE_1F_str_b4 (the green lines) has initial magnetic field $B' = 4.0$

lead to factor of two changes in the initial v_A relative to the fiducial run so one might expect commensurate changes in the heating rate, which is nominally proportional to v_A in our streaming setup. This is qualitatively consistent with early times where the heating rates increase with increased magnetic field strength, but the systems assymptote to roughly the same values at late times. Even at early times, however, the increase (decrease) in v_A is offset by a decrease (increase) in P_c since our boundary condition targets a fixed F_c. At later times, the gradient of P_c is shallower for the higher magnetic field cases. The upshot is that dissipation varies with $\mathbf{B}$, but the dependence is somewhat weak over the range explored here for the constant F_c boundary condition.

When streaming dominates the energy transfer, the overall efficiency and partition between kinetic energy and heating depends on the injecting CR flux as shown in Figure 3.14. A higher injected CR flux leads to smaller ratio between heating and kinetic energy. The kinetic energy term is proportional to fluid velocity v_x, while the heating term is proportional to local Alfvén velocity. The gas is accelerated to higher velocity in the larger CR flux simulations, so the kinetic energy term rises. In our highest CR flux run (HSE_20F_str), the kinetic energy and heating are roughly comparable to each other.

The end result is that CR acceleration of outflows is most efficient when heating is limited. This is trivially achieved in our non-streaming runs where heating is absent. This result is in qualitative agreement with the results found by Quataert et al. (2021), who found that CRs drive much weaker mass outflows when streaming is present than in the pure diffusion limit (Quataert et al., 2021). Quantitatively, they see a larger difference between pure diffusion and streaming runs than we do, but this may be attributed to their use of an isothermal equation of state, which would be equivalent to adopting a much stronger cooling regime. If streaming operates, increasing the injected CR flux accelerates the gas more rapidly, lowering the ratio of gas velocity to the streaming (Alfvén) velocity. This highlights the importance of understanding the detailed dynamics of CR transport in star-forming galaxies and, if streaming is important, introduces stronger dependence on CR flux than might be anticipated by a simple comparison of the CR flux to our derived Eddington flux.

3.5.2 Implications for CR Feedback in Galaxies

In this section, we vary our characteristic scales to infer properties of CR outflows in different galactic environments. Our target location within a galaxy is the atmosphere of the gas disk, where a wind might be launched. We focus on winds launched solely by CRs, but of course other mechanisms such as supernova driving and radiation pressure are likely operating in real systems. This motivates characteristic densities and lengthscales intermediate between the disk interior and the extended halo.

Following Socrates et al. (2008), we estimate the CR flux F_c from galaxies based on the surface star formation rate $\dot{\Sigma}_\star$ and scaling the CR production as a fraction of the expected supernova rate. Here we adopt the scaling of Crocker et al. (2021)

$$F_c \simeq 1.85 \times 10^{-3} \left(\frac{\dot{\Sigma}_\star}{M_\odot \text{ kpc}^{-2}\text{yr}^{-1}} \right) \text{erg cm}^{-2} \text{ s}^{-1}. \tag{3.11}$$

This assumes a Chabrier (2005) initial mass function so that, on average, there is a supernova every $90 M_\odot$ stellar mass. Each supernova event roughly converts $\sim 10\%$ of kinetic energy $E_{\text{SN}} \simeq 10^{51}$erg into CR energy. Assuming these assumptions are correct, this flux is an upper limit because it ignores any CR losses that may present, such as those resulting from pion production after collision with ISM particles or 'adiabatic' losses during transport (Socrates et al., 2008; Lacki et al., 2010; Chan et al., 2019).

In Section 3.3.2, we derived an estimate for the CR Eddington flux by balancing the CR force with gravity. We estimate the gravity g in Equation 3.4 according to disk surface density as $g = 2\pi G \Sigma_{\text{gas}}/f_{\text{gas}}$, where f_{gas} is gas fraction, which we scale to 0.5 for simplicity. With these assumptions, the scaling between different galaxies is primarily dependent on choosing $\dot{\Sigma}_\star$ and Σ_{gas}.

The remaining ambiguity is in the choice of ρ to use in this estimate since it can vary significantly within the galaxy. The equations imply that for sufficiently low densities, there will always be some level of outflow, which is broadly consistent with our numerical results. For small enough densities, however, we do not expect significant mass loss. For simplicity we adopt $\rho = \Sigma_{\text{gas}}/(2z_{\text{d}})$, where z_{d} is an estimate of disk scale height. We emphasize that this is an estimate that would be expected to yield significant feedback from the disk galaxy and not simply one that would drive an

observable outflow. Finally, for the streaming case we estimate $v_s = \sqrt{2k_B T/(\mu m_p \beta)}$, where β is the ratio of magnetic to gas pressure. With these assumptions, the corresponding Eddington flux in streaming and diffusion limits are

$$
\begin{aligned}
F_{\text{edd,str}} = 1.8 \times 10^{-4} \left(\frac{\Sigma_{\text{gas}}}{100 M_\odot \text{pc}^{-2}} \right)^2 \left(\frac{T}{10^4 K} \right)^{1/2} \\
\left(\frac{f_{\text{gas}}}{0.5} \right)^{-1} \left(\frac{\beta}{1.0} \right)^{-1/2} \left(\frac{H_\rho}{0.1 z_{\text{d}}} \right) \text{erg cm}^{-2} \text{ s}^{-1},
\end{aligned}
\tag{3.12}
$$

and

$$
\begin{aligned}
F_{\text{edd,diff}} = 5.9 \times 10^{-2} \left(\frac{\Sigma_{\text{gas}}}{100 M_\odot \text{pc}^{-2}} \right)^2 \left(\frac{\kappa}{10^{29} \text{cm}^2 \text{s}^{-1}} \right) \\
\left(\frac{f_{\text{gas}}}{0.5} \right)^{-1} \left(\frac{z_{\text{disk}}}{100 \text{pc}} \right)^{-1} \text{erg cm}^{-2} \text{ s}^{-1}.
\end{aligned}
\tag{3.13}
$$

We can estimate the surface density and star formation rates where a galaxy might be expected to exceed the CR Eddington limit and drive outflow by setting Equation 3.11 equal to either Equation 3.12 or Equation 3.13 when streaming or diffusion (respectively) dominates. The results are shown as magenta and green solid lines in the upper panel of Figure 3.16. The upper left region of each line is where the CR flux is above the Eddington limit, and vice versa. We also show normal galaxies measured in Kennicutt Jr & De Los Reyes (2021) and de los Reyes & Kennicutt Jr (2019) in Figure 3.16.

We see that at low surface densities galaxies mostly lie near or above these estimates for the Eddington limit, suggesting that CR can drive powerful winds in these galaxies. This could be an indication that we have either overestimated the CR flux in the wind launching region due to CR losses during transport through the gas disk or underestimated the Eddington ratio. Alternatively, it may mean that these galaxies are all driving outflows due to CRs but that the mass loading factors are not large enough to completely quench star formation. At higher surface densities, it would seem that CRs alone are less efficient at driving outflows powerful enough so that they would feed back significantly on star formation in the disk. Our simple estimates are broadly consistent with those of Crocker et al. (2021), who include further Σ_{gas} dependence in f_{gas}, the disk scale height (through the ISM velocity dispersion), and streaming velocity to sound speed ratio.
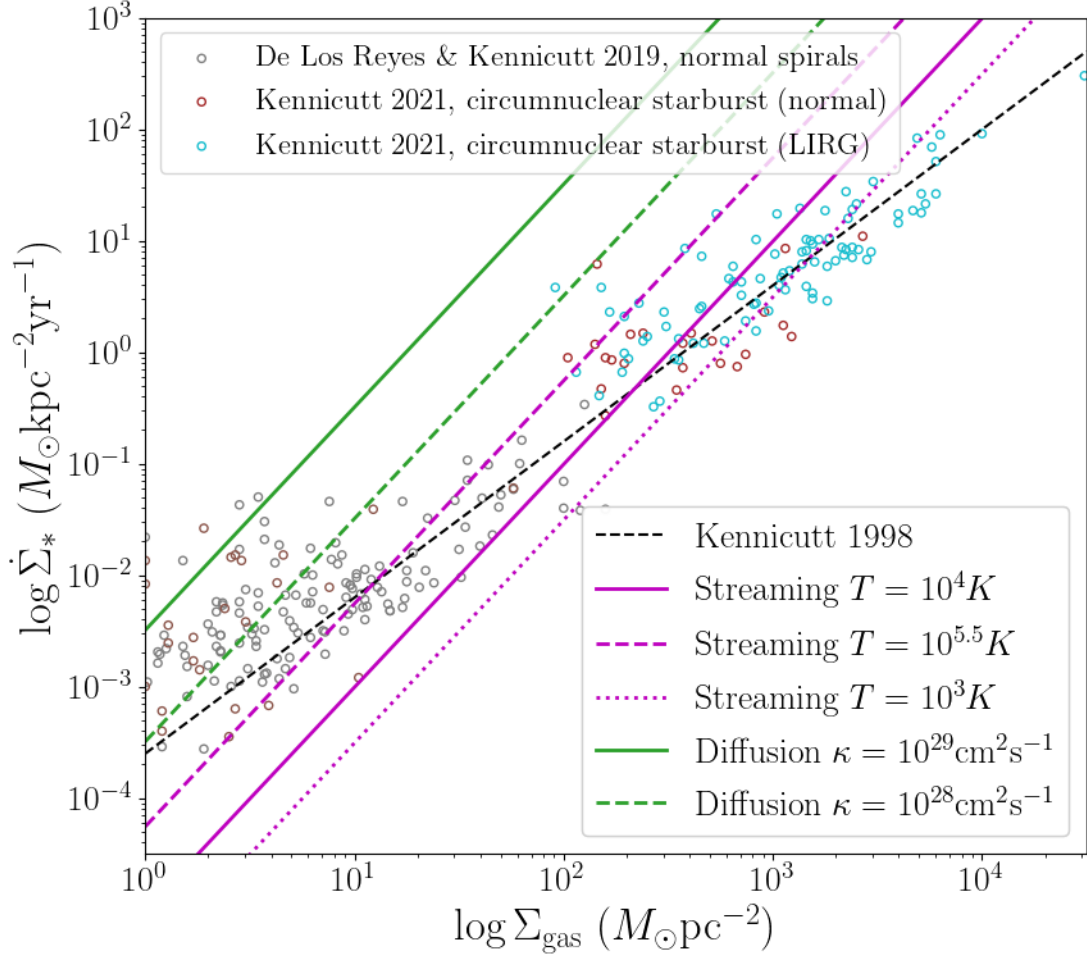
Figure 3.16: The magenta lines show the Eddington limit where the CR flux (Equation 3.11) equals to CR Eddington flux in streaming limit (Equation 3.12). The line style corresponds to different choices of temperature in Equation 3.12 (solid: $T = 10^4$K, dashed:$T = 10^{5.5}$K, dotted:$T = 10^3$K). The green lines are in diffusion limit. The line style corresponds to different diffusivity in Equation 3.13 (solid: $\kappa_{\mathrm{diff}} = 10^{29}$cm^2/s, dashed:$\kappa_{\mathrm{diff}} = 10^{28}$cm^2/s). The black dashed line shows the classical Kennicutt-Schmidt relation (Kennicutt Jr, 1998). The non-filled circles are observational data from de los Reyes & Kennicutt Jr (2019) and Kennicutt Jr & De Los Reyes (2021).

Thus far, we have not utilized our simulation results directly, other than to justify the adoption of an Eddington flux condition for the driving of outflows. The primary value of the simulations is that they give us an estimate of the mass outflow rate $\dot{M}_{\text{out}}$ for a given F_c and g. As discussed in section 3.3.3, the non-radiative simulations are scaled to physical units by choosing a density scale ρ_0, length scale l_0, and temperature scale T_0. These, in turn, are constrained by matching our simulation results to galaxies using physical units via

$$\frac{2\pi G \Sigma_{\text{gas}}}{f_{\text{gas}}} = \left(\frac{k_b T_0}{\mu l_0}\right) g', \tag{3.14}$$

$$F_c = \rho_0 \left(\frac{k_b T_0}{\mu}\right)^{3/2} F_c'. \tag{3.15}$$

Here, g' and F_c' have primes to denote the dimensionless gravity and injected CR flux prescribed in the simulation, and the left hand side values are in physical units. Using Equation 3.11, we can rewrite our characteristic scales as

$$l_0 = 21 \left(\frac{T_0}{10^4 K}\right) \left(\frac{\Sigma_{\text{gas}}}{100 M_\odot \text{pc}^{-2}}\right)^{-1} \left(\frac{f_{\text{gas}}}{0.5}\right) \left(\frac{g'}{0.826}\right) \text{pc}, \tag{3.16}$$

$$\rho_0 = 7.6 \times 10^{-23} \left(\frac{F_c'}{15}\right)^{-1} \left(\frac{T_0}{10^4 K}\right)^{-3/2} \left(\frac{\dot{\Sigma}_\star}{M_\odot/\text{kpc}^2/\text{yr}}\right) \text{g/cm}^3.. \tag{3.17}$$

Once we fix the injecting CR flux, each data point in the $\Sigma_{\text{gas}} - \dot{\Sigma}_\star$ plane provides two constraints on the scaling parameters. We adopt the convention of choosing the temperature and using Σ_{gas} and $\dot{\Sigma}_\star$ to determine l_0 and ρ_0 for given T_0.

With these scaling we can estimate the column of material impacted by our CR driven outflows via

$$\frac{\rho_0 l_0}{\Sigma_{\text{gas}}} = 0.24 \left(\frac{F_c'}{15}\right)^{-1} \left(\frac{T_0}{10^4 K}\right)^{-1/2} \left(\frac{\dot{\Sigma}_\star}{M_\odot/\text{pc}^2/\text{Myr}}\right)$$
$$\left(\frac{\Sigma_{\text{gas}}}{100 M_\odot \text{pc}^{-2}}\right)^{-2} \left(\frac{f_{\text{gas}}}{0.5}\right) \left(\frac{g'}{0.826}\right). \tag{3.18}$$

For objects lying on or near the Kennicutt-Schmidt relation, this will lead to a decrease in the fraction of the atmosphere impacted at higher Σ_{gas}. We can also estimate the mass outflow per unit area as $\dot{M}_{\text{out}} = \dot{m}' v_0 \rho_0$, where $\dot{m}'$ is the dimensionless out-

flow mass per area in our simulations. We find

$$\frac{\dot{M}_{\text{out}}}{\dot{\Sigma}_\star} = 0.034 \left(\frac{F_c'}{15}\right)^{-1} \left(\frac{\dot{m}'}{0.00252}\right) \left(\frac{T_0}{10^4 K}\right)^{-1/2}. \tag{3.19}$$

Our simulations yield $\dot{m}' = 0.00252$, 0.0130, 0.0396, and 0.0707 for $F_c' = 15$, 60, 135, and 300, respectively or approximately $\dot{m}' \propto F_c'$ over the range we have explored. This means that the implied mass loading factor is approximately constant for the simulations and is a few percent of the star formation rate for $T_0 \simeq 10^4$K. It is important to emphasise that the density at the base of the simulation has a large effect on the implied mass loading in all models. Equation 3.17 shows that for a given $\dot{\Sigma}_\star$, the highest densities correspond to the lowest temperatures, with the highest mass loading corresponding to $T_0 \lesssim 10^3$K.

A lower temperature is broadly consistent with the larger fractions of dense molecular gas in LIRGS and ULIRGs but poses a self-consistency problem for the CR transport models adopted here, which assume the gas is sufficiently ionised so that CRs stream at nearly the Alfvén speed and have diffusivities similar to the Milky Way. If ionisation fractions are low, the effective Alfvén speed may be significantly higher. Furthermore, the streaming instability or turbulent fluctuations that underlie diffusive models may be strongly damped in molecular gas (Bustard & Zweibel, 2020). This may increase the escape of CRs from the highest density regions and reduce the impact of destruction processes like pion production, but could also lower the coupling between CRs and outflowing gas unless sufficiently high ionisation fractions are present in the wind launching regions of the galaxy, which are presumably closer to the disk surface. Resolving these questions is beyond the scope of this work, but is central to addressing the question of how much CR feedback can impact galaxies with high molecular gas fractions.

3.5.3 Acoustic Instability

In all our simulations with streaming, a series of shocks grow and saturate while gas is being accelerated by CRs. For example, the shocks in the gas density and velocity in Figure 3.2, or the horizontal bands in the 2D gas density snapshots in Figure 3.3 and Figure 3.6. These shocks do not form in our diffusive only simulations. We find that the growth of these shocks are consistent with cosmic rays acoustic instability, and our present whenever the resolution is sufficiently high.

Begelman & Zweibel (1994) studied the CR acoustic instability in the streaming limit with a uniform background. They found that the growth rate varies with $m \equiv v_A/c_s$ and $c \equiv c_{CR}/c_s$, where v_A, c_s and c_{CR} are Alfvén speed, sound speed and CR acoustic speed (see definitions in Appendix A). Tsung et al. (2021) extends this work and discusses the physical origin of the shock structures and various relevant microphysical processes. In this section, we refer to the gradient in gas density, gas pressure and CR pressure as the "background gradient", and derive the dispersion relation in Appendix A.

The emergence and growth of shocks in our simulation is spontaneous and dynamical. They usually appear after the gas density and pressure are redistributed to the larger scale height compared to the initial condition. The shocks are approximately even-spaced and have similar amplitude. We measure the average shock amplitude increment over time to estimate the acoustic instability growth rate.

We first filter the high spatial frequency shocks and fit a smooth curve to the y direction averaged gas density using the LOWESS (Locally Weighted Scatterplot Smoothing) method. Then we take the weighted volume average residual as the shock amplitude $\delta\rho'$. We show the resulting amplitude evolution as the solid curves in Figure 3.17 for three simulations. The shocks experience an initial linear growth, which we fit with the dashed lines, before dropping at a later time. The drop in the average amplitude at later time reflects that the shocks begin to be advected out of the domain with the fluid.

We solve dispersion relation of the CR acoustic instability (see Appendix A) to obtain theoretical growth rates and compare them with the above measurements. Our calculation is based on the sampling relevant y direction averaged quantities at the time and location where we first see the shocks. The calculation for HSE_1F_str is based on the profiles at $t = 6.7t_0$ and $x = 33.0l_0$, HSE_4F_str is based on the profiles at $t = 3.6t_0$ and $x = 25.0l_0$, and HSE_1F_ld uses profile at $t = 3.2t_0$ and $x = 25.0l_0$. The estimated growth rates are 0.2, 0.5 and 0.8 for HSE_1F_str, HSE_4F_str and HSE_1F_ld respectively (the corresponding slopes in Figure 3.17). The good correspondence between estimated growth rates and measured growth rates is consistent with shocks being seeded by the acoustic instability.

The expected growth rates in our simulation are relatively low due to the low ratio between CR pressure and gas pressure in the diffuse region. Figure A.2 shows the growth rate for the $k = 1$ mode, the yellow circles label some typical $c_{CR}/c_s - v_A/c_s$
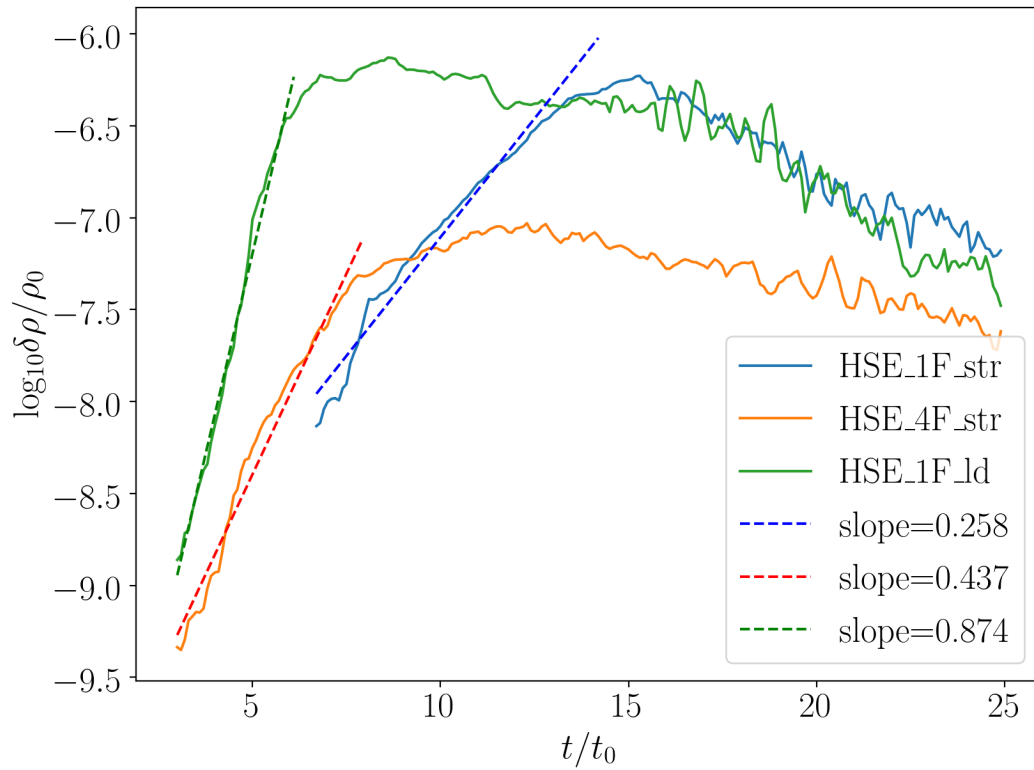
Figure 3.17: The growth rate of the shocks caused by acoustic instability for HSE_1F_str (blue), HSE_4F_str (orange) and HSE_1F_ld (green). The dashed line is the fitted growth rate, with slopes noted in the legend. The estimated slopes from solving the dispersion relation are 0.2, 0.5 and 0.8 respectively.

pairs in our simulations near the position and time the shocks starts to grow. The "bottleneck" slows down CR propagation in dense gas and yields a low CR pressure in diffuse region, while the gas is heated by the initial CR shock. As a result, the low $c_{\mathrm{CR}}/c_{\mathrm{cs}}$ and high $v_{\mathrm{A}}/c_{\mathrm{s}}$ constrains the growth rate to low level in the simulations.

The instability eventually saturates and the shock amplitudes are relatively constant over time. The shocks spacing increase as the pressure scale heights increase (Tsung et al., 2021), and advects with the gas. The instability creates multiple "stairs" in CR pressure. The steep pressure gradients at shock fronts dominate the CR heating at later time when the overall CR pressure gradient is shallow.

3.6 Summary and Conclusions

Many studies have identified CR pressure and heating as promising mechanisms for driving galactic outflows and ISM turbulence. In this work, we studied the dynamical interaction due to an imposed CR flux at the base of an initially hydrostatic atmosphere to investigate the outflow launching process. We derived estimates for the CR Eddington flux in the streaming limit (equations 3.4) and diffusion limit (equations 3.5). We performed simulations with different CR transport models including streaming, streaming-diffusion and diffusion. In the set of streaming simulations, we vary the injected CR flux from sub-Eddington to super-Eddington to quantify how this impacts the atmosphere and outflow that develops. We measured the outflow rate from simulations and scale simulated systems to realistic star forming environments. We also consider simulations with radiative cooling, showing that cooling modifies the wind density and pressure profile, resulting in generally more inhomogeneous and cooler outflow.

We measured the momentum and energy transfer efficiency from CR to gas, and summarised how it changes with the injected CR flux and the relative importance between streaming and diffusion. We summarise our results as follows:

- Star forming systems near the classical Kennicutt-Schmidt relation are likely to produce super-Eddington CR fluxes (Figure 3.16) if a large fraction of the CRs survive transfer through the gas to reach the surface. This contribution should be most important in environments with lower star-formation rates and surface densities, where even relatively high gas densities near the midplane are impacted. More generically, we expect that for a wide range of galaxy properties,

there will be a column of low density gas that can be driven to outflow, but this represents a smaller fraction of the gas in galaxies with higher surface densities. The expected mass outflow is a few percent of the star formation rate for an initially warm atmosphere ($\sim 10^4 K$).

- We identify the growth and saturation of CR acoustic instability in our streaming simulations. However, the presence of instability does not limit the momentum transfer from CR to gas. The momentum transfer efficiency is usually $\gtrsim 95\%$ regardless the CR flux and does not strongly depend on whether streaming or diffusion dominates transport, suggesting that CR and gas remain well-coupled in our simulations.

- The energy transfer between CR and gas is sensitive to CR flux and the dominant CR transport mechanism. The fraction of total energy transferred to gas from CRs increases with CR flux. When streaming is included, a substantial fraction of transferred energy is in the form of Alfvén wave heating, resulting in larger pressure scale height and outflowing gas hotter than the initial temperature by more than one order of magnitude. Typically $\lesssim 10\%$ of the total CR energy is imparted to gas kinetic energy. Pure diffusion without the Alfvén wave heating leads to roughly twice as much energy being transferred to the kinetic energy of the outflow.

- For the transport scheme used here, streaming tends to limit the CR force applied to the gas for a given CR flux. In the absence of streaming, a lower diffusivity requires a larger CR pressure gradient to transport the same CR flux, leading to a large CR force on the gas. In contrast, when streaming operates with a low diffusivity and a relatively high streaming speed, it will dominate the transport of CRs relative to diffusion, providing a weaker CR pressure gradient and a lower CR force. For a sufficiently high diffusivity, CR diffusion can again dominate the transport but will then produce a weaker CR pressure gradient and subsequently weaker force.

- Radiative cooling is potentially important, especially in sub-Eddington and near-Eddington systems in terms of setting the gas temperature and pressure profile of the extended atmosphere and outflow. When the CR flux is highly super-Eddington, CR pressure is more important than gas pressure and cooling

has a weaker effect on mass loss. Cooling significantly lowers the wind temperature, promoting gas condensation near the density irregularities seeded by acoustic instability, resulting generally cooler and less homogeneous outflow.

CHAPTER 4

Cosmic-Ray-driven Multiphase Gas Formed via Thermal Instability

4.1 ABSTRACT

Cosmic rays (CRs) are an important energy source in the circum-galactic medium (CGM) that impact the multi-phase gas structure and dynamics. We perform two-dimensional CR-magnetohydrodynamic simulations to investigate the role of CRs in accelerating multi-phase gas formed via thermal instability. We compare outflows driven by CRs to those driven by a hot wind with equivalent momentum. We find that CRs driven outflow produces lower density contrast between cold and hot gas due to non-thermal pressure support, and yields a more filamentary cloud morphology. While entrainment in a hot wind can lead to cold gas increasing due to efficient cooling, CRs tend to suppress cold gas growth. The mechanism of this suppression depends on magnetic field strength, with CRs either reducing cooling or shredding the clouds by differential acceleration. Despite the suppression of cold gas growth, CRs are able to launch the cold clouds to observed velocities without rapid destruction. The dynamical interaction between CRs ad multi-phase gas is also sensitive to the magnetic field strength. In relatively strong fields, the CRs are more important for

direct momentum input to cold gas. In relatively weak fields, the CRs impact gas primarily by heating, which modifies gas pressure.

4.2 INTRODUCTION

The circumgalactic medium (CGM) is the halo of gas lying outside the galactic disk but within the viral radius. The CGM is an important baryon component of the galaxy, playing a key role in gas cycling by interactions with gas inflow and outflow, and affecting star formation fueling and feedback (Veilleux et al., 2005; Tumlinson et al., 2017). Tracing the structure and dynamics of CGM gas is important for us to understand galaxy evolution. One of the main techniques probing CGM composition and kinematics is through absorption line spectroscopy (Tumlinson et al., 2017). The hot $\sim 10^6$K CGM gas is has long been known as the "galactic corona". Recent observations suggest the existence of $\sim 10^5$K intermediate temperature gas (Wakker et al., 2012) that can reach ~ 100km s^{-1} bulk velocity. On the lower temperature end, the cold gas traced by low ionization lines is likely to be clumpy, while warm gas traced by high ionization lines is diffuse and potentially in coherent large structures up to kpc scale (Werk et al., 2019; Bish et al., 2019). The COS-Halo survey reveals the presence of multi-phase gas in other galaxies (Tumlinson et al., 2013; Werk et al., 2014). Observations seem to suggest the picture of outflow including fast-moving cold $\sim 10^4$K clouds embedded in hot $\sim 10^6$K background gas, with intermediate temperature gas around 10^5K. Understanding this multi-phase outflow is essential to CGM physics and galaxy evolution.

The origin and dynamics of cold CGM gas is an important puzzle. The cold clumps can either be launched from the gas disk (Klein et al., 1994; Cooper et al., 2009; Scannapieco & Brüggen, 2015; McCourt et al., 2015; Gronke & Oh, 2018; Scannapieco et al., 2020) or formed *in situ* from the hot gas via thermal instability (Field, 1965; Sánchez-Salcedo et al., 2002; Sharma et al., 2010b; McCourt et al., 2012; Pal Choudhury et al., 2019; Girichidis et al., 2021). In a realistic CGM environment, it is likely that both mechanisms are operating. While there are extensive effort to disentangle cloud launching and cold gas formation, reconstructing the interplay between the two processes is also important to bridge cloud-scale physics with a broader picture of multiphase outflow in a dynamical CGM environment.

Cosmic rays (CRs) are also potentially important energy source in CGM, which impacts both the cold cloud acceleration and thermal instability. These charged parti-

cles originate from supernovae explosions and propagate through the CGM, imparting energy and momentum to the gas. Recent numerical and theoretical work suggests that CRs can alter the pressure balance and phase structure in the CGM (Salem et al., 2016; Ji et al., 2020; Hopkins et al., 2020), and launch outflow or potentially prevent accreting inflows (Booth et al., 2013; Ruszkowski et al., 2017; Crocker et al., 2021b; Quataert et al., 2021; Hopkins et al., 2021). CRs may modulate thermal instability (Sharma et al., 2010b; Butsky et al., 2020), launch cold clouds (Wiener et al., 2019; Brüggen & Scannapieco, 2020; Bustard & Zweibel, 2021), and produce potentially observable modifications to absorption line profiles (Butsky et al., 2021).

Although CRs are an interesting and important component in galaxy evolution, incorporating CR physics in numerical simulations is not trivial. This is partly due to our limited knowledge about CR transport itself. Different CR transport models are assumed such as self-confinement streaming (Wentzel, 1974; Crocker et al., 2021a; Quataert et al., 2021), super-Alfvénic streaming associated with turbulent damping (Ruszkowski et al., 2017; Holguin et al., 2019; Hopkins et al., 2020), and isotropic or anisotripic diffusion (Salem et al., 2016; Wiener et al., 2017). A number of works suggest that CR transport models significantly impact CR interaction with gas and ability to drive galactic outflow (Uhlig et al., 2012; Butsky & Quinn, 2018; Buck et al., 2020; Huang & Davis, 2021).

At the same time, the numerical difficulties associated with the moments equations make the implementation of CR transport challenging. For example, Sharma et al. (2010a) adopt a regularization scheme to smooth out the step-function-like streaming velocity near CR pressure maximum. Jiang & Oh (2018) resolve this issue by solving two-moment formulation of the CR equations, facilitating the integration of CR transport in both streaming and diffusion limits. Thomas & Pfrommer (2019) and Chan et al. (2019) also explore CR two-moment implementations with slightly different approaches. Thomas & Pfrommer (2021) compares closure relations for CR two-moment equations and found that the impact is small in the streaming limit, where scattering is neglected. Hopkins et al. (2021a) derive and implement moment-equations that can also handle CRs in the strong scattering limit with generalized source terms.

In this work, we primarily focus on CR transport in the self-confined streaming limit, with one supplemental CR diffusion run as comparison to the relatively fast streaming. We use the Athena++ implementation of Jiang & Oh (2018). By solving

both CR energy and flux equations, the scheme is less diffusive than the single-moment method and better preserves the CR energy behavior where it decouples with gas.

Recent simulations provide us a physical picture of how CR streaming can accelerate cold gas via a "bottleneck" (Wiener et al., 2019; Brüggen & Scannapieco, 2020; Bustard & Zweibel, 2021; Huang & Davis, 2021). By studying cloud-CR interaction in a relatively well-controlled environment, the cloud scale simulations provide useful theoretical insights about CR acceleration, cloud crushing timescales and CR-modified density contrast in multi-phase gas. They also raise concerns, however, due to the idealized set-up. Particularly for CR streaming, it seems important to recover some key environmental factors in the CGM such as clumpiness, irregular cloud morphology, and non-uniform magnetic fields.

In addition to the dynamics, CR pressure may also impact the formation of multi-phase gas. Studies show that unlike the classical isobaric thermal instability, CR mediated thermal instability can be an isochorical process (Sharma et al., 2010a; Kempski & Quataert, 2020). The CR pressure provides non-thermal support to the cooling gas and prevents rapid contraction. Butsky et al. (2020) estimates that density contrast of the multi-phase gas formed from thermal instability will be reduced due to the presence of CRs. Their work also suggests that in a CR pressure dominated halo, cold clouds are potentially an order of magnitude larger than what is predicted by the cloud scale in purely thermal medium. Kempski & Quataert (2020) studied the effect of CRs on linear thermal instability, and found that ratio of CR to gas pressure controls the transition from isobaric to isochoric. Although CR heating does not directly change the instability growth rate in isobaric or isochoric limits, the perturbed CR heating make gas entropy mode oscillatory.

Given various complexities brought by CRs, in this work, we do not set the cold and hot gas in pressure balance, instead we study the interaction of CRs with multi-phase gas structure that formed *in situ* due to thermal instability. Thermal instability spontaneously yields $\sim 10^4$K cold clouds in diffuse $\sim 10^6$K hot gas with $\sim 10^5$K interface, emulating the observed multi-phase CGM gas (Sharma et al., 2010b; Jennings & Li, 2020). A key focus is to study if CR can accelerate cold gas without successively destroying it, especially in a more realistic environment where the background is not initially uniform. Another goal is to compare CR with a hot wind as outflow-driving mechanisms. While both mechanisms are thought to originate from supernovae, their interactions with multi-phase gas can be intrinsically different, potentially leading to

different outflow properties.

We introduce the simulation set-up and relevant scaling in Section 4.3. We present the results in Section 4.4, where we compare CRs and a hot wind accelerating and modifying multi-phase gas. In Section 4.5 we discuss CR streaming in turbulent magnetic fields, describe factors affecting cold gas survival and connect our results with previous work. We summarize our conclusions in Section 4.6.

4.3 SIMULATION SET-UP

4.3.1 Equations

The equations we solve are ideal magneto hydrodynamics (MHD) equations and cosmic rays (CR) transportation equations, which is based on the two-moment scheme proposed by Jiang & Oh (2018). We discussed the details numericla method in Chapter 1.2, here we list the two CR transport equations for the convenience of discussions in this work.

In this work, we set the conductivity parallel and perpendicular to the magnetic field to be $\kappa_\parallel = 2.0 \times 10^9 \mathrm{erg\ K^{-1}\ s^{-1}\ cm^{-1}}$ and $\kappa_\perp = 4.0 \times 10^8 \mathrm{erg\ K^{-1}\ s^{-1}\ cm^{-1}}$. Note that the $\kappa_\parallel/\kappa_\perp$ assumed here is potentially lower than the realistic value. We choose this ratio in order to resolve the Field length (Equation (4.1)) in both x- and y-directions (Koyama & Inutsuka, 2004).

We assume optical thin cooling and supplemental heating is $-n_{\mathrm{H}}^2 \Lambda(T) + n_{\mathrm{H}} \Gamma$, where n_{H} is the gas number density. The cooling function $\Lambda(T)$ is an approximation to fit the CLOUDY data with solar metallicity from Wiener et al. (2019). The heating constant is initialized as $\Gamma = 6 \times 10^{-24} \mathrm{erg\ s^{-1}}$. We cut off the radiative cooling and supplemental heating for gas with temperature below $4 \times 10^4 \mathrm{K}$. We plot the cooling function in Figure 4.1.

4.3.2 Characteristic Scales

Sharma et al. (2010b) studied the formation of cold filaments via thermal instability with adiabatic cosmic rays. They found that the fastest growing mode of thermal instability tends to be elongated along the magnetic field lines with a characteristic length scale of the Field length:

$$L_F = 2\pi \left[\frac{\chi t_{\mathrm{cool}}}{d\ln(T^2/\Lambda)/d\ln T} \right]^{1/2}, \tag{4.1}$$
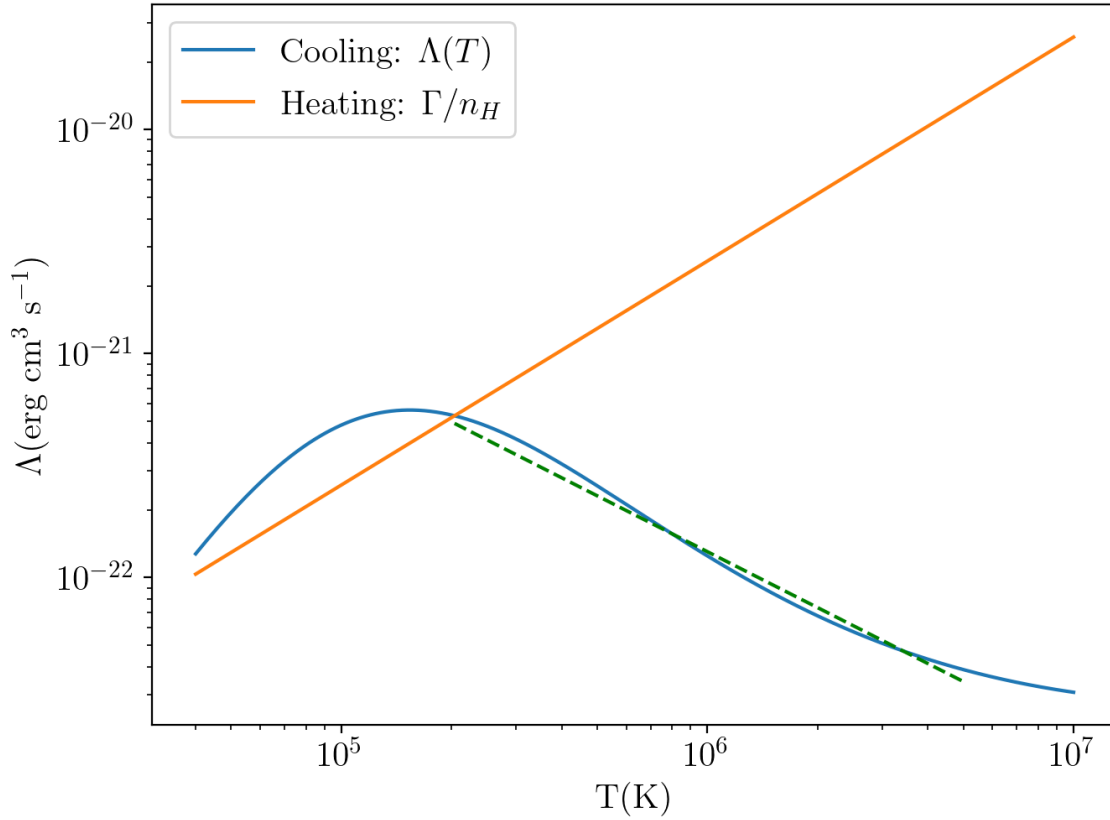
Figure 4.1: The cooling curve we adopted in all simulations from Wiener et al. (2019). We assume constant pressure of $P_{\text{gas},0} = 2.33 \times 10^{-21}$dyne cm^{-2} in the plot. The blue solid line is the cooling term $\Lambda(T)$, while the orange solid line is the supplemental heating term Γ/n_{H}. The green solid line is the power-law fitting to the unstable branch with index -0.83. We truncate the cooling and heating for gas with temperature $T < 4 \times 10^4$K.

where $\chi_\parallel = \kappa_\parallel/n_e k_B$ ($\chi_\perp = \kappa_\perp/n_e k_B$) is the scaled conductivity, and $t_{\rm cool}$ is the cooling timescale, and the denominator can be approximated by the power law index of the unstable branch of the cooling function. In our simulations, the unstable branch corresponds to the temperature range $T \gtrsim 2 \times 10^5 K$ with the negative slope in Figure 4.1, which can be approximated by power law with the index of -0.83 (the green dashed line).

When a cloud is accelerated by a hot wind, an important timescale that roughly describes the time it takes the wind to deform the cold cloud is the cloud crushing time (Klein et al., 1994):

$$t_{\rm cc} = \sqrt{\frac{\rho_c}{\rho_h}} \frac{R_c}{v_{\rm hot}}, \qquad (4.2)$$

where ρ_c and ρ_h is the cold and hot gas density, $v_{\rm hot}$ is the wind speed. For cold clouds formed in our simulation, the sizes of the cloud R_c are usually about one to a few L_F.

When the cloud is accelerated by CR streaming, we estimate the expected acceleration using the following simplified model. When the flow velocity is relatively small compared to the Alfvén velocity, the CR flux $F_{\rm CR} \approx 4 v_A P_{\rm CR}$. If the time dependent term in CR momentum equation is relatively unimportant, the CR force on gas is roughly the CR pressure gradient $\partial P_{\rm CR}/\partial x \approx (P_{\rm CR,l} - P_{\rm CR,r})/R_c$. Assuming CR pressure on the irradiated side $P_{\rm CR,l}$ is significantly larger than the shaded side $P_{\rm CR,r}$, the CR acceleration can be approximated as:

$$a_{\rm CR} = f \frac{F_{\rm CR}}{4 v_A L_F \rho_c} \qquad (4.3)$$

where f is a factor added to account for deviations from our assumptions.

4.3.3 Scaling and Initialization

In this work, we perform seven simulations in total. The simulations are labeled B2CR, B2CRdiff, B2CR_LC, B2HW, B1CR, B1HW and B05CR. The naming convention uses "B2, B1, B05" to denote the initial magnetic field strength, while the following characters denote the acceleration mechanism, with "CR" for cosmic rays streaming, "CRdiff" for cosmic rays diffusion, and "HW" for hot wind. We also present an additional run B2CR_LC with slightly different conductivity than the other six simulations to explore the effect of varying the heating constant Γ relative to other

parameters.

We solve the dimensionless equations with the following scaling: The temperature unit is the initial equilibrium temperature $T_0 = 2.04 \times 10^5$K. The density unit is ρ_0. The velocity unit is set to be the sound speed at T_0. The initial cooling time $t_{c,i}$ is :

$$t_{c,i} = \frac{k_B}{\mu m_p} \frac{\rho_0 T_0}{n_{H,0}\Gamma} \tag{4.4}$$

The time unit is $t_0 = 10t_{c,i}$, and the length unit $l_0 = 10v_0 t_{c,i}$, where k_B is Boltzmann constant, $\mu = 0.6$ is the mean molecular weight, and $n_{H,0} = \rho_0/\mu m_p$ is the initial number density. The heating constant $\Gamma = n_{H,0}\Lambda(T_0)$.

We use the same initial equilibrium temperature $T_0 = 2.04 \times 10^5 K$ for all simulations. However, we have a degree of freedom of rescaling the simulations to different density unit ρ_0. When rescaling ρ_0, we also change the corresponding heating constant Γ. We scale the cooling function to $\Lambda(T_0) = 5.28 \times 10^{-22}$erg s^{-1} cm^3, which is the cooling rate at T_0. We can write the dependence of ρ_0 and Γ, l_0 and L_F as:

$$\Gamma = 5.27 \times 10^{-24}\text{erg s}^{-1}\left[\frac{\Lambda(T)}{\Lambda(T_0)}\right]\left(\frac{\rho}{10^{-26}\text{g cm}^{-3}}\right) \tag{4.5}$$

$$l_0 = 91.6\text{pc}\left(\frac{T}{T_0}\right)^{3/2}\left[\frac{\Lambda(T)}{\Lambda(T_0)}\right]^{-1}\left(\frac{\rho}{10^{-26}\text{g cm}^{-3}}\right)^{-1} \tag{4.6}$$

$$L_F = 106.5\text{pc}\left(\frac{T}{T_0}\right)^{1/2}\left(\frac{\kappa_\|}{2\times10^9\text{erg K}^{-1}\text{ s}^{-1}\text{ cm}^{-1}}\right)^{1/2}$$
$$\times\left[\frac{\Lambda(T)}{\Lambda(T_0)}\right]^{-1/2}\left(\frac{\rho}{10^{-26}\text{g cm}^{-3}}\right)^{-1} \tag{4.7}$$

When reporting results in c.g.s units, we adopt $\rho_0 = 1.14 \times 10^{-26}$g cm^{-3}, length unit $l_0 = 2.48\times10^{20}$cm and the temperature unit $T_0 = 2.04\times10^5$K for most simulations except for B2CR_LC. This implies the heating constant $\Gamma = 6 \times 10^{-24}$erg s^{-1}. The velocity unit is set to be the sound speed at T_0, $v_0 = 5.29 \times 10^6$cm s^{-1}, and the time unit corresponds to the sound crossing time $t_0 = 1.49$Myr.

In B2CR_LC, we scale the simulation to $\rho_0 = 1.14 \times 10^{-27}$g cm^{-3}, $l_0 = 2.48 \times 10^{21}$cm, $T_0 = 2.04 \times 10^5$K, and $\Gamma = 6 \times 10^{-25}$erg s^{-1}. We lower $\kappa_\| = 2.0 \times 10^7$erg K^{-1} s^{-1} cm^{-1} and $\kappa_\perp = 4.0 \times 10^6$erg K^{-1} s^{-1} cm^{-1} in order to keep L_F fixed and form clouds with similar physical sizes as other simulations (see Section 4.3.2). In the following sections, we report quantities in dimensionless code units with a prime, unless otherwise specified.

All simulations are two-dimensional, and the domain size is $L_x \times L_y = 400l_0 \times 50l_0$ with 8000×1000 cells on each side, given the equivalent resolution of 4.02pc in both x- and y-directions. In B2CR_LC, we use a smaller domain of $L_x \times L_y = 40l_0 \times 5l_0$ in order to resolve L_F with the same resolution.

There are two main stages in each simulation: (1) the multi-phase gas formation via thermal instability and (2) the acceleration by CR or hot wind. To model the multi-phase gas formed *in situ*, we first perturb the initially uniform gas from thermal equilibrium, so that thermal instability generates multi-temperature gas that remains roughly in pressure equilibrium. We assume a low background CR energy density in this stage. Once the multi-phase gas reaches an approximate steady state, we inject a uniform CR flux or a hot wind from the left x boundary to model the energy and momentum input from star forming region. Here we describe the two stages accordingly.

Initially, we place a uniform slab with density $\rho'_{\rm init} = 1.0$ between $50 < x' < 150$, and set the temperature to be the equilibrium temperature $T_{\rm init} = T_0$. The background gas density is set to a density floor $\rho_{\rm bkgd} = 10^{-6}\rho_0$ and in pressure equilibrium with the slab. We add small random perturbations to the gas density in order to perturb it from the equilibrium, $\rho' = 1 + 0.1\delta\rho'$, where $\delta\rho'$ is randomly distributed between -1 and 1. Initially, the magnetic field is uniform along the x-direction with $\beta_{\rm init} = 0.5$, 2.0, 8.0 in simulations noted by B2, B1 and B05. We set a low background CR energy density $E'_{\rm CR,init} = 0.3$.

The y-direction boundary conditions are periodic. In the x-direction, the boundary conditions are different in multi-phase gas formation stage and acceleration stage. In the first stage, the x-direction hydrodynamic and CR boundary conditions are outflow, where the ghost zones copy values from the last active zone. The only exception is B2CRdiff, where we set the velocity to be single-direction outflow to avoid any unwanted diffusive flux from boundary. The ghost zones copy velocity from last active zone but set any inward velocity to be zero.

In the second stage, in B2CR, B2CRdiff, B1CR and B05CR, we set the left hydro boundary to be reflecting. The left CR boundary fixes CR flux $F'_{\rm CR}$ in the x-direction, and copies other variables from the last active zone. We set $F'_{\rm CR} = 60$, corresponding to $F_{\rm CR} \approx 2.5 \times 10^5 L_\odot {\rm kpc}^{-2}$. Using the CR flux estimate from Crocker et al. (2021a), this flux roughly corresponds to systems with surface star formation rate $\dot{\Sigma}_* \approx 0.05 M_\odot \ {\rm kpc}^{-2}{\rm yr}^{-1}$. In B2HW, B1HW, we inject a hot wind at the left bound-

ary with ghost zone density ρ'_{wind} and velocity v'_{wind}. Other variables obey outflow boundary conditions (see the exact values in Section 4.4.2). The right hydrodynamic boundary is single-direction outflow that only allows outward flux. We also imposed a temperature upper limit of $T' < 200$ for gas in ghost zones to control the heat flux into the domain.

In both stages, the magnetic field boundary conditions are set to be continuous for the perpendicular component and zero across the boundary for the parallel component in the x-direction, and periodic in the y-direction. The thermal conduction boundaries are reflecting.

4.4 Results

We perform three main sets of simulations with differing initial magnetic field: strong field, $B'_{x,\text{init}} = 2$, $\beta_{\text{init}} = 0.5$ (B2CR and B2HW), $B'_{x,\text{init}} = 1$, $\beta_{\text{init}} = 2.0$ (B1HW and B1CR) and $B'_{x,\text{init}} = 0.5$, $\beta_{\text{init}} = 8.0$ (B05CR).

4.4.1 Formation of Multi-phase Gas via Thermal Instability

The initial slab is in thermal equilibrium with small random perturbation. Thermal instability develops because we perturb the gas temperature to fall into the unstable branch of the cooling curve, so that when the gas cools and collapses, the cooling is enhanced and eventually triggers runaway cooling. With our initialization and choice of cooling function (See Section 4.3.3 and Figure 4.1), we estimate $L'_{F,\parallel} \approx 1.16$ in the x-direction and $L'_{F,\perp} \approx 0.38$ in the y-direction, which is well resolved by ~ 24 cells in the x-direction and ~ 8 cells in the y-direction.

The initial cooling timescale for the perturbed gas is $t'_{c,i} \approx 0.1$. We run the simulation to $t' = t'_{\text{inj}} = 30 \approx 300 t'_{c,i}$, where t'_{inj} denotes the time when we inject CR flux or hot wind. The gas evolution is in a quasi-steady state, and the gas density and temperature distribution are relatively constant. Figure 4.2 shows the gas density and temperature before we inject CRs or hot wind. In all simulations, the cold phase reaches the cooling function's lower temperature limit of 4×10^4K. The hotter gas ($\sim 10^{6-7}K$) expands and fills part of the domain but leaves $x' \gtrsim 200$ close to the initial density and temperature.

The cold gas is clumped and forms clouds with sizes of roughly a few Field lengths. The over-dense structures (e.g. filaments) preferentially align with the magnetic field, and there is a trend for structure to become less orientated when the magnetic field is
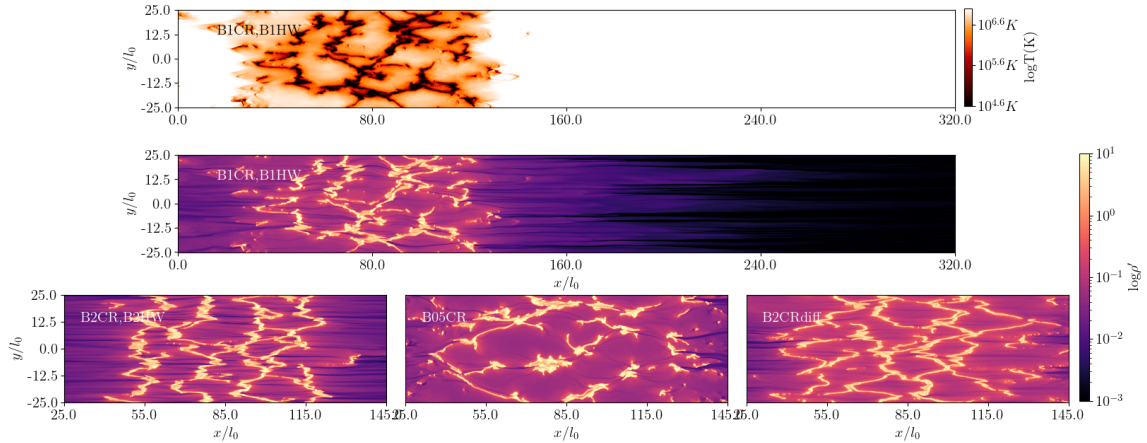
Figure 4.2: Multi-phase gas formed via thermal instability. The first row shows a gas temperature snapshot for the fiducial runs B1CR and B1HW, while the second row shows the corresponding density snapshot at $t' = 30 \approx 300t_{\rm c,i}$. The third row shows the snapshots before we inject CR flux or hot wind in other sets of simulations, from left to right: B2CR and B2HW at $t' = 30$, B05CR at $t' = 30$, B2CRdiff at $t' = 25$

weaker. The overall morphology is consistent with previous MHD thermal instability studies (Sharma et al., 2010b; Jennings & Li, 2020).

The density contrast is related to the balance between gas, CRs and magnetic pressure. The temperature contrast is primarily set by the cooling curve. Hereafter we define *cold gas* as gas with temperature $T \leq 7 \times 10^4$K, corresponding to the dense, clumped gas; *intermediate temperature gas* as $7 \times 10^4 K < T \leq 2 \times 10^5 K$, roughly corresponding to the temperature where cooling is maximized; *warm gas* as $2 \times 10^5 K < T \leq 10^6 K$, where supplemental heating dominates cooling; and *hot* gas as $T \geq 10^6$K, where density is relatively low and both the cooling and heating are moderate.

We expect that the spontaneously formed multi-phase gas provides a more realistic initialization to study CR and hot wind driven outflow. The perturbed magnetic field and irregular cloud morphology in our initialization are also important when studying CR streaming in a CGM-like environment. Moreover, the non-uniform pressure distribution and the continuous gas temperature range better approximates the multi-phase gas in CGM, adding complexity to the classical cold gas survival and acceleration problem.

4.4.2 Acceleration by Hot Wind: B1HW

We first show the results from B1HW and B1CR, a set of simulations with the same fiducial magnetic field. We implement a hot wind boundary condition so that it provides a comparable momentum flux to the CR flux in B1CR. In CR runs, we inject uniform, constant CR flux $F'_{\rm CR} = 60$ from the left x boundary at $t' = 30$ ($t' = 25$ for B2CRdiff). In B1HW and B2HW, the density of hot wind is set to be the average gas density at $x' \lesssim 10$, yields $\rho'_{\rm w} = 0.015$ in B2HW and $\rho'_{\rm w} = 0.069$ in B1HW.

The wind velocity $v'_{\rm wind} = 7.83$ in B2HW and $v'_{\rm wind} = 5.55$ in B1HW. We calculate the wind velocity by $\rho'_{\rm w} v'^2_{\rm w} = F'_{\rm CR}/4v'_{\rm A}$ according to the following estimation. The momentum flux carried by the hot wind is assumed to be equivalent to the momentum flux of CR, which leads to $\rho'_{\rm w} v'^2_{\rm w} = \int f'_{\rm CR} dx'$, where $f'_{\rm CR}$ is the CR force. With the steady state assumption, $\int f'_{\rm CR} dx' \sim \int \nabla P_{\rm CR} dx \sim P'_{\rm CR,left} - P'_{\rm CR,right}$, $P'_{\rm CR,left}$ and $P'_{\rm CR,right}$ is the CR pressure at the left and right boundary. At a relatively early time, $P'_{\rm CR,right} \ll P'_{\rm CR,left}$. In the streaming limit, the injected CR flux $F'_{\rm CR} \approx 4v'_{\rm A} P'_{\rm CR}$, where $v'_{\rm A} = B'_{\rm x}/\sqrt{\rho_{\rm h}}$ is the local Alfvén velocity, give the above estimation of $v_{\rm w}$. The injected winds are subsonic in both simulations.

Figure 4.3 shows the gas density snapshots from B1HW. When accelerated by a thermal wind, the clouds are compressed and some clouds merge together. During acceleration, the clouds are stretched in the direction of the wind, but some filaments from initial thermal instability maintain filamentary morphology. The clouds formed are nearly spherical, with a typical diameter similar to few initial Field length. The field lines wrap around the spherical clouds and form hoops, increasing local field strength and preventing deformation.

Figure 4.4 shows the cold gas mass evolution and average velocity. The cold gas evolution is generally consistent with quasi-linear acceleration with slight fluctuations. The cold gas mass increases before $t' - t'_{\rm inj} \sim 30$, and becomes more constant over time.

The cold gas growth is likely due to the efficient cooling of hot gas. Recent studies indicate that in multi-phase gas, a thin, turbulent layer forms between the cold and hot phases where they mix (Gronke & Oh, 2020; Fielding et al., 2020; Tan et al., 2021). The mixing layer is likely to be at the temperature that maximizes radiative cooling. The inhomogeneous and rapid cooling in turn redistributes pressure, potentially causing small-scale pressure gradients that further enhance turbulent mixing.
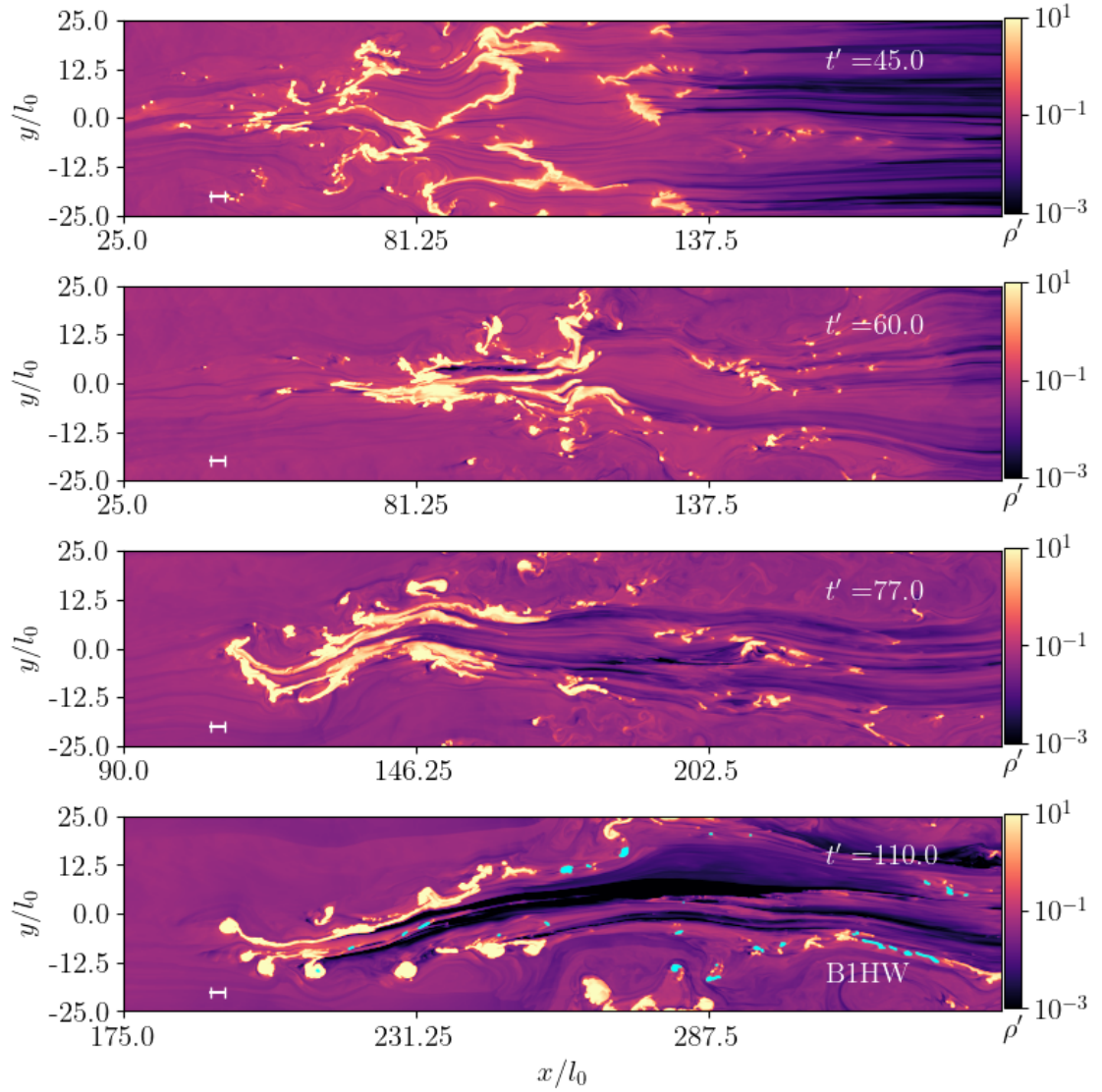
Figure 4.3:   The gas density snapshots of B1HW, from top to bottom: $t' = 45, 60, 77, 110$. The cyan masked regions in the last row are the small clouds we selected (see Section 4.5.2). The total cold gas fraction in the small clouds (masked by cyan in the last row) is $\sim 5\%$. The white line segment in the lower left corner shows five times of the initial Field length in the x-direction.

As a result, the cold gas can grow due to the mixing-induced condensation of hot gas. Gronke & Oh (2018) proposed a framework for quantifying the cold gas mass evolution when entrained in a hot wind. It estimates the timescales for the two competing processes that dominate cold gas mass evolution: the compression and strong shock by the hot wind that destroys cold gas, and the radiative cooling of hotter gas that supplies the cold gas. To estimates the shock-induced cold gas destruction, we use the mass-weighted average density of the cold gas for $\rho'_c \approx 6.01$ to estimate the cloud crushing time $t'_{cc} \approx 3.56$. Magnetic fields can modify the cloud crushing process (McCourt et al., 2015) and potentially slow down cloud crushing. However, the magnetic field is relatively moderate in our simulation, so t'_{cc} should provide order-of-magnitude estimation. The cold gas growth via condensation from hotter gas is characterized by the mixing layer cooling time $t'_{cool,mix}$. In their picture, the interface between cold and hot gas is a layer of intermediate temperature gas with ongoing mixing. Their model estimates the mixing layer temperature $T'_{mix} \sim \sqrt{T'_c T'_h}$. For CGM-like values of cold gas with $T'_c \sim 10^4$K and hot gas with $T'_h \sim 10^6$K, $T'_{mix} \sim 10^5$K, which is roughly the temperature that maximizes cooling. Following Gronke & Oh (2018), in B1HW and B1CR, we estimate the cooling time of the mixing layer as:

$$t'_{cool,mix} = \frac{\rho'_c}{\rho'_h} \frac{\Lambda(T_{cold})}{\Lambda(T_{mix})} t'_{cool,cold} \approx 0.30 \tag{4.8}$$

where $T'_c \sim 0.20$ and $\rho'_c \sim 7.93$ are the mass-weighted average temperature and density of the cold gas, $T'_{mix} \sim 1.86$, and $t'_{cool,cold} \sim 0.01$ is the cooling time in the cold gas. In B1HW, $t'_{cool,mix} \ll t'_{cc}$, suggesting that the efficient cooling from the mixing layer is likely to compensate the cold gas destruction by dynamical processes and seed cold gas growth. Consistent with the estimation, the cold gas mass increases in B1HW.

4.4.3 Acceleration by Cosmic Rays: B1CR

Figure 4.5 shows the gas density snapshots of B1CR. Similar to B1HW, the initial clouds merge into clumps with sizes of few initial Field lengths, but are then stretched in the x-direction. At late time, various fragmented small clouds are formed on the right side of cold gas (for example, the clouds marked by cyan in the last row of Figure 4.5).

The bigger clouds are primarily pushed by the CR "bottleneck effect", which refers
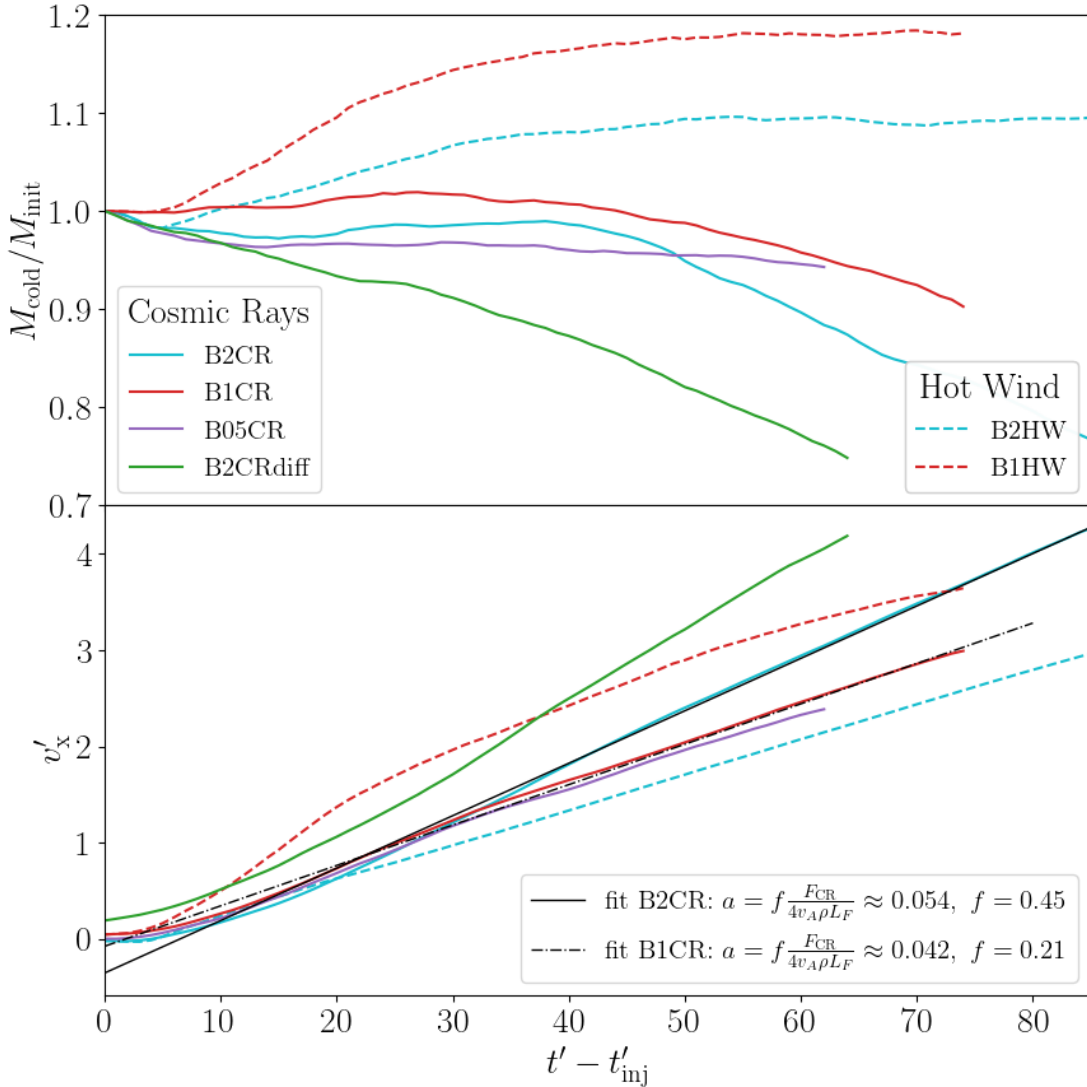
Figure 4.4: Upper panel: The mass evolution of cold gas for CR driven runs (solid lines) and hot wind driven runs (dashed lines), with the mass scaled to the initial mass. The color notes the initial magnetic field or CR transport, cyan is B2CR and B2HW ($\beta_{\text{init}} = 0.5$), red is B1CR and B1HW ($\beta_{\text{init}} = 2$), purple is B05CR ($\beta_{\text{init}} = 8$) and green is B2CR diff ($\beta_{\text{init}} = 0.5$). Lower panel: mass-weighted average cold gas velocity in the x-direction. The black solid and dash-dotted line are the linear fits according to Equation (4.3). We scale the start time to roughly when CR flux first intact with the cloud at $t'_{\text{inj}} = 39$.
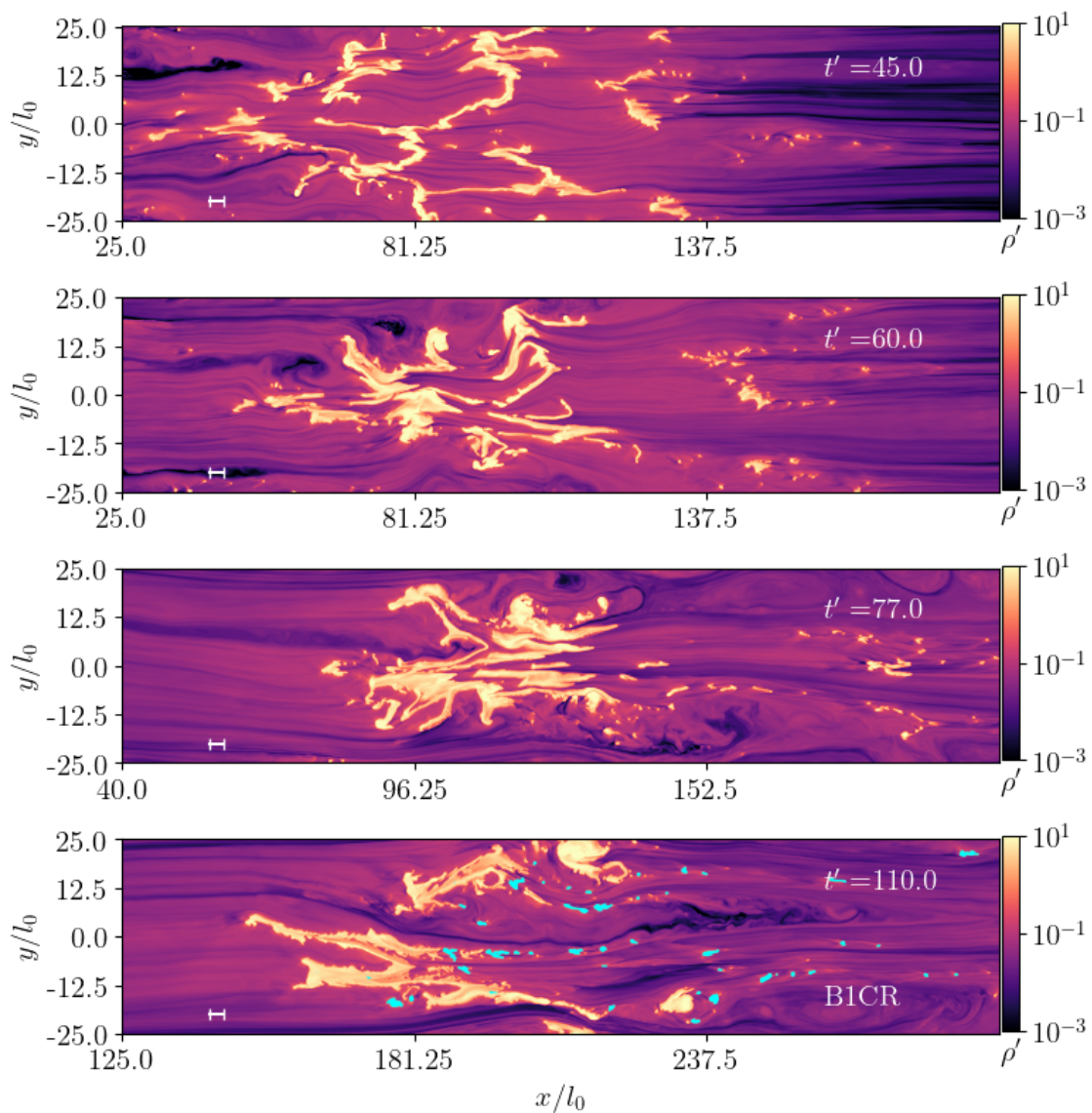
Figure 4.5: The gas density snapshots of B1CR, from top to bottom: $t' = 45, 60, 77, 110$. The cyan masked regions in the last row are the small clouds we selected (see Section 4.5.2). The total cold gas fraction in the small clouds (masked by cyan in the last row) is $\sim 5\%$

to the CR pressure gradient formed when CRs stream into high density regions from low density regions. The bottleneck arises when CRs stream at the local Alfvén velocity down the CR pressure gradient. When they enter dense, cold gas, the Alfvén velocity drops and CRs are slowed down. For static flow and magnetic field, $P_{CR}v_A^{4/3}$ is approximately constant at steady-state(Breitschwerdt et al., 1991; Jiang & Oh, 2018; Hin Navin Tsung et al., 2021). So more CRs pile up near the interface, increasing CR pressure, and the resulting CR pressure gradient can accelerate the cold, dense gas.

The cold gas mass and mass-weighted average velocity evolution are shown in Figure 4.4 as the red solid lines. The acceleration of cold gas is nearly constant. We fit a straight line according to the constant acceleration estimated by Equation (4.3). Our results are consistent with $f \approx 0.21$, in agreement with the similar f estimated in Brüggen & Scannapieco (2020), where a single, spherical cloud is accelerated by CR streaming.

The cold clouds in B1CR (Figure 4.5) are generally more diffuse and stretched than B1HW (Figure 4.3). The mass-weighted gas density distribution of B1CR and B1HW is shown in Figure 4.6, the two peaks corresponds to the $\sim 10^6$K diffuse gas and $\sim 10^4$K dense clouds. Compared to the initial distribution (gray dashed lines), acceleration by a hot wind enhances the density contrast, while acceleration by CR streaming preserves or slightly decreases the density contrast. If we estimate density contrast as the ratio between the two peaks, B2CR and B1CR yield $\rho_c/\rho_h \sim 80, 115$, while B2HW and B1HW has $\rho_c/\rho_h \sim 660, 340$.

The difference in density contrast is related to the driving mechanism. For entrainment in a hot wind, the cloud is driven by the thermal pressure shock formed at the interface between cold and hot gas. For CR streaming, the clouds are accelerated by the CR "bottleneck". Unlike the thermal shocks that preferentially compress the clouds, the CRs can penetrate into the cloud, providing non-thermal pressure support. When CR pressure in the cloud increases, the cloud needs a lower thermal pressure to reach pressure equilibrium with the surrounding hot gas. But the cloud temperature is constrained by the cooling function and already low, it cannot drastically drop. Instead, the cloud stretches, resulting in lower cloud density and the elongated morphology. A similar reduction of cold gas density by CRs is observed in recent works (Wiener et al., 2019; Butsky et al., 2020).

In contrast to B1HW (red dashed line), the cold gas mass decreases in B1CR despite using the same initial condition and cooling function. In order to understand
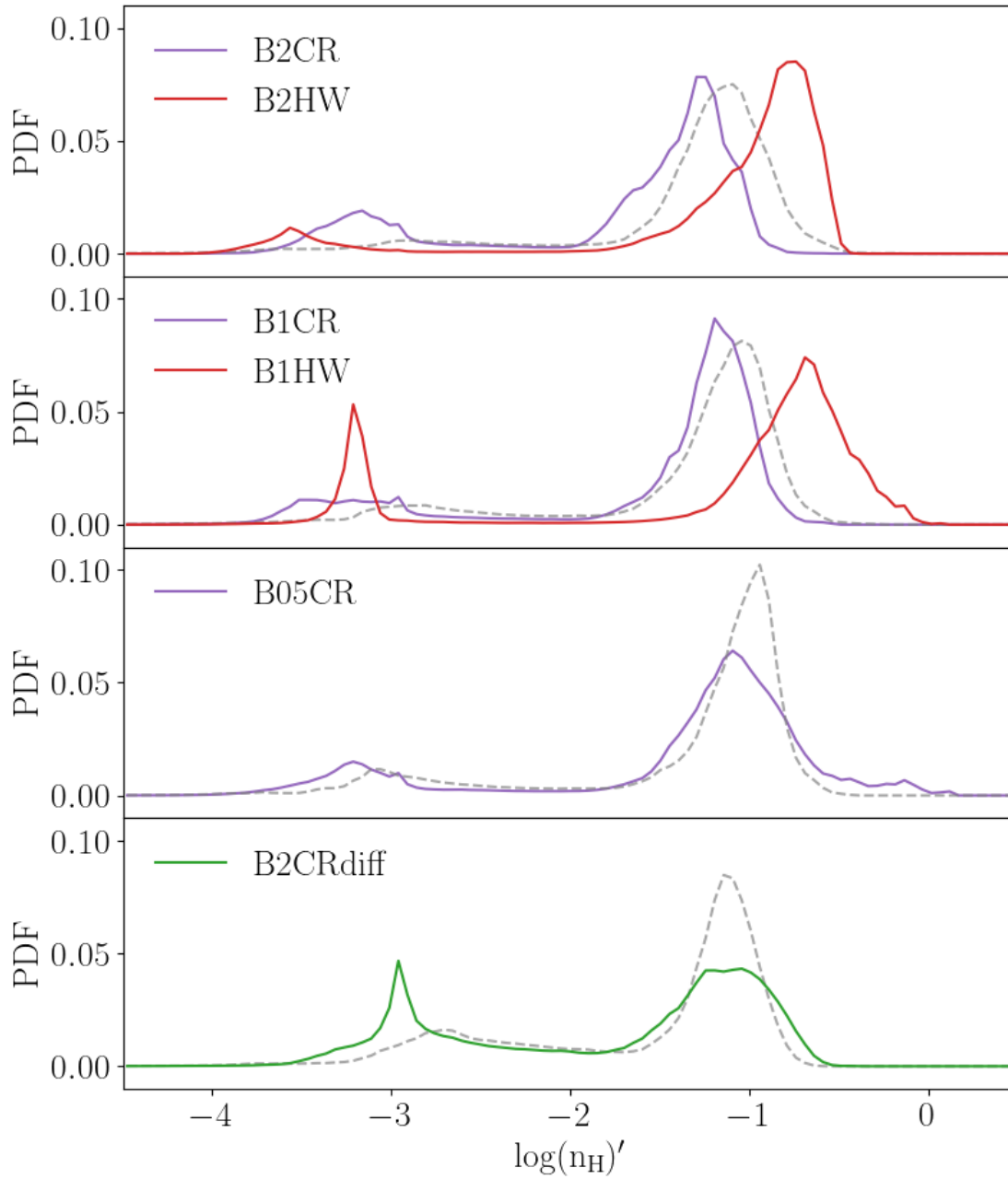
Figure 4.6: The mass weighted density probability distribution of different sets of simulations sampled at specific time: B2CR and B2HW with initial $\beta = 0.5$ (the first row, $t' = 115$), B1CR and B1HW with initial $\beta = 2.0$ (the second row, $t' = 120$), B05CR with initial $\beta = 8.0$ (the third row, $t' = 90$), and B2CRdiff $\beta = 0.5$ (the fourth row, $t' = 90$). In each panel, the gray dashed line shows the distribution before injection of CR flux or hot wind, they are $t' = 30$, 30, 30, 26 from the first row to the fourth row.

the cold gas drop, we consider the heating and cooling structure. Inside the dense, cold cloud ($T \lesssim 7 \times 10^4 \mathrm{K}$) where the temperature is close to the floor temperature, cooling and heating are moderate. Surrounding the dense cloud, a thin layer of intermediate temperature gas ($7 \times 10^4 K \lesssim T \lesssim 2 \times 10^5 K$) has the strongest cooling per volume. Around this thin cooling layer, the warm gas is dominated by supplemental heating term $n_{\mathrm{H}}\Gamma$. We note that it is possible that the heating constant Γ is over-estimated in our simulation. Before injecting CR flux or hot wind, the multi-phase gas is in quasi-steady state, optical thin cooling term $n_{\mathrm{H}}^2\Lambda$ roughly balances the supplemental heating. But supplemental heating in diffuse background gas is amplified after interacting with injected CR or hot wind. We lower the heating constant by an order of magnitude in more diffuse gas with $\rho' \leq 0.1$ to minimize the effect from the non-equilibrium background after injecting CR flux or hot wind.

The thin layer of intermediate temperature gas ($7 \times 10^4 K \gtrsim T_{\mathrm{gas}} \gtrsim 2 \times 10^5 K$) around the cold gas dominates the volumetric emission, and the mixing and cooling in this layer strongly impacts the cold gas mass evolution. Similar cloud emission structure is observed in Gronke & Oh (2020). Figure 4.7 shows the average density and total volume (area in 2D) of intermediate temperature gas in B1HW and B1CR. Intermediate temperature gas in B1CR has larger total volume, but lower average density than B1HW due to CR pressure support. The optically thin cooling is proportional to n_{H}^2, so B1CR has lower net cooling than B1HW despite the higher total volume.

The stronger cooling in B1HW also impacts the cooling timescale in the intermediate temperature gas. Figure 4.8 shows the mass-weighted distribution of intermediate gas cooling timescale. Compared to the initial distribution (the gray lines), hot wind acceleration enhances cooling rate and decreases the cooling time, in contrast to CR acceleration. Note, however, both the mass growth in B1HW ($\lesssim 20\%$) or the drop ($\lesssim 10\%$) in B1CR is relatively moderate given the fact that the duration is about $\approx 21 t'_{\mathrm{cc}}$.

Meanwhile, the cold gas ($T \lesssim 7 \times 10^4 \mathrm{K}$) is directly heated by both the supplemental heating of our net cooling function and the calculated CR heating. The corresponding heating time (the dashed line in Figure 4.8) is, however, long compared to the cooling time of intermediate gas, suggesting that the cold gas is not effectively heated. So the change of cold gas mass is more affected by cooling and dynamical processes.

Another factor that could influence cold gas evolution is the generation of small
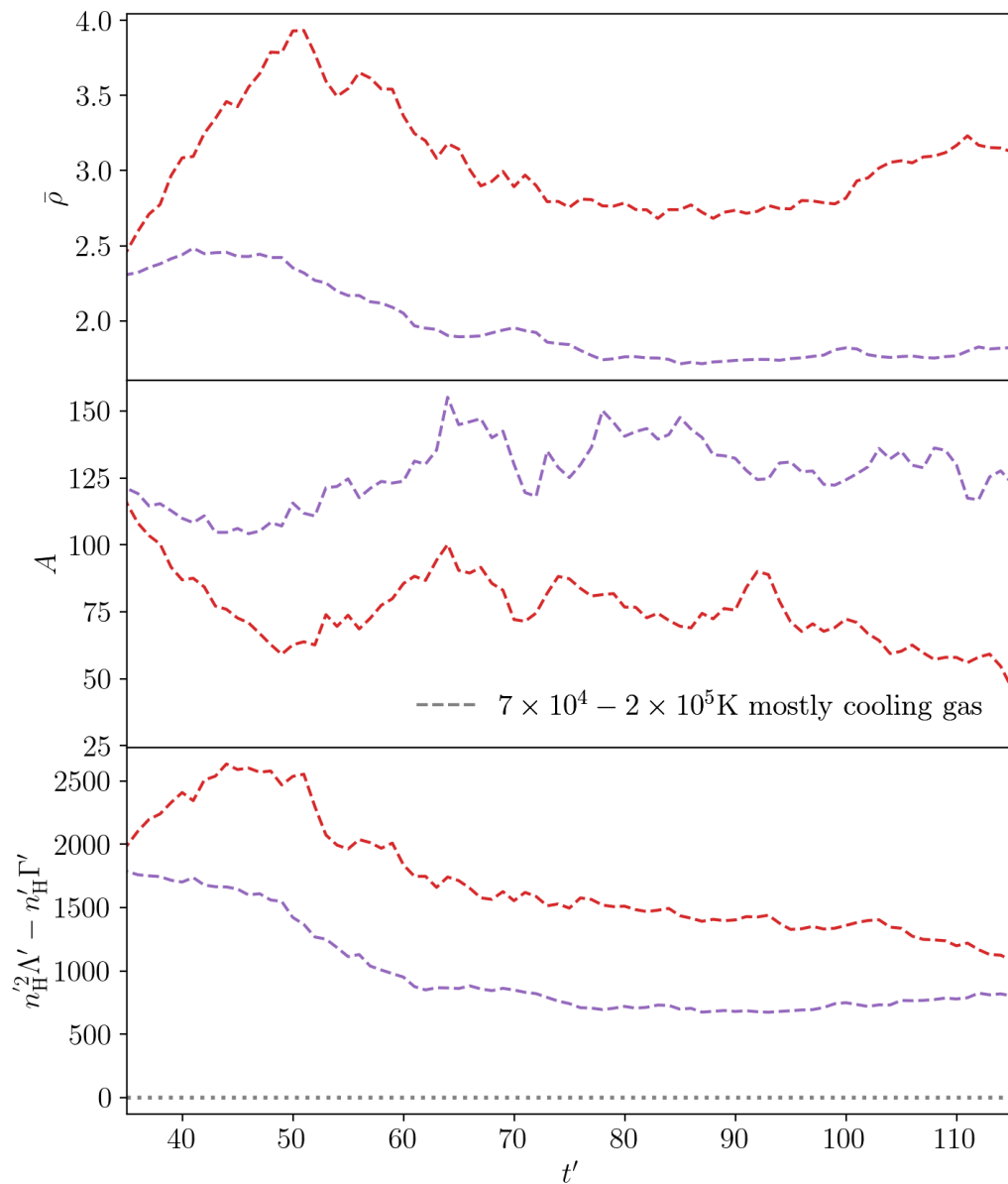
Figure 4.7: The average density (the first row), total volume (the second row), and total emission (the third row) for the intermediate temperature gas (dashed lines) in B1CR (purple) and B1HW (red).
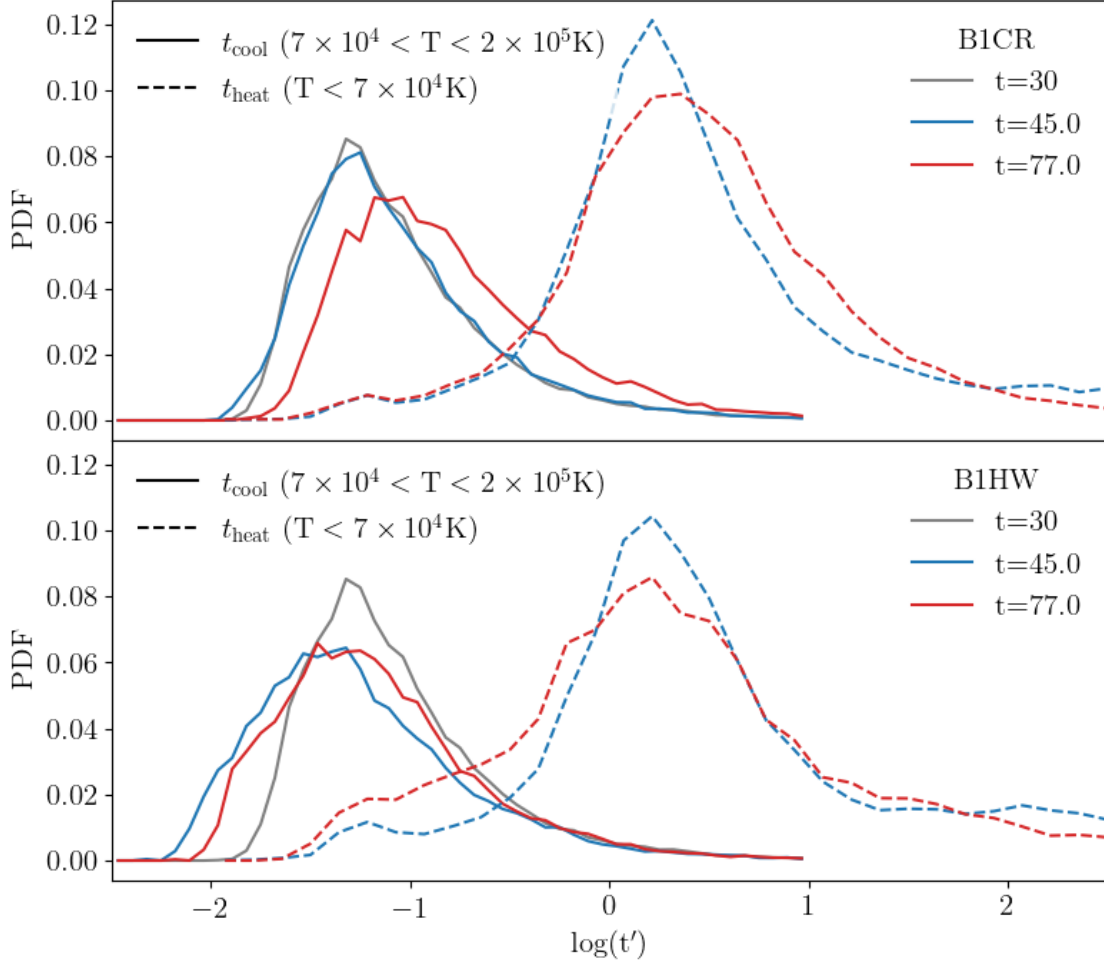
Figure 4.8: Probability distribution of cooling time for intermediate temperature gas with $7 \times 10^4 K \lesssim T_{\mathrm{gas}} \lesssim 2 \times 10^5 K$ (the solid lines) and heating time for cold gas $T_{\mathrm{gas}} \lesssim 7 \times 10^4 K$ (the dashed lines) for B1CR (the first row) and B1HW (the second row). The grey lines show the initial cooling time. During the acceleration, CR interaction with gas increases the cooling time while hot wind shortens the cooling time. The heating time of cold gas is usually long compare to the cooling time of intermediate temperature gas.

clouds at later times (marked by cyan in the last row of Figure 4.5). These smaller clouds are more likely to be destroyed in acceleration (Gronke & Oh, 2018; Gronke et al., 2021), which should lead to cold gas loss. Using the method discussed in Section 4.5.2, we estimate the total cold gas mass in small clouds, but find that it is a small fraction for these fiducial runs. The generation of fragmented small clouds are observed in B1HW too with similar low cold gas mass fraction. Thus, we conclude that the decreasing cold gas mass seen in B1CR is mostly the result of the suppressed cooling in the mixing layer.

4.4.4 Strong magnetic field: B2CR and B2HW

Dynamics

We increase the initial magnetic field by a factor of two in B2HW and B2CR, giving an initial $\beta = 0.5$. The first column in the third row of Figure 4.2 shows the gas density snapshot before injecting CR or hot wind.

The right column of Figure 4.9 shows a series of the gas density snapshots from B2HW. The initially distributed cold clouds are pushed together by the thermal wind, and mostly merge into a single cloud, experiencing a collective acceleration. The cloud morphology differs from B1HW. The strong magnetic field constrains the fluid to be more laminar, and prevents the formation of spherical clouds.

B2HW also experiences total cold gas growth (see Figure 4.4). We use Equation (4.2) to estimate the cloud crushing time $t'_{\mathrm{cc}} \approx 4.90$, and the mixing layer cooling time is estimated to be $t'_{\mathrm{cool,mix}} \approx 0.46$. We find $T'_{\mathrm{c}} \sim 0.20$ and $\rho'_{\mathrm{c}} \sim 6.52$ for the mass-weighted average temperature and density of the cold gas, $T'_{\mathrm{mix}} \sim 1.66$. We find $t'_{\mathrm{cool,mix}} \ll t'_{\mathrm{cc}}$, consistent with the cold gas growth we observe.

The left column in Figure 4.9 shows the gas density snapshots of B2CR. The dynamics includes two major stages: when $t' \lesssim 75.0$, the initially distributed clouds are pushed by CRs and merge. After $t' \gtrsim 75.0$, the merged cloud is accelerated by CR streaming along the initial magnetic field direction.

Figure 4.10 shows the gas density, temperature and pressure profiles across the merged cloud at $t' = 115.0$ for B2CR and B2HW. In B2CR, a CR pressure gradient is formed across the merged cloud (the bottleneck $225 \lesssim x' \lesssim 250$), and the gas pressure in the cloud is small. In B2HW, at $x' \sim 192$, thermal pressure forms a shock at the cloud interface and drops as one moves to the right within the cloud,
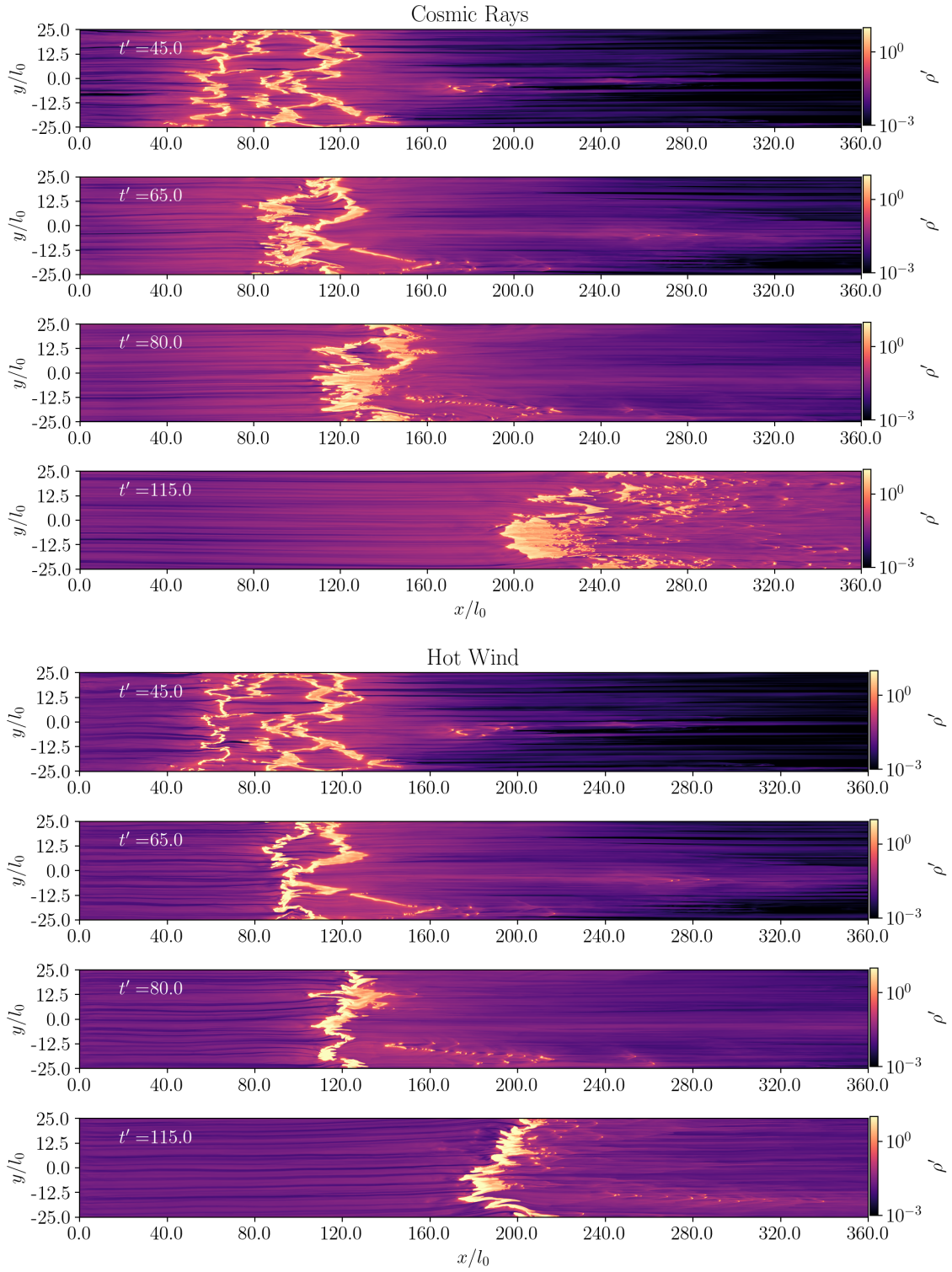
Figure 4.9: Gas density snapshots of CR driven runs (the left column) and hot wind driven runs (the right column). From top to bottom, the snapshots are taken at $t' = 45.0, 65.0, 80.0, 115.0$.
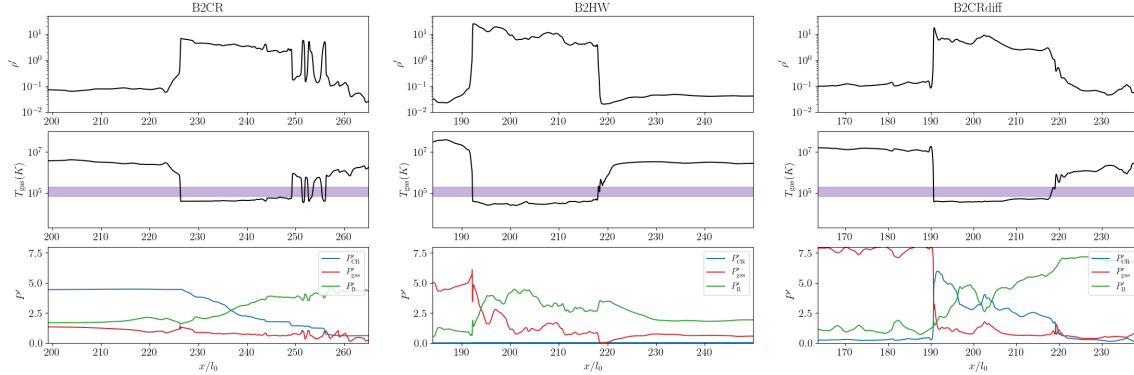
Figure 4.10: Representative merged cloud structure at late time in B2CR, B2HW and B2CRdiff. The density (the first row), temperature (the second row), and pressure (the third row) are profiles of a line cut through the gas from $x' = 119.0$ to $x' = 265.0$ at $y' = -16.5$, for B2CR (the first column); $x' = 119.0$ to $x' = 265.0$ at $y' = -15.7$ B2HW (the second column); and at $t' = 115$ and B2CRdiff from $x' = 163.5$ to $x' = 238.5$ at $t' = 90$ (the third column). In the third row, the blue solid line is the CR pressure, the red solid line is gas pressure and the green solid line is magnetic pressure. The purple band in the second row labels the intermediate temperature gas ($7 \times 10^4 K \lesssim T_{\text{gas}} \lesssim 2 \times 10^5 K$)

while the CR pressure is unimportant. Notice that the gas pressure in B2HW and CR pressure in B2CR in hot gas on the left side are similar ($P' \sim 5.0$) due to the equivalent momentum flux supplied at the boundary in the two simulations. In both runs, magnetic pressure plays an non-negligible role in the multi-phase gas.

Dynamically, the cloud merging is an important process that modifies the CR pressure distribution in our simulations. Figure 4.11 shows a typical cloud merging process. At $t' = 50$, three CR "bottlenecks" forms when encountering three clouds (the grey filled region in the first row) at $x' \sim 72, 96$, and 136. The CR pressure jump usually occurs at a local minimum of $v'_x + v'_A$. As the clouds merge and CRs penetrate into the clouds, the bottlenecks are "merged" too. At $t' = 63$, CRs roughly decouple with gas in the region $x' \lesssim 110$, resulting nearly flat CR pressure despite the local density variation. The stair-like CR pressure profile present with multiple moving clouds and final merged cloud profile are consistent with the theoretical study of CR bottlenecks in Hin Navin Tsung et al. (2021).

After cloud merging, the cold gas experiences a collective bulk acceleration. During acceleration, we observe that multiple small-scale clouds are formed on the right side of the merged cloud (the fourth row in Figure 4.9). These clouds are usually
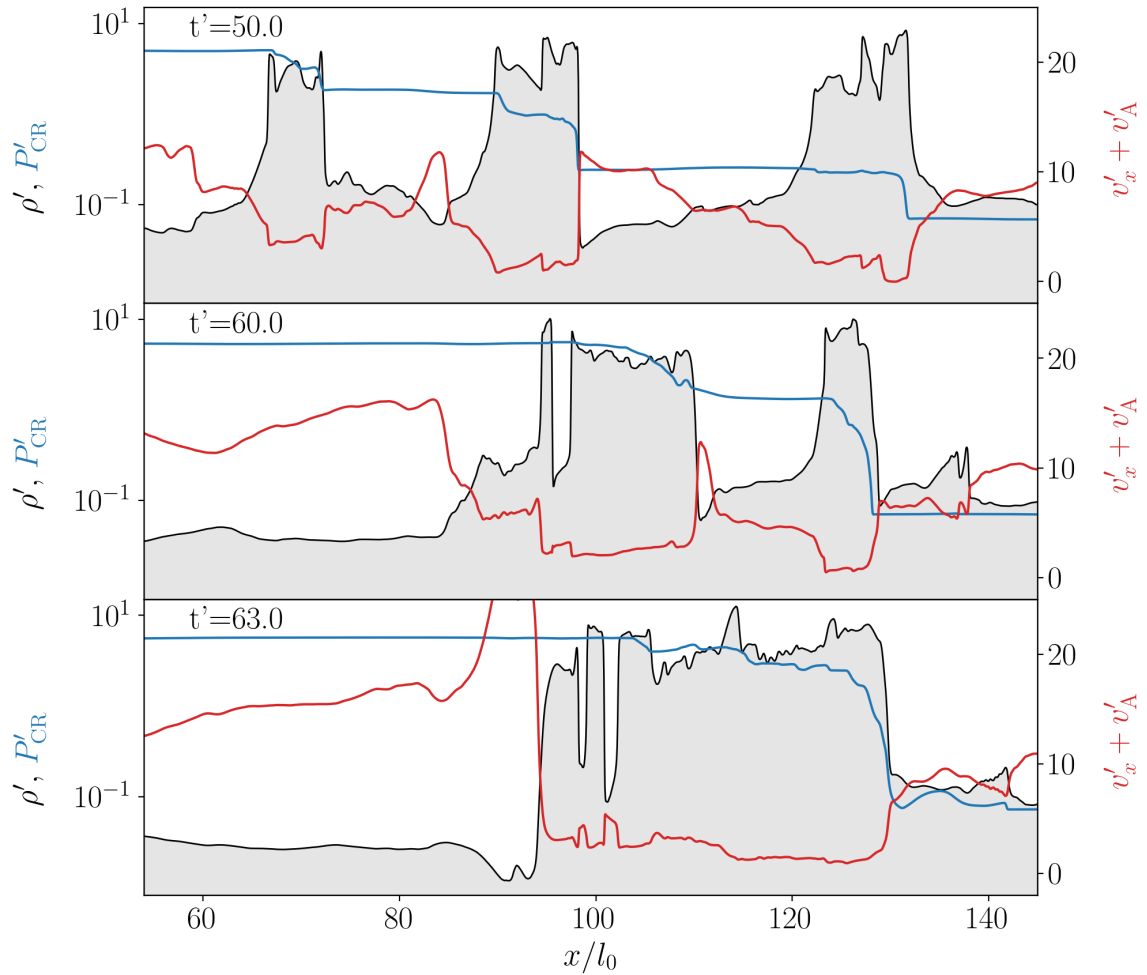
Figure 4.11: The time series of gas density (the black solid line and shaded region), CR pressure (the blue solid line), and the sum of flow velocity and Alfvén velocity (the red solid line) at $y' = -11.4$ at $t' = 50$ (the first row), $t' = 50$ (the second row) and $t' = 63$ (the third row) from B2CR.

smaller than the initial Field length, and tend to quickly mix with the hot background gas. Similar small clouds are also observed in B1CR at later time. But the effect seems to be enhanced in B2CR. We discuss the formation and destruction of these small clouds in Section 4.5.2.

The first row of Figure 4.6 shows the density distribution in B2CR and B2HW. Similar to B1CR and B1HW, the density contrast is reduced in B2CR due to CR pressure support, and enhanced in B2HW due to the thermal pressure compression.

The total cold gas mass and average velocity of B2CR is plotted in Figure 4.4. The acceleration is also linear and is well fit by Equation (4.3). The average Alfvén velocity is higher than B1CR due to the stronger magnetic field, but $f \approx 0.45$ is also higher than B1CR, resulting in similar acceleration.

The higher f seems to be a result of larger effective area. The merged clouds in B2CR are not significantly compressed in y-direction and maintain the initial covering fraction. The strong magnetic field alignment is not significantly altered by thermal instability (see also Jennings & Li (2020)), CR streaming is relatively uniform in the y-direction in B2CR and B2HW, so that the clouds maintains the "shell" morphology, and thus larger effective area. This differs from B1CR, where the magnetic field is distorted by thermal instability. CRs preferentially stream through the channels between the cold clouds, resulting in a CR pressure gradient in the y-direction that compresses the merged cloud and reduces the effective area.

Cold gas evolution

B2CR experiences cold gas loss during the acceleration while B2HW has cold gas growth, consistent with what we observed in B1CR and B1HW. We find that in B2CR and B2HW, however, the intermediate temperature gas has a similar cooling timescale in the two runs. The cooling timescale distribution has similar shape to B1CR (see Figure 4.8), with the peak shifted to $\log(t_{\rm cool})' \sim -1.1$. We subtract all external thermal sources including supplemental and CR heating when calculating the net cooling timescales. The effect of CR heating $\sim v_{\rm A} \cdot \nabla P_{\rm CR}$ is generally unimportant in the intermediate temperature gas. We also find that heating of cold gas seems to be unlikely to drive the observed mass change in B2HW and B2CR.

The similarity of intermediate temperature gas arises from the pressure support. Figure 4.10 shows that the magnetic pressure is significant in both runs. On the right side of the cloud, opposite the incoming CRs or hot wind, gas is supported by

magnetic pressure. The purple band in the temperature plot labels the intermediate temperature gas, which occupies a larger volume on the right side of the cloud too. So the intermediate temperature gas density is primarily set by the magnetic pressure, which is similar in B2HW and B2CR.

Figure 4.12 shows the total emission, emission from the intermediate temperature gas, and the rate of change of cold gas in B2CR and B2HW. Because the intermediate temperature gas has similar properties between the two simulations, the emission in the two runs is also similar (dashed lines in the lower panel). The thin solid lines show the total emission from all gas. Interestingly, in B2HW, the emission from intermediate temperature gas (dashed red line) traces the total emission (thin solid red line) well, suggesting that the net heating and cooling from the gas with other temperature in the simulation roughly balance each other. In B2CR, the intermediate temperature gas (dashed purple line) emission is similar to hot wind, but the negative overall emission (thin solid purple line) suggests that the gas with other temperature experience net heating. We found that the net heating in B2CR is due to larger volume of warm gas ($\sim 10^{5.3-6} K$) compared to B2HW. The warm gas usually surrounds cold clouds and forms from mixing, and it is dominated by supplemental heating. The CR-supported cold clouds have larger surface area, where mixing happens, leading to a higher volume of warm gas, and thus, total heating.

If the cold gas evolution is primarily determined by the cooling and heating, the total emission should be roughly proportional to cold gas mass rate of change (Fabian, 1994). The lower panel of Figure 4.12 shows that the total emission (the thin solid lines) strongly correlates with the cold gas mass rate of change (the thick solid lines), but deviates from the proportionality in the acceleration stage ($t \gtrsim 70$ for B2CR), suggesting that there are other factors affecting the cold gas evolution.

Figure 4.9 shows that at later time, B2CR produces multiple small clouds on the right side of the merged cloud. The small clouds mix more easily with the hot background gas or are destroyed by deformation. We estimate that in B2CR, $\sim 20\%$ of the cold gas is in the form of small clouds, while the fraction is usually $\lesssim 5\%$ in B2HW. The morphological difference seems to explain the mass loss in B2CR. We discuss the effect of small clouds in further detail in Section 4.5.2.
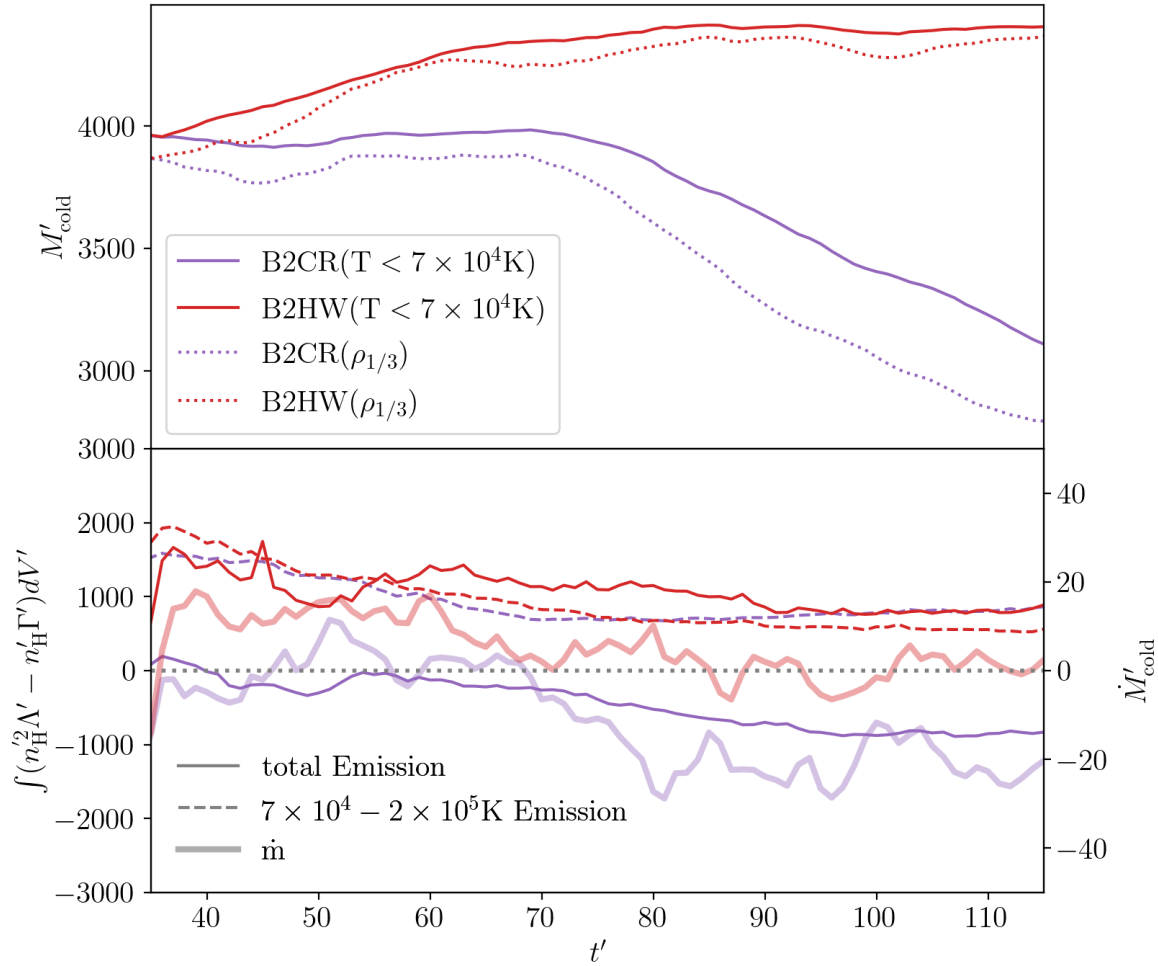
Figure 4.12: The cold gas mass and emission as a function of time, line color denotes the driving mechanism: the purple lines are for CR driven, and the red lines are for hot wind driven runs. Upper panel: the cold gas mass evolution. The solid lines are defined as gas with temperature $T_{\mathrm{gas}} < 7 \times 10^4 K$, while the dotted lines are defined as gas with density lower than $1/3\bar{\rho}$, where $\bar{\rho}$ is the mean density. Lower panel: thin solid lines and dashed solid lines with labels on the left are the net emission from gas. The thin solid lines are total emission from the simulation domain, while the dashed lines are the emission from intermediate temperature gas. The thick solid lines, with labels on the right, are the derivatives of the cold gas mass (the solids lines in the top panel.)

4.4.5 Weak magnetic field: B05CR

We decrease the initial magnetic field by a factor of two in B05CR, given initial $\beta = 8.0$. The second column in the third row of Figure 4.2 shows the gas density snapshot before injecting CRs. The overall dynamics of B05CR is similar to B1CR. Thermal instability creates more fragmented small clouds scattered at $x' \gtrsim 112.5$. We observe a similar stretched cloud morphology during the acceleration. The average cold gas mass and velocity is similar to B1CR, too. Figure 4.13 shows that the magnetic field, however, is more turbulent in this simulation. The initial uniform magnetic field strength is $B'_{\text{init}} = 0.5$. The upper panel shows the snapshot before we inject the CR flux, and the magnetic field strength in the cold gas has already been enhanced by thermal instability. In the lower panel, after CRs enter the domain, their interaction with multi-phase gas further modifies the magnetic field, and the magnetic pressure in cold gas can be an order of magnitude larger than the initial value.

CRs stream along the entangled magnetic field, resulting in a CR pressure gradient in both the x- and y-directions. In addition, B'_y is amplified, making $v_{\text{A,y}}$ comparable to $v_{\text{A,x}}$ in some of the hot gas. In these regions, the CR pressure gradient in the y-direction is also comparable to the x-direction, leading to additional CR heating in the y-direction ($\sim v'_{\text{A,y}} \partial_y P_{\text{CR}}$). The cooling in background gas is generally inefficient and the CR heating can not be quickly radiated away. The heating time of this gas $t'_{\text{heating}} \sim 0.03$ can be $1-2$ order of magnitude smaller than those in strong magnetic field runs. As a result, gas pressure in the original $\sim 10^6$K gas is increased, cold gas is accelerated by both gas and CR pressure. For the x-direction acceleration, the average fractional contribution from the enhanced gas pressure is ~ 5.2 times the CR pressure. In turbulent magnetic field, CR streaming drives turbulence and heats gas. CRs alone are relatively inefficient to accelerate gas in a preferred direction.

Although cold gas is not primarily accelerated by CRs, the intermediate temperature gas is still supported mainly by CR pressure. So the intermediate temperature gas properties, cooling timescale and cold gas rate of change is similar to B1CR. In the later period of acceleration, CRs penetrate into the cold gas, and the cloud is again supported by CR pressure so that the density contrast of the multi-phase wind is similar to B1CR.
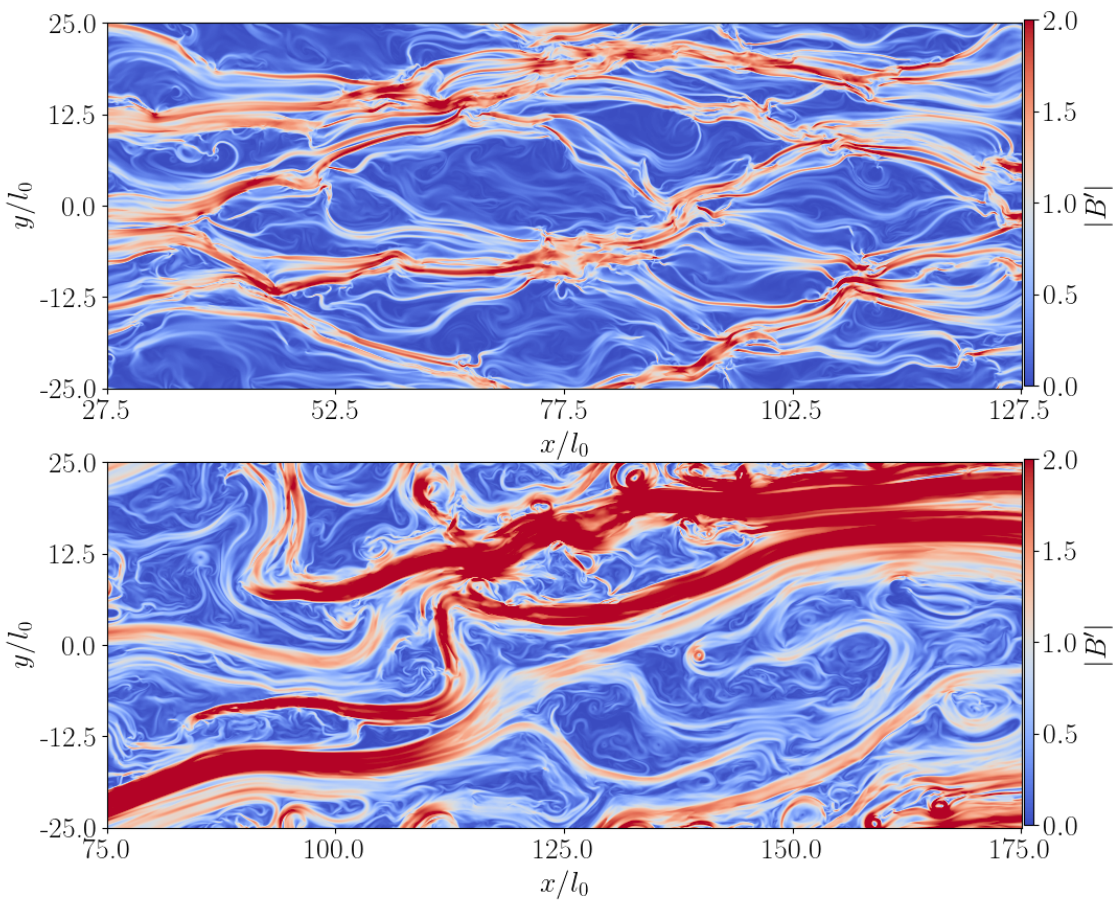
Figure 4.13: The magnetic pressure in B05CR before injecting CR flux ($t' = 30$, the upper panel) and after the clouds are accelerated by CRs ($t' = 75$, the lower panel). Notice that we show the magnetic pressure where most of the cold gas is located, so these two panels has different x-coordinate ranges.

4.4.6 The Effect of Conductivity

We now explore the effect of lowering the conductivity, which allows us to have a lower value of the Field length at fixed density or keep the Field length fixed while lowering the density. In B2CR_LC, we lower the conductivity ($\kappa'_\parallel$ and $\kappa'_\perp$) by a factor of 100. This allows the physical value of the Field length, and therefore cloud size, to remain constant while lowering the density by a factor of ten. This also corresponds to a factor of ten reduction in the heating constant Γ as described in Section 4.3.3. Hence, the a motivation for B2CR_LC is to explore the relative impact of the heating constant, while keeping cloud sizes to be a few 100pc.

We only run the thermal instability to $t' = t'_{\mathrm{inj}} = 10$ in B2CR_LC, as formed multiphase gas reaches quasi steady state faster than B2CR due to the lower conductivity. We inject $F'_{\mathrm{CR}} = 60$ in to the domain from the left boundary as in B2CR, so that the CR pressure is similar relative to the gas pressure and magnetic pressure.

The overall dynamical process is similar to B2CR despite some morphological differences. The cold clouds initially formed from thermal instability are less clumped than those in B2CR, but the cloud sizes are still comparable to the Field length. After interacting with CRs, the clouds are slightly less merged compared to the bulk cloud in B2CR. This is likely due to the smaller cloud column density. When accelerated by CR, the clouds are also stretched in the x-direction, and several small clouds are formed in the acceleration. Similar to B2CR, we found a noticeable fraction of cold gas ($\sim 25\%$ at late time) is in the form of small clouds.

Figure 4.14 shows the cold gas mass evolution and acceleration of B2CR_LC. The cold gas evolution is similar to B2CR. We find that the cooling and heating structure is not sensitive to the lower conductivity, density unit and heating constant. The intermediate temperature gas is still a thin layer between the cold and hot gas that emits the most per volume. The warm gas ($\sim 10^{5.3-6}$K) is also still dominated by supplemental heating despite the order of magnitude reduction in the heating constant. In addition, we do not observe significant growth of the thin intermediate temperature gas layer, and the average density of the gas is similar to B2CR. Interestingly, at late times the magnetic pressure has smaller fractional contribution to support the intermediate temperature gas compared to B2CR. The lower magnetic pressure in intermediate temperature gas might be related to both the different magnetic field distortion in thermal instability stage and the lower level of merging that occurs in
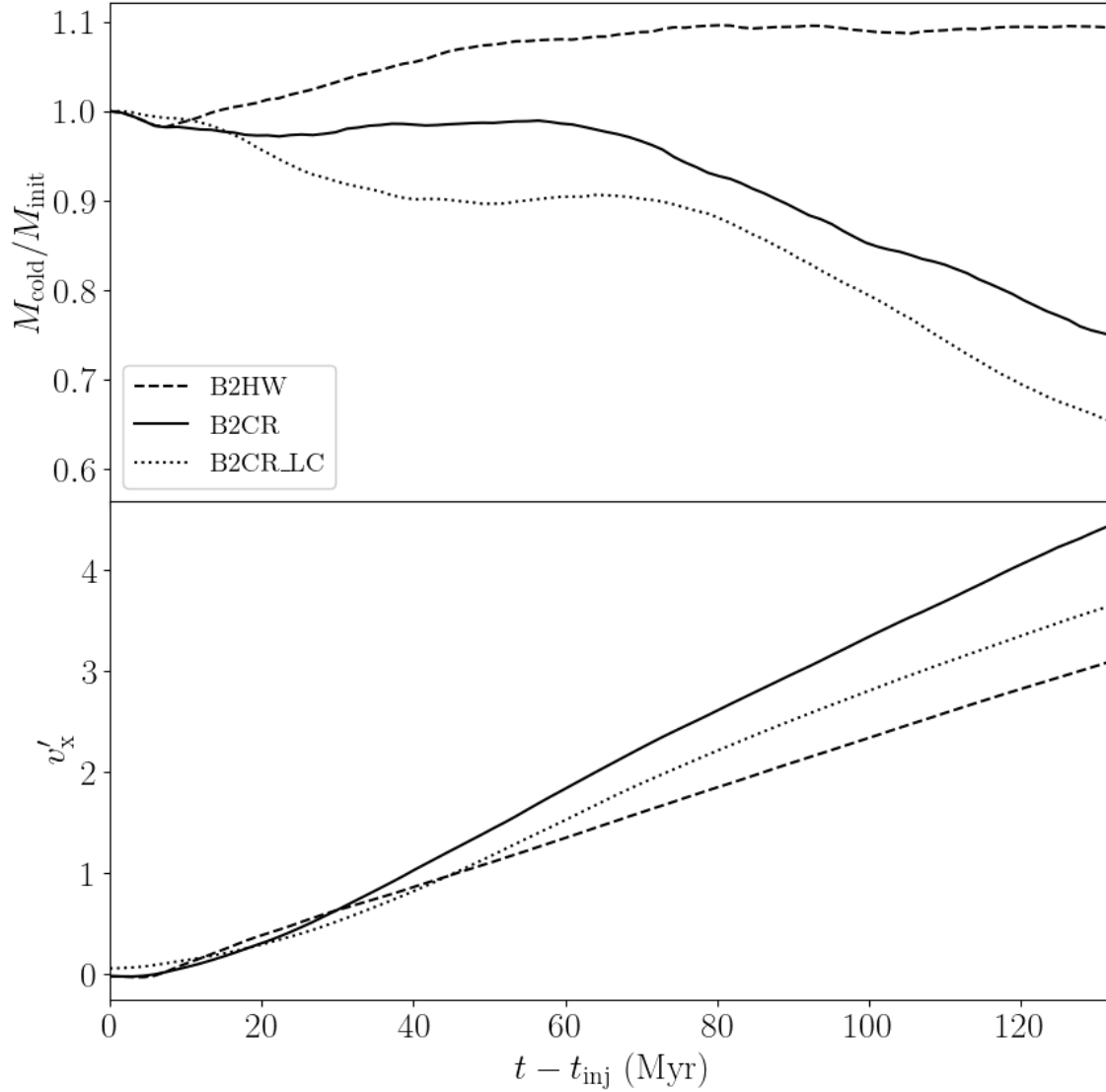
Figure 4.14: Similar to Figure 4.4. Upper panel: The mass evolution of cold gas B2CR (solid lines) , B2HW (dashed lines) and B2CR_LC (dotted lines). Lower panel: mass-weighted average cold gas velocity in the x-direction. We scale the start time to roughly when CR flux first intact with the cloud at t'_{inj}.
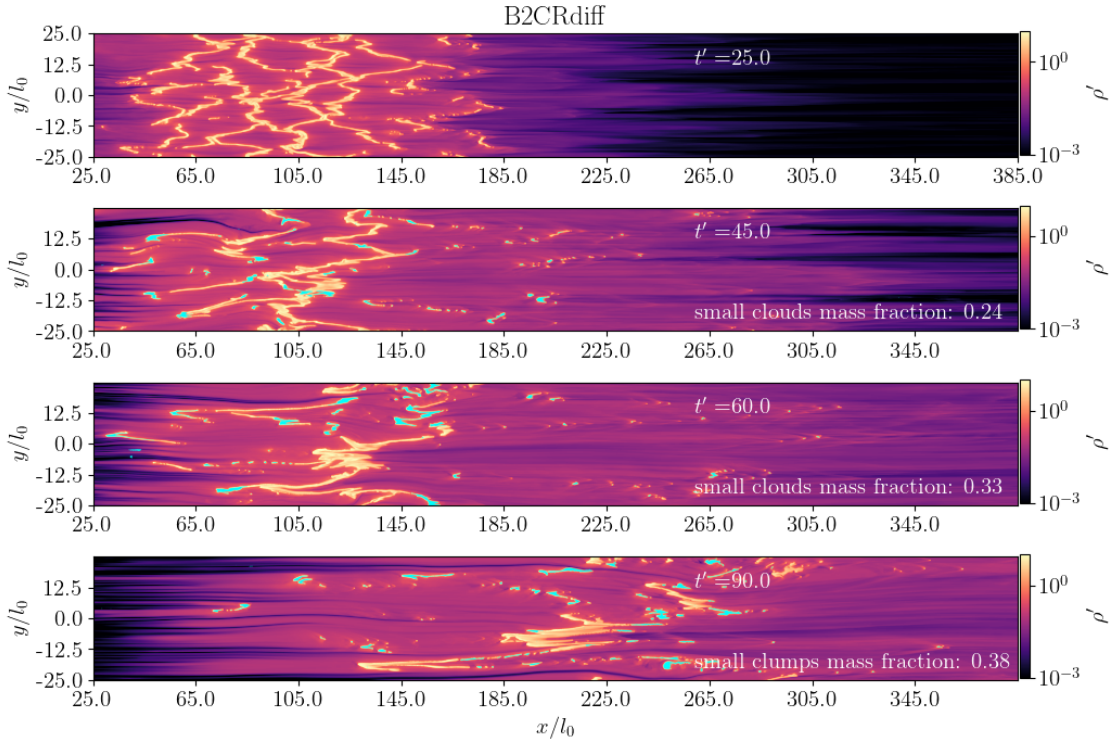
Figure 4.15: Gas density snapshots from B2CRdiff, which from top to bottom are taken at $t' =$25.0, 45.0, 60.0, 90.0. In the last row, the blue masked regions are the small cold clouds with temperature $T < 7 \times 10^4$K. The small clouds fraction is about $\sim 25\%$

the acceleration stage.

4.4.7 CR Diffusion

In B2CRdiff, we assume that CR transport is diffusive and turn off CR streaming ($\mathbf{v}_s = 0$). The diffusivity $\kappa_{\mathrm{diff}} = 1.73 \times 10^{26} \mathrm{cm}^2\ \mathrm{s}^{-1}$ is constant, giving the diffusion timescale $t'_{\mathrm{diff}} \sim L_{\mathrm{F}}^2/\kappa_{\mathrm{diff}} \approx 10.27$, about two order of magnitudes longer than the initial cooling time. The long diffusion timescale means that CRs travel slowly through gas, in contrast to the relatively fast streaming in B2CR. This choice of κ_{diff} is smaller than what is usually considered likely to occur in realistic systems. Hence, a shorter diffusion time may be expected in more realistic systems.

Figure 4.15 shows the density snapshots of B2CRdiff. The clouds are stretched in the x-direction and accelerated without significant merging. This produces a different cloud morphology from streaming, with clouds connected by filaments along

the magnetic field direction, which is consistent with the findings in Sharma et al. (2010b).

Figure 4.6 shows that the accelerated clouds roughly maintain their initial density contrast in B2CRdiff. The third column in Figure 4.10 shows the density, temperature, and pressure of a typical stretched cloud in B2CRdiff. The diffusion time in our simulation is substantially longer than other dynamical timescales, and CRs are trapped in the dense cloud, giving a high CR pressure in cold gas. When CR flux enters the domain, it compresses the warm and background gas, increasing the gas pressure. The high gas pressure forms a shock at the cloud interface and accelerates the cold gas. B2CRdiff has somewhat higher acceleration than B2CR, which we attribute to this increasing gas pressure and the dropping total cold gas mass.

The overall higher density leads to shorter cooling time in the intermediate temperature gas. This short cooling time, however, does not increase the cold gas mass. In fact, B2CRdiff has the largest fractional cold gas loss among all the simulations. We attribute the loss to the production of small clouds and their efficient destruction in B2CRdiff. In Figure 4.15 we denote the small clouds with cyan masked regions. At $t' = 45$, 60, 90, the fractions are $\sim 24\%$, 33%, 38%.

The mechanism for generating small clouds is also different from that in the CR streaming case (B2CR). A noticeable fraction of small clouds are formed at both sides of the shell even at early time. We find that they primarily originate from the breakup of filaments. Figure 4.16 shows a typical small cloud generation process: a filament (noted by the red rectangle) at $t' = 30$ breaks into several small clouds. We further discuss the formation of small clouds in Section 4.5.2.

Diffusion and streaming operate intrinsically differently when creating and accelerating multi-phase gas. Sharma et al. (2010b) suggest that the filamentary structure is a natural result of thermal instability with anisotropic conductivity. The fastest growing mode is parallel to the magnetic field, in which the conductivity is optimal, resulting filaments along the magnetic field. This morphological difference of the resulting clouds leads to different cold gas evolution.
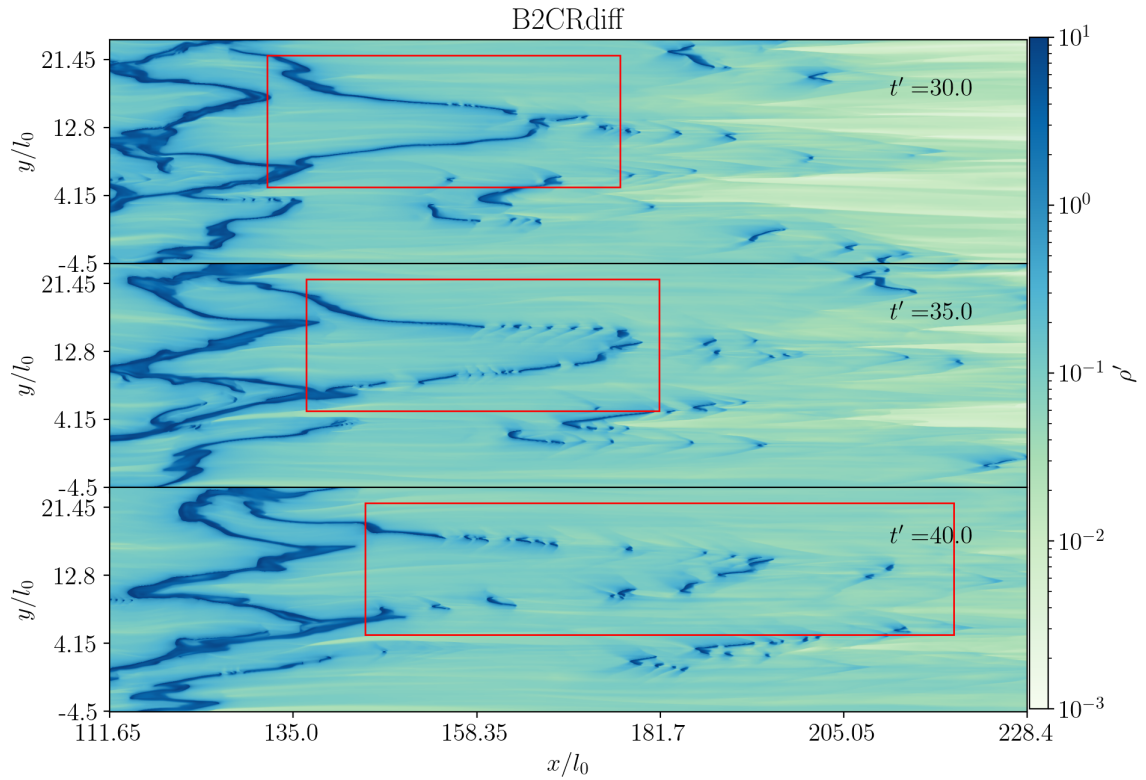
Figure 4.16: Zoom-in density snapshots of B2CRdiff at $t' = 30, 35, 40, 45$ (from top to bottom panel). The snapshots show that the filament structure (highlighted by the red rectangle) at $t' = 30$ breaks into several small clouds distributed between $158 \lesssim x' \lesssim 228$ from $t' = 30 - 45$.

4.5 Discussion

4.5.1 CR streaming in non-uniform magnetic field

Figure 4.13 shows that the initial weak magnetic field can be amplified by thermal instability and CR streaming. In B05CR, the initial $\beta_{\text{init}} = 8$. Before injecting CRs, the average β of cold gas is amplified by thermal instability to $\bar{\beta}_{\text{cold}} \approx 1.5$. At $t' = 90$, CR acceleration further enhances magnetic pressure in cold gas to $\bar{\beta}_{\text{cold}} \approx 0.75$, which is reduced by about an order of magnitude compared to the initial value. The interaction also entangles field lines, resulting in a highly non-uniform and dynamical magnetic field. Although CR interaction with a cold cloud in a relatively uniform magnetic field is investigated by recent works (Wiener et al., 2019; Brüggen & Scannapieco, 2020), CR streaming in non-uniform magnetic fields is less studied. In this section, we discuss the CR interaction with multi-phase gas in the non-uniform magnetic field created by thermal instability in our simulations.

When magnetic field lines are well-aligned with the direction of incoming CR flux (x-direction), CR pressure shows the classical "bottleneck" that drives cold clouds. When the field lines are entangled, CR streaming does not directly provide strong acceleration in the x-direction. But how are CRs distributed along the magnetic field line? The lower panel of Figure 4.17 shows the CR pressure along a distorted magnetic field line (the black solid line in the upper panel) in B05CR. Interestingly, the CR pressure and gas density show typical "bottleneck" (similar to Figure 4.11). The red line shows the magnitude of total CR streaming velocity in lab frame along the magnetic field $|\mathbf{v}'_{\parallel} + \mathbf{v}'_{A,\parallel}| = (\mathbf{v}' + \mathbf{v}'_{A}) \cdot \mathbf{e}_{\parallel}$, where $\mathbf{e}_{\parallel}$ is the unit vector tangent to field line. However, when we project the CR pressure gradient onto the x-direction, the acceleration is small for two reasons. Firstly, the magnetic field is highly non-uniform. In some regions, the enhanced magnetic field in the colder gas compensates for the high density, making the v_{A} comparable to nearby hotter gas. So the "bottleneck" is reduced and the CR pressure gradient is shallower. Secondly, the turbulent magnetic field is inefficient in transporting CRs preferentially along the x-direction. At early time $t' \lesssim 60$, CR pressure in cold gas can be even lower than the gas pressure. The smaller CR pressure and shallower pressure gradient constrains CRs' ability to directly drive cold gas.

Nevertheless, CRs are an interesting source of energy and momentum with a
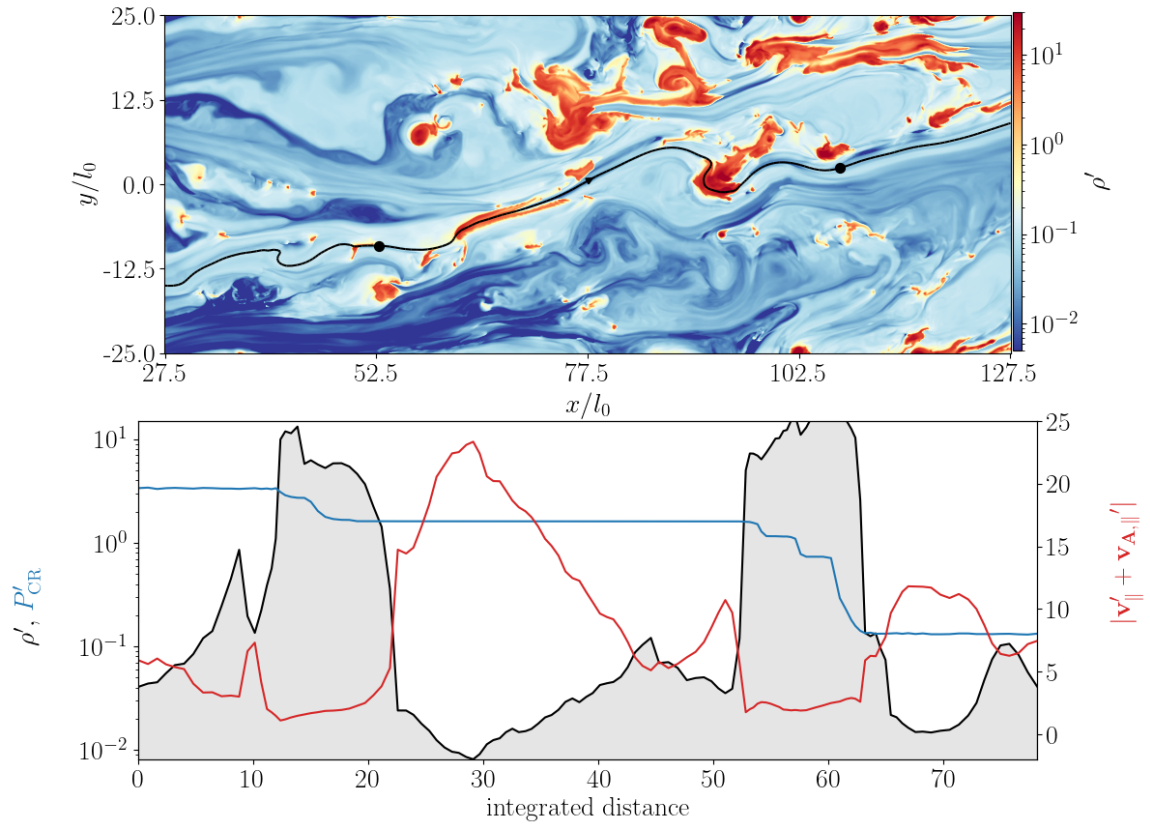
Figure 4.17: Upper panel: gas density from B05CR at $t' = 65$. The black solid line label a typical magnetic field line, the two black dots shows the start and end points of the segment we plot in the lower panel profiles. Lower panel: the gas density (black solid line and grey shades), CR pressure (the blue solid line), and total projected velocity.

turbulent magnetic field. As discussed in Section 4.4.5, B05CR produces the most CR heating among the three CR streaming simulations. The turbulent magnetic field helps CR heating by amplifying $v_{\mathrm{A,y}}$ and providing CR pressure gradient in both directions. The hotter gas plays an important role in accelerating the colder gas. From a momentum point of view, CRs streaming along a turbulent magnetic field increase the velocity dispersion in both $\sim 10^4$K and $\sim 10^6$K gas. In B2CR and B1CR, the velocity dispersion of $\sim 10^4$K gas σ_{v} peaks in the cloud merging stage and drops during the collective acceleration. However, σ_{v} constantly grows in B05CR. At $t' = 90$, $\sigma_{\mathrm{v}} \approx 80$km s^{-1} in B05CR, which is about a factor of two larger than B1CR and B2CR.

4.5.2 The generation and destruction of small clouds

In B2CR and B2CRdiff, the generation of small clouds is an important process for driving the cold gas loss seen in our simulations. In B2CR, part of the cloud detaches from the merged cloud structure and further break into smaller pieces. In B2CRdiff, the filaments break into multiple small clouds. In this section, we discuss their formation and potential impact on cold gas survival.

We find that the small clouds represent a non-negligible fraction of cold gas mass in B2CR and B2CRdiff. We track the evolution of small clouds in simulation and found almost all of them are mixed with hot background and destroyed within t'_{cc}, contributing to the observed cold gas loss. In order to quantify the cold gas fraction in the form of small clouds, we use the image segmentation algorithm Watershed from scikit-image (Van der Walt et al., 2014). A similar technique is adopted in studies with morphology-based image segmentation (Lin et al., 2016; Krieger et al., 2021). For example, Figure 4.18 shows the density snapshots at $t' = 115$ from B2CR and B2HW. The regions masked by blue are the selected small clouds.

We use the sub-domain of $245 < x' < 320$ for B2CR and $215 < x' < 295$ for B2HW to apply Watershed. First, we make a mask by selecting gas with $T_{\mathrm{gas}} \leq 7 \times 10^4$K. Then we obtain the Euclidean distance transform of the mask array (by using the distance_transform_edt function). Next, we find the local maximums of the distance array and use their coordinates as the seed for Watershed. The minimum separation of local maximum peaks is set to be 40 pixels, but we adjust it when calculating other density snapshots to obtain the optimal segmentation. Finally, we select out the segmented regions with total area less than $A'_{\mathrm{tot}} \leq A_{\mathrm{cut}}$. We tested

$A_{\text{cut}} = 7.5, 10, 11.25$ and found our results are not sensitive to this choice, adopting $A_{\text{cut}} = 10$ for the results shown here. Some regions within the big cloud are mis-selected due to over-segmentation, we tested different parameters in above selection pipeline, or manually excluded the mis-selected regions. At $t' = 115$ the cold gas mass in small clouds is about $\sim 22\%$ in B2CR, and only $\sim 3\%$ in B2HW. We also checked the snapshot at $t' = 85, 100$, the fractions are about $\sim 17\%$, $\sim 19\%$ in B2CR and $\sim 3\%$ in B2HW. An important consequence is that these small clouds are easier to destroy by mixing in later dynamical process, which is consistent with the evolution we observe in the simulations.

In contrast, the small clouds are a less important factor in B1HW, B1CR and B05CR (see e.g. Figure 4.3 and Figure 4.5). The fraction of cold gas in small clouds at $t' = 110$ is $\sim 5\%$ for B1CR and $\sim 5\%$ for B1HW. We also checked the cold gas fraction in small clouds at $t' = 77$ and $t' = 90$, and find it to be $\sim 5\%$ and $\sim 4\%$ in B1CR, $\sim 5\%$ and $\sim 5\%$ in B1HW respectively. Similar low fraction is found in B05CR at multiple time, $\sim 7\%$ for $t' = 65$ and $t' = 95$.

The small cloud generation is related to CR-gas interaction. In B2CR, small clouds are created when cold gas detaches from the merged clouds. We find that the differential acceleration by CR bottleneck is the primary reason. For example, Figure 4.11 shows that when magnetic field is relatively uniform and the Alfvén velocity almost solely depends on density, the bottleneck is strongest when CRs exit the cold clouds. At the incoming side, CRs decouple from gas and stream freely at the reduced light speed. At the exiting side, the gas density gradient is the same as the streaming direction, CRs re-couple with gas, stream at v_{A}, creating a CR pressure gradient. Hence, the far side usually experiences stronger acceleration.

Figure 4.19 compares the total acceleration from CR and thermal pressure on cold gas. As explained, B2CR has the strongest acceleration on the far side. This gas constantly experiences enhanced CR acceleration until the CRs decouple from gas. The irregular shape of the clouds also contributes to the non-uniform acceleration following detachment. After the fast-moving cloudlets leave the merged bulk, they fragment into smaller clouds. In contrast, B2HW has the strongest acceleration on the wind incoming side, the net effect is compression of the cloud, and the far side gas is free from excessive acceleration.

The effect also depends on magnetic field. In B2CR, the differential acceleration location is relatively fixed in the comoving frame, which is essential for stripping
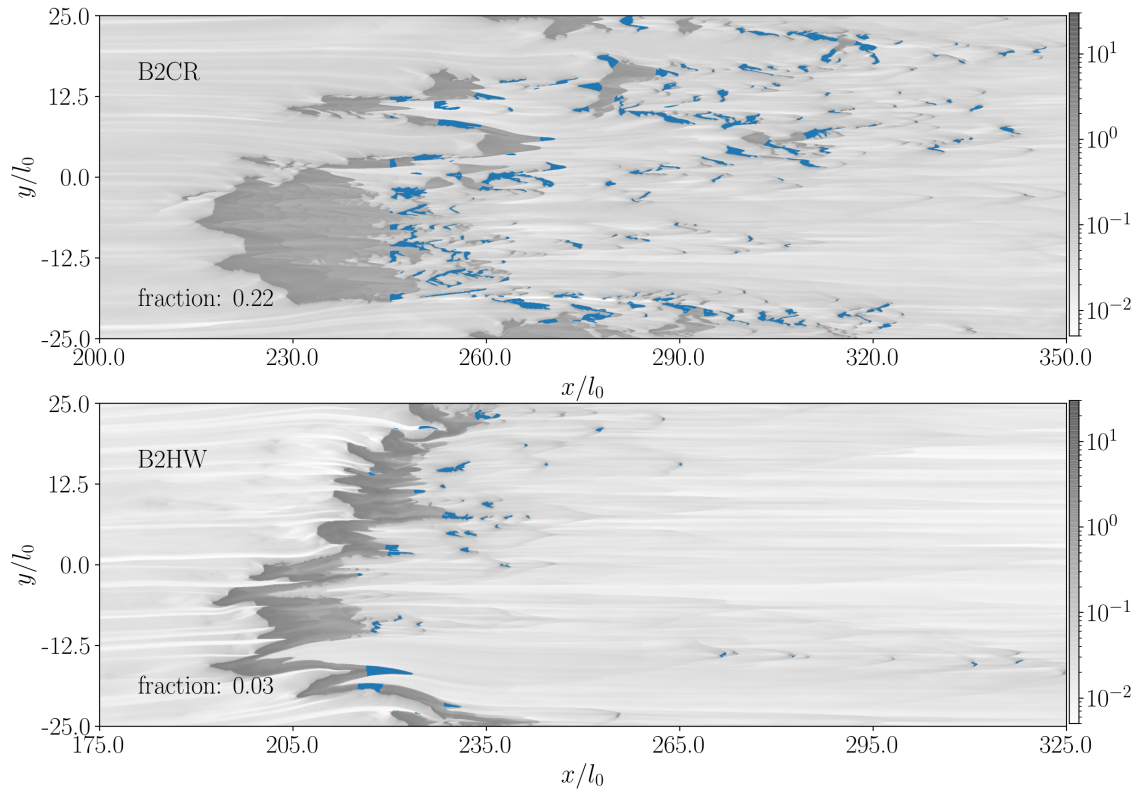
Figure 4.18: Small clouds (masked by blue) identified by Watershed in B2CR (upper panel) and B2HW (lower panel) at $t' = 115$. The fraction of cold gas mass in the small clouds are $\sim 21\%$ in B2CR and $\sim 5\%$ in B2HW.
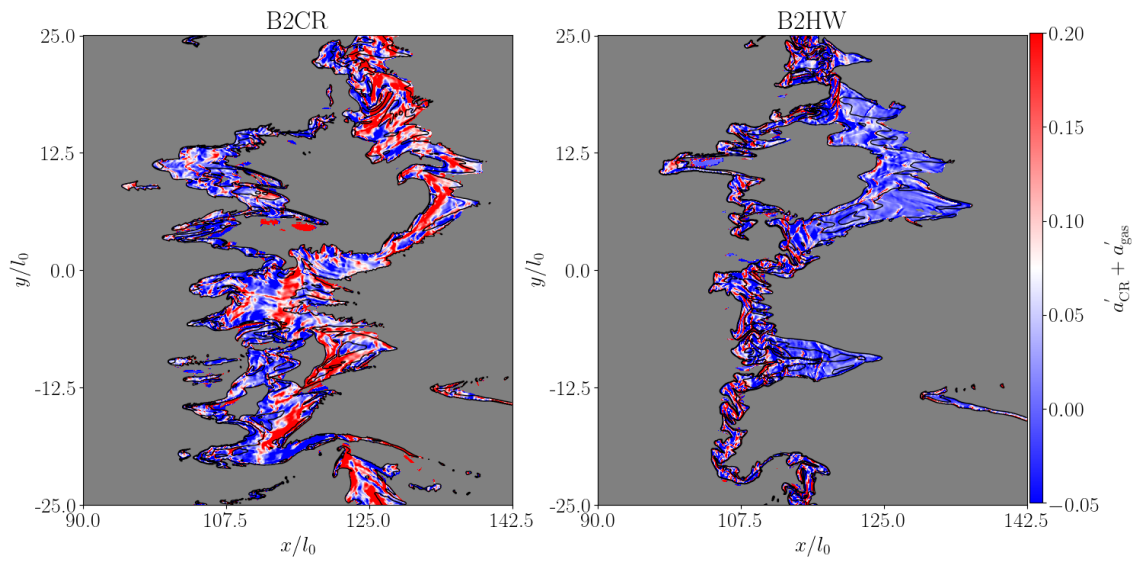
Figure 4.19: The sum of CR acceleration $a'_{\mathrm{CR}} = \sigma'_{c,xx}(F'_{\mathrm{CR}} - 4v'_x P'_{\mathrm{CR}})$ and thermal pressure acceleration $a'_{\mathrm{gas}} = -\partial P'_{\mathrm{CR}}/\partial x'$ in x-direction. Gas with temperature $T \geq 10^5 K$ is masked by grey, the black lines draw contour for $\rho' = 2.5$, 10. CRs or a hot wind comes in from the left side, so that B2CR (left) experiences stronger acceleration on the far side while B2HW (right) experiences stronger acceleration on the incoming side.

clouds from the bulk. However, in weaker magnetic field simulations, the field lines are not well-aligned along the x-direction, CRs stream in both the x- and y- directions. Generally, the cold gas motion is more turbulent, so the location of maximum CR pressure gradient changes in the comoving frame. The differential acceleration and following cloud fragmentation is less significant in B1CR, B1HW and B05CR.

When streaming is turned off and "bottleneck" disappears in B2CRdiff, the breaking filaments are the main source of small clouds. Due to their elongated morphology, filaments are fragile to even moderate non-uniform acceleration. Since these filaments are created by thermal instability, cold gas loss starts as soon as the diffusive CR flux intact with gas (Figure 4.4). This differs from B2CR, where the differential acceleration happens after the cloud merging, so the drop starts at later time. Nevertheless, as shown in Figure 4.15, B2CRdiff also has a significant fraction of cold gas in the form of small clouds despite the morphological difference, with $\sim 24\%, \sim 33\%, \sim 38\%$ at $t = 45,\ 60,\ 90$.

Since the rate of production of small clouds impacts the rate of cold gas destruction, it is important to note that some of the smallest clouds in B2CR are only resolved by a few cells, and therefore may be destroyed too quickly in the simulation. To assess this, we estimate their final fate based on theoretical considerations. Gronke & Oh (2018) and Gronke et al. (2021) propose that cold gas will survive in the acceleration if the cooling is fast compared to cloud crushing and following mixing. We follow their scheme to estimate the fraction of small clouds that are unlikely to survive in later acceleration (see also Section 4.4.4).

For each selected small cloud, Watershed also calculates the major axis length and eccentricity of the centroid ellipse with equivalent area. We retrieve the approximate diameter, average density and temperature of each selected small cloud to estimate the cooling timescales and destruction timescale. In B2HW, we compare $t'_{\mathrm{mix,cool}}$ with the cloud crushing time t'_{cc}. In B2CR, we compare $t'_{\mathrm{mix,cool}}$ with an analogy to a cloud crushing time t'_{cc}, where we replace v'_{hot} by the relative velocity of cloud and background hot gas. For multiple time snapshots, we estimate that roughly $\sim 40\%$ of the small clouds are inefficiently cooled and likely to be destroyed. This potentially leads to less cold gas loss than what is observed in B2CR if all small clouds are well resolved.

In summary, non-uniform acceleration shreds the merged cloud structure or break the filaments, redistributing cold gas into smaller clouds. The destruction of these

small clouds contributes to the cold gas loss in B2CR ad B2CRdiff. Although some small clouds are not well-resolved in our simulations, and the exact cold gas loss in this channel might depend on resolution, we estimate that a large fraction of the mass in these cold clouds will not survive.

4.5.3 Comparison to previous works

Radiative Mixing Layer: In Section 4.4.4, we show that the thin layer between cold and hot gas dominates the volumetric cooling, the intermediate temperature gas and their emission in this layer strongly impacts the evolution of cold gas. Tan et al. (2021) and Fielding et al. (2020) study the detailed structure of the interface between cold and hot gas. Assuming gas enters the mixing layer and can be quickly cooled, the in-flowing velocity to the mixing layer is then a key quantity to decide the cold gas growth rate. These works derive scaling relations for the mass flux into the turbulent radiative mixing layer, providing a useful quantification of the emission and cold gas growth rate in multi-phase gas. Analogous to thermal combustion, Tan et al. (2021) propose that the mixing layer can be characterized by the ratio of cooling timescale and mixing timescale. When cooling is fast compared to mixing, the interface gas will be fragmented and forms a multi-phase structure.

We observe a similar cooling-efficient, multi-phase region at the cloud interface in our simulations. Consistent with their study, the local velocity dispersion maximum is co-spatial with the strongest emission per volume, and the Damköhler number generally divides the single-phase and multi-phase regions. Nevertheless, when we estimate the velocity of mass flux into the turbulent mixing layer for the two sets of CR and thermal wind simulations (B1CR-B1HW and B2CR-B2HW), we do not obtain a mass flux difference that can explain the diverging cold gas evolution seen in the CR and hot wind simulations. We attribute this to differences in our set-up and the impact of CRs. Firstly, the cold and hot gas in our simulations do not always experience laminar shearing due to CR streaming along the perturbed magnetic field. Secondly, the CR heating can be an important external energy source. Although CR heating is relatively small compared to net cooling in mixing gas, it can be important in hot gas. The CR heating in cold gas is also strong but quickly radiated away. These effects change the gas properties and emission in the hot and cold gas that supplies mixing. Finally, the gas pressure in cold and hot gas is not always in balance due to CR and magnetic pressure. These various non-thermal factors complicate

quantitative estimation. Dynamically, given the small clouds generated by differential CR acceleration, accounting for the cold gas loss in small clouds is necessary in our set-up.

Fielding et al. (2020) show that the surface area of the mixing layer gas is another important factor impacting cold gas evolution. The efficient mixing creates corrugated, fractal interface between cold and hot gas, which generally increases surface area and promotes cooling. Although the process might not be resolved in our cloud scale simulations, understanding how the scaling relations changes with the presences of CR is an interesting topic for future work.

Previous studies also suggest the importance of resolution of the Field length to reach convergence (Gressel, 2009; Sharma et al., 2010a). Although we did not carry out resolution study, with our choice of parameters, the initial Field length is resolved by ~ 70 cells in the x-direction and ~ 20 cells in the y-direction. Interestingly, Tan et al. (2021) suggest that even if the Field length is under-resolved, the total emission from mixing tends to converge if thermal conduction is present. In leiu of a resolution study, we also ran zoom-in, cloud-crushing simulations of selected irregular clouds formed in thermal instability with three times higher resolution on each side. The overall dynamics is similar to the simulations reported in the paper, no significant additional small-scale instability is observed.

Cloud Survival: In our simulations, thermal instability creates multiple irregular $\sim 10^4$K clouds, which are accelerated by CRs or a hot wind in a "wind-tunnel"-like set up. Despite the different cloud morphology and non-idealized background, the CR-cloud interaction and cloud survival are qualitatively consistent with idealized single cloud CR-cloud-crushing simulations. Wiener et al. (2019) first studied the dynamics of a spherical $\sim 10^4$K cloud that irradiated by transient incoming CR energy flux in hot $\sim 10^6$K background gas. Despite the different numerical treatments for CR streaming, we find similar elongated cloud morphology due to CR pressure support. When the incoming CR energy flux and magnetic field is relatively strong, the CR "bottleneck" is the main momentum source driving the cloud.

However, with the same cooling function and a lower constant heating rate, Wiener et al. (2019) shows that the radiative cooling is able to seed cold gas growth, while our simulations show cold gas loss with comparable resolution. One difference is that the dynamics in their simulation are nearly one-dimensional and less turbulent. Even with the strongest CR source that can deform magnetic field, their cloud is primarily

accelerated in the x-direction in roughly laminar flow. In our set-up, the magnetic field is entangled by thermal instability, and the clouds are accelerated in both x- and y-directions. By the time we stop the simulation, the velocity dispersion of cold gas in CR driven cold gas generally reaches $\sim 50 - 80 \mathrm{km\ s^{-1}}$ due to the turbulent motion.

In contrast, Brüggen & Scannapieco (2020) suggest that radiative cooling has limited effect on cloud dynamics and mass evolution. They studied the dynamics of an initially cold cloud irradiated by a constant CR source. The difference in set-up includes that they decouples CR momentum with high temperature background gas. They also do not include CR heating, so CRs cannot directly heat the gas. In our simulation, CR heating contributes a total energy to the multi-phase gas that comparable to the net cooling, and shapes subsequent dynamics. For example, in B05CR, CR heating increases the hot gas thermal pressure and provides initial acceleration to the cold gas. Brüggen & Scannapieco (2020) also explores a wide range of $P_{\mathrm{CR}}/P_{\mathrm{gas}}$, magnetic field and density contrast, overlapping with our simulation parameters. For example, the elongated and fragmented cloud morphology seen in their $\beta = 10, 3$ runs with density contrast of $300, 100$ seems similar to some stretched, fragmented clouds in B1CR and B05CR with comparable local density contrast and β. With the perturbed magnetic field and irregular cloud shape, however, we did not observe a significant "two-tail structure" near the cloud boundary. Their work also indicates that the cloud acceleration is relatively insensitive to magnetic field strength, in agreement with our results.

Bustard & Zweibel (2021) investigate the cloud-CR interaction with plasma based streaming transport. However, their work shows that magnetic field strength changes cloud acceleration given the transient CR flux from the boundary, especially in fully ionized clouds. As in our set-up, CRs stream along the field lines, so the topology of magnetic field affects the CR pressure distribution. In fully-ionized clouds, intermediate magnetic field allows the field lines to wrap around the cloud, preventing CRs from quickly entering the cloud and eliminating the pressure gradient, which is more favorable for strong acceleration. Interestingly, in our simulations, thermal instability forces the field lines to thread through the cloud instead of wrapping around it, which might reduce the CR pressure gradient compared to isolated clouds in initially plane-parallel magnetic field. They also find that the ionization fraction shapes the "stairs" of CR pressure gradient at the cloud interface. Relaxing our assumption of

fully ionized streaming in multi-phase gas formed from thermal instability would be an interesting topic for future work.

Bustard & Zweibel (2021) also compares the effect of dimensionality and found two-dimensional and three-dimensional results differs from one-dimensional results. Gronke & Oh (2020) studied clouds accelerated by thermal wind and suggest that when radiative cooling is included, the cold gas can increase in three-dimensional cloud but decrease in comparable two-dimensional cloud. Investigating our set-up in three dimensions will be a useful goal for future work.

4.6 CONCLUSION

We studied multi-phase outflows formed from thermal instability, comparing CR driven outflow to outflow driven by a hot wind with an equivalent momentum flux (pressure). We mainly focus on the streaming limit and vary the initial magnetic field (with $\beta_{\mathrm{init}} = 0.5, 2, 8$) to study the CR-gas interaction, cold gas survival, and acceleration. We summarize our conclusions as follows:

(1) Density contrast: Unlike a hot wind that compresses the cold gas during acceleration, streaming allows CRs to penetrate into the cold gas, so that CR pressure provides non-thermal support, yielding lower density for cold gas in the multi-phase outflow. In our simulations, the density contrast between $\sim 10^4$K and $\sim 10^6$K gas (Figure 4.6) in CR driven outflow is $\rho_{\mathrm{c}}/\rho_{\mathrm{h}} \sim 100$, which is lower than the gas density contrast in hot wind driven outflow (Section 4.4.3).

(2) Cold gas evolution: In our simulations, CR driven outflow shows cold gas loss, while their hot wind counterpart shows cold gas growth. We note that the dropping cold gas, however, does not indicate inefficient cooling. The simulation runs $\sim 20 - 30 t_{\mathrm{cc}}$ (Section 4.4.2, 4.4.4), and the cold gas drop is $\lesssim 20\%$ for streaming runs, suggesting that cooling prevent the quick disruption of cold gas. CR streaming does not lead to strong shear between the cold and hot gas in bulk acceleration, so that the different phases are moving with only moderate relative velocity. The cold gas evolution is impacted by both the supply of cold gas from cooling and the dynamical processes destroying cold gas. The origin of cold gas loss varies with magnetic field strength and CR transport mechanism.

When magnetic pressure is sub-dominate ($\beta_{\mathrm{init}} = 2, 8$), the intermediate temperature gas in the mixing layer is primarily supported by CR (gas) pressure when accelerated by CR streaming (hot wind). CR pressure provides non-thermal support

and yields less compression, so the intermediate temperature gas density is lower. Since cooling is proportional to n_{H}^2, it is reduced compared to the hot wind accelerated outflow where the intermediate temperature gas is more compressed.

When the magnetic field is strong ($\beta_{\mathrm{init}} = 0.5$), intermediate temperature gas is supported by magnetic pressure, which is similar for both CR and hot wind acceleration. So intermediate temperature gas density and cooling is similar. But the strong magnetic field constrains the flow motion to be less turbulent. CR streaming forms a "bottleneck" that preferentially accelerates the side of the cloud opposite to the CR source. This leads to the differential acceleration on this side of the cloud, so the fast-moving gas detach from the bulk and form small clouds (Section 4.5.2). We estimate that $\sim 25\%$ of cold gas mass is in the form of small clouds and nearly half of them are unlikely to survive during acceleration, which largely contribute to the dropping cold gas mass in CR acceleration.

In the slow diffusion limit, CRs compress both hot and cold gas, resulting in overall higher gas densities with $\rho_{\mathrm{c}}/\rho_{\mathrm{h}} \sim 70$, and consequently more cooling. Changing CR transfer from streaming to diffusion alters the evolution of thermal instability, resulting in significant filaments along the magnetic field. The filaments are fragile to even moderate differential acceleration and tend to break into small clouds (Figure 4.16). We estimate $\sim 20 - 40\%$ of cold gas mass is in the form of small clouds, leading to the largest cold gas loss ($\sim 30\%$ by $t' = 70$) among CR runs.

(3) CR streaming in non-uniform magnetic field: B05CR provides an interesting case study of CR streaming in a turbulent magnetic field. First, the initially weak and uniform magnetic field is modified by thermal instability and CR streaming. The field lines thread through the cold gas, and β in the $\sim 10^4$K gas can be an order of magnitude larger than the initial value (Section 4.5.1).

CRs stream along the perturbed field lines in both the x- and y-direction, leading to significant CR pressure gradients in both directions. Due to the enhanced magnetic field and CR pressure gradient in the y-direction, CR heating in $\sim 10^6$K gas becomes significant. The thermal pressure of hot gas largely contributes to cold gas acceleration in x-direction. We estimate that the fractional contribution from heated background gas pressure is about 5 times that of CR pressure (Section 4.4.5). We find that even in the turbulent, non-uniform magnetic field, CR streaming forms "bottlenecks" along the magnetic field line (Figure 4.17). Consequently, turbulent magnetic field is not efficient in transporting CRs via streaming along a preferred direction, resulting in

relatively small CR acceleration in the x-direction. At the same time, streaming along entangled field lines leads to high velocity dispersion in cold gas ($\sim 60 \mathrm{km\ s^{-1}}$).

(4) CR acceleration: In all simulations, we inject a CR flux of $F_{\mathrm{CR}} \approx 2.5 \times 10^5 L_\odot \mathrm{kpc^{-2}}$ in the x-direction. When streaming is enabled, the CR acceleration is relatively linear (Figure 4.4), as expected from Equation (4.3). Stronger magnetic field can slightly increase the acceleration by constraining the flow motion to be more laminar. By the time we stop the simulation ($\sim 100 \mathrm{Myr}$), the cold gas ($T \sim 10^4 \mathrm{K}$) reaches a mass-weighted average x-direction velocity of $v_{\mathrm{cold,x}} \approx 210,\ 230,\ 130 \mathrm{km\ s^{-1}}$ in B1CR, B2CR and B05CR. The velocity dispersion of cold gas is $\sigma_{\mathrm{cold}} \approx 35,\ 45,\ 60 \mathrm{km\ s^{-1}}$ in B1CR, B2CR and B05CR. The average cold gas velocity is similar in their hot wind counterparts. The hot gas $T \sim 10^6 \mathrm{K}$ is also *accelerated* to nearly comoving with cold gas, with slightly lower average velocity $v_{\mathrm{hot,x}} \approx 170,\ 180 \mathrm{km\ s^{-1}}$ in B1CR, B2CR. For B05CR, the turbulent motion accelerates hot gas to $v_{\mathrm{hot,x}} \approx 230 \mathrm{km\ s^{-1}}$, which is about twice as fast as the average cold gas velocity.

CHAPTER 5

EMISSION FROM STREAM-STREAM COLLISION IN TIDAL DISRUPTION EVENTS

5.1 INTRODUCTION

The tidal disruption of a star by a black hole can power a bright transient flare in multiple wavebands (Rees, 1988; Phinney, 1989; Evans & Kochanek, 1989; Ulmer, 1999). These tidal disruption events (TDEs) happen when the pericenter of star's orbit is within the tidal radius $R_{\mathrm{T}} = R_*(M_{\mathrm{BH}}/M_*)^{1/3}$, where M_* and R_* are the mass and radius of the star, and M_{BH} is the mass of the black hole. After disruption, roughly half of the material escapes the black hole's gravity, while other gravitationally bound gas returns to the pericenter in a highly eccentric orbit.

The fallback and circularization of the debris can produce prominent emission, resulting in luminous transient events peaked in optical-ultraviolet (UV) or X-ray. The decay timescale of TDE candidates often approximately follows the $t^{-5/3}$ scaling, which is a theoretical prediction for the mass fallback rate of the debris (Rees, 1988; Phinney, 1989). TDEs are important probes for studying the black hole properties such as mass (Ramirez-Ruiz & Rosswog, 2009; Stone & Metzger, 2016; Wevers et al., 2017; Mockler et al., 2019) and spin (Kesden, 2012; Gafton & Rosswog, 2019). The chemical composition and light curve also constrain the structure and evolution stage

---

This chapter is adapted from an article submitted in the Astrophysical Journal. The original title is as follow: X. Huang, S. W. Davis., Y. Jiang, "A Bright First Day for Tidal Disruption Event"

of the disrupted star (Lodato et al., 2009; MacLeod et al., 2012; Kochanek, 2016; Ryu et al., 2020; Law-Smith et al., 2020).

TDEs were first detected as strong X-ray flares from quiescent galaxies (Grupe et al., 1999; Greiner et al., 2000) by *ROSAT*. More X-ray events have subsequently been captured by or identified in *XXM-Newton*, *Chandra* and *Swift* (Lin et al., 2011; Saxton et al., 2012; Komossa, 2015; Gehrels & Cannizzo, 2015; Lin et al., 2018a; Wevers et al., 2019). Complimenting X-ray observations, the optical/UV is another important channel to detect TDEs. In the recent decade, optical transient surveys have played an increasing role in identifying TDEs, including for example the Sloan Digital Sky Survey (SDSS), Pan-STARRS and ASAS-SN surveys(Van Velzen et al., 2011; Hung et al., 2017; Kochanek et al., 2017; Gezari, 2021; Van Velzen et al., 2021; Goldtooth et al., 2023). This sample is expected to greatly increase with the upcoming Large Synoptic Survey Telescope (LSST) of the Vera Rubin Observatory (Bricman & Gomboc, 2020; Gezari, 2021; Hambleton et al., 2022) and Ultraviolet Transient Astronomy Satellite (ULTRASAT) (Ben-Ami et al., 2022).

Interestingly, the optical/UV and the X-ray identified candidates may represent different populations of emission sources. First, optical/UV bright TDEs rarely show X-ray emission. Second, the continuum temperature derived in optical/UV TDEs is usually an order of magnitude lower than the X-ray TDEs. The inferred blackbody temperature of X-ray TDEs is roughly consistent with emission from a hot accretion disk formed from the captured debris. This suggests that the optical candidates, with much lower temperature, may originate from other emission mechanisms.

One theoretical resolution of this dichotomy involves reprocessing of X-ray emission by a quasi-spherical, optically thick layer around the accretion disk (Loeb & Ulmer, 1997; Strubbe & Quataert, 2009; Metzger & Stone, 2016; Roth et al., 2016), or a quasi-spherical, radiation supported disk such as the "Zero-Bernoulli accretion flows", or "ZEBRAs" model (Coughlin & Begelman, 2014; Eyles-Ferris et al., 2022)). In parallel, the reprocessing of disk emission could be due to an optically thick wind from the disk (Lodato & Rossi, 2011; Miller, 2015; Metzger & Stone, 2016; Kara et al., 2018). Dai et al. (2018) proposed a unified model for a typical TDE system, including the highly asymmetric geometry of radiation supported thick disk, optically thick wind and hot corona or jet. This model suggests that the emission from such systems will naturally cover both the optical-UV and soft X-ray bandwidth, with viewing angle effects dominating the appearance in different wavebands (also see Thomsen et al.

(2022)).

The models explaining optical emission from TDEs generally involve gas circularization and radiation generation by viscous processes, which will likely to happen near or after the peak optical light curve. But observations indicate that the inferred photosphere of some TDEs experience quick expansion during the pre-peak time, where the size can increase for one to two orders of magnitudes within days to weeks (Mockler et al., 2019; Van Velzen et al., 2021). It is likely that additional emission or reprocessing mechanism is needed to explain the pre-peak light curve for optical TDEs.

A potentially important pre-peak emission mechanism is the stream-stream collision, which happens when the apsidal precession shifts the stream orbit and leads to stream self-intersection (Shiokawa et al., 2015; Piran et al., 2015; Dai et al., 2015; Dittmann, 2022). When the fallback stream and the returning stream collide, some of the streams kinetic energy will be dissipated. The intersection region can become radiation pressure dominated, if the post-shock gas is sufficiently optically thick (Kim et al., 1999; Jiang et al., 2016). Consequently, the stream-stream collision can affect the pre-peak emission through different channels. First, it might directly contribute to optical emission by converting kinetic energy to radiation. Alternatively, it might create a radiation-pressure driven outflow, which reprocesses the emission from the hot, shocked gas into optical emission (Jiang et al., 2016; Bonnerot & Stone, 2021).

Recent global simulations that track the post-shock gas circularization seem to indicate that the stream-stream collision can efficiently redistribute debris angular momentum (Bonnerot & Stone, 2021; Curd, 2021; Steinberg & Stone, 2022; Andalman et al., 2022). In fact, recent work has suggested the fallback debris may be slow to circularize and form an accretion disk, implying that the majority of emission could be powered by various shocks including those from stream self interaction. The exact outcome of collision such as relative importance of luminosity and kinetic energy is sensitive to TDE system physical parameters as well as numerical treatment. Jiang et al. (2016) and Lu & Bonnerot (2020) performed local simulations of stream-stream collision. They show that the post-shock gas is likely to form optically-thick outflow, and the stream-stream collision itself is also an important pre-peak emission source. In this paper, we adopt similar approach and study the stream-stream collision in a localized calculation domain. The domain is optimized for resolving the streams and radiation mediated collision, while radially extended to track the post-shock

gas evolution. We focus on the radiation's role in redistributing gas momentum and energy, determining the pre-peak emission, and affecting the downstream gas evolution.

We introduce our numerical set-up in Section 5.2. In Section 4.4, we describe a case study of Eddington mass fallback rate. We also compare the effect of different mass fallback rates of the streams, the collision angle between the streams, and the collision radius relative to the black hole. Table 5.1 lists the key orbital parameters. In Section 4.5, we discuss the implied prompt emission luminosity, the estimated photosphere evolution and compare our results with previous studies. We elaborate the details of gravity implementation in Appendix B, and show convergence study in Appendix C.

5.2 Simulation Set-up

5.2.1 Equations and Units

We solve the following equations in Athena++ with the explicit radiation transfer module (Jiang, 2021).

We use OPAL opacity (Iglesias & Rogers, 1996) for the $\kappa_{\delta P}$ and κ_a based on the local gas density and temperature, and assume $\kappa_s = 0.34$ cm^2 g^{-1}. Figure 5.1 shows example opacity as functions of temperature for a range of gas densities. In the code, we solve the unit-less equations with the scaling of density $\rho_0 = 10^{-10}$g cm^{-3}, velocity $v_0 = 0.01c$ and length $l_0 = r_s = 2.95 \times 10^{12}$cm. In the rest of paper, we report unit-less quantities unless explicitly specified.

5.2.2 Calculation Domain and Resolution

We preform the local simulations in spherical-polar coordinates, but with the origin displaced relative to the black hole. We adopt a simulation domain that centers the collision point in the ϕ direction, and varies with different stream orbits. As an example, Figure 5.2 shows the domain we adopt for A122 runs (A122Edd1, A122Edd01, A122Edd001 and A122Edd10). As we will elaborate in Section 5.3.1, resolving the streams and the collision region is the primary motivation for us to adopt such a local simulation domain. In the rest of the section, we note the variables in the coordinate with the black hole at the origin with subscript 1. We first integrate $\ddot{r}_1$, $\ddot{\theta}_1$ and $\ddot{\phi}_1$ from Tejeda & Rosswog (2013) in the $\theta = \pi/2$-plane to obtain the ballistic trajectory
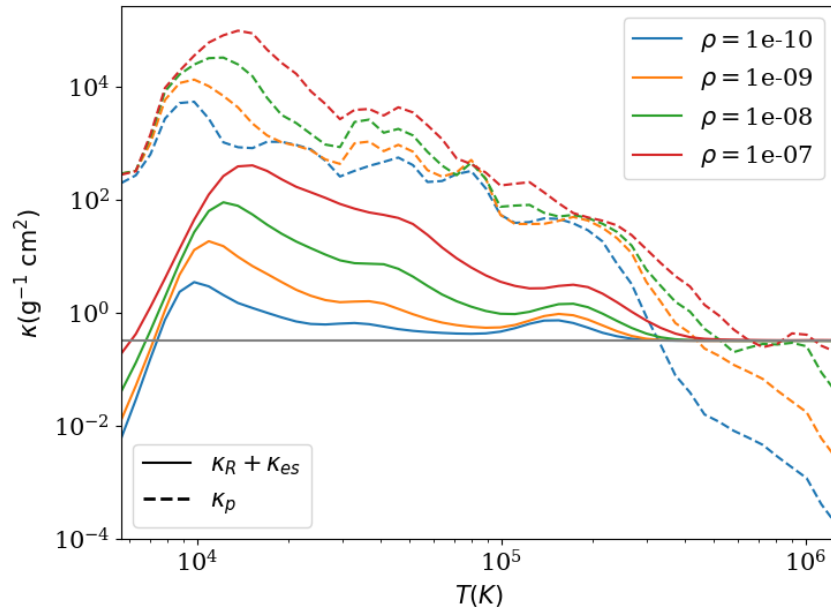
Figure 5.1: Examples of adopted OPAL opacity including the Planck mean opacity (dashed lines) and combined electron scattering and Rosseland mean opacity (solid lines), corresponding to densities from $\rho = 10^{-10}, 10^{-9}, 10^{-8}, 10^{-7}$ g cm^{-3} (blue, orange, green and red lines).

with stream-stream collision radius $r_{\mathrm{coll},1}$ and collision angle $\phi_{\mathrm{coll},1}$ with respect to the black hole. We set the black hole and star mass to $M_{\mathrm{BH}} = 10^7 M_\odot$ and $M_* = M_\odot$ respectively, and the stellar radius is $R_* = R_\odot$. We assume the orbit eccentricity e_{orb} estimated as Dai et al. (2015)

$$e_{\mathrm{orb}} \approx 1 - 0.02 \left(\frac{M_*}{M_\odot} \right)^{1/3} \left(\frac{M_{\mathrm{BH}}}{10^6 M_\odot} \right)^{-1/3} \beta^{-1}, \tag{5.1}$$

where $\beta = r_{\mathrm{T}}/r_{\mathrm{p}}$ is the orbit penetration factor. $r_{\mathrm{T}} = R_*(M_{\mathrm{BH}}/M_*)^{1/3}$ is the tidal radius, and r_{p} is the pericenter radius. So by choosing β, we obtain the initial condition for a Newtonian elliptical orbit as an approximation to the orbit of most bound material. The initial position and velocity are $(r_{\mathrm{SMA}}, \ \pi/2.0, \ 0.0)$ and $(0.0, \ 0.0, \ v_{\phi,\mathrm{SMA}})$ in r, θ, ϕ direction, here $r_{\mathrm{SMA}} = r_{\mathrm{p}}/(1 - e_{\mathrm{orb}})$ is the approximated semi-major axis, $v_{\phi,\mathrm{SMA}} = \sqrt{(GM_{\mathrm{BH}}/r_{\mathrm{SMA}})(1 - e_{\mathrm{orb}})/(1 + e_{\mathrm{orb}})}$ is the approximated initial ϕ direction velocity. The solid orange line in Figure 5.2 shows part of the orbit with $\beta = 1.0$, $r_{\mathrm{SMA}} \approx 1088 r_{\mathrm{s}}$, $v_{\phi,\mathrm{SMA}} \approx 0.002c$. With this orbit, the streams collide at $r_{\mathrm{coll},1} = 22.5 r_{\mathrm{s}}$ relative to the black hole with the colliding angle $\theta_{\mathrm{coll},1} = 122°$.

The domain is extended in r direction, to align with the net momentum direction of the collision. Instead of placing the black hole at the origin, we translate the black hole by L_{12}, so it is at $(-L_{12}, \ \pi/2, \ \pi)$. For A122 runs, $L_{12} = r_{\mathrm{coll},1}/\cos\phi_{\mathrm{coll},1} = 39.15 r_{\mathrm{s}}$. For A90Edd1 and A122R95Edd1, we chose $L_{12} = 69.48 r_{\mathrm{s}}$ and $L_{12} = 118.25 r_{\mathrm{s}}$. In the r direction, we use logarithmic grid spacing. For A122 runs, the domain is $(27 r_{\mathrm{s}}, 140 r_{\mathrm{s}}) \times (0.42\pi, 0.58\pi) \times (0.81\pi, 0.96\pi)$ in r, θ, ϕ direction, which is shown in Figure 5.2 by the black frame as the projection on $\theta = \pi/2$-plane. For A90Edd1, the domain is $(40 r_{\mathrm{s}}, 207 r_{\mathrm{s}}) \times (0.42\pi, 0.58\pi) \times (0.81\pi, 0.97\pi)$. For A122R95Edd1, the domain is $(44 r_{\mathrm{s}}, 228 r_{\mathrm{s}}) \times (0.42\pi, 0.58\pi) \times (0.64\pi, 0.79\pi)$.

We use static mesh refinement (SMR) in Athena++ to resolve the streams and the shock. The root level is resolved by $[64 \times 32 \times 64]$ cells in r, θ, ϕ direction directions. The blue and red regions in Figure 5.2 show the refined regions in A122Edd1, A122Edd01, A122Edd001 and A122Edd10. The blue region is at five levels of refinement and spans $(27 r_{\mathrm{s}}, 40 r_{\mathrm{s}}) \times (0.48\pi, 0.52\pi) \times (0.81\pi, 0.96\pi)$, it covers most of the stream trajectory before the stream-stream collision, giving the resolution $\delta R \approx R\delta\theta \approx 0.02 \approx 0.85 R_\odot$ in r and θ directions. The red region is at six levels of refinement and is $(31 r_{\mathrm{s}}, 34 r_{\mathrm{s}}) \times (0.49\pi, 0.51\pi) \times (0.82\pi, 0.97\pi)$. For A90Edd1, the level
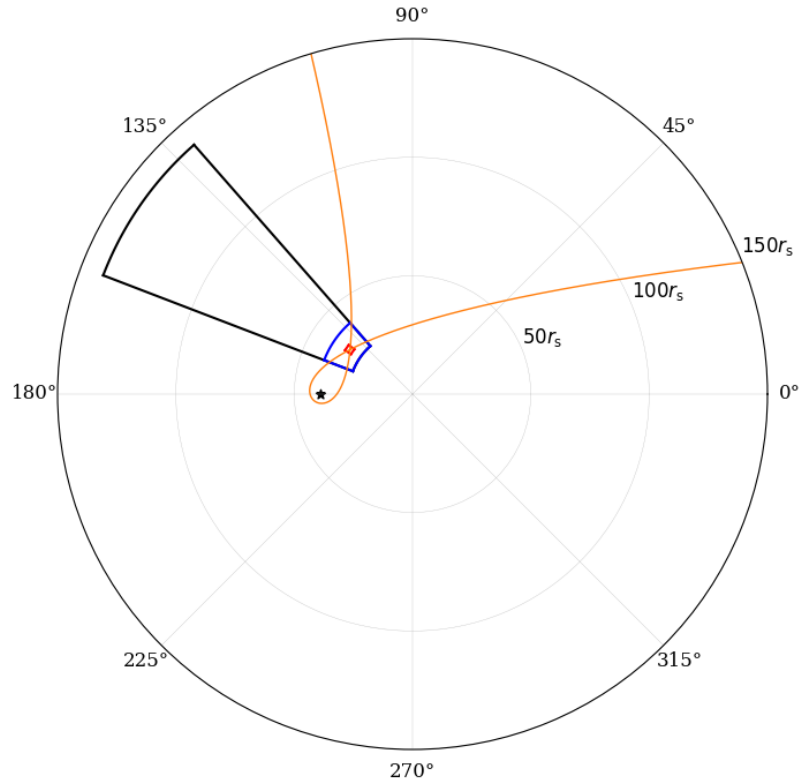
Figure 5.2: Schematic plot of calculation domain for a ballistic orbit (solid orange line) with $M_{\mathrm{BH}} = 10^7 M_\odot$, $M_* = M_\odot$, $R_* = R_\odot$, $\beta = 1.0$. The black solid frame shows the calculation domain we adopt in A122Edd1, A122Edd01, A122Edd001 and A122Edd10. The blue solid frames shows the static mesh refinement(SMR) region with level=5. The red solid frame shows the SMR region with level=6 near the shock. The black star symbol shows the position of the black hole $(-L_{12}, \pi/2, \pi)$.

five refinement region is $(44r_\mathrm{s}, 60.5r_\mathrm{s}) \times (0.42\pi, 0.58\pi) \times (0.81\pi, 0.97\pi)$, and level six refinement region is $(56.5r_\mathrm{s}, 59.5r_\mathrm{s}) \times (0.42\pi, 0.58\pi) \times (0.88\pi, 0.91\pi)$. For A122R95Edd1, the level five refinement region is $(45.0r_\mathrm{s}, 58.0r_\mathrm{s}) \times (0.42\pi, 0.58\pi) \times (0.64\pi, 0.79\pi)$, and level six refinement region is $(49.5r_\mathrm{s}, 54.0r_\mathrm{s}) \times (0.42\pi, 0.58\pi) \times (0.70\pi, 0.73\pi)$.

At the collision radius $r_\mathrm{coll,1}$, assuming the stream scale height H is determined by the vertical balance between tidal force and gas pressure gradient (Guillochon et al., 2014; Jiang et al., 2016), we estimate that $H \approx 2r_\mathrm{coll,1}\sqrt{(r_\mathrm{coll,1}/r_\mathrm{s})(k_\mathrm{B}T_\mathrm{str}/\mu c^2)}$. With a $M_\mathrm{BH} = 10^7 M_\odot$ black hole and $r_\mathrm{coll,1} \approx 20r_\mathrm{s}$ orbit, $H \approx 3R_\odot \sqrt{T_\mathrm{str}/10^6 K}$. With five levels of SMR, we can resolve the H by roughly four cells, assuming stream temperature $T_\mathrm{str} = 10^6$K before collision. Similar to Jiang et al. (2016), we assume higher T_str to calculate the scale height, but set the gas temperature in the stream to be $T_\mathrm{str} \approx 4 \times 10^5$K. Before collision, the kinetic energy density in the streams is about six orders of magnitude higher than internal energy density or radiation energy density. After the collision, the post-shock gas temperature is mostly in equilibrium with effective radiation temperature. As we will discuss in Section 4.4, the post-shock gas radiation energy density is primarily determined by the energy conversion from kinetic energy. Therefore, the internal energy in the stream prior to collision has limited effect on post-shock gas temperature.

5.2.3 Initial and Boundary Condition

Before injecting stream, we set the initial background density and pressure to be low values of $\rho_\mathrm{init} = 2.7 \times 10^{-5}$ and $P_\mathrm{init} = 2.65 \times 10^{-9}$. We set density and pressure floor for the hydrodynamic Riemann solver to be $\rho_\mathrm{floor} = 2 \times 10^{-5}$ and $P_\mathrm{floor} = 2 \times 10^{-9}$.

We model the stream-stream collision as a fallback stream and a returning stream injected from both ϕ boundaries in the $\theta = \pi/2$ plane, similar to Jiang et al. (2016). For each stream, we inject them at the radius of r_inj and $\theta_\mathrm{inj} = \pi/2$ by marking the four nearest ghost cells in r and θ direction as stream injection cells, and set uniform gas density ρ_inj, velocity $\mathbf{v}_\mathrm{inj}$ and pressure in these cells. We do not explicitly set the radiation intensity in ghost cells, once the gas streams enter calculation domain, they rapidly adjust to thermal equilibrium in just a few zones. The other cells at the ϕ direction boundaries are set to be single direction outflow for hydrodynamical variables, which copies all the values from the first active cells but set any velocity that enters the calculation domain to zero. The r and θ direction hydro boundaries are also single direction outflow. The radiation boundaries in the r, θ and ϕ direction

are "vacuum" radiation boundaries, which copies all the intensities with $\mathbf{n}$ pointing outward, but sets all intensities with $\mathbf{n}$ pointing inward to be zero.

For the stream injection cells at the ϕ direction boundaries, we set local velocity to be $\mathbf{v}_{\mathrm{inj}} = (v_{\mathrm{r,inj}}, \ 0, \ v_{\phi,\mathrm{inj}})$. The density in the stream injection ghost cells is set by $\rho_{\mathrm{inj}} = f_{\mathrm{Edd}} \dot{M}_{\mathrm{Edd}}/(v_{\phi,\mathrm{inj}} A_{\phi,\mathrm{inj}})$, where $\dot{M}_{\mathrm{Edd}} = 40\pi G M_{\mathrm{BH}}/(C\kappa_s)$ is the Eddington accretion rate, f_{Edd} is the Eddington ratio, and $A_{\phi,\mathrm{inj}} \approx H^2$ is the total injection area normal to ϕ direction. In simulations, $A_{\phi,\mathrm{inj}}$ varies as we change r_{inj} and ϕ_{inj}, so we use the numerically computed cell areas for better precision.

Note that in our set-up, we assume the fallback stream and the returning stream have the same entropy and ignore the potential stream width change due to the dissipation near the pericenter. We discuss the potential effects in Section 5.4.3, but leave the study of how nozzle shock dissipation, radiative cooling and numerical diffusion affect stream width after pericenter to future work.

To obtain r_{inj} and $\mathbf{v}_{\mathrm{inj}}$, we first integrate Equation B.5 to get the ballistic trajectory and velocity of an assumed point mass, then translate them by L_{12}. For A122Edd1, A122Edd01, A122Edd001 and A122Edd10, $r_{\mathrm{inj}} = 29.4r_s$, $29.7r_s$, $\mathbf{v}_{\mathrm{inj}} = (0.0534c, \ 0, \ 0.167c)$, $(0.0343c, \ 0, \ 0.235c)$ at the inner and outer ϕ direction boundary. For A122Edd1, $\rho_{\mathrm{inj}} = 7.076 \times 10^{-8}$g cm^{-3}, 4.974×10^{-8}g cm^{-3} at the inner and outer ϕ direction boundary to match $\dot{M}_{\mathrm{Edd}}$. The ρ_{inj} of A122Edd01, A122Edd001 and A122Edd10 are $1\%, 10\%, 1000\%$ of A122Edd1.

For A90Edd1, we keep the fallback stream the same as A122Edd1, but manually change the returning stream velocity so that it collides with the fallback stream at $r_{\mathrm{coll},1} = 24.1r_s$ and $\theta_{\mathrm{coll},1} = 90°$. We inject the streams at $r_{\mathrm{inj}} = 47.74r_s$, $52.89r_s$, with the density and velocity $\mathbf{v}_{\mathrm{inj}} = (0.092c, \ 0.0, \ 0.12c)$, $(0.0065c, \ 0.0, \ 0.18c)$ at the inner and outer ϕ direction boundary. Similarly, for A122R95Edd1, the fallback stream is a part of the same orbit as in A122Edd1, but we manually change the returning stream, so they collide with similar angle $\theta_{\mathrm{coll},1} = 125°$ but at a further radius $r_{\mathrm{coll},1} = 95.1r_s$. We inject the streams at $r_{\mathrm{inj}} = 47.94r_s$, $46.87r_s$, with the density and velocity $\mathbf{v}_{\mathrm{inj}} = (2.24\times10^{-2}c, \ 0.0, \ 8.81\times10^{-2}c)$, $(3.18\times10^{-2}c, \ 0.0, \ 0.115c)$ at the inner and outer ϕ direction boundary respectively.

5.3 Results

We present six simulations, including four A122 runs with the same orbit but different fallback rates, along with two runs to study the effect of the collision angle

Table 5.1: Summary of Parameters for Main
Simulations

Name	$\dot{M}/\dot{M}_{\mathrm{Edd}}$	$\theta_{\mathrm{coll},1}$	$r_{\mathrm{coll},1}$
A122Edd1	1.0	122°	$22.5r_{\mathrm{s}}$
A122Edd01	10^{-1}	122°	$22.5r_{\mathrm{s}}$
A122Edd001	10^{-2}	122°	$22.5r_{\mathrm{s}}$
A122Edd10	10.0	122°	$22.5r_{\mathrm{s}}$
A90Edd1	1.0	90°	$24.1r_{\mathrm{s}}$
A122R95Edd1	1.0	125°	$95.1r_{\mathrm{s}}$

(A90Edd1) and radius (A122R95Edd1). We list the stream orbital parameters in the
black hole-centered coordinate Table 5.1.

5.3.1 Importance of resolving the stream and radiation mediated shock

In this section, we show that the outcome of stream-stream collision in RHD
simulations is highly sensitive to spatial resolution. We compare a low resolution
simulation A122Edd1_LR and the fiducial resolution A122Edd1, where we reduce
the level-five and level-six refinement to level-two refinement. With the adjustment,
we have the resolution of $\delta R \approx R\delta\theta \approx 0.16$ in r and θ direction when injecting the
streams, meaning δR is about 1/8 times of the fiducial A122Edd1 resolution at the
same location. So we no longer resolve the estimated stream scale height H. As a
result, the stream cross-section $A \sim \delta R^2$ is artificially increased, so the stream density
$\rho_{\mathrm{inj}} \sim \dot{M}/Av_{\mathrm{inj}} \propto \delta R^{-2}$ is reduced at fixed $\dot{M}$. We set $\rho_{\mathrm{inj}} = 1.10 \times 10^{-9}$g cm^{-3}, $7.73 \times$
10^{-10}g cm^{-3} at the inner and outer ϕ direction boundary to match $f_{\mathrm{Edd}} = 1.0$ fallback
rate. Other simulation set-ups are the same as A122Edd1.

The choice of level-two refinement in A122Edd1_LR is motivated by the global
test calculation in Appendix B, which tracks the stream orbit around the black hole.
In the test simulation, we observe noticeably different gas dynamics after the stream-
stream collision compared to A122Edd1, despite the same stream orbit and compa-
rable mass injection rates.

In A122Edd1_LR, the stream density is artificially reduced due to insufficient res-

olution, which could affect the stream vertical optical depth, where $\tau_{\mathrm{str}} \sim \kappa_{\mathrm{s}}\rho_{\mathrm{inj}}\delta R \propto \delta R^{-1}$. We measure the initial vertical optical depth τ_{str} by integrating $\tau_{\mathrm{str}} = \int \kappa_{s}\rho dr$ from $r = 29.0$ to $r = 31.0$ at $\phi = 0.86\pi$ in r direction. We find that $\tau_{\mathrm{str}} \approx 6 \times 10^{2}$ in A122Edd1_LR, and $\tau_{\mathrm{str}} \approx 5 \times 10^{3}$ in A122Edd1. So before the collision, both streams are optically thick, but with order-of-magnitude different vertical optical depth.

Figure 5.3 shows the distinct downstream gas distribution in A122Edd1_LR and A122Edd1. After the two streams collide, the gas in A122Edd1 forms an expanding outflow that propagates radially outward in the orbital plane. Off the orbital plane, gas moves away symmetrically with respect to $\theta = \pi/2$-plane. The expanded downstream gas distribution suggests that the radiation pressure produced in the collision redistributes the gas. In contrast, post-shock gas in A122Edd1_LR is mainly concentrated in a merged stream that bends towards the black hole.

The different outflow morphology suggests different radiative acceleration near the shock in the two simulations. We find that the radiation energy density at stream-stream collision shock front in A122Edd1_LR is about two orders of magnitude lower than A122Edd1 (see Appendix C). This implies that less stream kinetic energy is converted to radiation energy locally by the collision, or more efficient cooling due to enhanced radiative diffusion resulting from the lower optical depth. These effects may be associated with the lower stream kinetic energy density and the less-resolved collision shock in A122Edd1_LR. Consequently, we find that the radiation pressure near the collision is lower in A122Edd1_LR , which is less likely to drive massive outflow.

The downstream gas optical depth is also different. We estimate the photosphere surface radius $R_{\tau=1}$ in the r direction as the radius at which :

$$\int_{R_{\tau=1}}^{R_{\mathrm{out}}} \kappa_{s}\rho dr = 1, \tag{5.2}$$

where R_{out} is the outer boundary radius the r direction. The green line in Figure 5.3 of each panel shows $R_{\tau=1}$ of these snapshots. At $t = 0.3$, average $R_{\tau=1}$ of A122Edd1 is generally larger than A122Edd1_LR. Hence, radiation diffusion takes longer and there is less cooling in the expanding outflow, the gas temperature at $R_{\tau=1}$ is higher in A122Edd1_LR.

The primary energy conversion in the simulation is between gas kinetic energy,
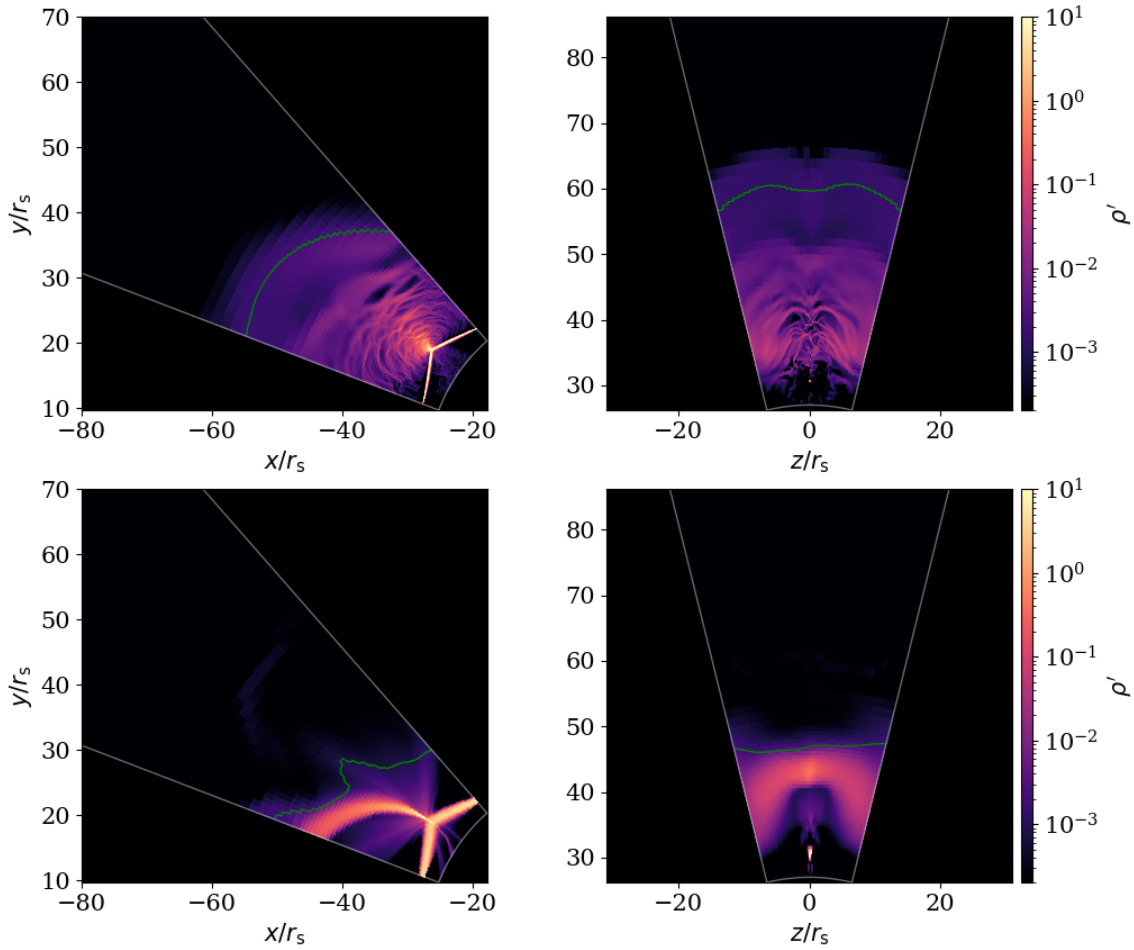
Figure 5.3: Gas density snapshots at $t = 0.3$ for A122Edd1 (the upper panel) and A122Edd1_LR (the lower panel), where A122Edd1 is the fiducial resolution simulation with $\delta R \approx 0.02$ (in unit of $r_{\rm s}$), and A122Edd1_LR is the low resolution simulation with $\delta R \approx 0.16$ (in unit of $r_{\rm s}$) when the streams are injected. In each row, the left plot shows volume average from $\phi = 1.56 - 1.59$ near $\theta = \pi/2$-plane, the right plot shows volume average from $\theta = 2.52 - 2.55$ near mid-ϕ-plane.
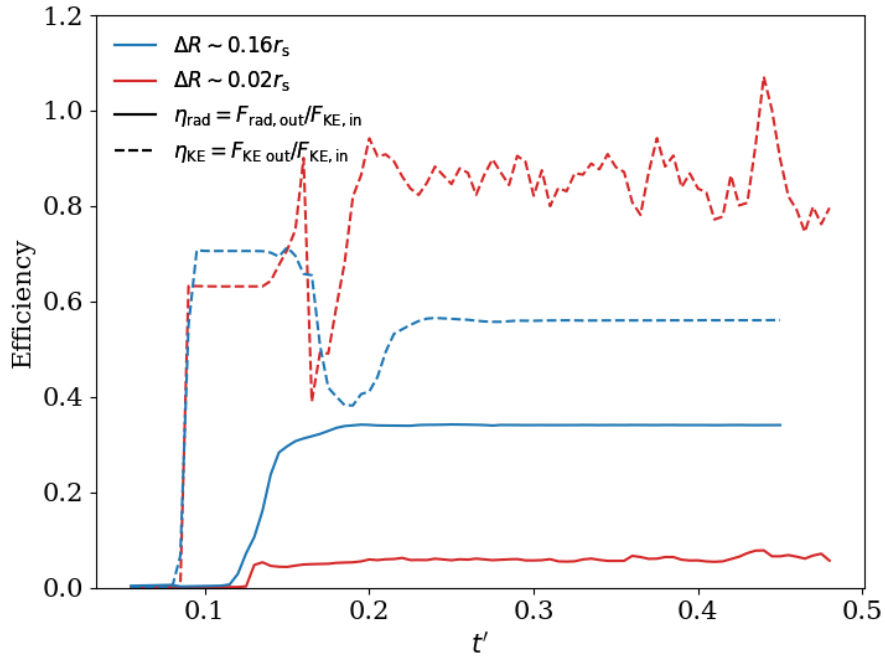
Figure 5.4: The radiative efficiency (the solid lines) and kinetic efficiency (the dashed lines) defined as Equation 5.4. The blue lines are A122Edd1_LR, and the red lines are A122Edd1. The efficiencies may slightly exceed 1.0 because of the conversion between kinetic energy and gravitational potential. The low resolution run A122Edd1_LR produces larger radiation luminosity than A122Edd1 and less kinetic energy.

gas gravitational potential and radiation energy. Tejeda & Rosswog (2013) defines the total conserved energy

$$E_\mathrm{G} \equiv \frac{1}{2}\left[\frac{r^2 v_r^2}{(r-r_\mathrm{s})^2} + \frac{r}{r-r_\mathrm{s}}(v_\theta^2 + v_\phi^2)\right] - \frac{GM_\mathrm{BH}}{r} \qquad (5.3)$$

In the rest of paper, we define "orbital energy" as E_G, "kinetic energy" as non-relativistic kinetic energy, and "gravitational potential" as the difference between E_G and kinetic energy.

In the optically-thick outflow of A122Edd1, the radiation force continuously accelerates gas until photons diffuse out from photosphere, so some radiation energy produced in the collision will be converted back to gas kinetic energy. To quantify the energy conversion, we define the net radiative efficiency η_rad and kinetic energy

efficiency η_{KE} as:

$$\eta_{\mathrm{rad}} = \frac{\int \mathcal{F}_{\mathrm{rad,out}} dA}{\int \mathcal{F}_{\mathrm{KE,in}} dA}, \ \ \eta_{\mathrm{KE}} = \frac{\int \mathcal{F}_{\mathrm{KE,out}} dA}{\int \mathcal{F}_{\mathrm{KE,in}} dA}, \tag{5.4}$$

where $\mathcal{F}_{\mathrm{KE,in}}$, $\mathcal{F}_{\mathrm{KE,out}}$, $\mathcal{F}_{\mathrm{rad,out}}$ are total injected kinetic energy flux, total outgoing kinetic energy flux and total outgoing radiation flux. The fluxes are integrated on all the surfaces of an enclosed volume.

Figure 5.4 shows the efficiencies as a function of time for A122Edd (red lines) and A122Edd_LR (blue lines). At $t \approx 0.12$, the streams collides, the radiation energy efficiency start to rise, followed by the kinetic energy efficiency drop. Later, as radiation forces accelerate gas and downstream gas gains kinetic energy, the kinetic energy efficiency rises again, eventually relaxing to the quasi-steady-state value. Compared to A122Edd1, more injected kinetic energy is converted to radiation in A122Edd1_LR. This is because the radiation produced in the collision diffuses through the more optically thin downstream gas without as much interaction with gas, yielding higher net radiative efficiency. Notice that the efficiencies are calculated from energy fluxes injecting and leaving the boundary surfaces of an enclosed volume within the calculation domain. Here we integrate over the surfaces of the simulation domain up to $r = 40.0$, equivalent to all the surfaces of the volume $(27, 40) \times (0.42\pi, 0.58\pi) \times (0.81\pi, 0.96\pi)$. We also calculated the efficiencies at the enclosed volume with outer radii of $r = 45.0$, 50.0 and did not find a significant difference.

When the resolution is insufficient, the reduced radiation production from the stream-stream collision may suppress the prompt luminosity, but the low optical depth in the post-shock gas may allow photons to diffuse out more easily, enhancing the prompt luminosity. Considering these competing factors, it is possible that in other sets of parameters, insufficient resolution might lead to underestimating luminosity if the effect of downstream gas optical depth is secondary.

5.3.2 Eddington mass flux: A122Edd1

Figure 5.5 and Figure 5.6 show the density snapshots from A122Edd1. After two streams collide, the downstream gas is accelerated by the radiation pressure, forming an optically-thick outflow that extends a few tens of r_{s}. The post-shock gas forms multiple shells near the collision site. The shell morphology is similar to Jiang et al. (2016), which is related to the shock-front obliqueness changing due to slightly unbalanced pressure.
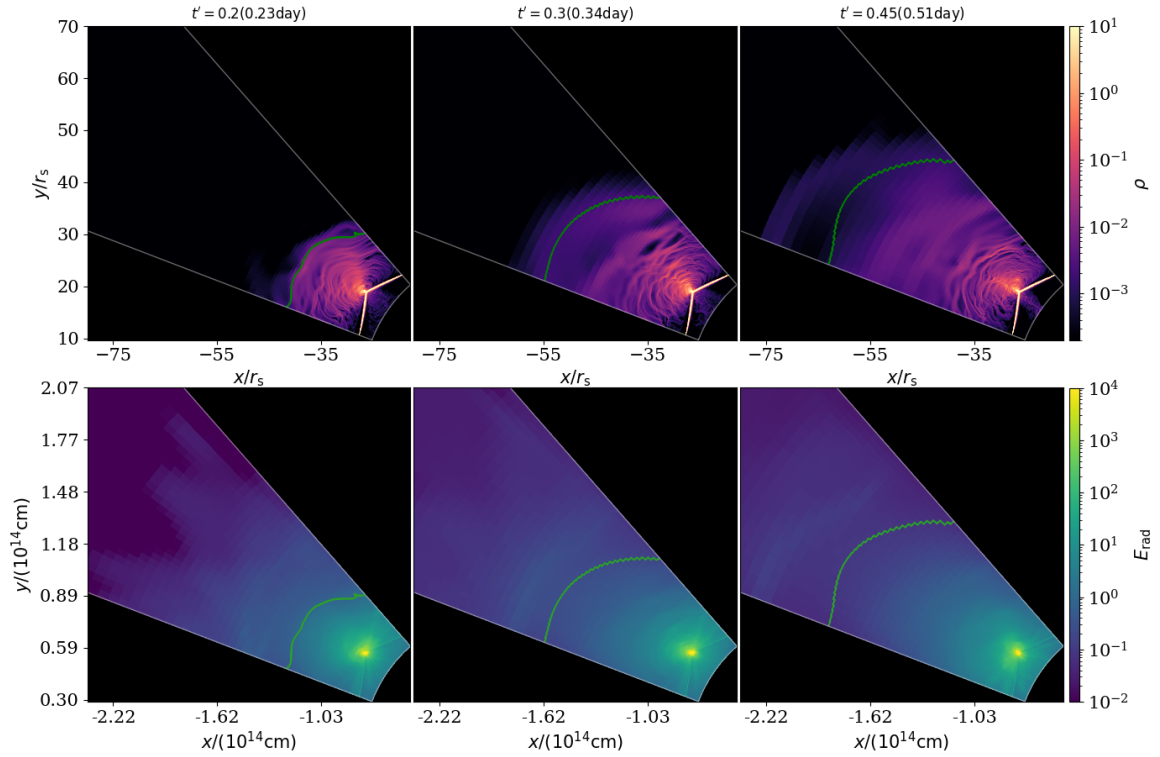
Figure 5.5: Gas density snapshots (the upper panel) and lab frame radiation energy density snapshots (the lower panel) at $t = 0.2$, 0.3, 0.45 (from left to right) of A122Edd1. The plotted variables are volume average from $\theta = 1.56 - 1.59$ near $\theta = \pi/2$-plane. In the lower panel, the ray effect near the collision point is likely due to angular discretization. In each plot, the green solid line is the photosphere surface as defined in Equation 5.2.

We find that the downstream gas is aspherical relative to the collision point and the black hole. Most gas stays within a cone of finite solid angle. For example, at $t = 0.3$, gas mainly stays in $25° \lesssim \theta_3 \lesssim 150°$, $100° \lesssim \phi_3 \lesssim 200°$, where θ_3, ϕ_3 are the altitude and azimuthal angle relative to the collision point. In the rest of paper, we use subscript 3 to note the variables relative to the collision point. Our calculation domain only covers part of the sky seen from the black hole, and the gas roughly fills the angular space of $60° \lesssim \theta_1 \lesssim 120°$, $55° \lesssim \phi_1 \lesssim 140°$ seen from the black hole. This picture is qualitatively similar to the estimated outflow morphology in Lu & Bonnerot (2020). The bottom panels in Figure 5.5 and Figure 5.6 show that the collision as a bright point on radiation energy density map. The radiation energy density is enhanced by about four orders of magnitudes (also see Figure C.1)
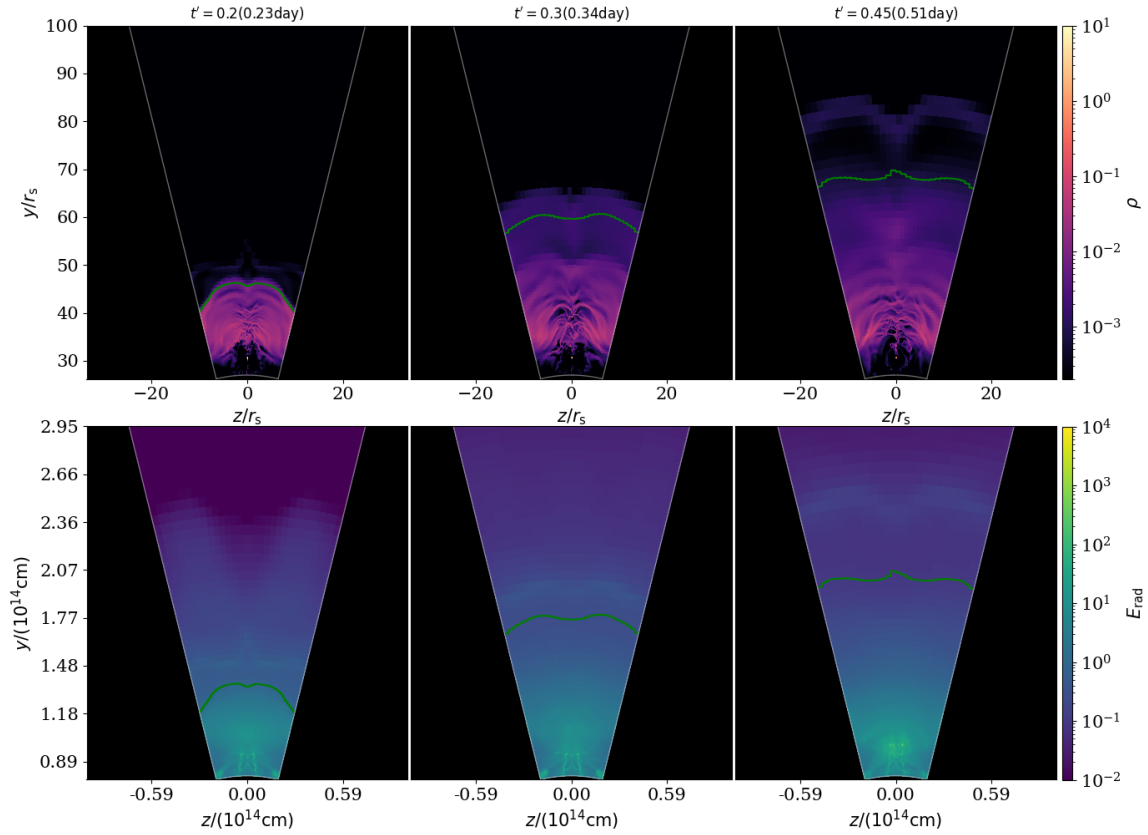
Figure 5.6: Gas density snapshots (the upper panel) and lab frame radiation energy density snapshots (the lower panel) at $t = 0.2$, 0.3, 0.45 for A122Edd1 respectively (from left to right). The plotted variables are volume average from $\phi = 2.52 - 2.55$ near mid-ϕ-plane. In the lower panel, the ray effect near the collision point is likely due to angular discretization. In each plot, the green solid line is the photosphere surface as defined in Equation 5.2.

at the collision, where gas experiences eruptive acceleration. Figure 5.7 shows the ratio between radiation acceleration and gravity in the r direction. Even if the mass fallback rate is just Eddington, the strong radiation pressure produced in the collision creates a super-Eddington that region extends a few $r_{\rm s}$ in the downstream gas.

As gas is accelerated by radiation pressure and propagates outward, it forms an optically-thick outflow. The green solid line in each density snapshot shows the photosphere radius $R_{\tau=1}$ (Equation 5.2). The average $R_{\tau=1} \approx 80r_{\rm s}$ in the quasi steady state, and is relatively uniform in θ and ϕ direction. Along θ and ϕ direction line of sight, however, the simulation does not capture the equivalent photosphere surface. The gas is partially optically thick at the θ and ϕ boundary surfaces. We note that $R_{\tau=1}$ is defined relative to the origin, instead of the black hole. We also calculated the $F_{\rm rad}/cE_{\rm rad}$ in lab frame, where $F_{\rm rad}$ is the radiation flux magnitude, and $E_{\rm rad}$ is the radiation energy density as another metric to measure the opaqueness. We compare the surface where $F_{\rm rad}/cE_{\rm rad} = 0.3, 0.4$ with $R_{\tau=1}$ and find rough agreement. Therefore, the gas outflow in A122Edd1 is optically thick and could potentially correspond to a reprocessing layer for optical TDEs at early time.

As the radiation force does work on the downstream gas, part of the gas gains energy and becomes unbound. Similar to Jiang et al. (2014), we define unbound gas as with $E_{\rm t} > 0$, where $E_{\rm t}$ is analogue to Bernoulli number:

$$E_{\rm t} = E_{\rm G} + \frac{\gamma P}{\gamma - 1} + \frac{4E_{\rm rad}}{3}, \tag{5.5}$$

where $E_{\rm G}$ is the total orbital energy defined in Equation 5.3. The second term is fluid enthalpy, and the third term assumes radiation acts as a fluid with adiabatic index of $\gamma = 4/3$. Hence, when radiation diffusion is present, this enthalpy is not a conserved quantity. The red solid line in Figure 5.10 shows the total unbound mass flux, normalized to the total injected mass flux carried by the original stellar streams. As the collision happens near $t = 0.18$, the unbound mass flux quickly increases to $\sim 15\%$, and eventually reaches quasi-steady state, suggesting that $\sim 18\%$ of injected mass flux becomes unbound when they leave the simulation domain. We found the unbound gas spatial distribution is anisotropic. Near the collision, the unbound gas has a mass-weighted average radial velocity of $v_{\rm ub,r3} \approx 0.17c$ at quasi-steady state relative to the collision, and decreasing to $v_{\rm ub,r3} \lesssim 0.1c$ away from the collision point outward. Therefore, the collision in A122Edd1 is able to create fast and relatively
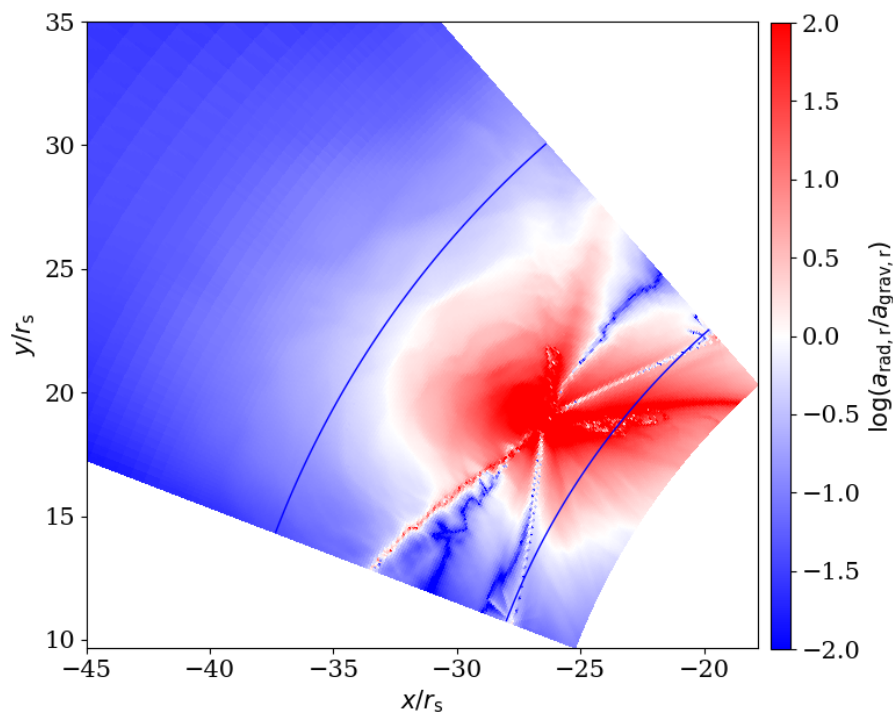
Figure 5.7: The ratio between radiation acceleration and gravity acceleration in r direction, averaged over $\pi/2 - 0.24 \leq \theta \pi/2 + 0.24$ near the $\theta = \pi/2$-plane. The two blue solid lines labels the radius $30r_\mathrm{s}$ and $40r_\mathrm{s}$. Due to the radiation pressure near the collision site, the r direction radiation force exceeds gravity in the downstream gas, creating a local super-Eddington region that extends few r_s from the collision.

dens unbound gas. But we also note that this "unbound" criteria E_t is sensitive to the stream initial condition. Unbound gas could also have orbits oriented towards the black hole. Since the initial stream is itself weakly bound, the delineation between bound and unbound gas after the collision will depend on the details of the global evolution.

5.3.3 Effect of Eddington ratio

To study the effect of mass fallback rate, we compare the simulations A122Edd001, A122Edd01 and A122Edd10 with the fiducial simulation A122Edd1. The range of Eddington ratio provides us with a sample of different TDE systems, as well as potential different time stamps before the peak, where the mass feeding rate may rise from sub-Eddington to super-Eddington.

We find that the outcome of collision is sensitive to the fallback rate, especially for sub-Eddington rates. The super-Eddington simulation A122Edd10 shows qualitatively similar outflow as A122Edd1. In contrast, when we lower the mass fallback ratio to 10% and 1% Eddington, the downstream gas distribution is changed significantly. Figure 5.8 shows gas density distribution from the two lower Eddington ratio simulations. In A122Edd001, the downstream gas is mainly confined in a thin stream and does not form an expanded outflow. In A122Edd01, the stream-stream collision redistributes gas to form an outflow, but this outflow has lower density when compare to the A122Edd1, and is also slightly bent towards the black hole.

In the simulations with different mass fallback rates, we assume the stream specific kinetic energy is the same. So lower mass fallback rate yields less available kinetic energy before collision. We find that compared to A122Edd1, the maximum radiation energy density at the shockfront is 0.55% in A122Edd001, 9.6% in A122Edd01, and 405.0% in A122Edd10, measured at $t' = 0.4$. Due to lower radiation pressure in sub-Eddington runs, they are less likely to drive massive outflows.

Figure 5.9 shows the radiative efficiency η_{rad} and kinetic energy efficiency η_{KE}. It shows the trend that higher Eddington ratio leads to lower radiative efficiency. We attribute the anti-correlation to energy exchange between radiation and kinetic energy in downstream gas. To first order, the radiative efficiency is affected by both the shock dissipation during the collision and the energy lost accelerating the post-shock gas.

When the downstream outflow is optically thick, before photons diffuse out, the radiation force accelerates gas and converts radiation energy to kinetic energy, yield-
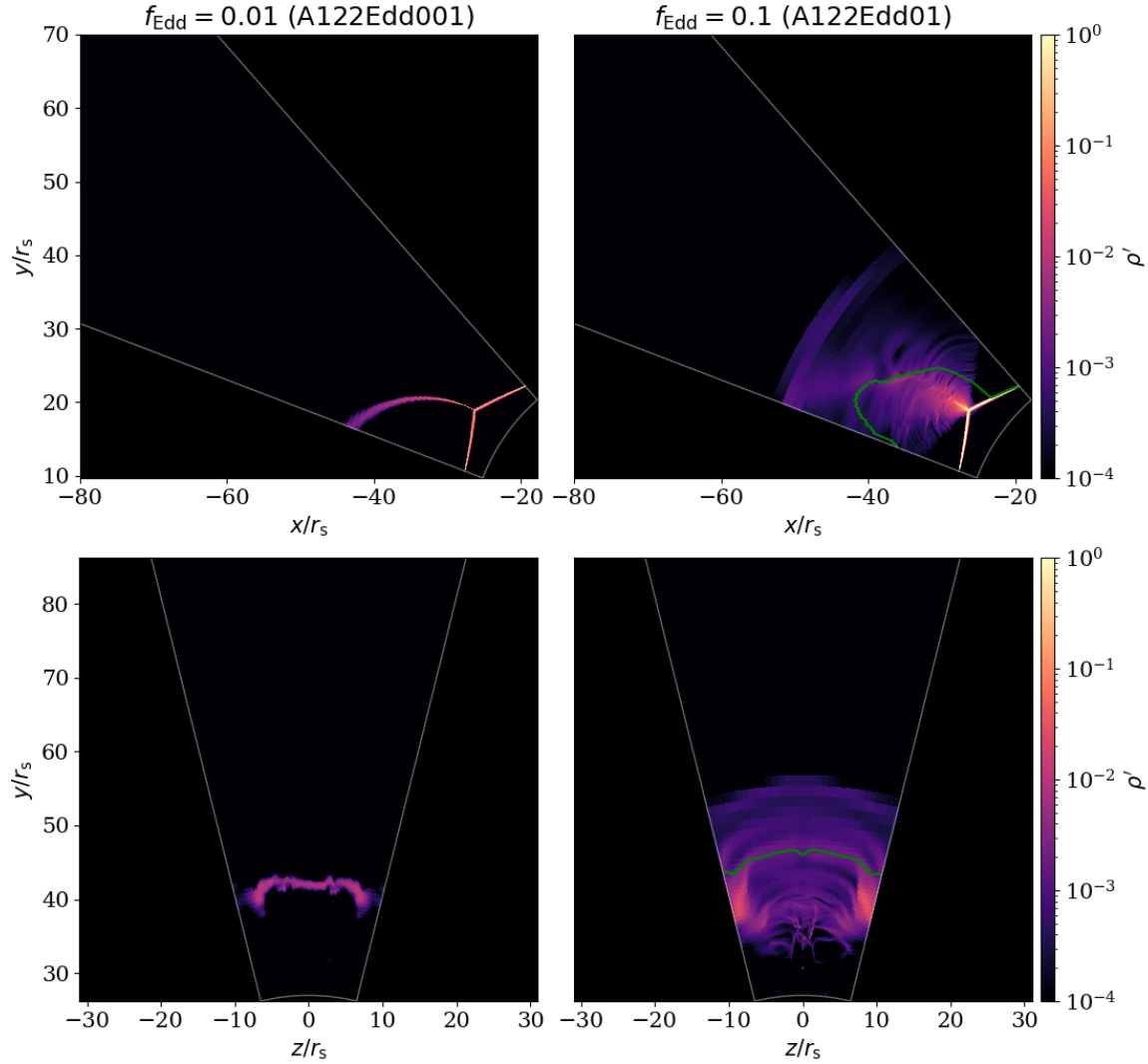
Figure 5.8: Gas density snapshots at $t = 0.3$ for A122Edd001 (the left column) and A122Edd01 (the right column). In each column, the upper panel shows the top view (volume average from $\theta = 1.56 - 1.59$ near $\theta = \pi/2$-plane), the lower panel shows the side view (volume average from $\phi = 2.52 - 2.55$ near mid-ϕ-plane). The green solid line is the photosphere surface as defined in Equation 5.2. When comparing with the fiducial simulation A122Edd1 (Figure 5.5 and Figure 5.6), notice the different color normalization in this plot to better show low density gas.
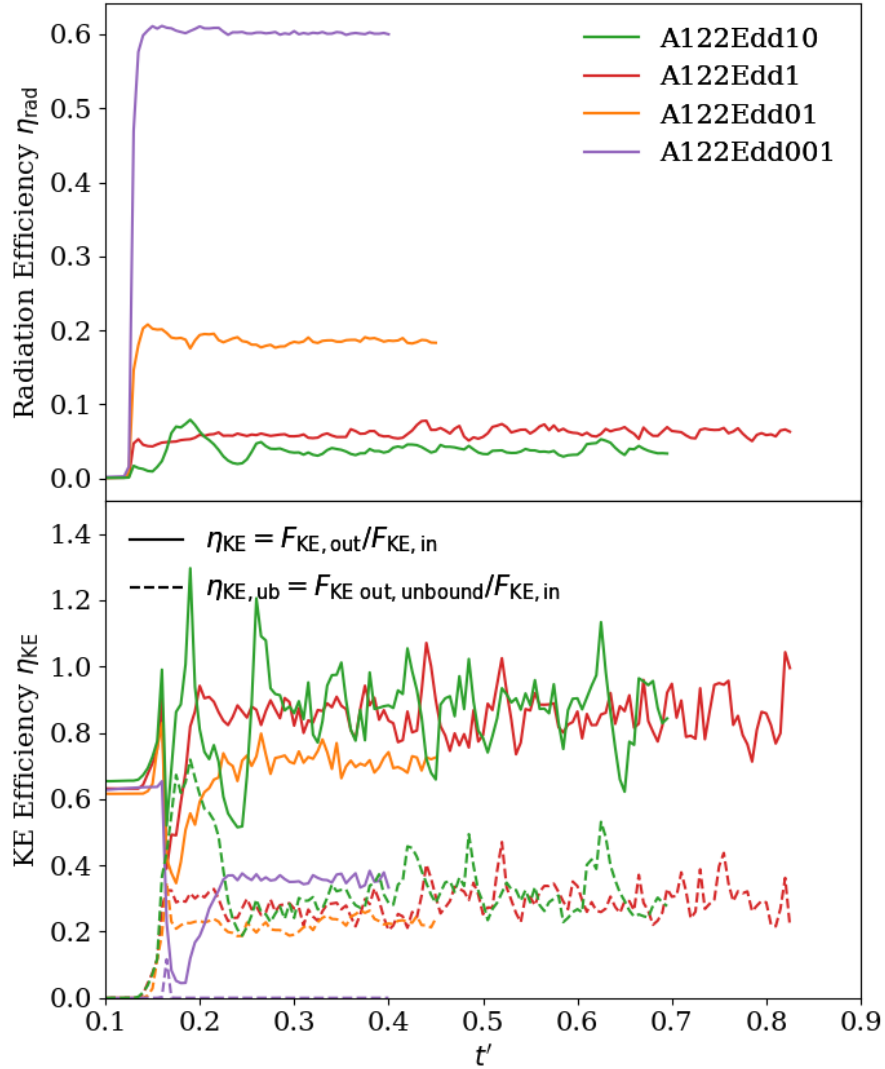
Figure 5.9: radiative efficiency η_{rad} (upper panel) and kinetic energy efficiency η_{KE} (lower panel, Equation 5.4) as a function of time. In the lower panel, the solid lines are total kinetic energy leaving simulation domain, the dashed lines are unbound kinetic energy fraction. The kinetic energy efficiency might be larger than 1.0 because of conversion with gravitational potential.

Table 5.2: Radiation efficiencies

$\dot{M}/\dot{M}_{\mathrm{Edd}}$	10^{-2}	10^{-1}	1.0	10.0
η_{rad}	$\sim 60.3\%$	$\sim 18.5\%$	$\sim 6.2\%$	$\sim 3.8\%$
$t_{\mathrm{diff}}/t_{\mathrm{adv}}$	~ 0.4	~ 2.0	~ 17.3	~ 133.4
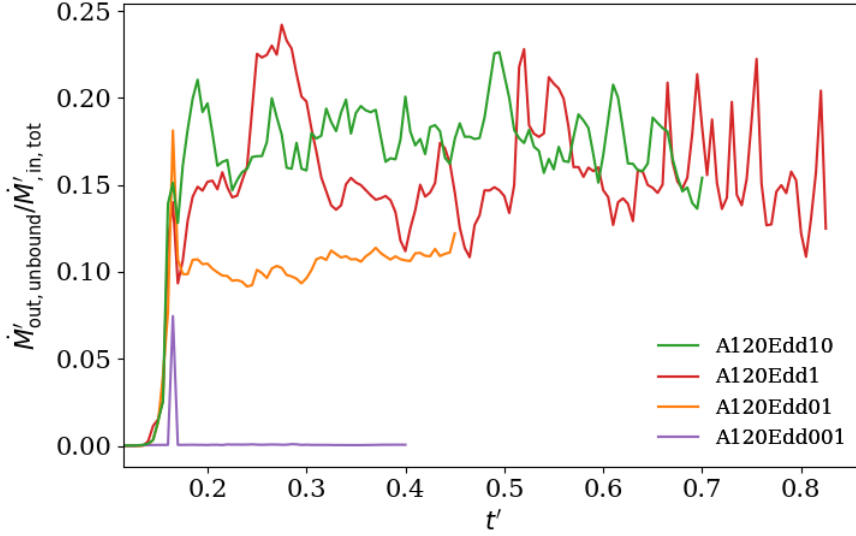
Figure 5.10: Total unbound mass flux as a function of time, normalized to the total injected mass flux. The fluxes are calculated at the simulation domain up to $r = 40.0$(i.e. integrated over all the surface of the volume $(27, 40) \times (0.42\pi, 0.58\pi) \times (0.81\pi, 0.96\pi)$). We also calculate mass flux at $r = 45.0$, 50.0 and did not find significant difference in the quasi steady state.

ing lower net radiative efficiency. We assess this by estimating the ratio of radiation diffusion time to the advection time in the downstream gas. We select outflowing gas as described in Section 5.4.3. Then we calculate the average optical depth and radial velocity measured relative to the collision point to estimate $t_{\mathrm{diff}} \sim \tau R/c$ and $t_{\mathrm{adv}} \sim R/v_{\mathrm{r}}$ respectively. We list the estimated $t_{\mathrm{diff}}/t_{\mathrm{adv}}$ in Table 5.2 together with the radiative efficiency. The sub-Eddington run A122Edd001 shows significantly shorter diffusion time than advection time, and $t_{\mathrm{diff}}/t_{\mathrm{adv}}$ increases as mass fallback rate becomes larger. The ratio $t_{\mathrm{diff}}/t_{\mathrm{adv}}$ of A122Edd1 and A122Edd10 are well above unity, suggesting photon diffusion is slow in these two runs. Interestingly, A122Edd1 and A122Edd10 show similar radiative efficiency despite the order of magnitude different fallback rate, which may suggest that there is a minimum radiative efficiency for a fixed stream orbit.

The kinetic energy efficiency is shown in Figure 5.9, including total kinetic energy η_{KE} (the solid lines) and the unbound kinetic energy $\eta_{\mathrm{KE,ub}}$ (the dashed lines). Consistent with the lower radiative efficiency, the higher mass fallback rate usually leads to higher kinetic energy efficiency. The unbound fraction seems to follow similar trend. The transient peak near $t \sim 0.16$ correspond to the time that the returning stream first encounters the fallback stream and breaks the fallback stream. Part of the broken stream left the domain as marginally-unbound gas, we note that this initial transient may be sensitive to details of domain set-up, and thus mainly focus on the quasi-steady-state energy conversion.

In Figure 5.10, we show the ratio between unbound mass flux and the total injected mass flux. A122Edd001 does not produce significant unbound mass, while A122Edd01 shows that $\sim 10\%$ injected mass flux becomes unbound, A122Edd1 and A122Edd10 shows $\sim 15\%$ unbound fluxes. We also find that the average velocity of unbound gas are factor of a few similar in A122Edd01, A122Edd1 and A122Edd10. The results are generally consistent with the unbound fraction found in Jiang et al. (2016) with comparable Eddington ratio.

5.3.4   Effect of collision angle

In A90Edd1, we adjust the orbital parameter of the returning stream to have collision angle $\approx 90°$, while keeping the collision radius similar to A122Edd1 ($r_{\mathrm{coll}} = 24.1r_{\mathrm{s}}$, Table 5.1). Figure 5.11 shows the gas density snapshots from A90Edd1 after it has reached a quasi-steady-state. The majority of downstream gas forms a stream-structure that expands in θ direction perpendicular to the orbital plane. We find that the stream-structure is bounded and falls towards the black hole.

The collision creates unbound gas away from the orbital plane. They are spatially divided into two groups. The first group of unbound gas stays in the inner side of the merged stream, with velocity oriented towards the black hole and leaving the calculation domain from the outer ϕ boundary. These unbound gas is relatively diffuse, with enhanced velocity due to the decreasing gravitational potential when approaching black hole. The second group of unbound gas is ejected from the outer side of the merged stream moving outward radially, with higher density than the first group. We find that the total unbound mass flux is $\sim 10\%$ of total injected mass flux, with $\sim 7.6\%$ in the r direction contributed by the second of unbound gas, and $\sim 2.4\%$ in the ϕ direction contributed by the first group of diffusing gas.
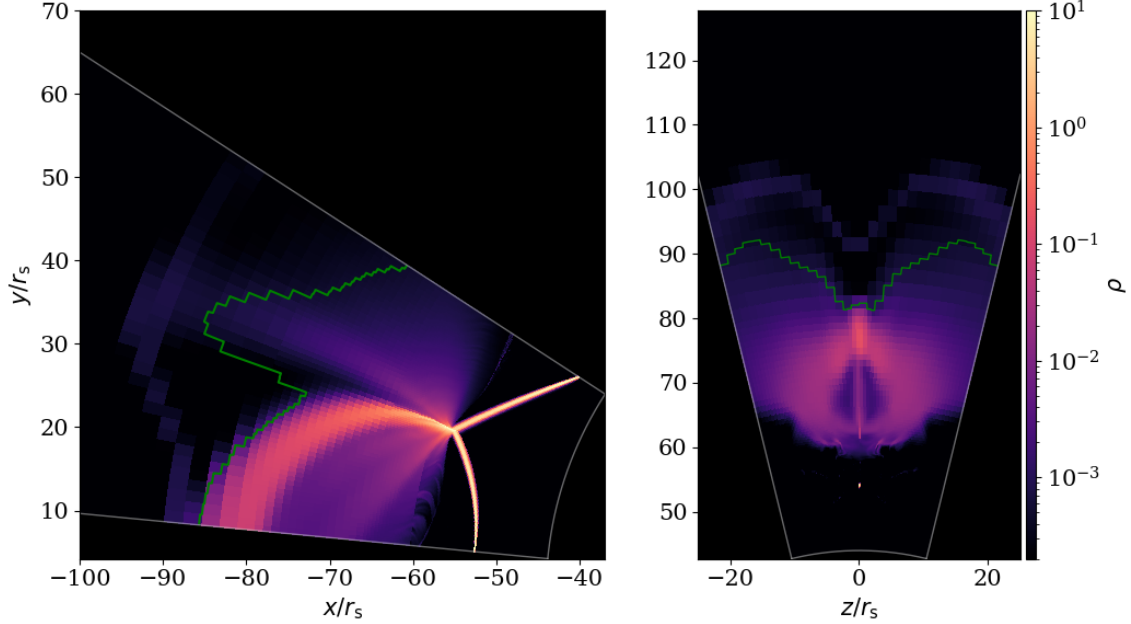
Figure 5.11: Gas density snapshots at $t = 0.45$ for A90Edd1. The left plot is at $\theta = \pi/2$-plane, the right plot is at mid-ϕ-plane. The green solid line shows the photosphere surface as defined in Equation 5.2.

Figure 5.12 compares the unbound kinetic energy efficiency and the radiative efficiency in A90Edd1 with A122Edd1. Despite the similar total unbound kinetic energy efficiency, the contribution from r, θ and ϕ boundaries are significantly different, suggesting different downstream gas morphology. We find that the $\sim 70\%$ of the unbound kinetic energy flux is from the r direction, carried by the second group of massive, fast unbound gas. The rest unbound kinetic energy flux is from the first group of diffuse unbound gas with lower velocity. The θ boundary contributions are negligible. The uneven distribution is in contrast with the relatively equal amount of unbound kinetic energy flux in the r, θ and ϕ boundaries in A122Edd1.

The radiative efficiency is also similar to A122Edd1. However, this does not imply a similar radiation energy production by the collision. We find that the maximum radiation energy at the collision shock front in A90Edd1 is about 5 times lower than A122Edd1. However, the downstream gas is more optically thin in A90Edd1. The green solid lines in Figure 5.11 show the photon $R_{\tau=1}$ at quasi-steady state. Compared to the extended optically thick region in A122Edd1, photons can diffuse out of downstream gas in A90Edd1 more easily.
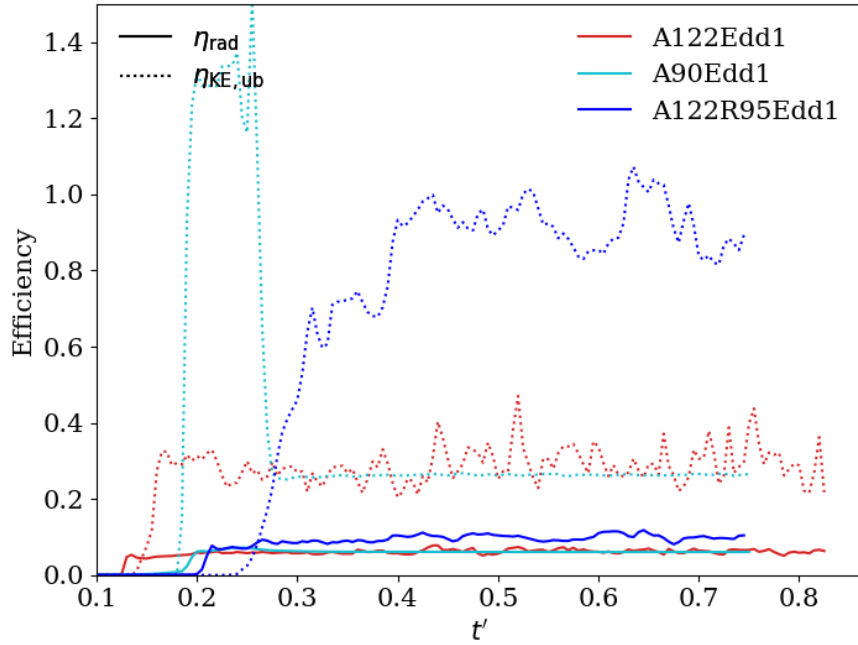
Figure 5.12: radiative efficiency (the solid line) and unbound kinetic energy efficiency (the dotted lines) as a function of time. The red lines are for A122Edd1, and the cyan lines are for A90Edd1, the dark blue lines are for A122R95Edd1. The kinetic energy efficiency might be larger than 1.0 because of conversion between kinetic energy and gravitational potential. In A90Edd1, there is also a transient phase ($0.17 \gtrsim t' \gtrsim 0.26$) with high unbound kinetic energy efficiency, which correspond to the time when the approaching stream is broke by the returning stream, the disrupted stream is marginally unbound and leaving the domain. We note that this transient high unbound rate is artifact due to our domain set-up.

Interestingly, the comparison between A90Edd1 and A122Edd1 shows that results deviate from a ballistic collision model. If the collision is inelastic and the collision angle is $\theta_{\rm coll}$, assuming a symmetric collision velocity vector on both side of the shock, the dissipated energy will roughly be $\propto \sin(\theta_{\rm coll}^2/2)$ (Dai et al., 2015), where only the velocity in the net-momentum direction is preserved. However, A90Edd1 and A122Edd1 show a similar radiative efficiency that does not scale as $\propto \sin(\theta_{\rm coll}/2)$, suggesting that the net luminosity does not solely depend on the collision angle, but also the optical depth of downstream gas.

5.3.5   Effect of collision radius

In A122R95Edd1, we adjust the returning stream to make the collision radius to be $\approx 95r_{\rm s}$, while keep the collision angle close to A122Edd1 (Table 5.1). The modified returning stream is on a slightly unbound orbit, with $v_{\rm tot,1} \approx 0.115c$ relative to the black hole before collision. The fallback stream is on the same orbit as A122Edd1, which is slightly bounded with $v_{\rm tot,1} \approx 0.097c$ before collision. These velocities are only about half of the velocity in A122Edd1 before collision. The set-up is designed to compare with A122Edd1 to study the effect of collision radius, the realistic stream orbit collides near this radius will likely to show smaller collision angle for a spin-less black hole (Dai et al., 2015; Bonnerot et al., 2021).

Figure 5.13 shows the gas density snapshot at $t' = 0.52$, which is at a comparable time after collision as A122Edd1 in Figure 5.5. The outflow morphology is similar to A122Edd1, but the gas flow is slower and propagates to smaller radius relative to the collision point. The gas is also less bent towards the black hole due to the weaker gravity.

When moving the collision radius outward, the available kinetic energy before collision will be reduced, in our case, the speed of both streams are roughly reduced by half. So the radiation energy density at the shock will potentially be lower, suppressing the immediate acceleration of gas near the collision. However, the effect of gravity is also weaker compare to A122Edd1, so the deceleration of downstream gas is reduced. These competing effects shape the collision and post-shock gas evolution.

Figure 5.12 shows that the radiative efficiency of A122R95Edd1 is only slightly higher than A122Edd1. We find that the gas compression rate at the shock (i.e. the ratio between stream density before and at the shock) is similar in the two simulations. The local radiation energy density in A122R95Edd1 is about five times lower, roughly
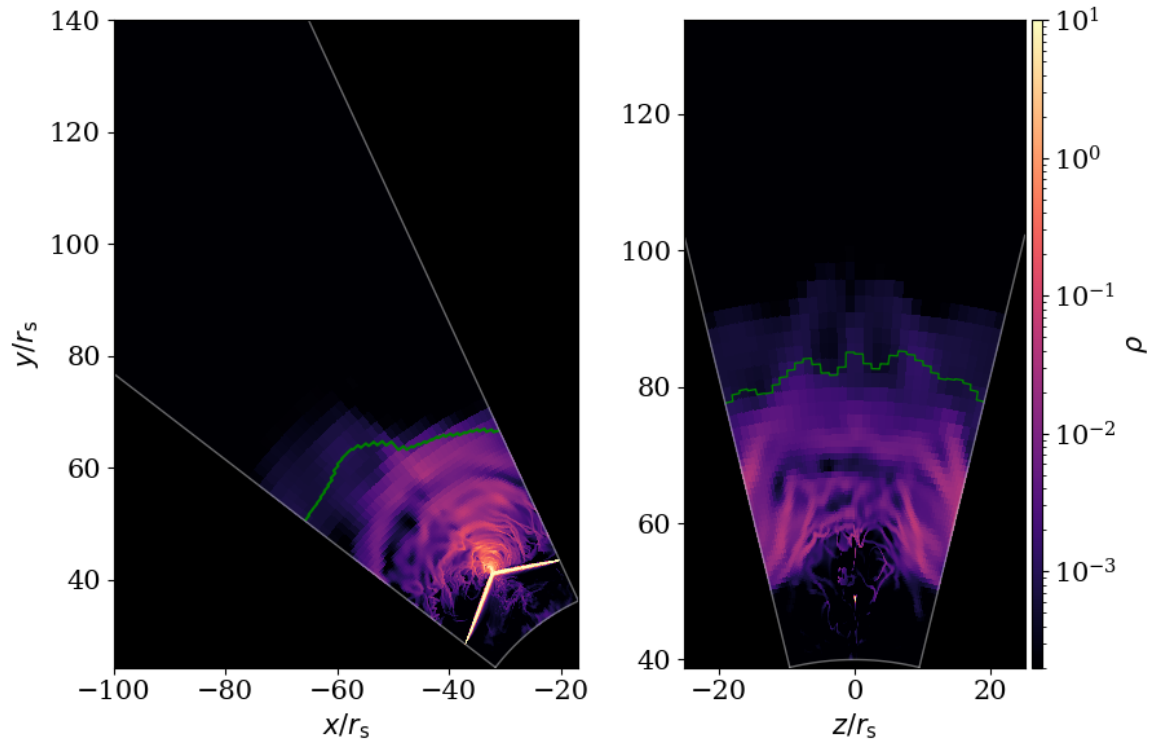
Figure 5.13: Gas density snapshots at $t' = 0.52$ for A122R95Edd1, about $\Delta t' \sim 0.34$ after the collision, which is comparable to $t' = 0.45$ in A122Edd1 (the third column in Figure 5.5). The left plot is the $\theta = \pi/2$-plane, the right plot is the mid-ϕ-plane. The green solid line shows the same average for the photosphere surface as defined in Equation 5.2.

consistent with the two times lower gas velocity at both sides of the shock.

However, the unbound kinetic energy and mass flux are significantly higher than A122Edd1. We find that the unbound and injected mass flux ratio is close to 1.0 at the quasi-steady state, suggesting more massive but slower unbound outflow. Figure 5.14 shows the angular distribution of radial velocity relative to the collision point $v_{\rm r,3}$. The outward velocities $v_{\rm r,3} > 0$ in A122R95Edd1 is generally smaller than A122Edd1. We note that our definition of unbound gas is sensitive to the initial stream orbital energy. Some unbound gas could move towards the black hole and potentially interact with other gas near pericenter before escaping from the system. So the high fraction of unbound downstream gas in A122R95Edd1 should not be directly interpreted as large expanding photosphere. We will discuss the implied photosphere evolution in Section 4.5.

5.4 DISCUSSION: STREAM-STREAM COLLISION'S ROLE IN PRE-PEAK TIME

5.4.1 Prompt emission and contribution to luminosity

The rise-to-peak light curve for optical TDEs seems to be more related to radiative diffusion timescale than the fallback timescale (Metzger & Stone, 2016; Van Velzen et al., 2021). Our simulation results roughly agree with this picture that the radiative efficiency varies with mass fallback rate. A higher fallback rate tends to produce a more optically thick outflow, which can reduce the net luminosity by reducing the diffusion rate out of the photosphere. Hence, the luminosity is not strictly proportional to the mass fallback rates.

Figure 5.15 shows the luminosities measured from the simulations. We measure the total luminosity by integrating the radiation flux on the boundary of the simulation domain $L_{\rm out} \sim \int \mathcal{F}_{\rm rad,out} dA$, with the exception that we truncate the measurement to surfaces interior to $r = 40$, rather than integrating out to the outer radial boundary. We find that the measured luminosity is not sensitive to the choice of this enclosed radius as long as $r \gtrsim 35.0$. The measured luminosity includes both the diffusive and advective radiation fluxes on the θ and ϕ boundaries. We expect that the radiation advected through these boundaries will eventually be radiated from the photosphere, which we do not capture within the simulation domain in these directions. Hence, the timescale for this radiation to escape will be longer than estimated here, potentially
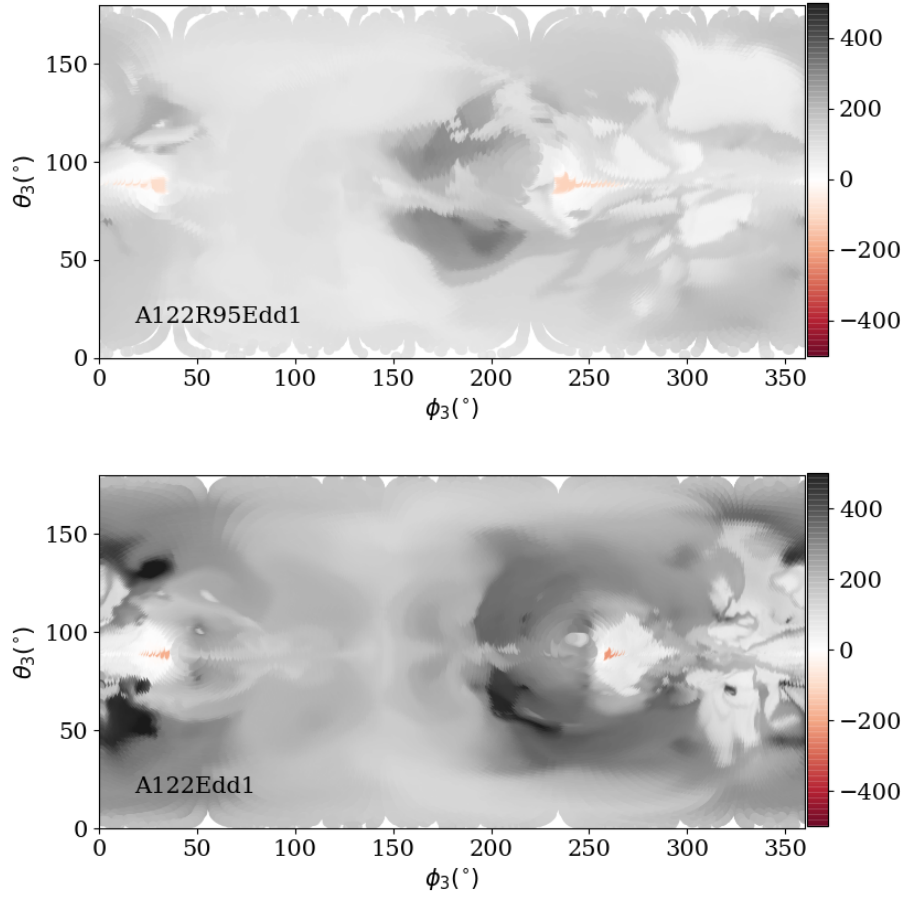
Figure 5.14: Angular distribution of radial velocity $v_{r,3}$ relative to the collision point for all the gas that $\approx 5r_s$ to the collision point. θ_3 and ϕ_3 is the polar and azimuthal angle relative to the collision, and ranges from $0 - \pi$ and $0 - 2\pi$ respectively. The negative $v_{r,3}$ corresponds to the injected streams, the positive $v_{r,3}$ is normal to the sphere and pointed outward, representing the outflowing gas. The upper panel shows the distribution for A122R95Edd1 at $t' = 0.52$. The lower panel shows the distribution for A122Edd1 at $t' = 0.45$, roughly the same time after collision.
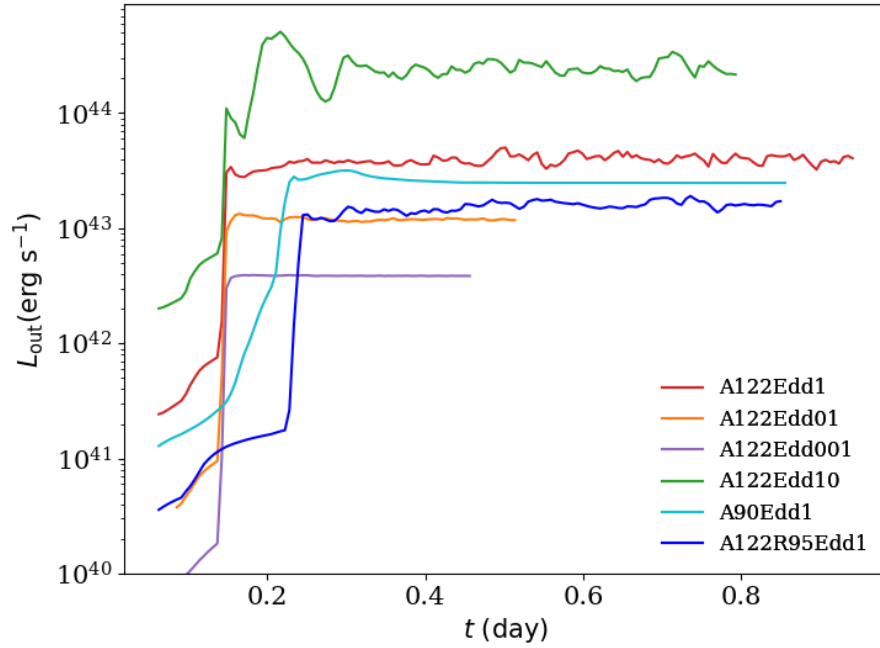
Figure 5.15:   The total luminosity measured from $(27, 40) \times (0.42\pi, 0.58\pi) \times (0.81\pi, 0.96\pi)$ (i.e. the simulation domain up to $r = 40.0$) as a function of time. The red, orange, purple, green solid lines for mass fallback rate with $f_{\mathrm{Edd}} = 0.01, 0.1, 1.0, 10.0$ respectively. The cyan line shows the smaller collision angle of $90°$ with $f_{\mathrm{Edd}} = 1.0$. The blue line shows the larger collision radius of $r_{\mathrm{coll}} \approx 95 r_{\mathrm{s}}$ with $f_{\mathrm{Edd}} = 1.0$.

leading to a lower peak luminosity but longer duration. Due to our relatively short simulation duration and the assumption of fixed mass fallback rates, our simulations can be thought of as modelling specific stages of the rising light curve. Capturing the full pre-peak luminosity rise requires consideration of time-dependent mass fallback rate in a global calculation domain that fully captures the photosphere.

Figure 5.15 shows that prior to the collision, the debris streams are the primary sources of luminosity. As stream-stream collision happens, all the simulations produce a prompt luminosity of $\sim 10^{42-44}$erg s^{-1}, making it an important pre-peak emission source. For the A122 runs, around $t = 0.12$ (0.13day), the stream-stream collision enhances the luminosity by about two to three orders of magnitude. The two simulations with different orbital parameters A90Edd1 and A122R95Edd1 produce similar order-of-magnitude emission as A122Edd1.

Although we find significant prompt emission, we infer that a one-time collision might not be sufficient to produce peak optical luminosity. This is the case even though we have adopted a favorable set-up for generating luminosity by the collision. We assume no vertical offset between the two streams, which may reduce prompt luminosity (Jiang et al., 2016), and we also scale the mass fallback rate to the Eddington rate for a $10^7 M_\odot$ black hole. As we discuss below, we also assume the returning stream is the same width as the fallback stream, and has not spread during pericenter passage. Nevertheless, it still requires a substantially super-Eddington fallback rate to produce luminosity $\gtrsim 10^{44}$erg s^{-1}, corresponding to some observed TDE peak optical luminosity (Mockler et al., 2019; Van Velzen et al., 2021; Gezari, 2021). For a less massive or spinning black hole, the results suggest that a highly super-Eddington fallback rate might be required to explain the peak optical luminosity by a single collision event.

Instead, it is possible that multiple collisions or collision-like events from early-circularizing gas might be able to provide accumulative emission that is consistent with the rise-to-peak optical light curve. Another possibility is that the TDE may be interacting with a preexisting lower luminosity accretion flow (Chan et al., 2021). The range of mass fallback rates we show in Section 5.3.3 may also represent different stages of an increasing mass fallback rate. Adding up the quasi-steady state luminosity for different $\dot{M}$ may yield increasing luminosity in the pre-peak time. In addition, when the fallback rate grows from sub-Eddington to super-Eddington, the downstream gas may change from optically-thin to optically-thick, potentially lead-

ing to spectral or luminosity variation. For a spinning black hole, the collision can
be significantly delayed (Guillochon & Ramirez-Ruiz, 2015; Hayasaki et al., 2016), so
the mass fallback rate may already settle to a relatively constant value when the first
encounter happens. We leave the further discussion of time-dependent mass fallback
rate to future studies.

5.4.2 Photosphere evolution and reprocessing layer

For all the simulations we present (except for A122Edd001), the stream-stream
collision can create an optically-thick outflow. The location of the corresponding
photosphere and its evolution will depend on the line of sight. We use the photosphere
radius $R_{\tau=1}$ (Equation 5.2) to estimate the scattering photosphere along the radial
lines-of-sight towards collision region.

Figure 5.16 shows the average $R_{\tau=1}$ for A122Edd01, A122Edd1, and A122Edd10.
The collision is able to enhance the average $R_{\tau=1}$ by one to two orders of magni-
tude, reaching the quasi-steady state size of $\sim 10^{14}$cm. The super-Eddington run
A122Edd10 shows a transition near $t \sim 0.25$ days, where we observe that the distri-
bution of $R_{\tau=1}$ changes from single-peak to bi-modal, and then becomes single-peak
again. This corresponds to a transient dynamical stage that a leading shell of gas be-
comes optically-thin as it expands, and the $R_{\tau=1}$ distribution starts to be dominated
by other later-accelerated gas. The sub-Eddington run A122Edd01 has a smaller $R_{\tau=1}$
and also a slower growth rate, consistent with lower radiation pressure acceleration.
In the middle row of Figure 5.16, we also plot the difference between $R_{\tau=1}$ and the
collision radius R_{coll} to better show the photospheric expansion.

The growth $R_{\tau=1}$ roughly follows power-law for the A122 simulations. In Fig-
ure 5.17, we show the extrapolation of the $R_{\tau=1}$ evolution up to ~ 60 days. However,
we also note that the extrapolation should not be interpreted as predicted photosphere
evolution. We will show later that, the weaker acceleration runs such as A122Edd01,
A90Edd1 and A122R95Edd1 indicate that the power-law usually can describe the
expansion stage, but the growth will flatten as the outflow decelerates. Properly con-
straining the long term gas dynamics and the inferred photosphere evolution requires
global simulations.

The solid lines in the lower panel of Figure 5.16 show the average gas temperature
$\overline{T}_{\text{gas}}$ measured at $R_{\tau=1}$ surface. Shortly after the collision, the hot post-shock gas
shows an average temperature $\sim 10^5$K. As the outflow expands and cools, the aver-
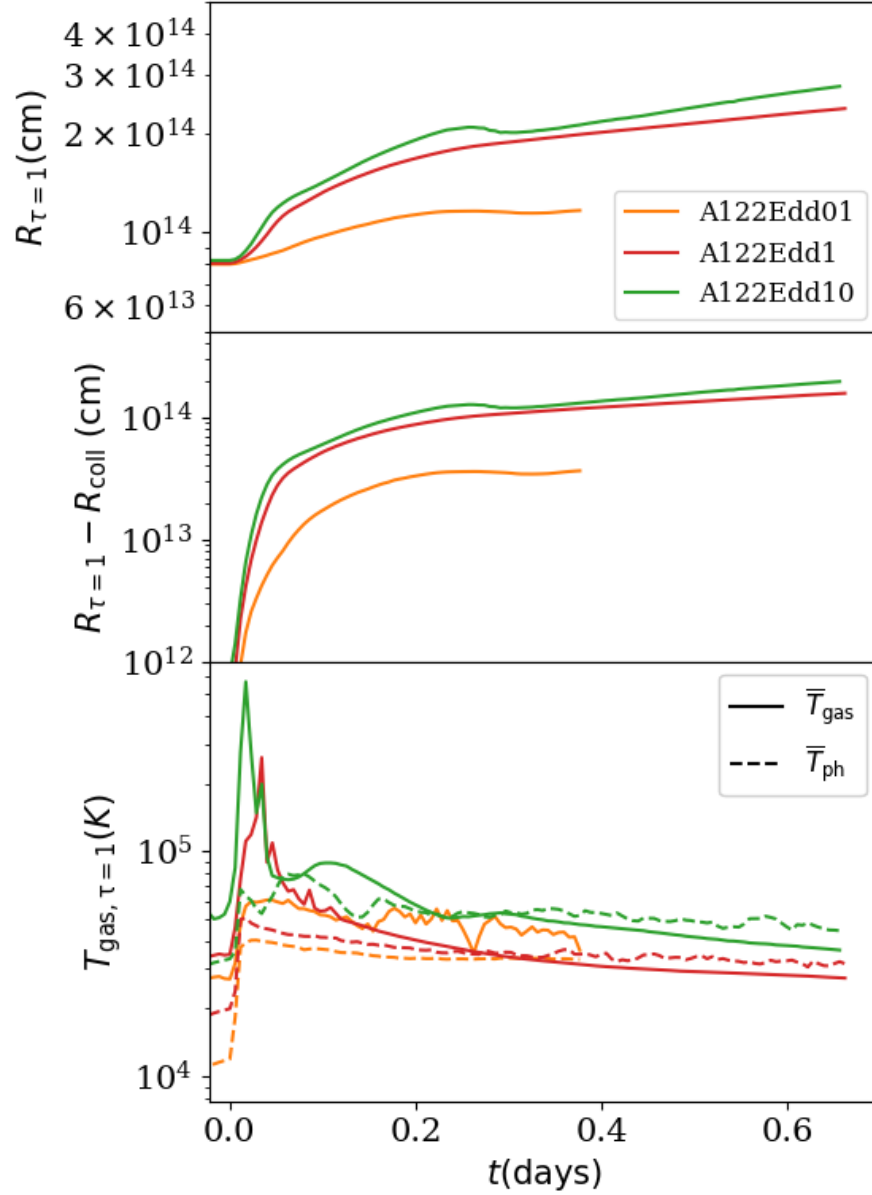
Figure 5.16: The evolution of average photosphere radius $R_{\tau=1}$ (the upper panel), the increment of $R_{\tau=1}$ (the middle panel) and the average temperature. The time is normalized to days since collision. In the lower panel, the solid lines are the measured average gas temperature at $R_{\tau=1}$ surface, and the dashed lines are the estimated radiation temperature according to Equation 5.6.
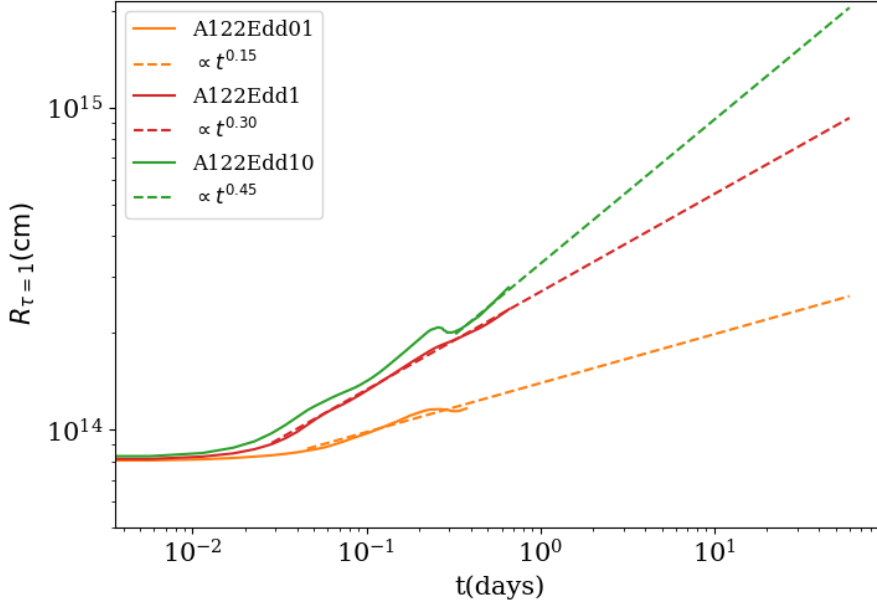
Figure 5.17: The extrapolated $R_{\tau=1}$ evolution for A122Edd01 (orange), A122Edd1 (red) and A122Edd10 (blue). The dashed line are the fitted power-law extrapolation, the slopes are 0.15, 0.30 and 0.45 for A122Edd01, A122Edd1 and A122Edd10.

age gas temperature asymptotes to a few 10^4K, consistent with commonly inferred blackbody temperature in optical/UV TDEs (Gezari, 2021).

We also define a photosphere temperature $\overline{T}_{\mathrm{ph}}$ based on $R_{\tau=1}$ and the total luminosity L_{tot} we measured in simulations (Figure 5.15) by:

$$\overline{T}_{\mathrm{ph}} = \left(\frac{L_{\mathrm{tot}}}{4\pi\sigma_{\mathrm{SB}}R_{\tau=1}^2} \right)^{1/4} \tag{5.6}$$

We plot $\overline{T}_{\mathrm{ph}}$ in Figure 5.16 as the dashed lines. They agree with average gas temperature $\overline{T}_{\mathrm{gas}}$ well at late time when the photosphere becomes more isotropic, but deviate from $\overline{T}_{\mathrm{gas}}$ at early time because of the anisotropy of photosphere.

We also estimated a thermalization radius R_{th}, which roughly characterizes the surface exterior to which a typical photon can be emitted and leave the domain without be absorbed (Rybicki & Lightman, 1986). Here we adopt a definition similar to $R_{\tau=1}$, but replace κ_s by $\sqrt{\kappa_s\kappa_a}$ (assuming $\kappa_s \gg \kappa_a$) in Equation 5.2. We found that the average R_{th} is generally smaller than $R_{\tau=1}$. For example, Figure 5.18 compares average R_{th} and $R_{\tau=1}$ in A122Edd1 and A122Edd10, where both quantities are rel-
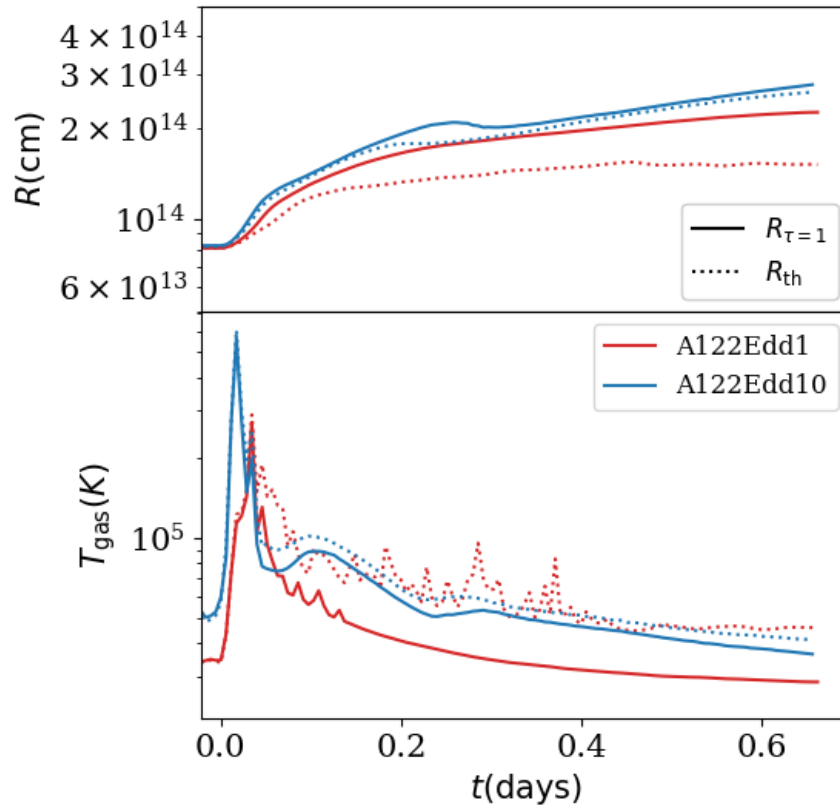
Figure 5.18: Upper panel: Comparing average scatter photosphere radius $R_{\tau=1}$ (the solid lines) and thermalization radius R_{th} (the dotted lines). The time is normalized to days since collision. Lower panel: the measured average gas temperature at $R_{\tau=1}$ (the solid lines) surface and R_{th} (the dotted lines) surface.

atively uniform. In both cases, $R_{\tau=1}$ is slightly larger than R_{th}. The downstream gas in A122Edd10 is more optically thick than A122Edd1, and the two radii track each other more closely and the average gas temperature shows less difference. In A122Edd001 and A122Edd01, the location of R_{th} is highly anisotropic about the collision point due to the downstream gas flow being more optically thin. Nevertheless, the results are qualitatively consistent with the higher fallback rate runs in that its location is interior to the photosphere and the temperature are larger than those at the photosphere.

Figure 5.19 shows $R_{\tau=1}$ for the two runs with modified orbits. The general evolution is similar to the A122Edd1. In A122R95Edd1, evolution of $R_{\tau=1}$ flattens more towards the end of simulation when compare to A122Edd1. But the the estimated photospheric temperature $\overline{T}_{\mathrm{ph}}$ is usually lower than $\overline{T}_{\mathrm{gas}}$ in quasi-steady state. We find that the average gas temperature at $R_{\tau=1}$ is relatively uniform, the discrepancy is more relevant to the inhomogeneous shape of photosphere. For A122Edd1 and A122Edd10, the angular distribution of $R_{\tau=1}$ and $\overline{T}_{\mathrm{gas}}$ is relatively uniform. In contrast, the angular distribution of $R_{\tau=1}$ show larger dispersion in A122Edd001, A122Edd01 and A90Edd1, suggesting that the photosphere is more ellipsoidal than spherical. For example, A122Edd1 has average photosphere radius $R_{\tau=1} \approx 67.10 r_{\mathrm{s}}$ with dispersion $\delta_{R_{\tau=1}} \approx 2.94 r_{\mathrm{s}}$ at $t = 0.45$, but A90Edd1 has $R_{\tau=1} \approx 78.68 r_{\mathrm{s}}$ with dispersion $\delta_{R_{\tau=1}} \approx 12.25 r_{\mathrm{s}}$ at $t = 0.45$. Using the spherical assumption can overestimate the surface area and underestimate $\overline{T}_{\mathrm{ph}}$, but it normally does not lead to an order-of-magnitude difference.

5.4.3 Comparison to Previous Studies

Angular Momentum of Downstream Gas: In our simulations, the strong radiation pressure produced in the stream-stream collision sufficiently redistributes downstream gas angular momentum. Lu & Bonnerot (2020) show that the collision is able to cause a significant spread in downstream gas angular momentum with respect to the original stellar orbital plane, enabling the formation of an extended accretion disk. Our findings also agree with this picture. Following Tejeda & Rosswog (2013), we define total angular momentum as $|l| = r_1^3 (\dot{\theta}_1^2 + \sin_1^2 \dot{\phi}_1^2)^{1/2}/(r_1 - r_{\mathrm{s}})$, and orbital-plane angular momentum as $l_{\mathrm{z}} = r_1^3 \dot{\phi}_1/(r_1 - r_{\mathrm{s}})$, where the velocities and radius corresponds to the black hole.

Figure 5.20 shows the distribution of outflow angular momentum, where we se-
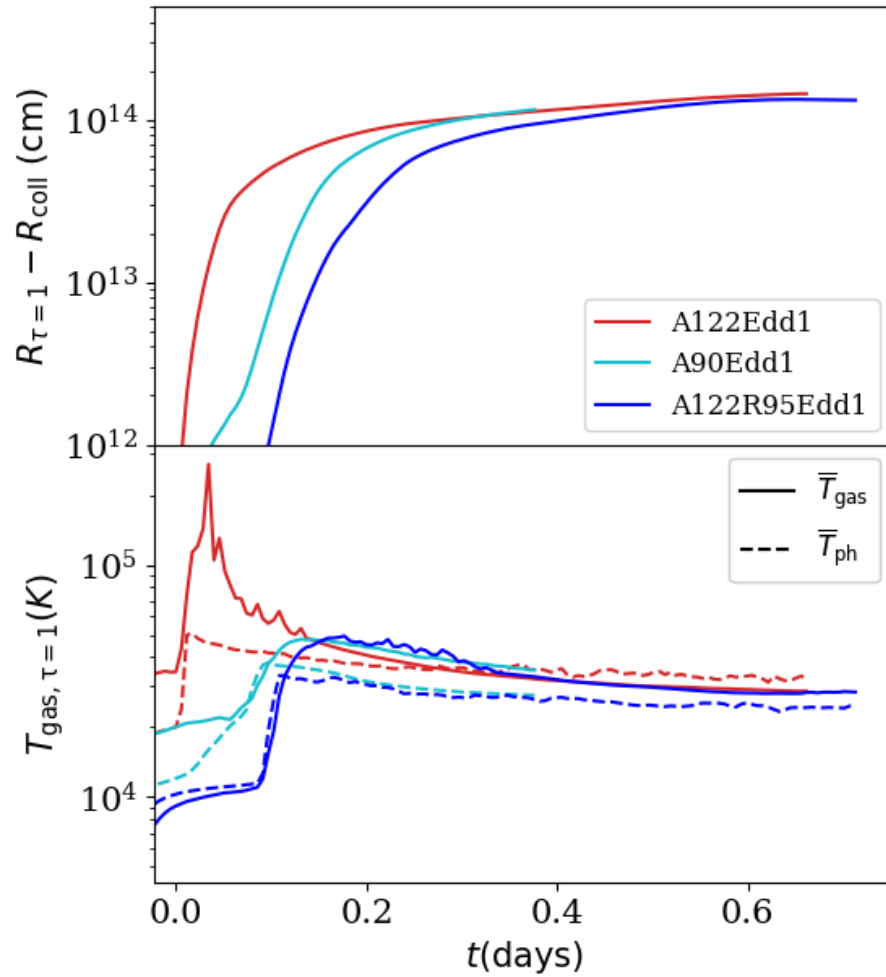
Figure 5.19: The evolution of average photosphere radius $R_{\tau=1}$ (the upper panel) and the average temperature for A122Edd1 (red), A90Edd1 (cyan) and A122R95Edd1 (blue), plotted time is normalized to days since the collision. In the lower panel, the solid lines are average gas temperature at $R_{\tau=1}$ surface, the dashed lines are the estimated photosphere temperature according to Equation 5.6
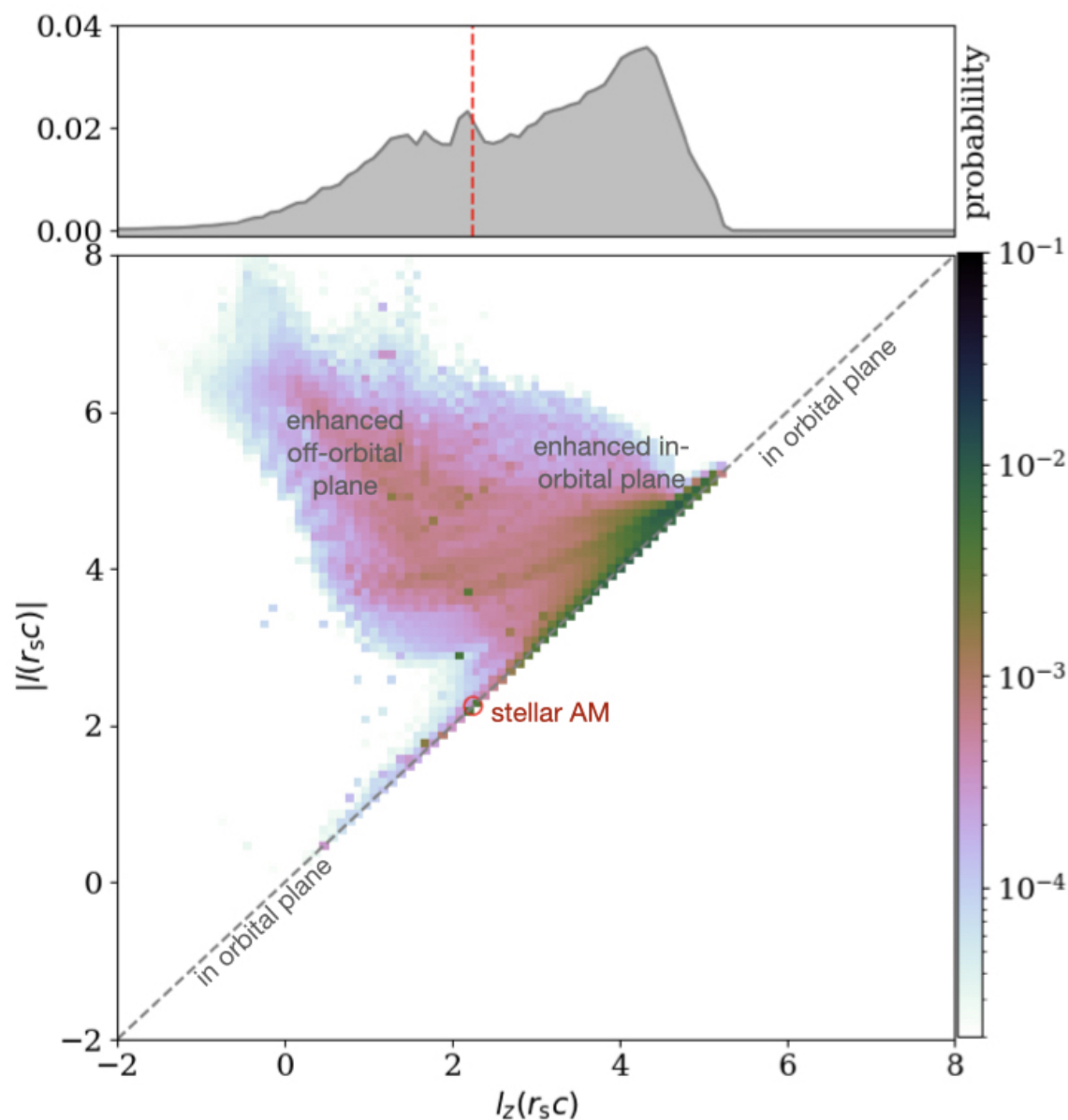
Figure 5.20: Downstream gas angular momentum distribution from A122Edd1 at t=0.3. We only show gas with positive radial velocity relative to the collision point $v_{r,3} > 0$. The first row shows the (mass weighted) angular momentum l_z distribution projected to the orbital plane. The red vertical line labels the original stellar debris stream angular momentum. The second row shows the distribution of total angular momentum magnitude $|l|$ and projected angular momentum l_z. The red circle shows the original stellar stream value, the gray dashed line labels the angular momentum within the orbital plane.

lect gas moving away from the collision point. The first row shows that orbital-plane angular momentum l_z is significantly spread by the collision. Compared to Lu & Bonnerot (2020), we find the distribution is more asymmetric relative to the initial stellar angular momentum and the retrograde fraction (negative l_z) is lower, potentially due to stronger radiative acceleration in the radial direction.

The second row of Figure 5.20 shows the distribution of $|l|$ and l_z. The gray dashed line labels the orbital plane, where $|l| = l_z$. In the orbital plane, a noticeable fraction of gas gains angular momentum. Off the orbital plane, some gas shows low l_z but enhanced $|l|$, we also find this gas is usually unbound, corresponding to the unbound outflow propagating away from the orbital plane. A122Edd10 shows a similar distribution, with a slightly stronger off-orbital plane outflow. Other simulations also show a significant spread in the specific angular momentum distribution, but the relative distribution of $|l|$ and l_z is sensitive to the outflow morphology. For example, A90Edd1 and A122R95Edd1 both show weaker off-orbital plane outflow, so a tighter distribution in $|l|$.

Previous studies had proposed a quasi-spherical envelope or wind from the early-circularizing gas to explain the reprocessed optical emission (Ulmer, 1999; Roth et al., 2016; Metzger, 2022). The off-orbital plane outflow with enhanced angular momentum we observed in A122Edd1 and A122Edd10 may contribute to the formation of such pressure-supported envelope at early times, but the long-term evolution of these outflow gas should be tracked in an extended calculation domain to confirm.

Outflow morphology: Some previous models for optical emission include a quasi-spherical wind near the disk. An important difference of the outflow observed in our simulations is its inhomogeneous, asymmetric morphology. Compared to Jiang et al. (2016), the inclusion of gravity changes the outflow morphology at larger radius, especially when the collision angle is small, such as in A90Edd1. Lu & Bonnerot (2020) tracks the streamlines of collision induced outflow elements, and estimates that the outflow gas distributes roughly within a cone-geometry. We also find that the outflow produced in A122Edd1, A122Edd10 and A122R95Edd1 is roughly within a cone centered on the collision point, but generally less oriented towards the black hole, potentially due to the redistribution by radiation pressure.

A commonly used assumption of the outflow/wind is quasi-spherical morphology with relatively constant radial velocity and $\propto r^{-\xi}$ density profile (Strubbe & Quataert, 2009; Jiang et al., 2016; Bonnerot et al., 2021). For example, assume a

spherical outflow the with density $\rho \propto r^{-2}$. Within the photon-trapping radius, the outflow expands nearly adiabatically, the radiation energy density $U_r \propto P_r \propto \rho^{4/3} \propto r^{-8/3}$ (Strubbe & Quataert, 2009), so the luminosity at a radius roughly follows $L \propto 4\pi r^2 U_r \propto r^{-2/3}$.

In A122Edd1, A122Edd10 and A122R95Edd1, we find that only within a cone of $\sim 45°$ with distance of $\lesssim 15r_s$ relative to the collision point, the average radial velocity is roughly constant ($\sim 0.1c$) and the density distribution roughly follows $\propto r^{-2}$. For example, at $t = 0.3$, A122Edd1 show an average density profile $\propto d_{coll}^{-2.3}$, where d_{coll} is the distance to collision point. We also find that within the cone, the radiation energy density profile $\sim d_{coll}^{-3.2}$, which is a slightly steeper drop than $\sim r^{-8/3}$, potentially due to the diffusive radiation flux. Outside the cone, the velocity distribution is anisotropic, especially near the streams. For example, the lower panel of Figure 5.14 shows the radial velocity distribution of A122Edd1 on a sphere that is $5r_s$ from the collision point. The velocity distribution within $100° \lesssim \phi_3 \lesssim 190°$, $v_{r,3}$ is relatively uniform, but it is anisotropic in other regions. In other simulations, the outflow morphology is even more anisotropic.

Such asymmetric outflow morphology may affect the radiative efficiency too. Compared to a purely adiabatic spherical outflow, radiation may preferentially diffuse out from the optically thin regions near the collision point during expansion. For simplicity, we can assume all the stream kinetic energy is deposited as luminosity L_{coll} immediately at collision within a spherical region of $r \sim H$, where H is the width of the stream. Assuming no diffusion and adopting the $L \propto r^{-2/3}$ dependence derived above, radiative efficiency can be roughly estimated as the ratio between L_{coll} and the luminosity escaping at $r_{\tau=1}$, so $\eta_{rad} \sim (r_{\tau=1}/H)^{-2/3} \sim ((R_{\tau=1}/10^{14}\text{cm})/(\text{H}/3\text{R}_\odot))^{-2/3} \sim 1.6\%$.

The radiative efficiency η_{rad} we found is usually higher than this estimation, consistent with enhanced radiative losses due to photon diffusion. Similar to the total luminosity $L_{out} \sim \int \mathcal{F}_{rad,out} \cdot \mathbf{dA}$ (Figure 5.15), we can estimate the "advective" part by replacing $\mathcal{F}_{rad,out}$ by $\mathcal{F}_{rad,adv} \sim \mathbf{v}E_{rad}$, where $\mathbf{v}$ is gas velocity. So the difference between total luminosity and the advection part provides an estimate of the diffusive part. We find the advective fraction increases as f_{edd} increases, consistent with previous speculation. But we also find even for higher mass flux runs, there is a non-negligible diffusive fraction. For example, for A122Edd1, the advection fraction is $\sim 80\%$ from the optically thick region near to the collision point, and drops to $\sim 68\%$

as gas moves outward. The total radiation flux from the ϕ direction boundaries has two to three times lower advection fraction than the other boundaries. These findings suggest the expansion of the outflow is not strictly adiabatic due to the photon diffusion within the anisotropic outflow.

Returning Stream Width: We assume the returning stream has the same width as the fallback stream in the simulations. Previous studies of TDEs with low mass ratios (Ramirez-Ruiz & Rosswog, 2009; Rosswog et al., 2009; Shiokawa et al., 2015) or deep penetration encounters (Sadowski et al., 2016) suggest thickened streams due to the strong nozzle shock near pericenter. Recent studies of TDEs by more massive black hole can also show significantly expansion in the returning stream, potentially changing the collision initial condition and outcome (Liptai et al., 2019; Curd, 2021; Andalman et al., 2022; Steinberg & Stone, 2022).

Bonnerot & Stone (2021) compares the potential outcomes of stream-stream collision with different returning stream widths. They suggest that a thickened returning stream with reduced density could sweep through the thin stream without significant deflection, suppressing the radiation pressure produced during stream-crossing, making it less likely to drive strong outflow. Steinberg & Stone (2022) adopt a equation of state including hydrogen recombination and suggests the recombination heating near pericenter can significantly expand the stream and potentially enhance the nozzle shock dissipation. Coughlin (2023) also suggest that the steam density can be lowered by the recombination processes near pericenter. Bonnerot & Lu (2022) performed high resolution study of the vertical compression of the stream and energy dissipation due to the nozzle shock. They, however, suggest that the stream is likely to stay relatively thin after the pericenter, and that the dissipation is sensitive to compression. The stream could be compressed to $\sim 0.1\%$ of the stellar radius in vertical direction and $\sim 10\%$ in the orbital plane. Such large compression rate requires sufficient resolution to minimize numerical dissipation and capture the stream expansion accurately after pericenter. We also note that our assumption of the same stream width at in-plane and vertical direction is idealized. Recent works (Bonnerot et al., 2022; Coughlin, 2023) suggest that the stream geometry is set by the interplay between tidal force, pressure support and self-gravity. The relative importance of these forces is likely sensitive to gas density. As the gas orbits around the black hole, the stream cross-section can deviate significantly from circular.

In the global test calculations with static mesh refinement (similar set-up to Fig-

ure B.1, not presented in this paper), we find qualitative consistent results. Without radiation, the hydro dynamical simulations do not show convergence to the returning stream width at our highest test resolution ($\delta R \sim 0.16 r_{\rm s}$). We find generally less spreading of the stream after pericenter as we increase the resolution. Interestingly, when we include radiation, the RHD test simulations (similar to Figure B.1, with same or lower resolution ($\delta R \gtrsim 0.16 r_{\rm s}$), not presented in this paper), we find the stream stays almost the same width after the pericenter regardless of resolution, but this may be due to insufficient resolution in the test calculations, leading to an overestimation of radiative cooling. When the thinnest part of the stream at the pericenter is only resolved by a few cells, the radiative cooling can be overestimated, reducing internal energy dissipated in the nozzle shock. Resolving the stream near the pericenter is essential to understanding the role of stream-stream collision as pre-peak emission mechanisms of TDEs. We plan to explore the collision between streams with different widths in the future work.

5.5 CONCLUSIONS

We study the stream-stream collision in TDEs through a series of three-dimensional RHD simulations. We adopt a stream orbit based on a $10^7 M_\odot$ black hole and a solar type star, with the penetration factor of $\beta = 1.0$. We compare the effect of different mass fall back rate ($f_{\rm edd} = 0.01, 0.1, 1.0, 10.0$), the collision angle ($\theta_{\rm coll} \approx 122°, 90°$), and collision radius ($r_{\rm coll} \approx 24 r_{\rm s}, 95 r_{\rm s}$). We study the radiation pressure driven outflow and potential optical emission from the stream-stream collision. We summarize our findings as follows:

(1) **Dependency on Resolution**: We find that RHD simulations of stream-stream collisions are very sensitive to resolution. Insufficient resolution may artificially thicken the stream, reducing the stream vertical optical depth and the kinetic energy density before collision. These effects suppress radiation energy generation at the collision, leading to a qualitatively inaccurate picture of downstream gas distribution (Figure 5.3). The under-resolved simulations might also underestimate the outflow optical-depth, allowing radiation to escape before it can interact sufficiently with gas. In our calculations, we use spatial resolution of $\sim 10^{-2} r_{\rm s}$ (or $\sim 0.85 R_\odot$). We find that minimum 48 angular bins for radiation is required in order to reach convergence in the properties of the post collision flow.

(2) **radiative efficiency and Luminosity**: With the assumption of thin streams

without vertical off-set, the stream-stream collision can convert $\gtrsim 5\%$ of kinetic energy to radiation, producing a luminosity of $\sim 10^{43-45}$erg s^{-1}. The radiative efficiency $\eta_{\rm rad}$ is affected by both the energy conversion at the collision and the interaction between radiation and downstream gas.

When the stream collision angle and radius is fixed, the radiative efficiency $\eta_{\rm rad}$ is sensitive to the mass fallback rates (Figure 5.9) and could range from $\sim 5\%-60\%$. The higher fallback rates usually show lower radiative efficiency. The radiation pressures produced in the collision are usually higher, but drive optically-thick outflows. In these outflows, radiation accelerates gas, converting radiation energy back to gas kinetic energy. In contrast, lower mass fallback rates usually yield more optically-thin downstream gas, where radiation diffuses out more easily, leading to higher luminosity and net radiative efficiency.

When the mass fallback rate and collision radius are fixed, the smaller collision angle usually produces less radiation from the collision, resulting in lower radiation pressure. This can lead to more optically-thin downstream gas, where radiation diffusion is enhanced. Due to the competing effects from the kinetic energy dissipation at the collision and downstream gas optical depth, A122Edd1 and A90Edd1 yield similar radiative efficiency despite the different collision angle. The radiative efficiency seems less sensitive to the collision radius. A122Edd1 and A122R95Edd1 shows similar shock structure at the collision and downstream gas distribution, resulting similar radiative efficiency.

(3) Radiation Driven Outflow: In the simulations, when the mass fallback rate is $\gtrsim 10\%$ Eddington, the radiation pressure can accelerates gas to form expanding optically-thick outflow, making $\sim 10\%-15\%$ mass of gas unbound. The unbound gas is preferentially propagating off the orbital plane, with an order-of-magnitude $\sim 0.1c$ radial velocity relative to the collision point.

The collision largely redistributes downstream gas specific angular momentum, resulting highly aspherical outflow. In A122Edd1, A122Edd10, A122R95Edd1, the outflow has an approximately conical geometry. Within the cone, the density profile roughly follows $\propto r^{-2}$, and gas moves radially away from the collision point with $\sim 0.1c$ velocity. In A90Edd1 and A122Edd001 show more anisotropic morphology of the outflow, where a majority of gas is within a stream-structure bent towards the black hole. The outflow morphology seems to show a potential trend from stream-structure to conical-geometry as radiation pressure increases. In all simulations, the

anisotropy of downstream gas leads to non-negligible radiative diffusion, and the outflow expansion is not strictly adiabatic.

(4) Photosphere Evolution: We estimate photosphere along the line-of-sight towards the collision region. We find that the stream-stream collision is able to expand $R_{\tau=1}$ by one or two orders of magnitude, resulting $\sim 10^{14}$cm photosphere. The average gas temperature $\overline{T}_{\mathrm{gas}}$ at $R_{\tau=1}$ is usually a few 10^4K. The estimated photosphere temperature $\overline{T}_{\mathrm{ph}}$ is generally consistent with $\overline{T}_{\mathrm{gas}}$ (Figure 5.16, Figure 5.19). These findings suggest that the stream-stream collision provides a promising mechanism to drive pre-peak photospheric evolution, and produces photosphere size consistent with optical observations.

The anisotropic outflows formed in our simulations may lead to inclination-dependent photospheric properties. For example, downstream gas could be noticeably more optically-thin outside the cone-like outflow in some runs. In other simulations, the outflow is also usually preferentially launched in some directions instead of expanding spherically relative to the collision point.

Caveats Our local calculation domain is optimized for resolving the collision shock and tracking gas motion in the net momentum direction, but the long-term outflow evolution and photosphere in θ and ϕ directions can be beyond the calculation domain. Studying the system in a global domain will be the focus of our future work. When modeling the streams, we ignored the effect of self-gravity (Guillochon et al., 2014; Coughlin et al., 2016), the debris energy distribution (Spaulding & Chang, 2021), or magnetic fields (Guillochon & McCourt, 2017; Bonnerot et al., 2017) on the stream structure. When modeling the black hole, we adopt an approximate gravity description best suited to a spin-less black hole. The spin can significantly change the stream orbit, resulting vertical offset between the streams and potential modifications to returning stream width (Guillochon & Ramirez-Ruiz, 2015; Hayasaki et al., 2016; Batra et al., 2023). Jiang et al. (2016) showed that the luminosity produced by the stream-stream collisions will be suppressed by the vertical offset if both stream are thin. Jankovič et al. (2023) explored the spin-induced collision angle modification and vertical offset, and found aspherical downstream gas can also be launched due to offsetting collision, potentially leading to similar enhanced radiation diffusion in postshock gas. We also fix the mass injection rate in the simulation, but we show that the outflow optical depth and potential photosphere property can change with mass fallback rate. Including the time-dependence of the mass fallback rate and potential

pre-peak emission variability is also an interesting focus for future work.

CHAPTER 6

SUMMARY AND FUTURE DIRECTIONS

This dissertation has discussed various projects of gas dynamics in extreme astrophysical environment. The projects have followed a common thread of exploring radiation and CR (magneto)hydrodynamics with the state-of-the-art numerical tool Athena++. This includes topics such as the launching of galactic wind on kpc-scale, turbulence that drives mixing in multiphase CGM gas at pc-scale, and accretion processes at the very inner gravitational radii near blackholes.

In Chapter 2, I studied the ability of radiation pressure to launch dusty molecular outflow using two-band RHD simulations, where the dusty gas absorbs UV radiation and re-emits infrared (IR) radiation. I find that the cloud survival time is sensitive to the ratio between IR and UV radiation flux. The radiation acceleration is most promising where IR dominates the spectral energy distribution (SED). Extending this work, I plan to model the radiation field using the new multi-group RT module in Athena++, to understand the effect of adopting a frequency-dependent dust opacity compared to the more commonly-used grey dust opacities.

In Chapter 3, I studied CRs ability to drive galactic outflow using the two-moment CR transfer module in Athena++. Analogous to radiation, we explore a CR Eddington limit and identify (extra-)galactic environments where CRs are potentially important to drive outflows, providing an approximate quantitative estimate of CRs ability to disperse gas against gravity and suppress star formation. Testing the model with numerical simulations, we find general agreement between the quantitative prediction and simulations. I also found that the efficiency of CR momentum and energy imparted to gas depends on various factors, including the magnitude of CR flux and the relative importance of CR transfer mechanisms such as diffusion and streaming.

In Chapter 4, I studied the interaction between CR and multiphase gas formed *in situ* via thermal instability. By creating multi-phase gas from thermal instability, our set-up preserves the phase-interface structure, the pressure confinement, and the non-uniform magnetic field.

I find the radiative cooling in turbulent mixing layer can lead to cold gas growth when entrained in a hot wind. In contrast, for CR driving, cold gas mass generally decreases, albeit more slowly than when radiative cooling is neglected. We conclude that the nature of CR and thermal pressure gradients near the interface of hot and cold gas are intrinsically different, leading to observable differences, such as the characteristic column densities and the velocity distribution of multiphase outflow. I will continue to explore how CRs and magnetic field affect the multiphase CGM/ISM gas structure via direct heating and momentum coupling, and fit them into the leading mixing layer or turbulence theories. I am also interested in improving modeling CR microphysics in numerical schemes, and incorporating these non-thermal physics into kpc-scale simulations.

Finally, in Chapter 5, I studied a potentially important pre-peak emission mechanism for TDE: stream-stream collision, which happens when the apsidal precession shifts the stream orbit and leads to stream self-intersection. The strong shock at the collision can efficiently convert kinetic energy into radiation. Dynamically, radiation couples with both gas momentum and energy, forming a local super-Eddington region near the collision shock.

I find that resolving the stream-stream collision in simulations is essential. The work shows that insufficient resolution gives a qualitatively incomplete picture of photosphere evolution. Under-resolved simulations could artificially thicken the stream, reducing radiation pressure produced in the collision, and decreasing the radiative acceleration of downstream gas. Therefore, the photosphere size can be significantly underestimated and even fail to form an optically-thick outflow.

The scaling between mass fallback rate and collision-induced luminosity deviates from a linear relation due to the interaction between radiation and post-shock gas. Our results suggest that the collision alone is usually insufficient to power the peak optical luminosity, but it can contribute $\sim 10^{42-44}$erg s^{-1} pre-peak luminosity by converting more than 8% of kinetic energy to radiation nearly instantaneously. More importantly, it can create an asymmetric, optical-thick reprocessing layer that roughly matches the observed pre-peak photosphere evolution.
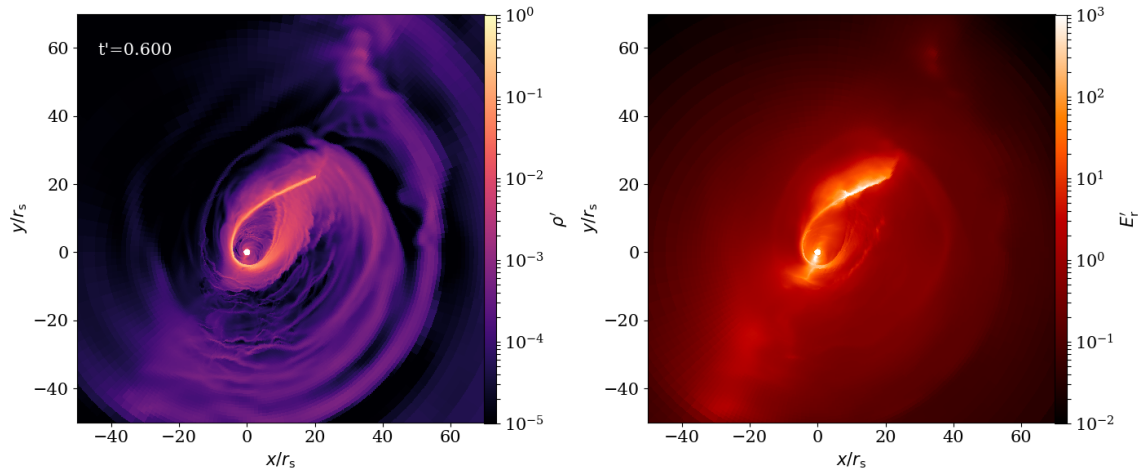
Figure 6.1: Gas density (left) and radiation energy density (right) in lab frame at orbital-plane from a test calculation. We model the debris stream as an uniform gas stream injected near $\sim 30 r_\mathrm{s}$. The stream is based on the orbit of $10^7 M_\odot$ disrupting a solar-type star, with orbital penetration factor $\beta = 1.0$. The stream will be expanded a little after the pericenter, modifying the stream-stream collision.

Moving forward, I plan to study the accretion of TDE fallback material with a series of three-dimensional (GR)R(M)HD simulations. Figure 6.1 shows a test calculation. I will exploit the adaptive mesh refinement (AMR) functionality in Athena++ to resolve the stream and the inner disk formation region, while extending the calculation domain to track a larger portion of the initial debris stream and the unbound gas. The interactions between the collision-induced outflow, the circularizing gas, and the continuous feeding stream are the potential origins of multi-band emission. The work will also include Monte Carlo post-processing to generate synthetic observable.

Appendix A

CR Acoustic Instability Dispersion Relation

We briefly summarise the acoustic instability dispersion relation based on CR transport equations for the conditions relevant to our simulations. We refer the reader to Tsung et al. (2021) for a more thorough discussion of the instability . To keep the problem tractable, we assume a one-dimensional geometry with a 1-moment approximation similar to that used in previous work (Begelman & Zweibel, 1994). The 1-moment and 2-moment scheme gives similar results in the derived growth rate (Tsung et al., 2021). We first define the scale height for the background CR pressure L_c, gas pressure L_g and gas density L_ρ as:

$$L_\mathrm{c}^{-1} \equiv -\frac{\partial \ln P_\mathrm{CR}}{\partial x}, \quad L_\mathrm{g}^{-1} \equiv -\frac{\partial \ln P_\mathrm{g}}{\partial x}, \quad L_\rho^{-1} \equiv -\frac{\partial \ln \rho}{\partial x} \tag{A.1}$$

We also define the scaled diffusivity l_c

$$l_\mathrm{c} \equiv \frac{\kappa_\mathrm{diff}}{c_\mathrm{s}} \tag{A.2}$$

Using WKB approximation with perturbations $\propto \exp(i\omega t - ikx)$, when $kL \gg 1$, we can rewrite the perturbed equations as:

$$\omega\delta\rho = \left(1 - \frac{i}{kL_\rho}\right)k\rho\delta v$$

$$\omega\delta v = \frac{k}{\rho}\delta P_{\mathrm{g}} + \frac{k}{\rho}\delta P_{\mathrm{CR}} - i\frac{\delta\rho}{\rho}g$$

$$\omega\delta P_{\mathrm{g}} = \left(1 - \frac{i}{\gamma_{\mathrm{g}}kL_{\mathrm{g}}}\right)\gamma_{\mathrm{g}}kP_{\mathrm{g}}\delta v \tag{A.3}$$

$$+ \; i(\gamma_{\mathrm{g}} - 1)\frac{P_{\mathrm{CR}}v_{\mathrm{A}}}{L_{\mathrm{c}}}\frac{\delta\rho}{2\rho} + (\gamma_{\mathrm{g}} - 1)kv_{\mathrm{A}}\delta P_{\mathrm{CR}}$$

$$\omega\delta P_{\mathrm{CR}} = \left(1 - \frac{i}{\gamma_{\mathrm{c}}kL_{\mathrm{c}}}\right)\gamma_{\mathrm{c}}kP_{\mathrm{CR}}\delta v \tag{A.4}$$

$$+ \; (kv_{\mathrm{A}} + i\kappa_{\mathrm{diff}}k^2 + \frac{i\gamma_{\mathrm{c}}v_{\mathrm{A}}}{2L_\rho})\delta P_{\mathrm{CR}} \tag{A.5}$$

$$- \; (1 + \frac{3i}{2kL_\rho} - \frac{i}{\gamma_{\mathrm{c}}kL_{\mathrm{c}}})\gamma_{\mathrm{c}}kv_{\mathrm{A}}P_{\mathrm{CR}}\frac{\delta\rho}{\rho} \tag{A.6}$$

The quantities with δ are the perturbed quantities, ω is the frequency and k is the wave number. To compare with Begelman & Zweibel (1994) and other previous work, these equations differ slightly from the equations evolved by Athena++ in two ways. Equation (1.13) is replaced by a relation for the CR flux of the form

$$F_{\mathrm{c}} = (v + v_{\mathrm{A}})(E_{\mathrm{c}} + P_{\mathrm{c}}) - \kappa_{\mathrm{diff}}\frac{\partial E_{\mathrm{c}}}{\partial x}. \tag{A.7}$$

This is generally a good approximation since the $\partial F_{\mathrm{c}}/\partial t$ term in equation (1.13) is negligible. Furthermore, previous treatments replace $\partial E_{\mathrm{c}}/\partial t$ with $\partial P_{\mathrm{c}}/\partial t$ in equation (1.12).

We adopt Begelman & Zweibel (1994) notation and define:

$$\nu \equiv \frac{\omega}{kc_{\mathrm{s}}}, \quad m \equiv \frac{v_{\mathrm{A}}}{c_{\mathrm{s}}}, \quad c \equiv \frac{c_{\mathrm{CR}}}{c_{\mathrm{s}}}, \tag{A.8}$$

where $c_{\mathrm{CR}} = \sqrt{\gamma_{\mathrm{c}}P_{\mathrm{c}}/\rho}$ is the CR acoustic speed with $\gamma_{\mathrm{c}} = 4/3$, and c_{s} is the sound
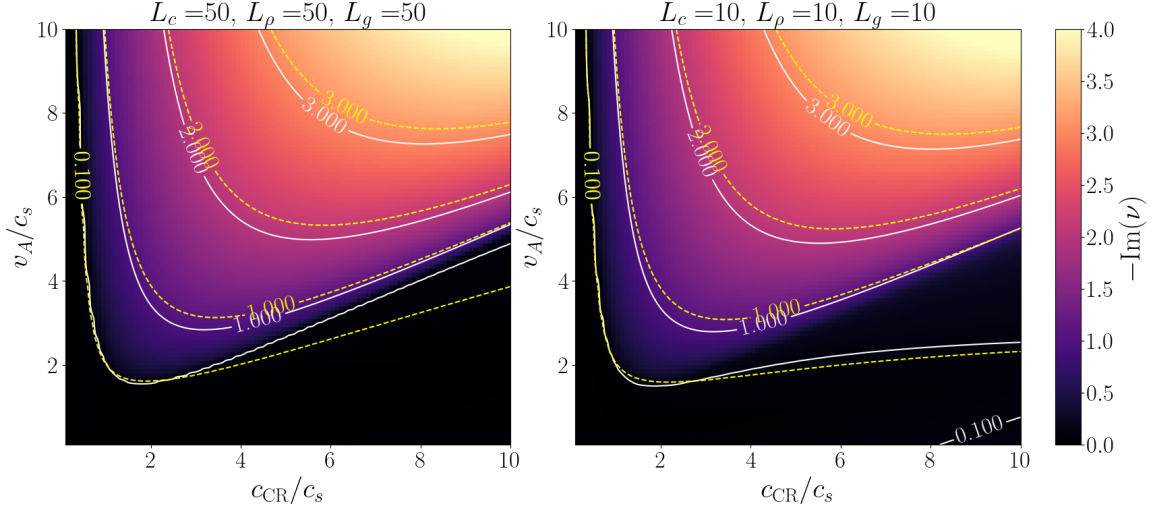
Figure A.1: The re-scaled growth rate -Im(ν) as a function of v_A/c_s and c_{CR}/c_s for different sets of scale height $L_c = L_\rho = L_g = 50$ (left) and $= 10$ (right). In both plots, the gravity $g = -0.826$, the magnetic field is assumed to be uniform and static. The white solid lines represent solutions with streaming transport, the yellow dashed curves are contours represent streaming with moderate CR diffusion.

speed. Solving the equations gives the dispersion relation:

$$
(-ikl_c - m + \nu - \frac{i\gamma_c}{2kL_\rho}m)\left[\left(1 - \frac{i}{kL_\rho}\right)\left(1 + \frac{g}{kc_s^2\nu^2}\right)\nu^3\right.
$$
$$
\left. -\nu\left(1 - \frac{i}{kL_g\gamma_g}\right) - i\frac{(1 - \frac{i}{kL_\rho})c^2 m(\gamma_g - 1)}{2L_c\gamma_c k}\right]
$$
$$
-c^2\nu^2(1 - \frac{i}{kL_c\gamma_c})(1 + \frac{m}{\nu}(\gamma_g - 1))
$$
$$
+\frac{1}{2}m^2c^2(1 - \frac{i}{kL_\rho})\left(1 + \frac{3i}{2kL_\rho} - \frac{i}{kL_c\gamma_c}\left(\frac{\nu}{m} + (\gamma_g - 1)\right)\right)
$$
$$
= 0 \qquad (A.9)
$$

When $kl_c \gg 1$ and the background is uniform (drop the L_ρ, L_c and L_g terms), without gravity g, Equation A.9 is equal to the Eq 3.18 in Begelman & Zweibel (1994) in 1D form.

Figure A.1 shows the re-scaled growth rate $-\text{Im}\nu$ for $k = 1$ mode (white contour) for two sets of scale heights $L_g = L_c = L_\rho = 50$ (left) and $L_g = L_c = L_\rho = 10$ (right) when streaming dominates, corresponding to $l_c = 10^{-8}$. The yellow curves
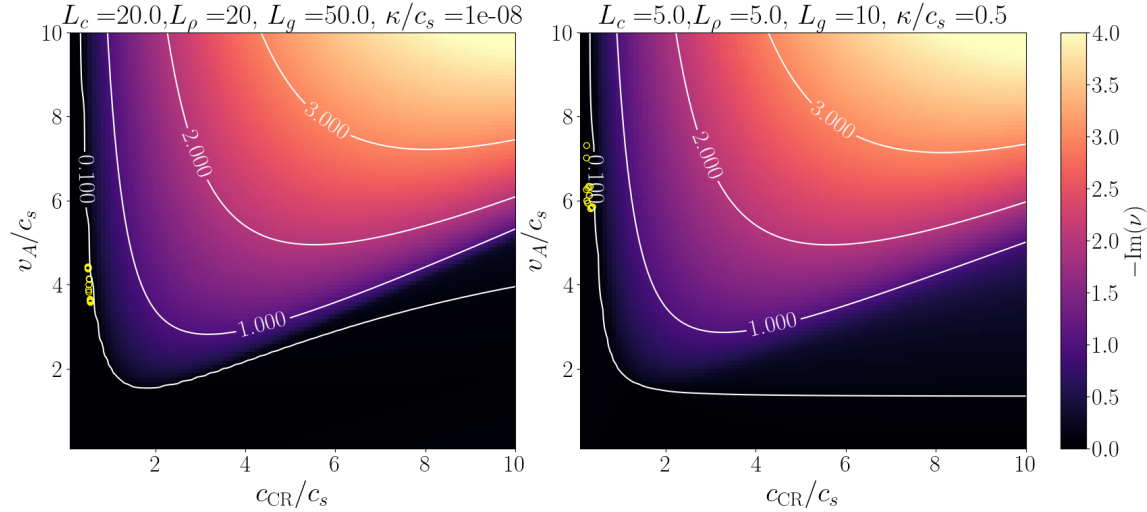
Figure A.2: The re-scaled growth rate -Im(ν) for two of the cases shown in Figure 3.17: HSE_1F_str (left) and HSE_1F_ld (right). In both plots, the white contours label the -Im(ν)=0.1, 1.0, 2.0 and 3.0. The yellow circles are typical $m - c$ pair samples relevant to the instability growth, averaged over y direction.

are contours for growth rate calculated with the same set of parameter, but with moderate diffusion $l_c = 1$. In this parameter space, adding moderate diffusion has limited impact to the growth rate.

Similarly, Figure A.2 shows the re-scaled growth rate solution with two sets of parameters that approximate the simulation HSE_1F_str (left) and HSE_1F_ld (right). The yellow circles label $c_{CR}/c_s - v_A/c_s$ pairs that sampled from the diffuse region in the atmosphere at early time, where the instability emergent. The "bottleneck" limits CR pressure, while strong CR heating preserves gas pressure. As a result, the low c_{CR}/c_{cs} and high v_A/c_s constrains the growth rate to relatively low level in the simulations.

In the left panel, we sample data from $t = 6.8t_0$ to $t = 7.2t_0$ with step $\Delta t = 0.1t_0$. In each time stamp, the data points are collected at location of $x = 25l_0, 30l_0, 35.0l_0$ averaging over the y direction. In the right panel, the sampling period is $t = 3.0t_0$ to $t = 3.5t_0$ with step $\Delta t = 0.1t_0$. In each time stamp, the data points are sampled at $x = 20l_0, 25l_0, 30.0l_0$, averaging over the y direction.

Appendix B

TDE Gravitational Acceleration

We note the variables in the coordinates relative to the black hole with subscript 1 (the black hole centered frame). According to Tejeda & Rosswog (2013), the $\ddot{r}_1$, $\ddot{\theta}_1$, $\ddot{\phi}_1$ and gravitational accelerations in the r_1, θ_1, ϕ_1 directions are:

$$a_{r,1} = -\frac{GM_{\rm BH}}{r_1^2}\left(1-\frac{r_{\rm s}}{r_1}\right)^2 + \frac{r_{\rm s}\dot{r}_1^2}{r_1(r_1-r_{\rm s})} - \frac{3}{2}r_{\rm s}(\dot{\theta}_1^2 + \sin^2\theta_1\dot{\phi}_1^2) \tag{B.1}$$

$$a_{\theta,1} = \dot{r}_1\dot{\theta}_1\frac{r_{\rm s}}{r_1-r_{\rm s}} \tag{B.2}$$

$$a_{\phi,1} = \dot{r}_1\dot{\phi}_1\sin\theta_1\frac{r_{\rm s}}{r_1-r_{\rm s}} \tag{B.3}$$

$$\ddot{r}_1 = a_{r,1}, \quad \ddot{\theta}_1 = -\frac{2\dot{r}_1\dot{\theta}_1}{r_1}\left(\frac{r_1-3/2r_{\rm s}}{r_1-r_{\rm s}}\right) + \sin\theta_1\cos\theta_1\dot{\phi}_1^2, \tag{B.4}$$

$$\ddot{\phi}_1 = -\frac{2\dot{r}_1\dot{\theta}_1}{r_1}\left(\frac{r_1-3/2r_{\rm s}}{r_1-r_{\rm s}}\right) - 2\frac{\dot{\phi}_1\dot{\theta}_1}{\tan\theta_1} \tag{B.5}$$

where G is gravitational constant and $M_{\rm BH}$ is the mass of black hole. r_1, θ_1, ϕ_1 are the coordinate with respect to the black hole, $\dot{r}_1$, $\dot{\theta}_1$, $\dot{\phi}_1$ are the corresponding first derivatives, $\ddot{r}_1$, $\ddot{\theta}_1$, $\ddot{\phi}_1$ are the corresponding second derivatives .

To calculate the gravitational accelerations relative to the origin, first we obtain the coordinates r, θ, ϕ and velocities $v_{\rm r} = \dot{r}$, $v_\theta = r\dot{\theta}$, $v_\phi = r\sin\theta\dot{\phi}$, then transform them into Cartesian coordinates by

$$x = r\sin\theta\cos\phi, \quad y = r\sin\theta\sin\phi, \quad z = r\cos\theta \tag{B.6}$$

$$\dot{x} = \dot{r}\sin\theta\cos\phi + r\dot{\theta}\cos\theta\cos\phi - r\dot{\phi}\sin\theta\sin\phi \tag{B.7}$$

$$\dot{y} = \dot{r}\sin\theta\sin\phi + r\dot{\theta}\cos\theta\sin\phi + r\dot{\phi}\sin\theta\cos\phi \tag{B.8}$$

$$\dot{z} = \dot{r}\cos\theta - r\dot{\theta}\sin\theta \tag{B.9}$$

Next, we transform the positions and velocities to the black hole centered frame by:

$$x_1 = x + L_{12}, \quad y_1 = y, \quad z_1 = z \tag{B.10}$$

$$\dot{x}_1 = \dot{x}, \quad \dot{y}_1 = \dot{y}, \quad \dot{z}_1 = \dot{z} \tag{B.11}$$

From the Cartesian coordinate positions and velocities, the spherical polar coordinate positions and velocities $\dot{r}_1, \quad \dot{\theta}_1, \quad \dot{\phi}_1$ are:

$$r_1 = \sqrt{x_1^2 + y_1^2 + z_1^2}, \quad \theta_1 = \cos^{-1}(z_1/r_1), \quad \phi_1 = \tan^{-1}(y_1/x_1) \tag{B.12}$$

$$\dot{r}_1 = \frac{x_1\dot{x}_1 + y_1\dot{y}_1 + z z_1}{r_1}, \quad \dot{\theta}_1 = \frac{-\left(x_1^2 + y_1^2\right)\dot{z}_1 + z_1(x_1\dot{x}_1 + y_1\dot{y}_1)}{r_1^2\sqrt{x_1^2 + y_1^2}}, \quad \dot{\phi}_1 = \frac{x_1\dot{y}_1 - y_1\dot{x}_1}{x_1^2 + y_1^2} \tag{B.13}$$

Inserting Equation B.12 and Equation B.13 into Equation B.3 and Equation B.5, we can get the accelerations and coordinate derivatives in the black hole centered frame. The acceleration in the black hole centered frame and the accelerations in our domain (relative to the origin) are the same in Cartesian coordinates, so

$$\ddot{x} = \ddot{x}_1 = -r_1\ddot{\phi}_1 \sin\theta_1 \sin\phi_1 + r_1\ddot{\theta}_1 \cos\theta_1 \cos\phi_1 + \ddot{r}_1 \sin\theta_1 \cos\phi_1$$
$$-2\dot{r}_1\dot{\phi}_1 \sin\theta_1 \sin\phi_1 + 2\dot{r}_1\dot{\theta}_1 \cos\theta_1 \cos\phi_1 - 2r\dot{\theta}_1\dot{\phi}_1 \cos\theta_1 \sin\phi_1$$
$$-r\dot{\theta}_1^2 \sin\theta_1 \cos\phi_1 - r\dot{\phi}_1^2 \sin\theta_1 \cos\phi_1 \tag{B.14}$$
$$\ddot{y} = \ddot{y}_1 = \ddot{r}_1 \sin\theta_1 \sin\phi_1 + r\ddot{\phi}_1 \sin\theta_1 \cos\phi_1 + r\ddot{\theta}_1 \cos\theta_1 \sin\phi_1$$
$$+2r\dot{\theta}_1\dot{\phi}_1 \cos\theta_1 \cos\phi_1 + 2\dot{r}_1\dot{\theta}_1 \cos\theta_1 \sin\phi_1 + 2\dot{r}_1\dot{\phi}_1 \sin\theta_1 \cos\phi_1$$
$$-r\dot{\theta}_1^2 \sin\theta_1 \sin\phi_1 - r\dot{\phi}_1^2 \sin\theta_1 \sin\phi_1 \tag{B.15}$$
$$\ddot{z} = \ddot{z}_1 = -r\ddot{\theta}_1 \sin\theta_1 + \ddot{r}_1 \cos\theta_1 - 2\dot{r}_1\dot{\theta}_1 \sin\theta_1 - r\dot{\theta}_1^2 \cos\theta_1 \tag{B.16}$$

Accordingly, the accelerations in $r, \theta \phi$ directions can be obtained from the Cartesian accelerations

$$a_r = \ddot{x} \sin\theta \cos\phi + \ddot{y} \sin\theta \sin\phi + \ddot{z} \cos\theta \tag{B.17}$$

$$a_\theta = \ddot{x} \cos\theta \cos\phi + \ddot{y} \cos\theta \sin\phi - \ddot{z} \sin\theta \tag{B.18}$$

$$a_\phi = -\ddot{x} \sin\phi + \ddot{y} \cos\phi \tag{B.19}$$

In gas momentum and energy equation, the gravitational acceleration $\mathbf{a}_{\text{grav}}$ refers to $\mathbf{a}_{\text{grav}} = (a_r, a_\theta, a_\phi)$.
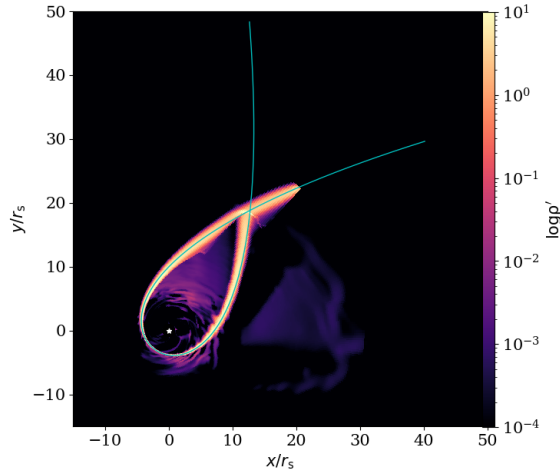
Figure B.1: $\theta = \pi/2$-plane gas density snapshot of A122Edd1 at $t' = 40$, overlapped with the ballistic trajectory we adopt (the cyan solid line, see also Figure 5.2): $M_{\mathrm{BH}} = 10^7 M_\odot$, $M_* = M_\odot$, $R_* = R_\odot$, $\beta = 1.0$. The good match between the streams before collision and ballistic orbit validates our gravity implementation. The white star marks the black hole location.

In order to verify the gravity implementation, we compared the stream trajectory before stream-stream collision with the ballistic trajectory integrated according to Equation B.5 in Figure B.1. Before the collision, gravity dominates the stream momentum and energy source. In the local simulations reported in this paper, the stream accurately follows the ballistic trajectory before collision, showing that the gas indeed is steered by gravity.

In addition to the reported simulations, we also show the gas trajectory before the stream-stream collision in a test global calculation. The test simulation is performed with the same equations and scaling as listed in Section 5.2. However, instead of injecting streams at ϕ direction boundaries, we inject gas at $r = 30.25 r_s$ with velocity $\mathbf{v}_{\mathrm{inj}} = (-0.158c,\ 0.0,\ 7.19 \times 10^{-2} c)$. The stream density is also calibrated to $f_{\mathrm{Edd}} = 1.0$, with initial temperature $T_{\mathrm{inj}} = 10^5 \mathrm{K}$. The test calculation has spherical polar coordinate domain of $(1.1 r_s, 140.0 r_s) \times (0, \pi) \times (0, 2\pi)$. The root level is also resolved with $[64 \times 32 \times 64]$ cells. Three levels of static mesh refinement is applied to the region of $(1.2 r_s, 30.0 r_s) \times (0.48\pi, 0.52\pi) \times (0, 2\pi)$ in r, θ, ϕ direction. With this set-up, we cannot resolve the stream scale height H at the injection site, according to estimation in Section 5.2. At the stream injection site, the stream cross-section is about ~ 200 times larger than in the local simulations.

Figure B.1 shows the $\theta = \pi/2$-plane gas density snapshot at $t' = 0.27$, the cyan solid line shows the same orbit we adopt in the reported local simulations. The gas stream follows the ballistic trajectory well before collision, and is able to reproduce the collision angle and radius when intersecting with itself. The slight deviation from the ballistic trajectory after the pericenter is due to the slight angular momentum dissipation due to radiation force in the pericenter. We will elaborate the set-up detail and pursue further studies with similar global set-up in a subsequent paper.

APPENDIX C

TDE RESOLUTION STUDY

In order to understand better how resolution affects the radiation mediated shock at stream-stream collision site, Figure C.1 shows the gas and radiation profile along the two streams. In the left panel, we show the gas density snapshot for our fiducial resolution of A122Edd1, the black solid lines are part of the ballistic trajectory shown in Figure 5.2. It also shows that before the collision, the radiation energy and thermal energy are small compared to stream kinetic energy.

Along the stream, we sample some data points (as shown in the red crosses) to study gas properties. From top to botoom, right panels in Figure C.1 show the gas density, gas temperature, and radiation energy density as a function of distance to the stream injection site at the left ϕ direction boundary. The blue lines are for A122Edd_LR and red lines are for A122Edd. The gas density is lower in the low resolution simulation due to the larger stream cross-section. The peak radiation energy density in A122Edd_LR at the shock, however, is about two orders of magnitude lower than in A122Edd, suggesting that less kinetic energy is converted to radiation energy at the shock. The lower efficiency is likely due to both the under-resolved shock and the lower local optical depth in A122Edd_LR.

We perform the simulations with the resolution specified in Section 5.2, where the streams before collision are resolved with five levels of SMR and the shock region is resolved with six levels of SMR, and the radiation field is resolved with 48 angles. In the following resolution study, we present two more simulations: A122Edd_R45 and A122Edd_R45_N80. Both simulations are with lower spatial resolution where the streams before collision are resolved with four levels of SMR and the shock region is resolved with five levels of SMR. However, we set $n_\mu = 4$ angles per octant in
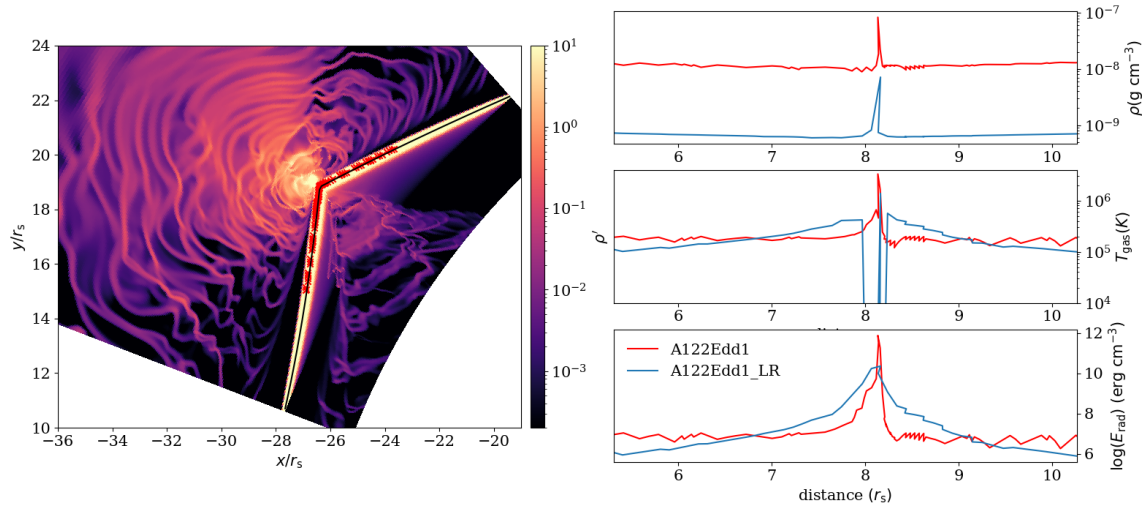
Figure C.1: Left: gas density snapshot of A122Edd1 volume average from $\phi = 1.56 - 1.59$ near $\theta = \pi/2$-plane, zoom-in view of Figure 5.3 upper left panel. The black solid line is part of the ballistic trajectory, equivalent to the orbit shown in Figure 5.2. Red cross data points are the sampled data points for the right column plots. Right: gas density (the first row), gas temperature (the second row) and radiation energy density (the third row) as a function of distance to the stream injection point at the inner ϕ boundary. The curves are plotted with the data sampled from the left panel along the stream before collision (indicated by the red cross points). The blue lines are for A122Edd1_LR, the red lines are A122Edd1.

A122Edd_R45_N80, so there are $n_{\mathrm{oct}}n_{\mu}(n_{\mu}+1)/2 = 80$ angles in total.

Figure C.2 compares density snapshots of these three simulations on different planes. The overall gas density distribution are similar. The lower spatial resolution (compare the second column to the first column) simulations produce less structure after the collision, but did not significantly change the photospheric radius. Increasing the number of discretization angles (compare the second column and the third column) in the radiation field has a only weak effect on the morphology of downstream gas.
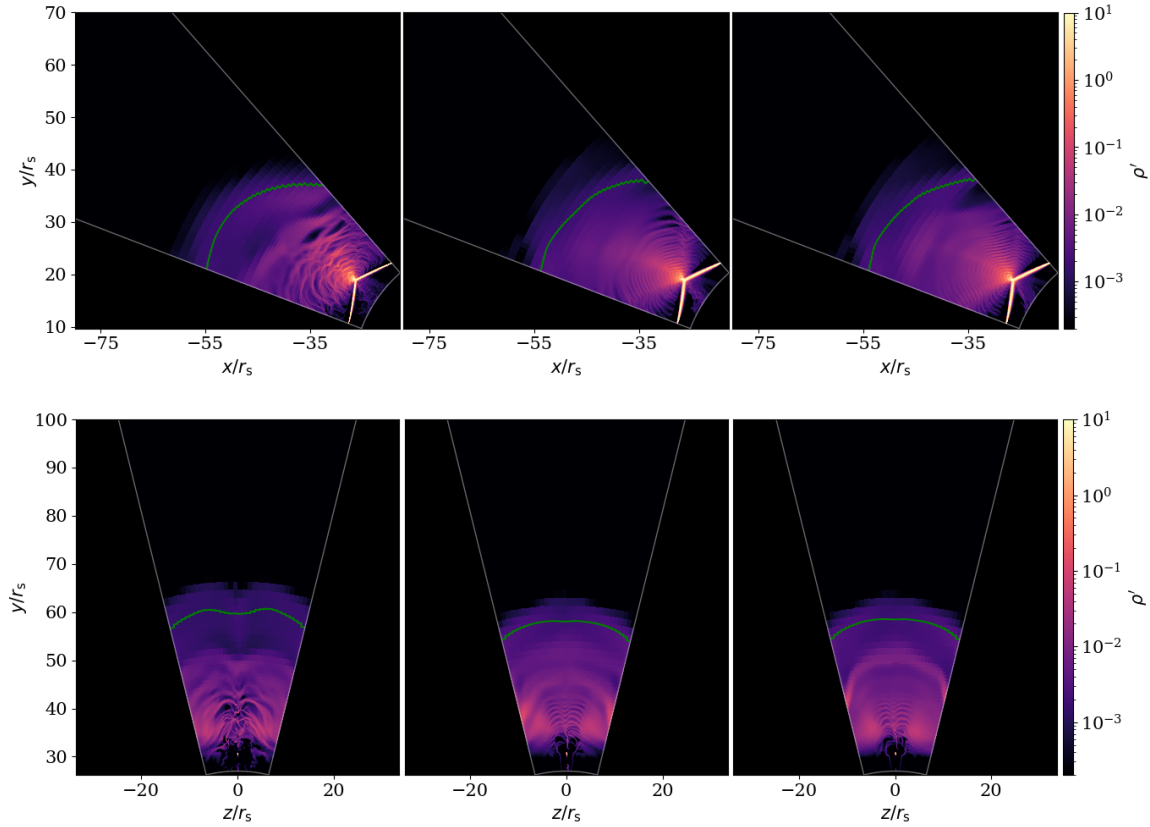
Figure C.2: Similar to Figure 5.3, gas density snapshots at $t = 0.3$ for A122Edd1 (the first column) A122Edd1_R45 (the second column) and A122Edd1_R45_N80 (the third column). A122Edd1 is the fiducial simulation, A122Edd1_R45 has one level lower of SMR compared to the fiducial simulation, A122Edd1_R45_N80 has one level lower of SMR, but higher angular resolution for radiation transfer. In each column, the upper plot shows volume average from $\phi = 1.56 - 1.59$ near $\theta = \pi/2$-plane, the lower plot shows volume average from $\theta = 2.52 - 2.55$ near mid-ϕ-plane. The green solid line shows the same average for the photosphere radius $R_{\tau=1}$ as defined in Equation 5.2.

REFERENCES

Aguirre, A., Hernquist, L., Katz, N., Gardner, J., & Weinberg, D. 2001, The Astrophysical Journal Letters, 556, L11

Andalman, Z., Liska, M., Tchekhovskoy, A., Coughlin, E., & Stone, N. 2022, AAS/High Energy Astrophysics Division, 54, 206

Bai, X.-N., Ostriker, E. C., Plotnikov, I., & Stone, J. M. 2019, The Astrophysical Journal, 876, 60

Bambic, C. J., Bai, X.-N., & Ostriker, E. C. 2021, arXiv preprint arXiv:2102.11877

Banda-Barragán, W. E., Parkin, E. R., Federrath, C., Crocker, R. M., & Bicknell, G. V. 2016, Monthly Notices of the Royal Astronomical Society, 455, 1309

Batra, G., Lu, W., Bonnerot, C., & Phinney, E. S. 2023, Monthly Notices of the Royal Astronomical Society, 520, 5192

Begelman, M. C., & Fabian, A. C. 1990, Monthly Notices of the Royal Astronomical Society, 244, 26P

Begelman, M. C., & Zweibel, E. G. 1994, The Astrophysical Journal, 431, 689

Ben-Ami, S., Shvartzvald, Y., Waxman, E., et al. 2022, in Space Telescopes and Instrumentation 2022: Ultraviolet to Gamma Ray, Vol. 12181, SPIE, 13–23

Benson, A. J., Bower, R. G., Frenk, C. S., et al. 2003, The Astrophysical Journal, 599, 38

Bish, H. V., Werk, J. K., Prochaska, J. X., et al. 2019, The Astrophysical Journal, 882, 76

Bolatto, A. D., Warren, S. R., Leroy, A. K., et al. 2013, Nature, 499, 450

Bonnerot, C., & Lu, W. 2022, Monthly Notices of the Royal Astronomical Society, 511, 2147

Bonnerot, C., Lu, W., & Hopkins, P. F. 2021, Monthly Notices of the Royal Astronomical Society, 504, 4885

Bonnerot, C., Pessah, M. E., & Lu, W. 2022, The Astrophysical Journal Letters, 931, L6

Bonnerot, C., Price, D. J., Lodato, G., & Rossi, E. M. 2017, Monthly Notices of the Royal Astronomical Society, 469, 4879

Bonnerot, C., & Stone, N. 2021, Space Science Reviews, 217, 1

Booth, C., Agertz, O., Kravtsov, A. V., & Gnedin, N. Y. 2013, The Astrophysical Journal Letters, 777, L16

Boulares, A., & Cox, D. P. 1990, The Astrophysical Journal, 365, 544

Bower, R. G., Benson, A. J., & Crain, R. A. 2012, Monthly Notices of the Royal Astronomical Society, 422, 2816

Breitschwerdt, D., McKenzie, J., & Völk, H. 1991, Astronomy and Astrophysics, 245, 79

—. 1993, Astronomy and Astrophysics, 269, 54

Bricman, K., & Gomboc, A. 2020, The Astrophysical Journal, 890, 73

Brüggen, M., & Scannapieco, E. 2016, The Astrophysical Journal, 822, 31

Brüggen, M., & Scannapieco, E. 2020, The Astrophysical Journal, 905, 19

Buck, T., Pfrommer, C., Pakmor, R., Grand, R. J., & Springel, V. 2020, Monthly Notices of the Royal Astronomical Society, 497, 1712

Buck, T., Pfrommer, C., Pakmor, R., Grand, R. J. J., & Springel, V. 2019, arXiv e-prints, arXiv:1911.00019

Bustard, C., & Zweibel, E. G. 2020, arXiv preprint arXiv:2012.06585

—. 2021, The Astrophysical Journal, 913, 106

Bustard, C., Zweibel, E. G., D'Onghia, E., Gallagher III, J., & Farber, R. 2020, The Astrophysical Journal, 893, 29

Butsky, I. S., Fielding, D. B., Hayward, C. C., et al. 2020, The Astrophysical Journal, 903, 77

Butsky, I. S., & Quinn, T. R. 2018, The Astrophysical Journal, 868, 108

Butsky, I. S., Werk, J. K., Tchernyshyov, K., et al. 2021, arXiv preprint arXiv:2106.14889

Chabrier, G. 2005, The Initial Mass Function 50 Years Later, 41

Chan, C.-H., Piran, T., & Krolik, J. H. 2021, The Astrophysical Journal, 914, 107

Chan, T., Keres, D., Hopkins, P., et al. 2019, Monthly Notices of the Royal Astronomical Society, 488, 3716

Chan, T. K., Kereš, D., Hopkins, P. F., et al. 2019, Monthly Notices of the Royal Astronomical Society, 488, 3716

Chevalier, R. A., & Clegg, A. W. 1985a, Nature, 317, 44

—. 1985b, Nature, 317, 44

Cicone, C., Maiolino, R., Sturm, E., et al. 2014, Astronomy and Astrophysics, 562, A21

Cooper, J. L., Bicknell, G. V., Sutherland, R. S., & Bland-Hawthorn, J. 2009, The Astrophysical Journal, 703, 330

Coughlin, E. R. 2023, Monthly Notices of the Royal Astronomical Society, stad1347

Coughlin, E. R., & Begelman, M. C. 2014, The Astrophysical Journal, 781, 82

Coughlin, E. R., Nixon, C., Begelman, M. C., & Armitage, P. J. 2016, Monthly Notices of the Royal Astronomical Society, 459, 3089

Crocker, R. M., Krumholz, M. R., & Thompson, T. A. 2021, Monthly Notices of the Royal Astronomical Society, 503, 2651

Crocker, R. M., Krumholz, M. R., & Thompson, T. A. 2021, Monthly Notices of the Royal Astronomical Society, 502, 1312

—. 2021a, Monthly Notices of the Royal Astronomical Society, 502, 1312

—. 2021b, Monthly Notices of the Royal Astronomical Society, 503, 2651

Curd, B. 2021, Monthly Notices of the Royal Astronomical Society, 507, 3207

Dai, L., McKinney, J. C., & Miller, M. C. 2015, The Astrophysical Journal Letters, 812, L39

Dai, L., McKinney, J. C., Roth, N., Ramirez-Ruiz, E., & Miller, M. C. 2018, The Astrophysical Journal Letters, 859, L20

Davis, S. W., Jiang, Y.-F., Stone, J. M., & Murray, N. 2014, The Astrophysical Journal, 796, 107

Davis, S. W., Jiang, Y.-F., Stone, J. M., & Murray, N. 2014, The Astrophysical Journal, 796, 107

Davis, S. W., Stone, J. M., & Jiang, Y.-F. 2012, The Astrophysical Journal Supplement Series, 199, 9

de los Reyes, M. A., & Kennicutt Jr, R. C. 2019, The Astrophysical Journal, 872, 16

Dittmann, A. J. 2022, Monthly Notices of the Royal Astronomical Society, 511, 3408

Erb, D. K. 2008, The Astrophysical Journal, 674, 151

Evans, C. R., & Kochanek, C. S. 1989, The Astrophysical Journal, 346, L13

Everett, J. E., Zweibel, E. G., Benjamin, R. A., et al. 2008, The Astrophysical Journal, 674, 258

Eyles-Ferris, R., Starling, R., O'Brien, P., Nixon, C., & Coughlin, E. R. 2022, Monthly Notices of the Royal Astronomical Society, 517, 6013

Fabian, A. C. 1994, Annual Review of Astronomy and Astrophysics, 32, 277

Fabian, A. C. 2012, Annual Review of Astronomy and Astrophysics, 50, 455

Ferriere, K. M. 2001, Reviews of Modern Physics, 73, 1031

Field, G. B. 1965, The Astrophysical Journal, 142, 531

Fielding, D., Quataert, E., & Martizzi, D. 2018, Monthly Notices of the Royal Astronomical Society, 481, 3325

Fielding, D. B., Ostriker, E. C., Bryan, G. L., & Jermyn, A. S. 2020, The Astrophysical Journal Letters, 894, L24

Finlator, K., & Davé, R. 2008, Monthly Notices of the Royal Astronomical Society, 385, 2181

Gafton, E., & Rosswog, S. 2019, Monthly Notices of the Royal Astronomical Society, 487, 4790

Geach, J. E., Tremonti, C., Diamond-Stanic, A. M., et al. 2018, The Astrophysical Journal Letters, 864, L1

Gehrels, N., & Cannizzo, J. 2015

Gezari, S. 2021, Annual Review of Astronomy and Astrophysics, 59, 21

Gezari, S., Martin, D., Forster, K., et al. 2013, The Astrophysical Journal, 766, 60

Girichidis, P., Naab, T., Hanasz, M., & Walch, S. 2018, Monthly Notices of the Royal Astronomical Society, 479, 3042

Girichidis, P., Naab, T., Walch, S., & Berlok, T. 2021, arXiv preprint arXiv:2101.08269

Goldtooth, A., Zabludoff, A. I., Wen, S., et al. 2023, Publications of the Astronomical Society of the Pacific, 135, 034101

Greiner, J., Schwarz, R., Zharikov, S., & Orio, M. 2000, arXiv preprint astro-ph/0009430

Gressel, O. 2009, Astronomy & Astrophysics, 498, 661

Gronke, M., & Oh, S. P. 2018, Monthly Notices of the Royal Astronomical Society: Letters, 480, L111

—. 2020, Monthly Notices of the Royal Astronomical Society, 492, 1970

Gronke, M., Oh, S. P., Ji, S., & Norman, C. 2021, arXiv preprint arXiv:2107.13012

Grupe, D., Thomas, H.-C., & Leighly, K. 1999, arXiv preprint astro-ph/9909101

Guillochon, J., Manukian, H., & Ramirez-Ruiz, E. 2014, The Astrophysical Journal, 783, 23

Guillochon, J., & McCourt, M. 2017, The Astrophysical Journal Letters, 834, L19

Guillochon, J., & Ramirez-Ruiz, E. 2015, The Astrophysical Journal, 809, 166

Hambleton, K. M., Bianco, F. B., Street, R., et al. 2022, arXiv preprint arXiv:2208.04499

Hanasz, M., Lesch, H., Naab, T., et al. 2013, The Astrophysical Journal Letters, 777, L38

Hayasaki, K., Stone, N., & Loeb, A. 2016, Monthly Notices of the Royal Astronomical Society, 461, 3760

Heckman, T. M., & Best, P. N. 2014, Annual Review of Astronomy and Astrophysics, 52, 589

Heckman, T. M., Lehnert, M. D., Strickland, D. K., & Armus, L. 2000, The Astrophysical Journal Supplement Series, 129, 493

Heintz, E., Bustard, C., & Zweibel, E. G. 2020, The Astrophysical Journal, 891, 157

Heintz, E., & Zweibel, E. G. 2018, The Astrophysical Journal, 860, 97

Hin Navin Tsung, T., Oh, S. P., & Jiang, Y.-F. 2021, arXiv e-prints, arXiv

Holguin, F., Ruszkowski, M., Lazarian, A., Farber, R., & Yang, H. K. 2019, Monthly Notices of the Royal Astronomical Society, 490, 1271

Hopkins, P. F., Chan, T., Ji, S., et al. 2021, Monthly Notices of the Royal Astronomical Society, 501, 3640

Hopkins, P. F., Quataert, E., & Murray, N. 2012, Monthly Notices of the Royal Astronomical Society, 421, 3522

Hopkins, P. F., Squire, J., & Butsky, I. S. 2021a, arXiv preprint arXiv:2103.10443

Hopkins, P. F., Chan, T., Garrison-Kimmel, S., et al. 2020, Monthly Notices of the Royal Astronomical Society, 492, 3465

Huang, X., & Davis, S. W. 2021, arXiv preprint arXiv:2105.11506

Huang, X., Davis, S. W., & Zhang, D. 2020, The Astrophysical Journal, 893, 50

Hung, T., Gezari, S., Blagorodnova, N., et al. 2017, The Astrophysical Journal, 842, 29

Iglesias, C. A., & Rogers, F. J. 1996, The astrophysical journal, 464, 943

Ipavich, F. M. 1975, The Astrophysical Journal, 196, 107

Ipavich, F. M. 1975, The Astrophysical Journal, 196, 107

Jacquet, E., & Krumholz, M. R. 2011, The Astrophysical Journal, 730, 116

Janković, T., Bonnerot, C., & Gomboc, A. 2023, Spin-induced offset stream self-crossing shocks in tidal disruption events, , , arXiv:2303.16230

Jennings, R. M., & Li, Y. 2020, Monthly Notices of the Royal Astronomical Society

Ji, S., Chan, T., Hummels, C. B., et al. 2020, Monthly Notices of the Royal Astronomical Society, 496, 4221

Jiang, Y.-F. 2021, The Astrophysical Journal Supplement Series, 253, 49

Jiang, Y.-F., Davis, S. W., & Stone, J. M. 2013, The Astrophysical Journal, 763, 102

Jiang, Y.-F., Guillochon, J., & Loeb, A. 2016, The Astrophysical Journal, 830, 125

Jiang, Y.-F., & Oh, S. P. 2018, The Astrophysical Journal, 854, 5

Jiang, Y.-F., & Oh, S. P. 2018, The Astrophysical Journal, 854, 5

Jiang, Y.-F., Stone, J. M., & Davis, S. W. 2014, The Astrophysical Journal Supplement Series, 213, 7

Jiang, Y.-F., Stone, J. M., & Davis, S. W. 2014, The Astrophysical Journal, 796, 106

Jubelgas, M., Springel, V., Enßlin, T., & Pfrommer, C. 2008, Astronomy & Astrophysics, 481, 33

Kara, E., Dai, L., Reynolds, C., & Kallman, T. 2018, Monthly Notices of the Royal Astronomical Society, 474, 3593

Kempski, P., & Quataert, E. 2020, Monthly Notices of the Royal Astronomical Society, 493, 1801

Kennicutt Jr, R. C. 1998, The Astrophysical Journal, 498, 541

Kennicutt Jr, R. C., & De Los Reyes, M. A. 2021, The Astrophysical Journal, 908, 61

Kennicutt Jr, R. C., & Evans, N. J. 2012, Annual Review of Astronomy and Astrophysics, 50, 531

Kesden, M. 2012, Physical Review D, 86, 064026

Kim, J.-G., Ostriker, E. C., & Filippova, N. 2021, The Astrophysical Journal, 911, 128

Kim, S. S., Park, M.-G., & Lee, H. M. 1999, The Astrophysical Journal, 519, 647

Klein, R. I., McKee, C. F., & Colella, P. 1994, The Astrophysical Journal, 420, 213

Klein, R. I., McKee, C. F., & Colella, P. 1994, The Astrophysical Journal, 420, 213

Kochanek, C. 2016, Monthly Notices of the Royal Astronomical Society, 458, 127

Kochanek, C., Shappee, B., Stanek, K., et al. 2017, Publications of the Astronomical Society of the Pacific, 129, 104502

Komossa, S. 2015, Journal of High Energy Astrophysics, 7, 148

Koyama, H., & Inutsuka, S.-i. 2004, The Astrophysical Journal Letters, 602, L25

Krieger, N., Bolatto, A. D., Walter, F., et al. 2019, arXiv e-prints, arXiv:1907.00731

Krieger, N., Walter, F., Bolatto, A. D., et al. 2021, arXiv preprint arXiv:2105.07440

Krumholz, M. R., & Tan, J. C. 2007, The Astrophysical Journal, 654, 304

Krumholz, M. R., & Thompson, T. A. 2012, The Astrophysical Journal, 760, 155

Krumholz, M. R., & Thompson, T. A. 2012, The Astrophysical Journal, 760, 155

—. 2013, Monthly Notices of the Royal Astronomical Society, 434, 2329

Lacki, B. C., Thompson, T. A., & Quataert, E. 2010, The Astrophysical Journal, 717, 1

Law-Smith, J. A., Coulter, D. A., Guillochon, J., Mockler, B., & Ramirez-Ruiz, E. 2020, The Astrophysical Journal, 905, 141

Leroy, A. K., Walter, F., Martini, P., et al. 2015, The Astrophysical Journal, 814, 83

Lin, D., Carrasco, E. R., Grupe, D., et al. 2011, The Astrophysical Journal, 738, 52

Lin, D., Strader, J., Carrasco, E. R., et al. 2018a, Monthly Notices of the Royal Astronomical Society, 474, 3000

—. 2018b, Nature Astronomy, 2, 656

Lin, Y., Oh, S. P., Furlanetto, S. R., & Sutter, P. 2016, Monthly Notices of the Royal Astronomical Society, 461, 3361

Liptai, D., Price, D. J., Mandel, I., & Lodato, G. 2019, arXiv preprint arXiv:1910.10154

Lodato, G., King, A., & Pringle, J. 2009, Monthly Notices of the Royal Astronomical Society, 392, 332

Lodato, G., & Rossi, E. M. 2011, Monthly Notices of the Royal Astronomical Society, 410, 359

Loeb, A., & Ulmer, A. 1997, The Astrophysical Journal, 489, 573

Lu, W., & Bonnerot, C. 2020, Monthly Notices of the Royal Astronomical Society, 492, 686

MacLeod, M., Guillochon, J., & Ramirez-Ruiz, E. 2012, The Astrophysical Journal, 757, 134

Maksym, W., Ulmer, M., Eracleous, M., Guennou, L., & Ho, L. 2013, Monthly Notices of the Royal Astronomical Society, 435, 1904

Mao, S. A., & Ostriker, E. C. 2018, The Astrophysical Journal, 854, 89

Martin, C. L. 1998, The Astrophysical Journal, 506, 222

—. 2005, The Astrophysical Journal, 621, 227

Martin, C. L. 2005, The Astrophysical Journal, 621, 227

Martin, D. C., Fanson, J., Schiminovich, D., et al. 2005, The Astrophysical Journal Letters, 619, L1

McCourt, M., O'Leary, R. M., Madigan, A.-M., & Quataert, E. 2015, Monthly Notices of the Royal Astronomical Society, 449, 2

McCourt, M., O'Leary, R. M., Madigan, A.-M., & Quataert, E. 2015, Monthly Notices of the Royal Astronomical Society, 449, 2

McCourt, M., Sharma, P., Quataert, E., & Parrish, I. J. 2012, Monthly Notices of the Royal Astronomical Society, 419, 3319

Metzger, B. D. 2022, The Astrophysical Journal Letters, 937, L12

Metzger, B. D., & Stone, N. C. 2016, Monthly Notices of the Royal Astronomical Society, 461, 948

Miller, M. C. 2015, The Astrophysical Journal, 805, 83

Mockler, B., Guillochon, J., & Ramirez-Ruiz, E. 2019, The Astrophysical Journal, 872, 151

Morganti, R., Veilleux, S., Oosterloo, T., Teng, S. H., & Rupke, D. 2016, Astronomy and Astrophysics, 593, A30

Muñoz-Vergara, D., Nagar, N. M., Ramakrishnan, V., et al. 2019, Monthly Notices of the Royal Astronomical Society, 487, 3679

Murray, N., Ménard, B., & Thompson, T. A. 2011, The Astrophysical Journal, 735, 66

Murray, N., Quataert, E., & Thompson, T. A. 2005, The Astrophysical Journal, 618, 569

Namekata, D., Umemura, M., & Hasegawa, K. 2014, Monthly Notices of the Royal Astronomical Society, 443, 2018

Oosterloo, T., Raymond Oonk, J. B., Morganti, R., et al. 2017, Astronomy and Astrophysics, 608, A38

Oppenheimer, B. D., Davé, R., Kereš, D., et al. 2010, Monthly Notices of the Royal Astronomical Society, 406, 2325

Paglione, T. A. D., & Abrahams, R. D. 2012, The Astrophysical Journal, 755, 106

Pal Choudhury, P., Sharma, P., & Quataert, E. 2019, Monthly Notices of the Royal Astronomical Society, 488, 3195

Parker, E. N. 1966, The Astrophysical Journal, 145, 811

Phinney, E. 1989, in Symposium-International Astronomical Union, Vol. 136, Cambridge University Press, 543–553

Piran, T., Svirski, G., Krolik, J., Cheng, R. M., & Shiokawa, H. 2015, The Astrophysical Journal, 806, 164

Pollack, J. B., Hollenbach, D., Beckwith, S., et al. 1994, The Astrophysical Journal, 421, 615

Proga, D., Jiang, Y.-F., Davis, S. W., Stone, J. M., & Smith, D. 2014, The Astrophysical Journal, 780, 51

Proga, D., & Waters, T. 2015, The Astrophysical Journal, 804, 137

Puchwein, E., & Springel, V. 2013, Monthly Notices of the Royal Astronomical Society, 428, 2966

Quataert, E., Jiang, Y.-F., & Thompson, T. A. 2021, arXiv e-prints, arXiv:2106.08404

Quataert, E., Thompson, T. A., & Jiang, Y.-F. 2021, arXiv preprint arXiv:2102.05696

Ramirez-Ruiz, E., & Rosswog, S. 2009, The Astrophysical Journal, 697, L77

Ramzan, B., Ko, C., & Chernyshov, D. 2020, The Astrophysical Journal, 905, 117

Rees, M. J. 1988, Nature, 333, 523

Rosswog, S., Ramirez-Ruiz, E., & Hix, W. R. 2009, The Astrophysical Journal, 695, 404

Roth, N., Kasen, D., Guillochon, J., & Ramirez-Ruiz, E. 2016, The Astrophysical Journal, 827, 3

Rupke, D. S., Veilleux, S., & Sanders, D. B. 2002, The Astrophysical Journal, 570, 588

Ruszkowski, M., Yang, H.-Y. K., & Zweibel, E. 2017, The Astrophysical Journal, 834, 208

Ruszkowski, M., Yang, H.-Y. K., & Zweibel, E. 2017, The Astrophysical Journal, 834, 208

Rybicki, G. B., & Lightman, A. P. 1986, Radiative Processes in Astrophysics

Ryu, D., Kim, J., Hong, S. S., & Jones, T. W. 2003, The Astrophysical Journal, 589, 338

Ryu, T., Krolik, J., & Piran, T. 2020, The Astrophysical Journal, 904, 73

Sadowski, A., Tejeda, E., Gafton, E., Rosswog, S., & Abarca, D. 2016, Monthly Notices of the Royal Astronomical Society, 458, 4250

Salem, M., & Bryan, G. L. 2014, Monthly Notices of the Royal Astronomical Society, 437, 3312

Salem, M., Bryan, G. L., & Corlies, L. 2016, Monthly Notices of the Royal Astronomical Society, 456, 582

Sánchez-Salcedo, F., Vázquez-Semadeni, E., & Gazol, A. 2002, The Astrophysical Journal, 577, 768

Saxton, R., Read, A., Esquej, P., et al. 2012, Astronomy & Astrophysics, 541, A106

Scannapieco, E., & Brüggen, M. 2015, The Astrophysical Journal, 805, 158

Scannapieco, E., & Brüggen, M. 2015, The Astrophysical Journal, 805, 158

Scannapieco, E., Brüggen, M., Banda-Barragán, W., Federrath, C., et al. 2020, The Astrophysical Journal, 892, 59

Schulz, R., Morganti, R., Nyland, K., et al. 2018, Astronomy and Astrophysics, 617, A38

Semenov, D., Henning, T., Helling, C., Ilgner, M., & Sedlmayr, E. 2003, Astronomy & Astrophysics, 410, 611

Semenov, D., Henning, T., Helling, C., Ilgner, M., & Sedlmayr, E. 2003, Astronomy and Astrophysics, 410, 611

Sharma, P., Colella, P., & Martin, D. F. 2010a, SIAM Journal on Scientific Computing, 32, 3564

Sharma, P., Parrish, I. J., & Quataert, E. 2010b, The Astrophysical Journal, 720, 652

Shiokawa, H., Krolik, J. H., Cheng, R. M., Piran, T., & Noble, S. C. 2015, The Astrophysical Journal, 804, 85

Shopbell, P. L., & Bland-Hawthorn, J. 1998, The Astrophysical Journal, 493, 129

Skilling, J. 1971, The Astrophysical Journal, 170, 265

Skilling, J. 1971, The Astrophysical Journal, 170, 265

Skinner, M. A., & Ostriker, E. C. 2013, The Astrophysical Journal Supplement Series, 206, 21

—. 2015, The Astrophysical Journal, 809, 187

Socrates, A., Davis, S. W., & Ramirez-Ruiz, E. 2008, The Astrophysical Journal, 687, 202

Socrates, A., Davis, S. W., & Ramirez-Ruiz, E. 2008, The Astrophysical Journal, 687, 202

Somerville, R. S., & Davé, R. 2015, Annual Review of Astronomy and Astrophysics, 53, 51

Spaulding, A., & Chang, P. 2021, Monthly Notices of the Royal Astronomical Society, 501, 1748

Spilker, J. S., Aravena, M., Béthermin, M., et al. 2018, Science, 361, 1016

Spilker, J. S., Phadke, K. A., Aravena, M., et al. 2020, The Astrophysical Journal, 905, 85

Steinberg, E., & Stone, N. C. 2022, arXiv preprint arXiv:2206.10641

Stone, J. M., Tomida, K., White, C. J., & Felker, K. G. 2020, arXiv preprint arXiv:2005.06651

Stone, N. C., & Metzger, B. D. 2016, Monthly Notices of the Royal Astronomical Society, 455, 859

Strickland, D. K., & Heckman, T. M. 2007, The Astrophysical Journal, 658, 258

—. 2009, The Astrophysical Journal, 697, 2030

Strickland, D. K., & Heckman, T. M. 2009, The Astrophysical Journal, 697, 2030

Strubbe, L. E., & Quataert, E. 2009, Monthly Notices of the Royal Astronomical Society, 400, 2070

Tadhunter, C., Holden, L., Ramos Almeida, C., & Batcheldor, D. 2019, Monthly Notices of the Royal Astronomical Society, 488, 1813

Tan, B., Oh, S. P., & Gronke, M. 2021, Monthly Notices of the Royal Astronomical Society, 502, 3179

Tejeda, E., & Rosswog, S. 2013, Monthly Notices of the Royal Astronomical Society, 433, 1930

Thomas, T., & Pfrommer, C. 2019, Monthly Notices of the Royal Astronomical Society, 485, 2977

—. 2021, arXiv preprint arXiv:2105.08090

Thompson, T. A., Quataert, E., Zhang, D., & Weinberg, D. H. 2016, Monthly Notices of the Royal Astronomical Society, 455, 1830

Thomsen, L. L., Kwan, T. M., Dai, L., et al. 2022, The Astrophysical Journal Letters, 937, L28

Tsang, B. T.-H., & Milosavljević, M. 2015, Monthly Notices of the Royal Astronomical Society, 453, 1108

Tsung, T. H. N., Oh, S. P., & Jiang, Y.-F. 2021, arXiv preprint arXiv:2107.07543

Tumlinson, J., Peeples, M. S., & Werk, J. K. 2017, Annual Review of Astronomy and Astrophysics, 55, 389

Tumlinson, J., Thom, C., Werk, J. K., et al. 2013, The Astrophysical Journal, 777, 59

Uhlig, M., Pfrommer, C., Sharma, M., et al. 2012, Monthly Notices of the Royal Astronomical Society, 423, 2374

Ulmer, A. 1999, The Astrophysical Journal, 514, 180

Van der Walt, S., Schönberger, J. L., Nunez-Iglesias, J., et al. 2014, PeerJ, 2, e453

Van Velzen, S., Farrar, G. R., Gezari, S., et al. 2011, The Astrophysical Journal, 741, 73

Van Velzen, S., Gezari, S., Hammerstein, E., et al. 2021, The Astrophysical Journal, 908, 4

Veilleux, S., Cecil, G., & Bland-Hawthorn, J. 2005, Annual Review of Astronomy and Astrophysics, 43, 769

Veilleux, S., Cecil, G., & Bland-Hawthorn, J. 2005, Annu. Rev. Astron. Astrophys., 43, 769

Veilleux, S., Maiolino, R., Bolatto, A. D., & Aalto, S. 2020, The Astronomy and Astrophysics Review, 28, 1

Veilleux, S., Rupke, D. S. N., & Swaters, R. 2009, The Astrophysical Journal Letters, 700, L149

VERITAS Collaboration, Acciari, V. A., Aliu, E., et al. 2009, Nature, 462, 770

Wakker, B. P., Savage, B. D., Fox, A. J., Benjamin, R. A., & Shapiro, P. R. 2012, The Astrophysical Journal, 749, 157

Walter, F., Bolatto, A. D., Leroy, A. K., et al. 2017, The Astrophysical Journal, 835, 265

Waters, T., & Proga, D. 2016, Monthly Notices of the Royal Astronomical Society, 460, L79

Wentzel, D. G. 1974, Annual review of astronomy and astrophysics, 12, 71

Werk, J. K., Prochaska, J. X., Tumlinson, J., et al. 2014, The Astrophysical Journal, 792, 8

Werk, J. K., Rubin, K. H., Bish, H. V., et al. 2019, The Astrophysical Journal, 887, 89

Wevers, T., van Velzen, S., Jonker, P. G., et al. 2017, Monthly Notices of the Royal Astronomical Society, 471, 1694

Wevers, T., Pasham, D., van Velzen, S., et al. 2019, Monthly Notices of the Royal Astronomical Society, 488, 4816

Wiener, J., Oh, S. P., & Guo, F. 2013, Monthly Notices of the Royal Astronomical Society, 434, 2209

Wiener, J., Pfrommer, C., & Oh, S. P. 2017, Monthly Notices of the Royal Astronomical Society, 467, 906

Wiener, J., Zweibel, E. G., & Ruszkowski, M. 2019, Monthly Notices of the Royal Astronomical Society, 489, 205

Wiener, J., Zweibel, E. G., & Ruszkowski, M. 2019a, Monthly Notices of the Royal Astronomical Society, 1948

—. 2019b, arXiv e-prints, arXiv:1903.01471

—. 2019c, Monthly Notices of the Royal Astronomical Society, 489, 205

Wiersma, R. P., Schaye, J., & Smith, B. D. 2009, Monthly Notices of the Royal Astronomical Society, 393, 99

Zhang, D. 2018, Galaxies, 6, 114

Zhang, D. 2018, Galaxies, 6, 114

Zhang, D., & Davis, S. W. 2017, The Astrophysical Journal, 839, 54

Zhang, D., Davis, S. W., Jiang, Y.-F., & Stone, J. M. 2018, The Astrophysical Journal, 854, 110

Zhang, D., Davis, S. W., Jiang, Y.-F., & Stone, J. M. 2018, The Astrophysical Journal, 854, 110

Zhang, D., Thompson, T. A., Murray, N., & Quataert, E. 2014, The Astrophysical Journal, 784, 93

Zweibel, E. G. 2020, The Astrophysical Journal, 890, 67